

**Using Machine Learning to Identify and Map Controls of Growing-Season Carbon Dioxide
and Methane Fluxes in the Mackenzie Delta Region**

by

June Skeeter

MSc., The University of South Carolina, 2015

A THESIS SUBMITTED IN PARTIAL FULFILLMENT OF
THE REQUIREMENTS FOR THE DEGREE OF

DOCTOR OF PHILOSOPHY

in

GEOGRAPHY

THE UNIVERSITY OF BRITISH COLUMBIA

Vancouver

January 2022

© June Skeeter, 2022

The following individuals certify that they have read, and recommend to the Faculty of Graduate and Postdoctoral Studies for acceptance, the dissertation entitled:

Using Machine Learning to Identify and Map Controls of Growing-Season Carbon Dioxide and Methane Fluxes in the Mackenzie Delta Region

submitted by June Skeeter in partial fulfillment of the requirements for

the degree of Doctorate of Philosophy

in Geography

Examining Committee:

Co-supervisor

Co-supervisor

Supervisory Committee Member

University Examiner

University Examiner

Additional Supervisory Committee Members:

Supervisory Committee Member

Supervisory Committee Member

Abstract

Climate change is disproportionately impacting the Arctic. The permafrost soils in many regions of the Arctic are carbon-rich; collectively they contain more carbon than Earth's atmosphere.

The Mackenzie Delta in Canada's Western Arctic is one such region. In a warming climate, the permafrost carbon pool is at an increasing risk of destabilizing. Two field campaigns were conducted in the Mackenzie Delta Region to measure carbon dioxide and methane fluxes with eddy covariance methods in 2016 and 2017. Illisarvik, a drained thermokarst lake, was studied over a month during the peak growing season in 2016. Fish Island, a low center polygonal peatland, was studied over the 2017 growing season. Half-hourly fluxes were calculated and filtered with quality control tests. Flux footprints were calculated and overlaid on landscape classification maps to estimate the relative flux contributions from different vegetation types and microtopographic features. For both data sets, neural networks (NN) were trained to map flux responses to large sets of potential soil and climate drivers and flux contributions by landscape classification. The NN were pruned to identify the strongest drivers. The pruned NN were used to gap-fill the flux time series to calculate Net Ecosystem Exchange (NEE) and Net Methane Exchange (NME). The functional relationships identified by the NNs were visualized by plotting model derivates and projecting NN estimates across the domains of key drivers.

Radiative input and temperature were the primary determinants of NEE, and the NN were able to closely map the functional relationships. Spatial heterogeneity had a significant influence on NME and the NN estimates could not map the relationships as accurately. Further analysis was conducted with the Fish Island data. A limited set of surface observations from an automated weather station at Fish Island was paired with reanalysis and satellite data. Regression models were trained on the 2017 field data to estimate a time series of flux divers over the 2009 to 2019

snow-free seasons. The NN were then used to project NEE and NME over the estimated time series. Satellite data was used to assess the plausibility of flux estimates. These estimates contextualize the 2017 observations. They indicate Fish Island was a net growing seasons CO₂ sink and CH₄ source from 2009 to 2019, but shoulder season CO₂ emissions may offset growing season uptake in some years. They also indicated climate warming may reduce carbon uptake during the snow-free seasons.

Lay Summary

Carbon dioxide and methane are two important greenhouse gasses that influence climate change.

My research looks at how these greenhouse gases move into and out of two Arctic ecosystem in the Mackenzie Delta Region. The goal was to understand how these ecosystems influence climate change now, and how that influence may change in the future. The factors that control carbon dioxide and methane exchange in these ecosystems are not well understood. I used machine learning, which is sometimes known as artificial intelligence, to help figure out how weather, climate, soil, and vegetation influence carbon dioxide and methane exchange. I used this information along with climate and satellite data to better understand how the controls of carbon dioxide and methane exchange vary from year to year.

Preface

My supervisors Greg Henry and Andreas Christen helped develop the intial EC experiment design and provided guidance during the research process. I installed the EC system and collected all EC data at Illisarvik, Andre-Anne LaForce collected chamber data at Illisarvik, which I made use of in Chapter 2. Alice Wilson created a vegetation map for Illisarvik in 2016, which I modified slightly for the footprint analysis. I installed the EC system at Fish Island with the help of Rick Kettler and Edwin Amos, and collected all field data from Fish Island myself. I did all EC data processing and spatial analysis, and designed and implemented the neural network analysis.

A version of chapter 2 has been published: Skeeter, J., Christen, A., Laforce, A.-A., Humphreys, E., & Henry, G. (2020). Vegetation influence and environmental controls on greenhouse gas fluxes from a drained thermokarst lake in the western Canadian Arctic. *Biogeosciences*, 17(17), 4421–4441. <https://doi.org/10.5194/bg-17-4421-2020>. I collected and processed the eddy covariance data, conducted all statistical analysis and spatial analysis, wrote the full paper, and made all of the visualizations. Laforce A.-A and I collected the chamber flux samples. Laforce A.-A processed the chamber samples. Christen, A., Humphreys, E., and Henry, G. H. R provided guidance and feedback on the manuscript. Christen, A. and Henry, G. H. R. also helped formulate the design of the experiment.

A version of Chapter 3 has been published: Skeeter, J., Christen, A., & Henry, G. H. R. (2022). Controls on carbon dioxide and methane fluxes from a low-center polygonal peatland in the Mackenzie River Delta, Northwest Territories. *Arctic Science*, 1–27. <https://doi.org/10.1139/as->

[2021-0034](#). I collected and processed all data used in the study. I designed and implemented the statistical and spatial analysis, wrote the entire manuscript, and created all visualizations. Christen, A. and Henry, G. H. R. helped formulate the design of the experiment and provided guidance and feedback on the manuscript.

A version of Chapter 4 will be submitted for publication in Arctic Science, to serve as a follow up paper for the publication stemming from Chapter 3. I designed and implemented the statistical and spatial analysis, wrote the entire manuscript, and created all visualizations.

Christen, A., Henry, G. H. R., and Lantz, T. provided guidance and feedback on the manuscript. Kokelj, S. provided the data from the Fish Island AWS that was used in this analysis.

Table of Contents

Abstract	iii
Lay Summary	v
Preface	vi
Table of Contents.....	viii
List of Tables.....	xiv
List of Figures.....	xvii
List of Abbreviations	xxiv
Acknowledgements	xxix
Dedication	xxx
<i>Chapter 1: Introduction.....</i>	<i>1</i>
1.1 Framing the Problem.....	1
1.2 Tundra Carbon Fluxes.....	3
1.2.1 Components of the Carbon Balance	4
1.2.2 Seasonal Dynamics and Flux Drivers	5
1.2.2.1 Net Ecosystem Exchange	6
1.2.2.2 Net Methane Exchange	8
1.2.3 Spatial Heterogeneity	9
1.3 Defining the Study Area.....	11
1.3.1 Previous Studies in the Mackenzie Delta Region	13

1.3.2	Study Sites.....	13
1.3.2.1	Illisarvik.....	13
1.3.2.2	Fish Island	14
1.4	Eddy Covariance Methods.....	16
1.5	Machine Learning	17
1.5.1	Random Forests	18
1.5.2	Neural Networks	19
1.6	Research Objectives	21

*Chapter 2: Vegetation influence and environmental controls on greenhouse gas fluxes from a drained thermokarst lake in the western Canadian Arctic.....*22

2.1	Introduction.....	22
2.2	Methods	24
2.2.1	Study Site and Data Collection	24
2.2.2	Weather and Soil Measurements	28
2.2.3	EC Fluxes	29
2.2.4	Closed Chamber Measurements.....	32
2.2.4.1	Upscaling	34
2.2.5	Factor Selection and Gap Filling.....	35
2.2.5.1	Flux Partitioning.....	37
2.2.5.2	Factor Analysis.....	38
2.3	Results	38
2.3.1	EC Observations	40
2.3.2	Chamber Observations	41
2.3.3	NEE Response to Environmental Factors and Vegetation Type.....	44
2.3.4	NME Response to Environmental Factors and Vegetation Type	45
2.4	Discussion.....	45

2.4.1	Carbon balance and Controlling Factors	45
2.4.2	Upscaling	48
2.4.3	Future Trajectories.....	49
2.5	Conclusions.....	50
<i>Chapter 3: Controls on Carbon Dioxide and Methane fluxes from a Low-Center Polygonal Peatland in the Mackenzie River Delta</i>		52
3.1	Introduction.....	52
3.2	Materials and Methods	54
3.2.1	Study Site	54
3.2.2	Data Collection.....	56
3.2.2.1	EC Fluxes.....	59
3.2.2.2	Weather and Soil Measurements.....	62
3.2.2.3	Chamber Measurements	63
3.2.3	Feature Identification & Gap-Filling.....	64
3.2.3.1	Neural Networks.....	64
3.2.3.2	The Weights Method	66
3.2.3.3	Partitioning NEE.....	68
3.3	Results	69
3.3.1	Seasonal and Daily Trends	71
3.3.2	Net Ecosystem Exchange	74
3.3.2.1	Flux Drivers	74
3.3.2.2	Ecosystem Respiration	78
3.3.3	Net Methane Exchange.....	80
3.4	Discussion	83
3.4.1	Flux Drivers.....	83
3.4.1.1	Spatial Variability.....	84

3.4.1.2	Net Ecosystem Exchange: Flux Partitioning.....	86
3.4.1.3	Net Methane Exchange	87
3.4.2	Carbon Balance	89
3.5	Conclusions.....	92
 <i>Chapter 4: Modeling Interannual Variability of Carbon Fluxes at a Low-Center Polygon Ecosystem in the Mackenzie River Delta</i> 94		
4.1	Introduction.....	94
4.2	Data and Methods	96
4.2.1	Study Site	96
4.2.1.1	Flux Observations	98
4.2.1.2	Landscape Classification Map.....	101
4.2.2	Data Sources	103
4.2.2.1	Automated Weather Station	104
4.2.2.2	ERA5 Reanalysis.....	105
4.2.2.3	Additional Data.....	107
4.2.3	Creating the Flux Driver Time Series	109
4.2.3.1	Atmospheric Drivers	109
4.2.3.2	Soil Drivers.....	112
4.2.3.3	Seasonal Driver	114
4.2.3.4	Source Area Drivers	118
4.2.4	Temporal Upscaling	118
4.2.4.1	Seasonal Comparison	118
4.2.4.2	Flux Validation	120
4.2.4.3	Flux Partitioning and Independent Assessment	120
4.3	Results	121
4.3.1	Climatology	121

4.3.1.1	Snow-free Seasons	121
4.3.1.2	Flux Drivers	123
4.3.2	Flux Estimates	127
4.3.2.1	Carbon Balance.....	127
4.3.2.2	Flux Evaluation	128
4.3.3	Seasonal and Inter-Seasonal Variability.....	130
4.4	Discussion.....	133
4.4.1	Uncertainty	134
4.4.2	Spatial Representativeness.....	136
4.4.3	Carbon Balance	137
4.5	Conclusions and Future Research.....	141
<i>Chapter 5: Conclusion</i>	143
5.1	Summary of Results	143
5.2	Methodological Contributions.....	144
5.3	Implications & Future Research	145
5.3.1	Cold Season Fluxes	146
5.3.2	Methane Fluxes.....	146
5.3.3	Landscape Change and Remote Sensing	147
5.3.4	Neural Network Architecture.....	147
5.4	Reflections	148
Bibliography	150
Appendices	185
Appendix A	185
Appendix B	191

List of Tables

Table 2.1: Dominant species or landscape feature within the vegetation/cover classes. Unit codes correspond to the map Figure 1a.....	26
Table 2.2: The surface cover class fractions of the basin, along with the mean source area fractions of the footprint climatology (F_{Clim}) and the range of source area fractions for individual half hourly observations shown in brackets.....	31
Table 2.3: The ER temperature sensitivity (Q_{10}) and base respiration (R_{10}) estimated by Laforce (2018) and estimated from nighttime EC footprint observations.	35
Table 3.1 Descriptive statistics of the source area for half hourly NME Observations. Despite NEE having over 1,000 more half hourly observations, the quantiles for NEE were nearly identical ($\pm 1\%$). Column headers for the landscape class flux contributions show their fractional cover in landscape classification map. The adjusted landscape fraction (ALF) values shown at the bottom are the landscape fraction (LF) estimates weighted by $(1 - F_{out})$, using the 50 th percentile value of F_{out}	71
Table 3.2. The relative influence (RI) of the inputs of the pruned NN over NEE, along with their correlation (r) to half hourly NEE.....	76
Table 3.3. Environmental controls over NME identified by model pruning, along with their relative influence to the model and their Pearson's correlation coefficient to half hourly NME.	81
Table 4.1. Key drivers of CO ₂ fluxes identified by Skeeter et al. (2022) ranked by their relative influence (RI) in the NN model ensemble, determined using the weights method (Gevrey et al. 2003). Corresponds to Table 3.2 in Chapter 3	100

Table 4.2. Key drivers of CH ₄ fluxes identified by Skeeter et al. (2022) ranked by their relative influence (RI) in the NN model ensemble, determined using the weights method (Gevrey et al. 2003). Corresponds to Table 3.3 in Chapter 3	101
Table 4.3. The slope (m), intercept (b), coefficient of determination (r^2), and root mean squared error (RMSE) for the regression line: Y=m X + b, where Y are field season observations (FSO) from the EC station and X are the hourly AWS observations during the 2017 field season. These regression parameters were used to scale AWS observations for inclusion in the FDTS (see section 4.2.3.1).....	105
Table 4.4. A correlation matrix (Pearson r) showing the association between FSO drivers (rows) and ERA5 reanalysis estimates (columns).....	106
Table 4.5. The relative weight of each of the 11 inputs for the k-fold OLS models used to estimate each soil driver. Inputs from ERA5 data are shown in blue, inputs from the AWS hourly data in orange, and time averaged AWS inputs are shown in yellow. Validation statistics: coefficient of determination (r^2) and root mean square error (RMSE) values are shown in grey.	113
Table 4.6. The three criteria used to calculate the daily thaw parameter (t) and their respective multipliers, where the daily value is the product of the two snow-cover multipliers (s_1 and s_2) and a temperature multiplier (m1): $t = s_1 s_2 m_1$	117
Table 4.7. Validation statistics (r^2 and RMSE) and along with mean NEE and NME over the 2017 study season (DOY 174 – DOY 256) estimated using the Flux Drive Time Series (FDTS). Validation statistics are provided the hourly benchmarks NEE _B and NME _B as well. *Hourly NME were calculated using observed source area fractions substituted for the fixed source area	

values. (Validation for the original half hourly estimates are shown in parenthesis Skeeter et al. 2022 for reference)..... 129

Table 4.8. Pearson r correlation coefficient for NEE and NME with key flux drivers, averaged over the specified time intervals. Only correlations significant to $p < 0.05$ with $r^2 > 0.3$ are shown. 131

Table 4.9. Correlation statistics (Spearman ρ) for mean snow-free season NEE and NME and cumulative C exchange compared to select snow-free season variables. Only correlations with $p > 0.1$ are shown, correlations significant to $p < 0.05$ are shown in bold. To control for potential outliers, leave-one-out cross validation was used. The ρ and p values presented are the median values of the $n=11$ permutations..... 132

Table 4.10. Comparison of mean June – September NEE and F_{CH4} presented in Dengel et al. (2021) to modeled NEE and NME at Fish Island over the same time periods. From 2013 to 2015, and 2018, the snow-free season dates (denoted by the *) did not perfectly align with the averaging interval. Estimates for just the snow-free seasons are shown in black. Projections over the full time period are shown in blue only for comparison but should be taken with caution as model projections during flooding or snow cover are tenuous. Mean June – September air temperatures are also shown for both sites. 140

List of Figures

Figure 1.1 Arctic eddy covariance sites where CO ₂ and CH ₄ fluxes have been measured (Pallandt et. al 2021), shown relative to Arctic bioclimate zones (CAVM Team 2003).	3
Figure 1.2 Mean daily air temperature by month (August 2008 – July 2020) from a weather station at Fish Island (69°22'20.20"N, 134°52'51.92"W, WGS 84), a coastal site typical of the Low Arctic in Canada's Mackenzie Delta (NWT Water Resources Board).	6
Figure 1.3 False color composite LANDSAT8 image (bands 3, 4, and 5) of the Mackenzie Delta. Labeled on the map are the study sites at Fish Island and Illisarvik, communities in the delta region, and the boreal tree line. The inset map shows the extent of the Mackenzie River drainage basin outlined in blue.	15
Figure 2.1 a) Map of the distribution of vegetation classes at Illisarvik, with the footprint climatology (F_{Clim}) over the study period, the locations of the chambers and the eddy covariance (EC) system. The alphanumeric labels correspond to the unit codes in Table 2.1. b) Legend for the map in a. c) Oblique drone image of Illisarvik, take at 16:40 July 23rd 2016 view from E of DTLB towards W. The Basin and EC system are shown on the image using the same symbology as a).	27
Figure 2.2 a) Half hourly air and soil temperatures, displayed along with photosynthetic photon flux density (PPFD). b) Hourly soil volumetric water content and daily total precipitation. c) Half hourly F_{CO_2} (green) and NEE _{NN} (grey), and d) half hourly F_{CH_4} (red) and NME _{NN} (grey).	40
Figure 2.3: Boxplot of a) ER, b) NME and c) NME fluxes measured using closed chambers, grouped by vegetation class. The orange lines represent the median, blue stars represent means, the boxes indicate the interquartile range (Q3-Q1), the whiskers indicate Q1 -(1.5*IQR) and	

Q3+(1.5*IQR), and the circles represent outliers extending beyond the whiskers. Note the scale
for c) Sedge is different..... 43

Figure 3.1. False color composite 100 m resolution LANDSAT8 image (bands 3, 4, and 5) of
the Mackenzie Delta with imagery spanning the dates of the 2017 study period. Labeled on the
map are the study site at Fish Island and the nearby communities of Tuktoyaktuk and Inuvik.

The approximate bounds of the Big Lake Delta Plain are represented with the white hatch marks
(Morse & Burn, 2013). Coordinate Reference System: NAD83 UTM zone 10N. LANDSAT8
data is provided by the United States Geological Survey and was downloaded using Google
Earth Engine..... 56

Figure 3.2. a) The cumulative flux footprint climatology (25%, 50%, 75% and 90%) is shown
overlaid on the landscape classification map (LCM). Labels on the map correspond to: the EC
system (EC), soil stations 1-3 (S1, S2, S3), the power supply (PS), and the NWT Water Resource
Department's Automated Weather Station (AWS). b-e) Oblique drone photos showing the EC
system and vegetation at different points during summer and fall 2017: looking south-east on
DOY 174 (b.) and DOY 191 (c.) and looking northeast from behind the EC system on DOY 233
(d.) and DOY 256 (e.). f) Inset map showing the location of the EC station, 75% and 90% flux
footprint contours and the area covered by the LCM, and a 10cm orthophoto created from drone
imagery captured on June 23rd. This is overlain on a 10 m resolution composite Sentinel 2 image
generated using Google Earth Engine with imagery spanning the summer 2020. Also shown are
the location of the Taglu tower and the River Channel. Coordinate Reference System: NAD83
UTM zone 10N. Sentinel 2 data is provided by the Copernicus Sentinel Data and was
downloaded using Google Earth Engine..... 59

Figure 3.3. Climate and water level measurements during the 2017 study period: a) Daily mean T_a in red and daily mean T_s at 5 cm for polygon centers (dotted line) rims at 5cm (solid black line), and rims at 15cm (solid grey line) b) Mean daily PPFD and length of each night after the first sunset. c) Total daily precipitation (black bars) and mean daily W_{TD} (blue line). d) Daily maximum sustained half hourly wind speed at 2.89 m (black). 70

Figure 3.4. Daily measured NEE and NME (boxplot) and mean gap filled (black line) NEE and NME over the study period. For the boxplots, the red line indicates the median, the red square is the mean, the box represents the inner quartile range (Q1-Q3), the whiskers are 1.5 times the inner quartile range ending at the farthest data point within that interval, and circles represent outliers. Grey shading represents a net sink and no shading represents a net source. 73

Figure 3.5. Diurnal (hourly) course of measured NEE and NME (boxplot) and mean gap filled (black line) NEE and NME early in the study period (a & b) and late in the study period (c & d). For the boxplots, the red line indicates the median, the red square is the mean, the box represents the inner quartile range (Q1-Q3), the whiskers are 1.5 times the inner quartile range ending at the farthest data point within that interval, and circles represent outliers. Grey shading represents a net sink and no shading represents a net source. 74

Figure 3.6. The mean sum of squared derivatives (SSD) for six of the input factors for the NEE model are shown in red, with a 95% confidence interval shown in blue. Y-axis labels on the left correspond to the SSD values. Also shown (grey bars) are histograms of the distribution of the input variables in the training set. The Y-axis labels on the right correspond to the number of training samples (half-hourly observations). 77

Figure 3.7. Modeled estimated NEE under different conditions, unless otherwise specified, all inputs were fixed to their median value. a) Daytime NEE response to photon flux density at

optimal and high vapor pressure deficits. b) NEE response to thaw depth for daytime and nighttime. c) NEE response to polygon center temperatures at 5cm daytime and nighttime conditions, with a center-rim temperature gradients of 4°C and 1°C respectively. For each plot, the solid lines represent the mean modeled NME response, the dotted line is the mean response estimated outside conditions that were actually observed, and the shaded area bounded by the dots is the 95% confidence interval around the estimate..... 78

Figure 3.8. a) Nighttime NEE measurements plotted against modeled ER derived by the NN (blue) and logistic temperature response curve fit to $T_{Rim2.5}$ (red). b) Boxplots of the distribution of flux chamber observations of ER for polygon centers (ER_{Cnt} , n= 16) and rims (ER_{Rim} , n = 8) aggregated over the two measurement days. Also shown, are the nighttime ER observations from the EC system (n=186). For the boxplots, the red line indicates the median, the box represents the inner quartile range (Q1-Q3), the whiskers are 1.5 times the inner quartile range ending at the farthest data point within that interval, and circles represent outliers. Note the y-axis for a & b are not on the same scale. 79

Figure 3.9. The mean sum of squared derivative (SSD) for six of the input factors for the NME model are shown in red, with a 95% confidence interval shown in blue. Y-axis labels on the left correspond to the SSD values. Also shown (grey bars) are histograms of the distribution of the input variables in the training set. The Y-axis labels on the right correspond to the input counts for each bin. 82

Figure 3.10. Modeled estimated NME under different conditions. Unless otherwise specified, thaw depth was set to 0.3 m and all other inputs were fixed to their median value. a) NME response to net radiation for thaw depth (TD) representative of early season (0.3 m) and late season (0.45 m) conditions. b) NME response to polygon center temperatures ($TCnt15$) at two

water table depth (WTD). c) NME wind speeds (U) with friction velocity (u_*) set to 7% and 9.2% of U. For each plot, the solid lines represent the mean modeled NME response, the dotted line is the mean response estimated outside conditions that were actually observed, and the shaded area bounded by the dots is the 95% confidence interval around the estimate.	83
Figure 3.11. The cumulative daily Carbon balance in g C m ⁻² with and without accounting for NME.....	92
Figure 4.1. The Big Lake Delta Plain (BLDP) in green following the boundaries defined by Morse & Burn (2013). Land areas that are not part of the BLDP are shown in tan. Also shown is the EC Station at Fish Island as an orange triangle and the two Environment Canada gauge stations as blue circles. The inset map shows a false color composite MODIS image of the Mackenzie River Delta and surrounding uplands. The delta is visible in darker red while the surrounding uplands are in lighter red. The white squares show the location of the two Circumpolar Active Layer Monitoring (CALM) sites and the yellow circle shows the location of the community of Inuvik.....	97
Figure 4.2. a. The landscape classification map for Fish Island showing the distribution of Low-Center Polygons, shrub tundra and open water areas. b. The boundaries of Fish Island and the 90% contour of the cumulative flux footprint from Skeeter et al. (2022) are shown along with the location of the eddy covariance station and the automated weather station.	103
Figure 4.3 A comparison of observed T_{dew} from the 2017 field season (FSO) and ERA5 estimated T_{dew} is shown in (a.) The relative weights of the OLS model used to scale ERA5 T_{dew} to FSO T_{dew} are shown in (b.) and the resulting scaled estimates of T_{dew} are shown compared to FSO T_{dew} in (c.). The final estimate of VPD is shown compared to FSO VPD in (d.). In a., c., and d. the black lines represent at 1:1 relationship.	112

Figure 4.4. Estimation of daily thaw depth (TD) in 2017 using OLS regression as a function of the day of year (DOY), compared to estimating using EQ4.2. Grey circles represent the TD observations from the 2017 field season..... 117

Figure 4.5. The duration of the snow-free period from 2000 to 2020. The snow-free seasons from 2009 to 2019, coinciding with the FDTs are highlighted in light blue. The horizontal red dashed lines demarcate the mid-season period DOY 161 to 256. 123

Figure 4.6. Observed daily Photosynthetic Photon Flux Density (a.), Air Temperature (b.), estimated soil temperatures in polygon centers at 15 cm (c.), and estimated water table depth in polygon centers (d.). The solid blue lines show the mean daily values averaged across the 11 study years (2009 to 2019) and the shaded areas bounded by the dashed black lines represent the daily ranges (max/min hourly values). The vertical red dashed lines demarcate the growing season period (DOY 161 – 256). 125

Figure 4.7. Boxplots of mean growing season net radiation (a.), air temperatures (b.), vapor pressure deficit (c.), and polygon center temperatures at 15 cm (d.). Total growing season precipitation (2009 is missing) is shown in (e.) and mean growing season W_{TD} is in (f). Estimated maximum snow-free season TD is shown in (g.). The frequency of high wind events (Number of days per season with at least one hourly $U > 2\sigma$) per growing season is shown in (h.). Finally, maximum growing season NDVI is in (i.). The green lines represent the median, the boxes indicate the interquartile range (Q3-Q1), the whiskers indicate $Q1 - (1.5 * IQR)$ and $Q3 + (1.5 * IQR)$, and the circles represent outliers extending beyond the whiskers. The star represents the mean value for the 2017, when eddy covariance measurements were operated. 126

Figure 4.8. Modeled cumulative C fluxes (purple), separated into the growing season (DOY 161 - 256), and shoulder season (DOY < 161 + DOY > 256), averaged over the 2009 to 2019 period.

The component fluxes Net Ecosystem Exchange (green) and Net Methane Exchange (gold) are also shown. The growing season is always defined as 96 days, but the shoulder seasons are of variable length, ranging from 4 to 39 days each year.....	128
Figure 4.9. Comparison of our mean GPP estimates and MODIS derived GPP estimates. The black line represents a 1:1 relationship and the dashed line is the line of best. The error bars show the with 95% confidence intervals for NN estimated GPP.....	129
Figure 4.10 a. Mean daily NEE across all snow-free seasons. Shaded areas represent the 95% confidence interval. b. Mean NEE over each growing season. Error bars represent the 95% confidence interval. b. Shows the same as a. but for NME. d. Shows the same as b. but for NME. As in Figure 4.6, the vertical red dashed lines demarcate the growing season. The x-axis in (a. & b.) spans the median start and end dates of the snow-free season DOY 155 and 271 respectively. Averages/confidence in intervals outside of the growing season include some days which were not part of the snow-free season and are shown for reference.....	133
Figure A.5.1: The averaged mean squared error (MSE) of the bootstrapped Neural Network model validation datasets, with error bars showing one standard error (SE). The x axis shows models of increasing size from left to right (1-9 factors), and the label indicates the factor added to the model at each step. The blue line indicates the 1-SE rule threshold and the red bar indicates the model selected by the 1-SE rule.....	189
Figure A.5.2: F_{CH_4} estimated by a RF using the same factors as the NN model. The colours correspond to the scenarios in Fig 5a. VWC was estimated over the range 0.45 to 0.65.....	190

List of Abbreviations

Abbreviation	Units	Definition
C		Carbon
CH ₄		Methane
CO ₂		Carbon dioxide
<i>C_h</i>		Canopy Height
CALM		Circumpolar Active Layer Monitoring Network
DOY		Day of Year
DTLB		Drained Thermokarst Lake Basin
EC		Eddy Covariance
ER	µmol m ⁻¹ s ⁻¹ or g CO ₂ m ⁻¹ d ⁻¹ or g CO ₂ -C m ⁻¹ d ⁻¹	Ecosystem Respiration
<i>F_C</i>		Chamber Flux (CO ₂ or CH ₄)
<i>F_{CH4}</i>	nmol m ⁻¹ s ⁻¹	CH ₄ Flux
<i>F_{CO2}</i>	µmol m ⁻¹ s ⁻¹	CO ₂ Flux
<i>F_{Clim}</i>		Footprint Climatology
<i>F_{Sedge}</i>	%	Source Area Fraction (Sedge)
<i>F_{Shrub}</i>	%	Source Area Fraction (Shrub)
<i>F_{Grass}</i>	%	Source Area Fraction (Grass)
<i>F_{Upland}</i>	%	Source Area Fraction (Upland)

F_{Water}	%	Source Area Fraction (Water)
F_{Sparse}	%	Source Area Fraction (Sparse)
F_{Cnt}	%	Source Area Fraction (Polygon Centers)
F_{Rim}	%	Source Area Fraction (Polygon Rims)
F_{Rim}	%	Source Area Fraction (Outside Landscape Classification Map)
$f(x,y)_i$		Flux Footprint Function
G	W m^{-2}	Ground Heat Flux
GPP	$\mu\text{mol m}^{-1} \text{s}^{-1}$ or $\text{g CO}_2 \text{m}^{-1} \text{d}^{-1}$ or $\text{g CO}_2\text{-C m}^{-1} \text{d}^{-1}$	Gross Primary Productivity
IRGA		Infrared Gas Analyzer
L		Obukhov Length
LCP		Low Center Polygon
LW	W m^{-2}	Net Longwave Radiation
MSE		Mean Squared Error
NDVI		Normalized Difference Vegetative Index
NDSI		Normalized Difference Snow Index

NDWI		Normalized Difference Water Index
NEE	$\mu\text{mol m}^{-1} \text{s}^{-1}$ or $\text{g CO}_2 \text{m}^{-1} \text{d}^{-1}$ or $\text{g CO}_2\text{-C m}^{-1} \text{d}^{-1}$	Net Ecosystem Exchange
NME	$\text{nmol m}^{-1} \text{s}^{-1}$ or $\text{mg CH}_4 \text{m}^{-1} \text{d}^{-1}$ or $\text{mg CH}_4\text{-C m}^{-1} \text{d}^{-1}$	Net Methane Exchange
NN		Neural Network
OLS		Ordinary Least Squares
PPFD	$\mu\text{mol m}^{-1} \text{s}^{-1}$	Photon Flux Density
P_a	Pa	Air Pressure
RF		Random Forest
RH	%	Relative Humidity
RI	%	Relative Influence
r^2		Coefficient of Determination
r		Pearson Correlation Coefficient
RMSE		Root Mean Squared Error
R_N	W m^{-2}	Net Radiation
RSSI		Received Signal Strength Indicator
SD_m		Sum of Derivatives
SSD_m		Sum of Squared Derivatives
SE		Standard Error

SW	W m^{-2}	Net Shortwave Radiation
T_a	$^{\circ}\text{C}$ or K	Air Temperature
T_{Dew}	$^{\circ}\text{C}$ or K	Dewpoint
T_s	$^{\circ}\text{C}$	Soil Temperature
T_{Cnt5}	$^{\circ}\text{C}$	Soil Temperature (5cm Polygon Center)
T_{Cnt15}	$^{\circ}\text{C}$	Soil Temperature (15cm Polygon Center)
T_{Rim5}	$^{\circ}\text{C}$	Soil Temperature (5cm Polygon Rim)
T_{Rim15}	$^{\circ}\text{C}$	Soil Temperature (15cm Polygon Rim)
TD	m	Thaw Depth
U	m s^{-1}	Wind Speed
u_*	m s^{-1}	Friction Velocity
VPD	Pa	Vapor Pressure Deficit
VWC	%	Volumetric Water Content
W_{td}	m	Water Table Depth
z_m		Measurement Height
z_0		Aerodynamic roughness length
ρ		Spearman Correlation Coefficient

θ_w	%	Volumetric Water Content
------------	---	--------------------------

Acknowledgements

First and foremost, I would like to acknowledge that this research was conducted on Indigenous land. During my time at UBC, I have been living as an uninvited guest on the traditional, ancestral, and unceded territories of the xʷməθkʷəy̓əm (Musqueam), ə́lilwətaʔɬ (Tsleil-Waututh), and Skwxwú7mesh-ulh (Squamish) Nations. My field work was conducted in the Inuvialuit Settlement Region and I am thankful for the opportunity to work on Inuvialuit land. As a white settler and immigrant to Canada, I was unaware of the historical context behind Canada's relationship with Indigenous peoples and ignorant of how I as a researcher have perpetuated colonialism. I am working on educating myself and I aim to center decolonization in all my future academic endeavors.

I owe many thanks to my supervisors Andreas Christen and Greg Henry for the support they have provided, and to my committee members Trevor Lantz and Ian McKendry. Thanks to Andre-Anne LaForce, and Alice Wilson, Chris Burn, and Ellyn Humphreys for their assistance and comradery during my time at Illisarvik. I would like note the immensely helpful contributions I received from Rick Kettler assisting logistics and setting up the field site at Fish Island. Lastly, special thanks are owed to Edwin Amos. Without his local expertise and helpful hands, none of this work would have been possible. I learned a great deal from him during our time working together and I will be forever grateful for all that he shared with me along the way.

Credit to NSERC and CFI for funding this research and the NWT Water Resources for sharing data used in our temporal upscaling experiment.

Dedication

This work is dedicated to my parents, Brent and Cherie Skeeter. I owe them many thanks for the support and encouragement they provided while I worked through this difficult process.

Chapter 1: Introduction

1.1 Framing the Problem

Arctic amplification is accelerating warming in the northern high latitudes, making the Arctic a hotspot for the effects of climate change (Flato et al. 2019; IPCC 2021). Climate change is causing decreased snow and ice cover, permafrost degradation, changing precipitation patterns and extending growing seasons across the Arctic (Derkzen et al. 2019; Myers-Smith et al. 2020). Arctic tundra ecosystems are especially sensitive to warming (Forbes et al. 2001). Thaw depths and permafrost temperatures are increasing across the Arctic and satellite observations show increasing thermokarst activity and significant tundra greening in many areas (Streletschi et al. 2015; Frost et al 2020; Chen et al. 2021). These changes alter the carbon (C) balance of tundra ecosystems and influence the rate of climate warming globally. At a Pan-Arctic scale, models predict terrestrial ecosystems will gain biomass C and lose permafrost C (Schuur et al. 2015; Mekonnen et al. 2021). The magnitude of C gains vs. losses remains a significant source of uncertainty in climate projections (Fisher et al. 2018; Natali et al. 2021). Our current understanding of the C balance in tundra ecosystems is limited, which makes predicting their responses to climate change difficult (Lara et al. 2020).

Eddy covariance (EC) is one of the primary techniques for measuring ecosystem scale trace gas fluxes (See section 1.5 for a brief discussion of EC methods). Sites monitoring carbon dioxide (CO_2), and methane (CH_4) fluxes have been established around the world (Baldocchi et al. 2001; Delwiche et al. 2021). However, tundra ecosystems remain sparsely sampled due to the logistical challenges of working in remote northern ecosystems. Existing observations are biased towards more accessible sites, mainly in Alaska (Fig 1.1). The tundra ecosystems in Canada and

Siberia respectively account for 36% and 26% of terrestrial Arctic area and are under-represented (Walker et al. 2005; Pallandt et al. 2021).

Here I present the first research using eddy covariance to measure season CO₂ and CH₄ fluxes in tundra ecosystems in Canada's Mackenzie Delta Region. Machine learning was used to identify bioclimate factors controlling C fluxes and conduct a temporal upscaling experiment to model the influence of interannual climate variability on growing season C fluxes. This work helps to lessen the observation bias of Arctic EC studies and presents information that can be used to better understand the dynamics governing C fluxes in tundra ecosystems.

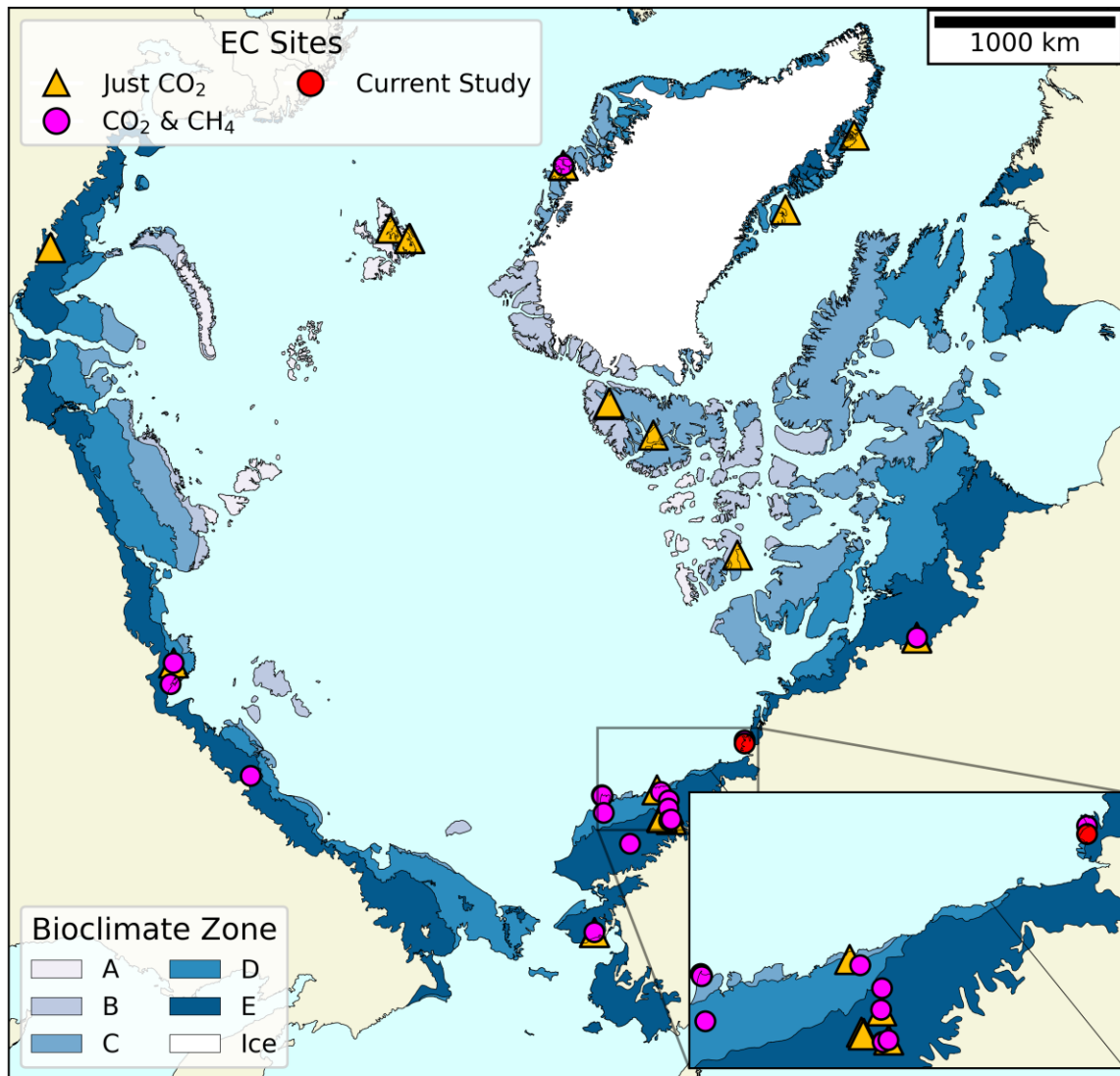


Figure 1.1 Arctic eddy covariance sites where CO₂ and CH₄ fluxes have been measured (Pallandt et. al 2021), shown relative to Arctic bioclimate zones (CAVM Team 2003).

1.2 Tundra Carbon Fluxes

Tundra ecosystems develop in the Arctic because short growing seasons prevent tree growth and limit vegetation to shrubs, graminoids, forbs, and non-vascular species (Bliss et al. 1973; Forbes et al. 2001). The duration of the Arctic growing season is determined by snow melt date, daylight regimes and summer temperatures, which follow a latitudinal gradient

modulated locally by elevation and maritime influences. The bioclimate zones in Figure 1.1 were developed based on summer temperatures and vegetation (CAVM Team 2003). Zones A-C are the coldest and least productive with scant precipitation and limited vascular plant cover (Forbes et al. 2001; Walker et al. 2005). Zones D and E have longer, more productive growing seasons and species diversity is higher, including erect shrub tundra and peat rich wetlands where sufficient precipitation falls (Forbes et al. 2001; Walker et al. 2005). Zones D-E have the highest concentrations of biomass and soil C in the Arctic and make up the majority (~63%) of Arctic land area (Walker et al. 2005; Hugelius et al. 2014). In North America, zones A-C and D-E are commonly referred to as the High Arctic and Low Arctic, respectively.

1.2.1 Components of the Carbon Balance

The land-atmosphere exchange of CO₂ and CH₄ are two principal components of the C balance in tundra ecosystems. The flux of CO₂ is the dominant pathway for C in and out of an ecosystem. This exchange can be quantified as Net Ecosystem Exchange (NEE), where: NEE =ER - GPP (Aubinet et al. 2012). Gross Primary Productivity (GPP) is the total photosynthetic uptake of CO₂ from the atmosphere by plants. Ecosystem Respiration (ER) is the sum of autotrophic (plants) and heterotrophic (bacteria, fungi, and animals) respiration. The sign convention for NEE is based on the atmosphere as the storage pool; negative NEE indicates net uptake of CO₂ (withdrawal of CO₂ from the atmosphere and accumulation of C in the ecosystem). Positive NEE indicates net emission of CO₂ (release of C from the ecosystem and accumulation of CO₂ in the atmosphere). Historically, tundra ecosystems have acted as net CO₂ sinks because frigid temperatures have suppressed ER more than GPP, resulting in the accumulation of C in permafrost soils (Schuur et al. 2008).

Net Methane Exchange (NME) quantifies the ecosystem-scale difference between methanogenesis (CH_4 production) and methanotrophy (CH_4 emission). Anoxic (oxygen depleted) conditions in wetland soils suppress autotrophic respiration in favor of anaerobic decomposition. Methanogens facilitate the final step of anaerobic decomposition and produce CH_4 as a byproduct (Lai 2009). In overlying aerated soils, methanotrophs oxidize CH_4 and release CO_2 as a byproduct (Serrano-silva et al. 2014). Positive NME indicates CH_4 emission and negative NME indicates CH_4 uptake. In the short-term, CH_4 emissions produce a strong radiative forcing, because the Global Warming Potential (GWP) is 27 times that of CO_2 on a 100-year time scale (IPCC 2021). However, anaerobic decomposition is a much less efficient pathway for decomposition (Lee et al. 2012). This helps maintain negative NEE in wetlands and promotes the accumulation of peat. Over millennial timescales, peatlands, including permafrost peatlands, have a negative effect on radiative forcing due to the short half-life of atmospheric CH_4 , the suppression of ER, and accumulation of peat (Frolking et al. 2006; Zhu et al. 2013).

1.2.2 Seasonal Dynamics and Flux Drivers

The majority of annual C exchange in tundra ecosystems occurs during the brief growing season when plants are active. In the High and Low Arctic, the growing season lasts 1.5-2.5 months and 3-4 months, respectively (Forbes et al. 2001). Figure 1.2 shows the annual course of temperatures typical of a coastal site in the Low Arctic. The growing season begins in June following spring snow melt when the active (thawed soil) layer begins to develop and leaf out occurs for deciduous species (Euskirchen et al. 2012; Sweet et al. 2015). Senescence begins in late August as the sun angle decreases and day length starts to decrease rapidly (Lafleur and Humphreys 2008). Root growth continues during the senescent period and active layer thickness reaches its annual maximum by September (Iversen et al. 2015; Blume-Werry et al. 2019).

Winter begins by early October when freezing temperatures return and the active layer starts to refreeze from the top and bottom (French 2017). Reduced levels of microbial activity persist through the early winter freeze-back period, which can last several months depending on snow depth and vegetation (French 2017; Commane et al. 2017). There is some concern that amplified winter warming will cause the Arctic to become a net C source by delaying and extending freeze-back (Commane et al. 2017; Natali et al. 2019). However, modelling indicates growing season C exchange is three times more sensitive to warming than cold season C exchange (Tao et al. 2021).

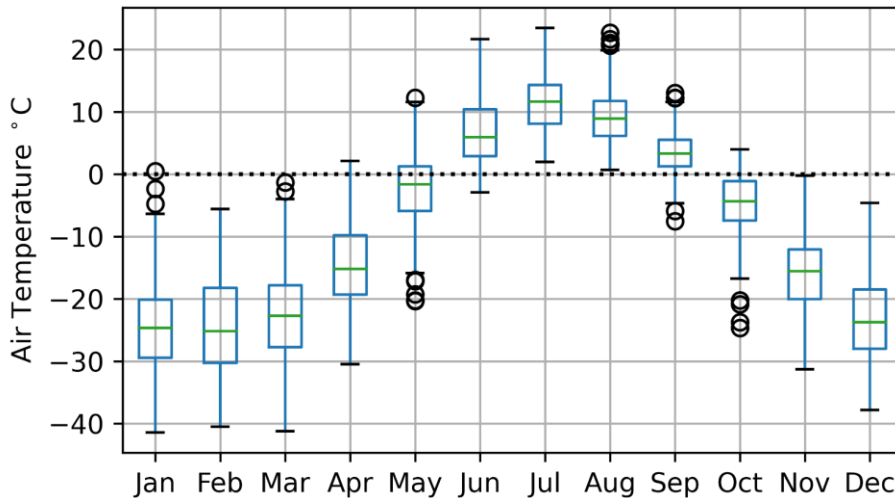


Figure 1.2 Mean daily air temperature by month (August 2008 – July 2020) from a weather station at Fish Island (69°22'20.20"N, 134°52'51.92"W, WGS 84), a coastal site typical of the Low Arctic in Canada's Mackenzie Delta (NWT Water Resources Board).

1.2.2.1 Net Ecosystem Exchange

Tundra ecosystems are typically net CO₂ sinks during the growing season (Lafleur et al. 2012). Over the growing season GPP follows a relatively predictable course dictated by plant growth, maturation, and senescence; ER is more sensitive to environmental conditions like temperature, and soil moisture and has a strong influence over the magnitude of CO₂ uptake

(Lund et al. 2010; Olivas et al. 2011; Holl et al. 2019; Dengel et al. 2021). The timing of snowmelt and senescence dictate the duration of the growing season and when the ecosystem shifts from a CO₂ source to a sink and vice versa (Lafleur and Humphreys 2008; Holl et al. 2019). Snowmelt has been occurring earlier in the Low Arctic in recent decades, resulting in slight net extension of the growing season in some locations (Myers-Smith et al. 2019). However, others have observed that the onset of senescence has also been occurring earlier for some Arctic species, resulting in little or no net change in growing season length at other sites (Myers-Smith et al. 2020). Many deciduous trees have fixed leaf lifespans (Keenan and Richardson 2015), and this may apply to some species in the Arctic species as well (e.g., *Salix arctica*) (Myers-Smith et al. 2019). Regardless, the onset of senescence is strongly influenced by decreasing light levels in August/September, so climate change is less likely to significantly delay the onset of senescence (Estiarte and Peñuelas 2014; Ford et al. 2017; Livensperger et al. 2019).

The primary control over GPP is photosynthetically active radiation. The rate of CO₂ assimilation follows a light responses curve, increasing with radiative input until saturation levels are reached (Aubinet et al. 2012). Saturation levels vary between species but are rarely reached in tundra ecosystems (Tieszen 2018). Vapor pressure deficit has a modulating effect on the light response curve, restricting GPP when conditions are dry (Aubinet et al. 2012). Autotrophic respiration corresponds to plant growth, while heterotrophic respiration is dependent upon substrate availability. Root exudates are the most accessible substrate but soil microbes will consume any organic matter available (Schaefer and Jafarov et al. 2016; Blume-Werry et al. 2019). Soil temperature is a main driver of ER and below ground biomass exceeds above ground biomass in tundra ecosystems (Iversen et al. 2015; Kim et al. 2016). The rate of ER is typically

described using exponential or logistic temperature response functions (Aubinet et al. 2012; Kim et al. 2016; Lee et al. 2017). Soil temperature decreases with depth, so the rate of respiration is much lower at the base of the active layer than near the soil surface (Lee et al. 2012). Soil moisture is an important secondary control over ER, it limits biologic activity under dry conditions and limits oxygen availability under saturated conditions (Aubinet et al. 2012). In wetlands, water table depth limits ER by determining the volume of soil available to respiration (Gagnon et al. 2017).

1.2.2.2 Net Methane Exchange

We have a decent understanding of factors influencing methanogenesis and methanotrophy under laboratory conditions and a theoretical framework for how that translates to natural environments (Lai 2009; Serrano-silva et al. 2014). However, the literature does not suggest any broadly applicable, well-defined functional relationships governing ecosystem scale NME (Irvin et al. 2021). Less than half of Arctic EC studies measure CH₄ fluxes, so the dynamics governing ecosystem CH₄ exchange remain poorly understood (Pallandt et al. 2021). Some well drained tundra uplands can be weak CH₄ sinks during the growing season, but moist and wet tundra ecosystems are growing season sources, emitting much more CH₄ than uplands sequester (Whalen et al. 1996; Zhu et al. 2013; McGuire et al. 2018). Growing season fluxes account for more than half of annual NME at the few tundra sites in Alaska with annual observations, but early winter fluxes can be substantial during freeze up because the refreezing active layer is frequently oxygen depleted (Zona et al. 2016; Bao et al. 2021).

Substrate availability and methane concentration, respectively, drive methanogenesis and methanotrophy, soil temperatures dictate their respective rates, and water table depth determines the volume of soil in which each can occur (Lai 2009; Serrano-silva et al. 2014). Soil

temperatures follow diurnal and seasonal patterns, while water table fluctuations are less predictable (Sachs et al. 2008; Nadeau et al. 2013). The mode of transport through the soil determines what fraction of CH₄ is actually oxidized. This process is difficult to model because there are three different pathways: diffusion, ebullition (bubbles), and vascular transport (Lai 2009). Diffusion is the slowest process and results in a greater fraction of CH₄ being oxidized (Whalen 2005). Upwards of 90% of the CH₄ produced in wetlands can be oxidized by methanotrophs when diffusion is the dominant transport process (Knoblauch et al. 2014; Mo et al. 2020). When the water table is close to the surface vascular transport and ebullition can rapidly move CH₄ through the soil profile, reducing methanotrophy (Lai 2009). Ebullition is heavily dependent upon peat texture; low porosity peat can store CH₄ bubbles for extended periods of time and release them in random bursts (Ramirez et al. 2015). Observations from a boreal bog suggest they account for between 2 and 8% of the annual CH₄ budget (Männistö et al. 2019). Rates of vascular transport are species dependent, making it a site-specific control over NME (Joabsson et al. 1999). Where vascular transport occurs, it can account for 70 to 90% of total CH₄ emissions (Knoblauch et al. 2014). Further complicating the matter, vascular transport aerates peat, simultaneously increasing CH₄ transport and decreasing CH₄ production (Joabsson et al. 1999). Transport and consumption dynamics are influenced by wind speed, air pressure, water table fluctuations, and plant activity; these factors combine to make NME unpredictable (Sachs et al. 2008; Nadeau et al. 2013; Rößger et al. 2019).

1.2.3 Spatial Heterogeneity

A latitudinal gradient of radiation and temperature dictates potential productivity of tundra ecosystems in the Arctic, while site specific factors govern ecosystem scale C fluxes (Lafleur and Humphreys 2012). Spatial heterogeneity has a substantial impact on tundra C

fluxes because permafrost and microtopography influence hydrologic conditions and vegetation composition. This causes CO₂ and CH₄ fluxes to vary drastically between adjacent tundra ecosystems (Zulueta et al. 2011; Lara et al. 2015). Polygonal landforms are widespread in coastal and other lowlands across the Arctic and are an extreme example of spatial heterogeneity in tundra ecosystems (French 2017). Polygonal landforms vary over small spatial scales (10 – 100 m²) and are poorly resolved by the coarse scale (> 1 km²) models used to project ecological response to climate change (Lara et al. 2020).

Ice wedge polygons form in ice rich permafrost lowlands with restricted drainage (French 2017). Where winter soil temperatures are sufficiently cold (< -13 °C) thermal cracking occurs and ice wedges develop which deform the land surface (Morse et al. 2013). In flat areas where permafrost is aggrading this creates a network of elevated ridges bounding low-center polygons (Mackay 2000). Polygon centers have high water tables which suppress ER and cause peat to accumulate, making them stronger CO₂ sinks than adjacent ridges (Olivas et al. 2011). Elevated water tables also cause low polygon centers to emit up to ten times as much CH₄ as adjacent ridges (Kutzbach et al. 2004; Sachs et al. 2010). At the ecosystem scale, low center polygons tend to be net CO₂ sinks and CH₄ sources, but the source/sink magnitude is strongly influenced by the distribution of rims/ridges at individual sites (van der Molen et al. 2007; Sachs et al. 2008; Holl et al. 2019; Dengel et al. 2021).

Permafrost degradation and thermokarst initiation can rapidly alter low center polygon landscapes. Subsidence can cause melt ponds to form which can evolve into thermokarst lakes through wave erosion and coalescence (French 2017). Melt ponds and thermokarst lakes can be net sources of both CO₂ and CH₄ (Martin et al. 2017; Serikova et al. 2019; Wickland et al. 2020; Cunada et al. 2021). Further erosion can cause lake drainage, resulting in polygonal

redevelopment or a transition to a new stable state (Billings and Peterson 1980; Mackay 2000). Ecological succession leads to net CO₂ uptake following lake drainage (van Huissteden et al. 2011; Zona et al. 2011; Zulueta 2011; Turetsky et al. 2020). Alternatively, low center polygons can transition to high center polygons when water tables drop (e.g., via adjacent lake drainage); ice wedges melt leaving depressed wet troughs (vegetated) or melt ponds (open water) bounding elevated polygon centers (Mackay 2000). High polygon centers can be net CO₂ sources because the elevated peat is exposed to rapid aerobic decomposition while CH₄ emissions are reduced. Adjacent wet troughs are CH₄ sources and CO₂ sinks while melt ponds are CO₂ and CH₄ sources (Martin et al. 2017; Wickland et al. 2020). Upscaling suggests high center polygon ecosystems may be net sources of both CO₂ and CH₄ (Wickland et al. 2020).

Ecosystem scale studies of polygonal tundra have been conducted at a limited number of locations (Pallandt et al. 2021). The majority of observations come from Alaska's North Slope near Utqiagvik (e.g. Kwon et al. 2006; Zona et al. 2009; Zona et al. 2010; Sturtevant et al. 2012; Raz-Yaseef et al. 2017; Dengel et al. 2021). Polygonal tundra sites have also been studied in Siberia at Samoylov Island in the Lena River Delta (e.g. Kutzbach et al. 2007; Wille et al. 2008; Runkle et al. 2013; Holl et al. 2019) and in the Indigirka lowlands (van Huissteden et al. 2005; van der Molen et al. 2007) and at a High Arctic site in Svalbard (Lüters et al. 2014; Cannone et al. 2019). Polygonal tundra is widespread in the Western Canadian Arctic, which has a warmer climate than any of the existing observation sites in Alaska and Siberia.

1.3 Defining the Study Area

The Western Canadian Arctic is one of the fastest warming regions in North America. From 1948 to 2016 mean winter (DJF) and summer (JJA) temperatures in this region have increased by 4.5 °C and 1.5 °C, respectively (Zhang et al. 2019). The 13,000 km² Mackenzie

River Delta is a central feature of this region. It stretches 200 km from Point Separation in the south to the Arctic Ocean in the North (Figure 1.3). The delta abuts the 1000 m+ high Richardson Mountains to the west and is bounded by low, rolling shrub tundra to the east. The Arctic tree line bisects the delta; separating the boreal forest in the south from Low Arctic tundra in the north. The northern delta is a mosaic of river channels, levees, peat rich polygonal tundra, thermokarst lakes, and drained lake basins of various ages (Burn and Kokelj 2009; Burn 2017). Most of the delta is underlain by continuous permafrost except patches of unfrozen ground along river channels and under lakes in the western and southern portions of the delta (Burn 2002; Burn and Kokelj 2009; Ensom et al. 2012). In the northeastern delta, permafrost is thick (>400 m), ice rich, and continuous (Morse et al. 2012).

Notable changes have been observed in the northern delta and surrounding tundra in response to climate warming. Permafrost temperatures increased by 2.5 °C in the northern delta from 1970 to 2008 (Burn and Kokelj 2009). Late summer thaw depth at Illisarvik in the northern delta have increased by 2.7 mm yr⁻¹ ($r^2 = 0.67$, $p < 0.001$) from 1983 to 2018 (Burn et al. 2021). Satellite data and air photos show increasing thermokarst activity in the region; including ice wedge degradation and accelerating thermokarst lake formation and drainage (Lantz and Kokelj 2008; Olthof et al. 2015; Steedman et al. 2017). Imagery and in situ observations also show a significant greening trend in the shrub tundra adjacent to the delta (Chen et al. 2021; Seider et al. 2022). High resolution analysis shows greening is not uniform. For example, high water tables in low center polygons buffer against shrub encroachment while high center polygons are more susceptible (Fraser et al. 2014; Moffat et al. 2016). Significant greening has not been observed in the delta (Chen et al. 2021). But storm surge events have caused vegetation die backs in the exposed coastal areas in the outer delta (Kokelj et al. 2012; Lantz et al. 2015).

1.3.1 Previous Studies in the Mackenzie Delta Region

The Mackenzie Delta Region is inaccessible except by boat or aircraft and it remains understudied from a carbon balance perspective, despite the fact that it contains massive deposits of SOC and could have hotspots for carbon emissions in a warming climate (Hugelius et al. 2014). A delta-wide aircraft campaign measured mid-summer CH₄ fluxes during a series of flights in July 2012 and July 2013 and found the Mackenzie Delta is a strong source of CH₄ emissions; geologic emissions (e.g., gas hydrate seeps) occur in the discontinuous permafrost of the southern and western delta and significant biologic emissions (31.8 to 58.4 mg CH₄ m⁻² d⁻¹) were observed north of the tree line (Kohnert et al. 2017; Kohnert et al. 2018). Additionally, a handful of studies have investigated dissolved organic carbon in the delta's waterways and considered their influence in terms of CO₂ and CH₄ fluxes (e.g., Tank et al. 2009; Weeks 2016; Cunada et al. 2018; Geeves 2019; Gareis and Lesak 2020). To my knowledge, the works presented here are the only existing eddy covariance measurements of terrestrial CO₂ fluxes and the only continuous, ecosystem scale observations of growing season carbon exchange available in the northern Mackenzie Delta Region.

1.3.2 Study Sites

We measured CO₂ and CH₄ fluxes with eddy covariance (EC) at two tundra sites. A brief (one month) campaign was conducted during the peak growing season at Illisarvik in 2016, and a longer (three months) campaign was over the growing season at Fish Island in 2017.

1.3.2.1 Illisarvik

Illisarvik is a coastal thermokarst lake basin located on Richard's Island that was experimentally drained in 1978 (Mackay 1981). Richard's Island is physiographically part of the Tuktoyaktuk Coastlands but it is separated from the mainland by the Mackenzie River's East

Channel (Burn et al. 2021). Richard's Island is characterized by low rolling upland tundra interspersed by lake-filled lowlands (Burn and Kokelj 2009; Burn et al. 2021). Since drainage, Illisarvik has undergone rapid ecological succession and has diverse set of vegetation communities (Wilson et al. 2019). Thermokarst lake drainage is a naturally occurring process that is anticipated to accelerate as the climate warms and acts as a buffer against climate change (van Huissteden et al. 2011; Turetsky et al. 2020). Maintenance of the outlet channel artificially lowers the water table at Illisarvik, meaning it is not perfectly representative of natural drainage events in the region. Nonetheless, it serves as a valuable benchmark for ecosystem C uptake following lake drainage events in the region.

1.3.2.2 Fish Island

Fish Island is an undisturbed low-center polygonal peatland located on the Big Lake Delta Plain, 10 km south of the Arctic coast (Burn and Kokelj 2009). The Big Lake Delta Plain is an elevated alluvial platform that experiences episodic flooding during the freshet with low sedimentation rates ($\sim 1 \text{ mm yr}^{-1}$) in the wetlands beyond channel levees (Morse & Burn, 2013). The plain is crisscrossed by a network of active syngenetic ice wedges that have produced low relief ridges ($\sim 20 \text{ cm}$) bounding low center polygons (Morse & Burn, 2013; Burn 2017). Vegetation consists of shrub tundra along levees transitioning to sedge and horsetail wetlands in the distal lowlands (Morse et al. 2012). Fish Island has remained protected from the storm surge events that impact the more exposed coastal wetlands to the west (Kokelj et al. 2012; Lantz et al. 2015). Protection from disturbance and low sedimentation rates have allowed peat deposits to develop at Fish Island, indicating the site has historically been a significant C sink. Observations from this site can serve as a benchmark for C exchange in “healthy” low center polygons in the Western Canadian Arctic.

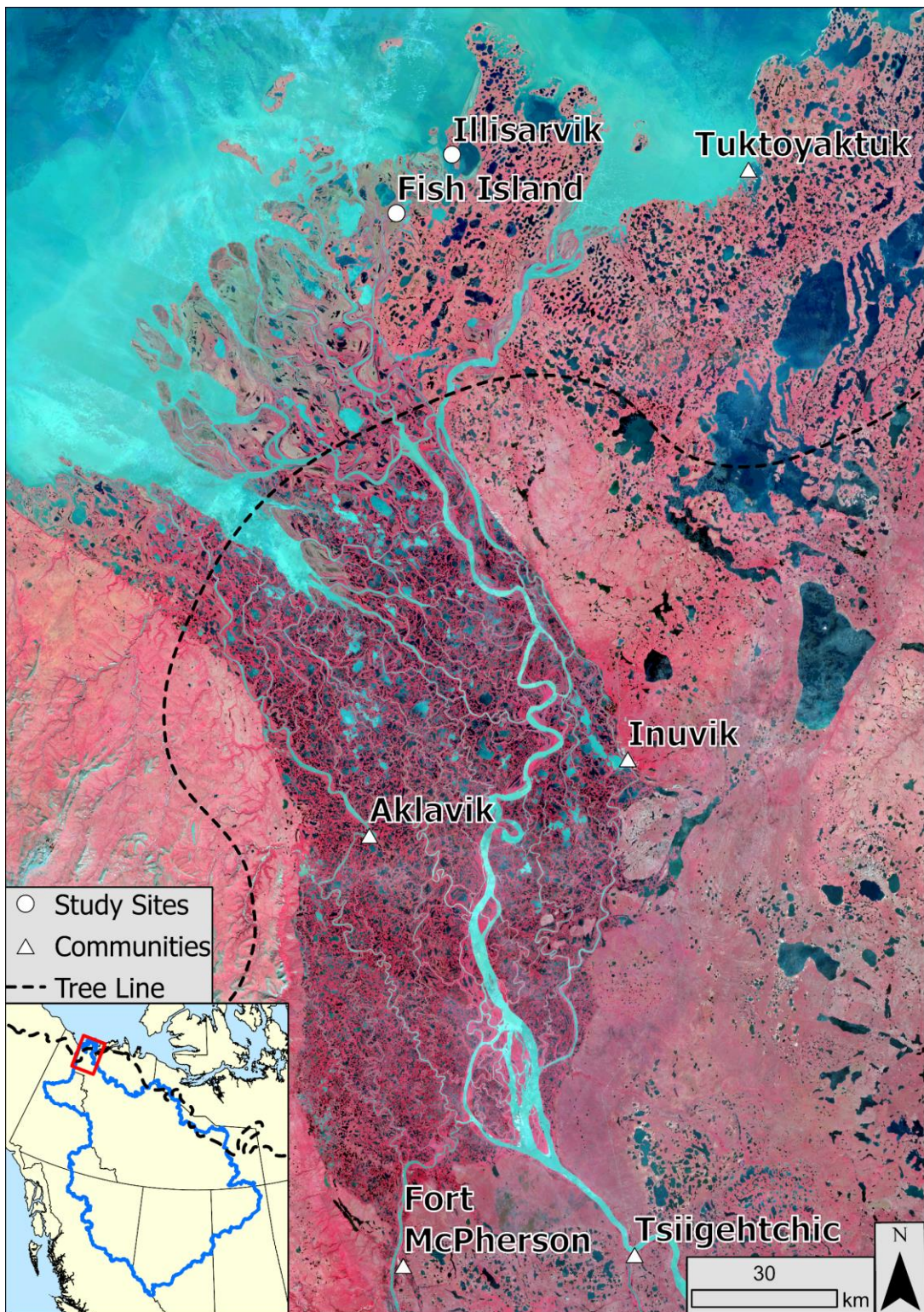


Figure 1.3 False color composite LANDSAT8 image (bands 3, 4, and 5) of the Mackenzie Delta. Labeled on the map are the study sites at Fish Island and Illisarvik, communities in the delta region, and the boreal tree line. The inset map shows the extent of the Mackenzie River drainage basin outlined in blue.

1.4 Eddy Covariance Methods

The primary techniques for measuring trace gas fluxes at the plot scale ($< 1 \text{ m}^2$) and ecosystem scale ($< 1 \text{ km}^2$) are gas chamber (GC) and eddy covariance (EC) methods, respectively (Norman et al. 1997; Baldocchi, 2003). The simplest and most popular GCs are static chambers, which are useful for obtaining a numerous samples from a variety of systems as they are cheap and easy to implement in remote locations (Virkkala et al. 2018). However, this method has drawbacks which can induce considerable bias to flux estimates, upwards of 15% (Nay et al. 1994; Healy, 1996). Further, limitations on the size of collars mean GCs are not a practical way to study NEE shrub or forest landscapes and manual sampling is an impractical way to obtain continuous flux measurements.

Over recent decades, EC methods have become increasingly popular following improvements in instrumentation, affordability, and computing power (Aubinet et al. 2012). EC methods are noninvasive, an EC tower minimally disturbs the landscape, and does not impact fluxes from the upwind study area. Additionally, they measure a much larger area than GCs and can provide continuous data sets, allowing for seasonal and diurnal fluctuations in fluxes to be measured with relative ease (Baldocchi, 2003; Vesala et al. 2008; Burba, 2013).

Flux estimation from EC observations requires a number of conditions be met: flat homogenous terrain, negligible mean vertical wind, negligible density fluctuations, turbulent flow, and stationarity (Stull, 1988). In practice, these assumptions are often impossible to perfectly satisfy, but careful site selection, flux corrections, quality control tests, and data filtering can minimize error (Papale et al 2006; Burba, 2013). Data filtering can result in substantial data loss, particularly for CH_4 fluxes, and it is not uncommon to lose more than 50% of half-hourly observations (Delwiche et al. 2021). Robust gap filling methods are required to

compensate for extended data gaps, but because there are not widely applicable response functions for NME, site specific response functions must be developed. For NEE, gap filling is typically straightforward; it involves modelling ER and GPP separately using temperature and light response curves respectively and estimating NEE as the sum of ER and GPP (Aubinet et al. 2012). However, this method has limited applicability in the Arctic during the growing season. Nighttime data are not available during the polar summer, making it difficult to isolate ER from GPP using EC data alone.

Spatial heterogeneity is a complicating factor for interpreting flux observations in polygonal tundra. Even for NEE, which is relatively well understood, having different levels of GPP and ER collocated within the footprint (upwind observation area) of the EC sensor means we cannot easily parameterize response functions. Footprint modelling can be used to map the source area of flux observations, but differential source/sink strength within the footprint can complicate interpretation (Schmid 2002). Combining landscape classification maps with footprint modelling to determine source area distribution by vegetation community can be a useful approach to assist with interpreting results in tundra ecosystems (Holl et al. 2019; Rößger et al. 2019a & b; Dengel et al. 2021). Even with landscape classification, the issue of flux attribution requires careful consideration. Collocating an EC tower with gas chambers can assist with mapping source/sink distribution (e.g. Sachs et al. 2008 and 2010). We employed chambers where possible, but continuous chamber observations are not feasible at remote tundra sites.

1.5 Machine Learning

Machine learning is a family of methods whereby an algorithm builds a predictive model from experience by learning patterns in training data. Algorithms can learn the functional relationships (and noise) in a dataset without them being explicitly programmed in advance

(Smith 1993). Care must be taken to prevent overfitting when using machine learning, but there are numerous methods available to account for this issue (Sarle 1995 & 2014; Khosravi and Nahavandi, 2011). Machine learning methods are particularly useful for analyzing CH₄ flux data because there is not a straightforward functional relationship governing CH₄ emissions and dynamics vary widely between different sites (Dengel et al. 2013; Kim et al. 2020; Irvin et al. 2021).

I elected to use machine learning methods for this work because they presented viable solutions to a number of issues: 1) They can map GPP and ER simultaneously to estimate NEE without requiring nighttime data. 2) They are one of the preferred methods for gap-filling NME. 3) They are flexible enough to incorporate source area distribution when mapping flux responses, which is useful for working in heterogeneous ecosystems. Below is a brief discussion of the pros and cons of two commonly used machine learning methods.

1.5.1 Random Forests

Random Forest (RF) regression is a powerful, lightweight machine learning method that can be applied with relative ease. It involves training a large number (e.g., $n \geq 100$) of regression trees on bootstrapped iterations of a dataset (Breiman 2001). Individual regression trees overfit the data they are exposed to, but the RF method relies on the law of large numbers to minimize the overfitting of the trees in aggregate. They are frequently applied in EC studies for gap filling because they are fast, easy to use, and produce high r^2 values in artificial gap filling experiments (eg. Kim et al. 2020; Irvin et al. 2021).

There are two key limitation issues with RF methods: 1) RF models are poorly suited for extrapolation. They cannot make projections outside the domain they were trained on and often perform worse than simple linear regression for projection problems (Hengl et al. 2018). Gaps in

EC data are frequently due to conditions in which the method is incapable of accurately measuring fluxes (e.g. precipitation events, low friction velocity, etc.) and using a RF model to predict fluxes during these intervals may not be the best approach. Artificial gap filling experiments do not address this issue because gaps are created from valid EC observations. 2) RF models do not yield response functions that can be inspected for physical plausibility. They fit training data by minimizing mean squared error through a series of binary splits, producing a complex stepwise function. Individual trees can be inspected, but the hundreds of trees in a RF model cannot be visualized in aggregate and it is essentially impossible to follow the flow of information through a RF model (see discussion in Appendix A).

1.5.2 Neural Networks

Neural networks (NN) are an incredibly flexible and powerful group of machine learning algorithms.. They are ideally suited for handling data with complex non-linear relationships because they make no prior assumptions about the distribution of a dataset (Hornik 1991; Melesse and Hanley 2005; Khosravi et al. 2011). They are frequently used for feature detection and pattern recognition for tasks like speech recognition and computer vision. They are much more computationally expensive than RF models and have historically been considered impractical because of the time required to train models and fine-tune hyper parameters. Recent advancements in hardware (e.g., GPU processing) and software (e.g., TensorFlow) have streamlined the NN training process.

A key advantage of NN models over RF models is they are capable of extrapolation. The continuous, non-linear response functions NNs produce can be used to estimate outputs for unseen inputs. This is useful for gap filling, but this point is not addressed in artificial gap filling experiments (e.g., Kim et al. 2020; Irvin et al. 2021). Because of their flexibility, NN are widely

used for gap filling EC observations of CO₂ fluxes (e.g., Papale et al. 2003; Moffat et al. 2007; Schäfer et al. 2019; Lee et al. 2021) and CH₄ fluxes (e.g., Dengel et al 2013; Knox et al. 2019; Rößger et al. 2019). Their predictive capacity also makes them useful for upscaling; they have been used for spatial upscaling (e.g., Eshel et al. 2019) and temporal upscaling (e.g. Melesse and Hanley 2005; Dou and Yang 2018). Additionally, NN have been successfully used to partition NEE into GPP and ER (Desai et al. 2008; Tramontana et al. 2020) and they have been applied to identify CH₄ flux drivers at wetland sites (Knox et al. 2016).

A commonly cited downside of NN algorithms is that trained models are “black boxes”. That is, they can be used to produce a final result but we cannot discern any information about the importance of input features or the functional relationships in the model (Melesse and Hanley 2005; Moffat et al. 2007; Irvin et al. 2021). However, this is not true. The Weights Method presented by Gevrey et al. (2003), provides a way to open up the “black box”. This method involves calculating the partial first derivatives of every input parameter (see Section 3.2.3.2 for an in-depth discussion). It can be used to evaluate the relative influence of inputs, prune inputs from high dimensional models, and visualize the functional relationships identified to ensure they are physiologically plausible (Amiri et al. 2020). To my knowledge this method has not formally been applied in any EC study outside of the work presented here. Moffat et al. (2010) used partial derivatives to visualize CO₂ flux responses to two and three input NN models, but they did not use the method to rank inputs or prune higher dimensional models. The application of the Weights Method to EC data is a key contribution stemming from this research.

1.6 Research Objectives

The aim of this research is to advance our understanding of the dynamics governing growing season C exchange in remote tundra ecosystems of the Mackenzie Delta Region. The three primary objectives of this work are:

- 1) Measure growing season fluxes of CO₂ and CH₄ at Illisarvik and Fish Island in the northern Mackenzie Delta Region, use gap-filling to estimate NEE and NME, and quantify the portion of CO₂ uptake offset by CH₄ emissions at both sites.
- 2) Use NN models to gain insight into the controls of ecosystem scale NEE and NME at Illisarvik and Fish Island.
 - a. Identify the dominant bio-climate drivers of NEE and NME and map the functional relationships identified.
 - b. Investigate and account for the influence of fine-scale spatial heterogeneity over ecosystem scale fluxes.
- 3) Investigate interannual climate variability at Fish Island and conduct a temporal upscaling experiment using NN models to estimate the possible influence of variability on growing season CO₂ and CH₄ fluxes at Fish Island.

Chapter 2: Vegetation influence and environmental controls on greenhouse gas fluxes from a drained thermokarst lake in the western Canadian Arctic

A version of chapter 2 has been published. Skeeter, J., Christen, A., Laforce, A.-A., Humphreys, E., & Henry, G. (2020). Vegetation influence and environmental controls on greenhouse gas fluxes from a drained thermokarst lake in the western Canadian Arctic. *Biogeosciences*, 17(17), 4421–4441. <https://doi.org/10.5194/bg-17-4421-2020>

2.1 Introduction

The northern permafrost region stores approximately 50% of global organic soil carbon in 16% of the terrestrial land area (Tarnocai et al. 2009). Thermokarst landscapes account for approximately 20% of the land area in this region and hold about half of its organic soil carbon (Olefeldt et al. 2016). Lake thermokarst landscapes are widespread in poorly drained, sedimentary permafrost lowlands with excess ground ice volume and constitute about a third of all thermokarst area (French, 2017; Olefeldt et al. 2016). Thermokarst lakes are a prominent landscape feature of the Western Canadian Arctic (Mackay, 1999; Marsh et al, 2009; Lantz & Turner, 2015). These lakes drain, sometimes catastrophically, forming drained thermokarst lake basins (DTLB) via bank overflow, ice wedge erosion, coastal erosion, and stream migration (Billings and Peterson, 1980; Mackay, 1999). Lake formation and drainage is a natural part of the thaw lake cycle, but it is anticipated that climate change will accelerate or disturb this cycle, potentially altering the regional carbon balance (Jones et al. 2018).

Net ecosystem exchange (NEE), ecosystem respiration (ER) and gross primary productivity (GPP), where $NEE = ER - GPP$ are lower in the Arctic than warmer regions but

have significant seasonal cycles and variability between vegetation types (Virkkala et al. 2018). Future trajectories in NEE will in large part be governed by ER (Biasi et al. 2008; Cahoon et al. 2012). Dominant vegetation types in the Western Canadian Arctic are erect-shrub tundra and wetlands (Walker et al. 2005). Growing season NEE is typically negative across these units throughout the Arctic indicating a net CO₂ sink as GPP exceeds ER in part due to cold and/or anoxic soil conditions (Virkkala et al. 2018; Lafleur et al. 2012). Annual NEE can be positive or negative with large variation in GPP linked to annual weather variability (Virkkala et al. 2018, McGuire et al. 2009). Arctic net methane exchange (NME) is positive because wetland areas are strong methane (CH₄) sources while upland areas with better drainage can be net sinks (Whalen and Reeburgh, 1990; McGuire et al. 2009; Sturtevant and Oechel, 2013).

Thermokarst lakes are well recognized sources of CH₄ (Walter et al. 2007) which is 27 times as potent as carbon dioxide (CO₂) on a 100-year time scale (Forster, 2021). Thermokarst lake formation and expansion is expected to exert a positive feedback on climate change and accelerate Arctic warming in the near term, but modelling suggests that drainage may limit expansion and result in decreased lake area by the end of the century (van Huissteden et al. 2011). Post drainage, DTLB undergo rapid ecological succession. In colder tundra environments, wet meadows or polygonal landscapes dominated by sedges, grasses and rushes will form (Lara et al. 2015). In slightly warmer, boreal and transitional regions, DTLB often become dominated by willows and other shrubs (Lantz and Turner, 2015).

Carbon exchange in DTLB of various ages has been examined in a few studies, almost exclusively focused on the Barrow Peninsula in Northern Alaska. DTLB NEE during the growing season is negative with greatest CO₂ uptake in younger basins and decreasing net uptake as basins age in this region (Zona et al. 2010; Zulueta et al. 2011; Sturtevant and Oechel, 2013;

Lara et al. 2015). DTLB source/sink strength of CH₄ was found to be highly variable depending on vegetation and ground conditions (Lara et al. 2015). NME is highest in wet meadows and remnant ponds but considerably reduced in areas with better drainage (Zona et al. 2009; Zona et al. 2012; Lara et al. 2015). There may be regional variations in the carbon balance of DTLB. For example, a shrub dominated ancient DTLB known as Katyk in the Indigirka lowlands of Siberia shows considerably higher growing season carbon uptake than young Alaskan DTLB with comparable NME (van der Molen et al. 2007; Parmentier et al. 2011). Similarly, DTLB in the Western Canadian Arctic may have different carbon fluxes than Alaskan DTLB due to differences in climate and vegetation composition.

In this study, fluxes of CO₂ and CH₄ were measured at Illisarvik, an experimentally drained thermokarst lake basin on Richards Island in the Western Canadian Arctic, Northwest Territories, Canada. Fluxes of CO₂ and CH₄ were measured during the peak growing season using a combination of closed chamber and eddy covariance (EC) measurements. NEE was calculated from fluxes and storage change and was separated into ER and GPP. Here we report on: 1) the spatial and temporal variability of the NEE and NME during the growing season, 2) the vegetation and environmental factors influencing NEE and NME, 3) how the growing season carbon balance at Illisarvik compares to other DTLB, and 4) potential future carbon balance trajectories as Illisarvik's vegetation communities continue to evolve.

2.2 Methods

2.2.1 Study Site and Data Collection

The study took place at Illisarvik, a DTLB on Richards Island (69°28'47.5" N, 134°35'18.7" W), that was drained experimentally in 1978 (Mackay, 1981). Illisarvik has since served as the focus of studies on permafrost growth, active layer development and vegetation

succession (Ovenden, 1986; Mackay and Burn, 2002; O’Neil et al. 2012; Wilson et al. 2019). At the nearby Tuktoyaktuk climate station mean annual air temperature (T_a) is -10.1 °C, July is the warmest month with a mean of 11°C and January is the coldest at -27°C. Mean annual precipitation is 160.7 mm yr⁻¹, the majority falling as rain in the summer and autumn. Snow cover typically lasts from mid-September or early October to late May (Environment Canada. 2016). Tuktoyaktuk is 60 km east of Illisarvik and in similar proximity to the coast so the climatology is expected to be similar at Illisarvik.

In the 39 years since drainage, Illisarvik has undergone rapid vegetation succession. After drainage, there were two remnant ponds. In the first five years after drainage, vegetation colonized the basin margins and wetter areas (Ovenden, 1986). By 1999, low vegetation had proliferated across most of the basin and taller willows had become established along the basin margins (Mackay and Burn; 2002). By 2010, some of the willows had grown to be 3 m in height (O’Neil and Burn; 2012). Current vegetation at Illisarvik is diverse relative to the dwarf-shrub tundra of the surrounding uplands (Table 2.1); the basin hosts a mix of woody shrubs (*Salix* spp., *Betula* spp., & *Alnus* spp), wetland vegetation (*Carex aquatilis*, *Arctophila fulva*, etc.), and various grasses (*Poaceae* spp.) (Wilson et al. 2019). The basin is partly ringed by a terrace of peat that formed after a partial drainage event ~ 5000 years BP and supports vegetation similar to the uplands (Michel et al. 1989). An ancient DTLB is located 100 m to the south of the Illisarvik basin and the Arctic Ocean is to the west of the basin, separated by a ridge of upland tundra about 50 m wide at its narrowest (Fig 2.1).

A vegetation survey of species composition and abundance was done on a 50 m grid in and around the basin during the 2016 study period (Wilson et al. 2019). A vegetation map was created with ten units based on plant functional type and vegetation structure, with sub-units

denoting sub-canopy vegetation. The unit boundaries between grid points were estimated visually by traversing the grid lines. Additional survey data on vegetation units and canopy height were collected manually with a GPS in the proximity of the EC station because greater resolution was needed for footprint modelling. Aerial imagery was collected on July 23rd over two flights using a Phantom 2 drone (DJI, Shenzhen, China). The GPS points and drone imagery were used to cross reference and modify the map of Wilson et al. (2019). The ten units were then aggregated into six broader surface cover classes (listed from largest to smallest areal fraction within the footprint climatology (F_{Clim}) see Section 2.3 for definition): shrub, grass, sedge, upland, sparse, and water classes (Fig 2.1 & Table 2.1).

Table 2.1: Dominant species or landscape feature within the vegetation/cover classes. Unit codes correspond to the map Figure 1a.

Unit Code	Vegetation Class	Dominant Species/Landscape feature
1a	Shrub	<i>Salix alaxnensis</i> (Tall Willow)
1b	Shrub	<i>Salix glauca</i> (Low Willow)
1c	Shrub	<i>Alnus viridis</i> subsp. <i>crispa</i> (Alder)
2a	Sedge Marsh	<i>Carex aquatilis</i> (Sedge)
2b	Sedge Marsh	<i>Arctophila fulva</i> (Pendant Grass)
3	Grass Meadow	<i>Poaceae</i> spp. (Grasses), <i>Eriophorum angustifolium</i> (Cotton Grass)
4a	Sparse Cover	Sparse Vegetation
4b	Sparse Cover	Bare Ground
5	Ponds	<i>Hippuris vulgaris</i> (Mare's Tail), Open Water
6a	Outside of Basin	Dwarf shrub tundra: <i>Salix</i> spp. & <i>Betula nana</i> (Birch)

6b	Outside of Basin	Fen
6c	Outside of Basin	Ocean

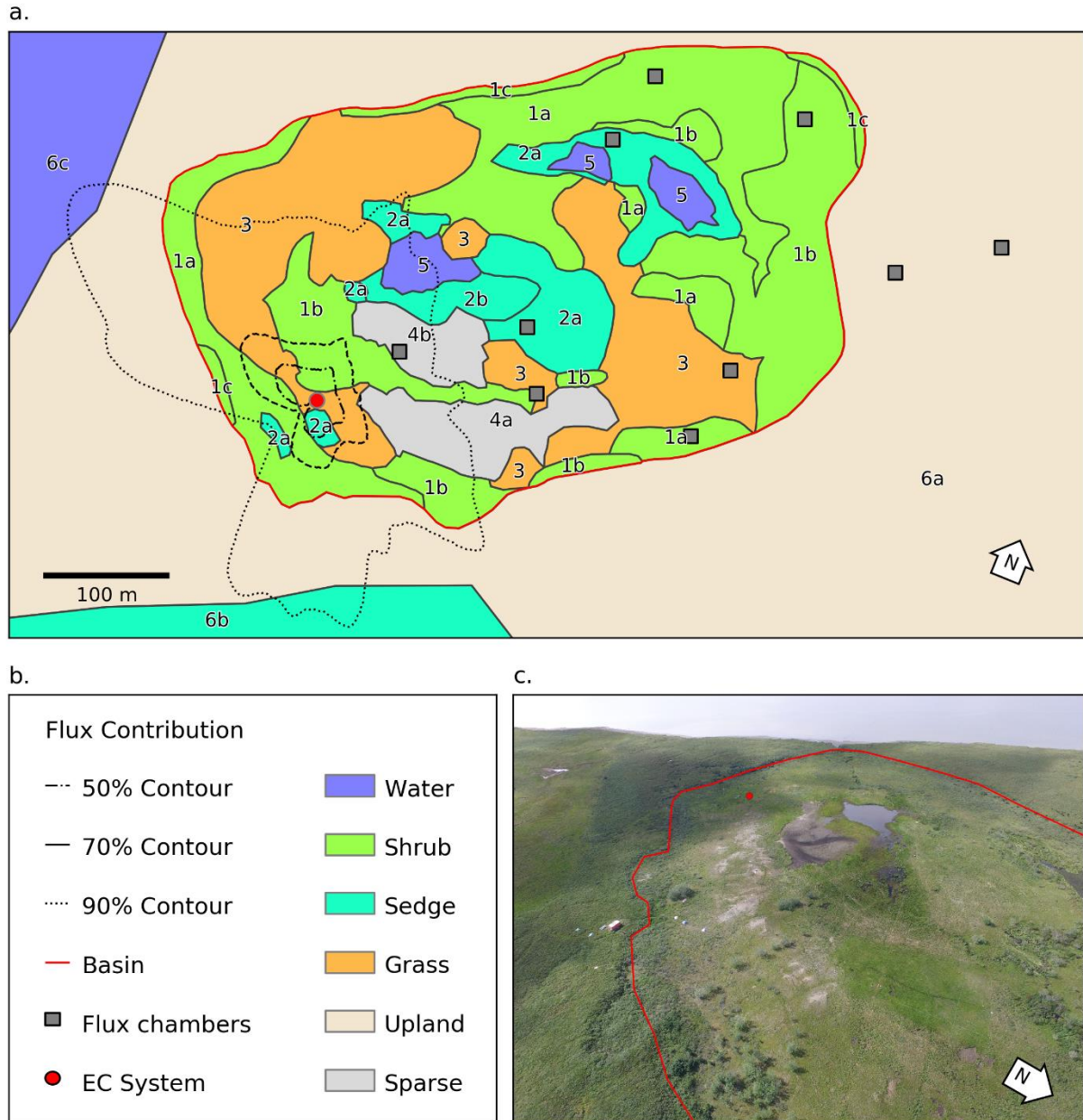


Figure 2.1 a) Map of the distribution of vegetation classes at Illisarvik, with the footprint climatology (F_{Clim}) over the study period, the locations of the chambers and the eddy covariance (EC) system. The alphanumeric labels correspond to the unit codes in Table 2.1. b) Legend for the map in a. c) Oblique drone image of

Illisarvik, take at 16:40 July 23rd 2016 view from E of DTLB towards W. The Basin and EC system are shown on the image using the same symbology as a).

2.2.2 Weather and Soil Measurements

Weather data were logged on a CR1000 datalogger (Campbell Scientific Inc, Logan, UT, USA; CSI) at 5-minute intervals. Net all-wave radiation (R_n) and photosynthetic photon flux density (PPFD) were measured with a NRLite net radiometer (Kipp & Zonen, Delft, Netherlands) and a SQ-110 quantum sensor (Apogee Instruments, Logan, UT, USA), respectively 3.2 m above the grass surface on the main EC system tripod (Fig 2.1). A shielded HMP35 (CSI) recorded T_a and relative humidity (RH) 2 m above the surface. A tipping bucket rain gauge (R.M Young Company, Travers City, MI, USA) was placed 3 m to the west of the main tripod. Soil temperature and moisture were measured within soil pits in two different vegetation types near the tripod: Grass (30 m to the east) and Shrub (40 m to the north). Measurements were made of ground heat flux (G) with custom-made heat flux plates, soil temperatures (T_s) with custom type-T thermocouples at depths of 0.08 m, and 0-20 cm integrated volumetric water content (VWC) with CS616 water content reflectometers (CSI). The soil measurements were recorded at 30-minute intervals on CR10x dataloggers (CSI). The climate and soil stations operated uninterrupted from July 10th (day 192) and July 11th (day 193), respectively, until August 7th, 2016 (day 220). On July 11th and August 6th thaw depth was measured at each of the 10 chamber sites (see below). Thaw depth was measured by inserting a graduated steel probe into the ground to point of refusal. Each site was probed five times: the median value has been used as the thaw depth at each location. On July 12th and 15th, a large herd of reindeer (500 + animals) visited Illisarvik. They mostly avoided the tripod but did graze near it for about an hour on July 12th which may have affected greenhouse gas fluxes.

2.2.3 EC Fluxes

An EC system was placed in the southwestern portion of the basin ($69^{\circ} 28' 47.82''$, $-134^{\circ} 35' 18.6''$) and measured fluxes of CO₂ (F_{CO_2}) and CH₄ (F_{CH_4}) for the full study period between July 10th and Aug 7th, 2016. The EC system consisted of an open-path infrared CO₂/H₂O gas analyzer (IRGA) (model LI-7500, LI-COR Inc., Lincoln, NK, USA; LI-COR), an open-path CH₄ analyzer (model LI-7700, LI-COR) and a CSAT3 sonic anemometer (CSI) mounted on a tripod at a measurement height (z_m) of 3 m (Fig 2.2). The EC data and air pressure (P_a) were logged at 10 Hz on the LI-7550 Analyzer Interface Unit (LI-COR). The CSAT3 was oriented to the northeast (40°) because climatology for Tuktoyaktuk indicated northerly and easterly winds are typical for July and August (Environment Canada, 2016).

Half-hourly fluxes were calculated with EddyPro V.6.2.0 (LI-COR). The software performed statistical assessments (Vickers and Mart, 1997), low and high frequency spectral corrections (Moncrieff et al. 1997 and 2004), a double rotation (Wilczak et al. 2001), applied the WPL correction to account for density fluctuations (Webb et al. 1980), and computed quality control (qc) flags (Mauder and Foken, 2004). Post processing treatments included: storage correction (calculating the net flux as the sum of the observed scalar flux and the rate of change in scalar concentration at z_m), filtering fluxes by friction velocities (u_*) below 0.1 m s^{-1} , removing qc flags = 2 (Mauder and Foken, 2004), and the mean absolute deviation spike removal algorithm (Papale et al. 2006). Additionally, observations with mean winds from $220^{\circ} \pm 30^{\circ}$ were removed to avoid uncertainties associated with the wake of the sonic anemometer, and observations were removed during precipitation events and when the open-path analysers indicated there were any other obstructions within the path (Aubinet et al. 2012). The data were gap-filled using neural networks (NN) which have been applied to F_{CO_2} and F_{CH_4} in other studies

(Moffat et al. 2010; Dengel et al. 2013). Details of the NN methodology are described in Appendix A.

The flux footprint represents the influence of upwind areas on a measured scalar flux and the footprint climatology is the average of individual footprints over a time period. Evaluation of the flux footprints and climatology help evaluate the reliability of the dataset and estimate the source area of each individual half-hourly EC flux measurement. A scalar flux F_c sampled at $(0,0,z_m)$, where z_m is the height of the EC instrumentation, can be represented as the integral of the flux footprint function $f(x,y)$ and the distribution of sources/sinks (Q_c) over a domain D (Kljun et al. 2015):

$$F_c(0,0,z_m) = \int_D Q_c(x,y)f(x,y) \quad \text{EQ 2.1}$$

The flux contribution of upwind source areas increases sharply upwind from the measurement location to a peak then decrease gradually with increasing distance (Schmid, 2002). The empirically derived flux footprint function of Kljun et al. (2015) was used to estimate the source area of each half hourly flux measurement.

The footprint model requires boundary layer heights which were not measured onsite. Half hourly boundary layer heights were interpolated from three-hour estimates obtained from the Global Data Assimilation System of the U.S. National Oceanic and Atmospheric Administration. The model also requires the aerodynamic roughness length (z_0) which is influenced by the canopy height and spacing. Canopy height (C_h) varied considerably within the basin (from >1 m in the north to ~0 m in the bare ground areas). Canopy height variability was lower in the vicinity of the EC tripod but ranged from 0.35- 0.55 m with a few taller shrubs approaching 1 m. Median z_0 was calculated for 30° wind sectors following Paul-Limoges et al.

(2013). This calculation was performed for near neutral conditions $-0.05 \leq \frac{z_m}{L} \leq 0.05$, where L is the Obukhov length. The z_0 for each wind sector was found to be insensitive to zero-plane displacement height, d , as $z_m \gg d$, so the mean value of d around the tripod was used, where $d = 2/3 C_h$. Zero-plane displacement did not change significantly over the course of the study so z_0 remained fixed over the study period for each wind sector.

For each half-hourly flux observation, $f(x,y)_i$ was solved at 1 m² resolution over a 1 km² domain centred on the EC tripod. Then, $f(x,y)_i$ were intersected with the surface classes to determine the relative contribution of each surface type to each flux observation (referred to as F_{Shrub} , F_{Sedge} , etc.). The footprint function is technically infinite so a fraction of each $f(x,y)_i$ was not contained within the model domain. The out-of-domain source fraction ranged from 1.8% to 4.9% with a mean of 3.2% and was assumed to have minimal impact on the analysis. The flux footprint climatology (F_{Clim}) was calculated by averaging the half hourly flux footprints over the study period and is shown in Figure 2.1. Table 2.2 shows the flux contribution of each vegetation class.

Table 2.2: The surface cover class fractions of the basin, along with the mean source area fractions of the footprint climatology (F_{Clim}) and the range of source area fractions for individual half hourly observations shown in brackets.

Surface Class	Basin	F_{Clim}
Shrub	48.3 %	36.0 % [0.0 – 79.0%]
Grass	27.9 %	39.0 % [1.1-78.1%]
Sedge	12.3 %	10.9 % [0.0 – 55.6%]
Sparse	8.4 %	2.2% [0.0 – 33.6%]
Water	3.1 %	0.2% [0.0 – 4.4%]
Upland	0%	6.2% [0.6 – 15.0%]

Outside Basin	0%	12.3% [0.2 - 28.0%]
---------------	----	---------------------

2.2.4 Closed Chamber Measurements

In addition to EC measurements, fluxes of CO₂ and CH₄ were sampled using a static non-steady state chamber flux technique on 11 dates between July 12 and August 5, 2016 (Laforce, 2018). Nineteen chamber collars were located at ten sites, eight sites within and two outside the basin (Fig 2.1). Each surface cover class was represented by at least one chamber site, except for open water. At each vegetated site a pair of collars were installed 20 cm apart, except at the ‘sparse’ site where only one collar was installed. The above ground biomass was removed from one of the collars at each vegetated site. There were three replicates (six collars) for the Shrub class, two for the Sedge, Grass, and Upland tundra, and no replicates for the Sparse class. PVC collars 30 cm long and 24.3 cm in diameter were inserted to a depth of approximately 15 cm. The chambers were 34 cm tall and made out of polycarbonate covered in black opaque tape to maintain dark conditions inside the chamber (for more details, see Martin et al. 2018). The chambers contained a small vent (10 cm coiled 1/8” diameter copper pipe) to ensure a constant pressure during measurements. The opaque chamber fluxes of CO₂ provided an independent estimation of ER. This helped characterize ER given the challenges with standard NEE partitioning techniques at high latitude sites during the Arctic summer as noted in section 2.2.5.1.

Chamber flux measurements were made between 9:00 and 17:00 starting at a different collar set each day to randomize the sampling order to avoid a bias due to diurnal patterns. During gas flux measurements, the chambers were sealed to the top of the collars within a groove filled with water and five 24 mL air samples were collected into evacuated 12 mL vials sealed with doubled septa. Each vial contained a small amount of magnesium perchlorate to dry

the air sample. Samples were collected at 0, 5, 10, 15 and 20 minutes after the chambers were set on the collars. Air within the chamber was mixed with a 60 mL syringe attached to a three-way stopcock before each air sample was taken. Samples were stored until analysis one month later at Carleton University. The integrity of the vials through shipping, storage and analysis was confirmed using a subset filled with helium before the field season began.

Concentrations of CO₂, CH₄ and N₂O were determined using a CP 3800 gas chromatograph (Varian Inc., Pao Alto, CA, USA) as described by Wilson and Humphreys (2010). Three replicates of five CO₂/CH₄ standards varying from 383.1 to 15212.6 ppm CO₂ and from 1.08 to 22.11 ppm CH₄ were included in every set of measurements to create a linear relationship between gas concentration and chromatogram area. The chamber fluxes of CO₂ and CH₄ (F_C) were calculated as follows:

$$F_C = \frac{VP}{ART} \frac{dc}{dt} \quad \text{EQ 2.2}$$

where (dc/dt) is the linear rate of change in the mixing ratio of the gas, A is the chamber area (0.0464 m³), V is the chamber volume (between 0.0182 and 0.0242 m³ adjusted for collar depth at each collar location), R is the ideal gas constant, P is pressure in Pa and T is the air temperature in Kelvin. P and T values corresponding to the time of each measurement were obtained from the EC station. Visual inspection of the linear trend of gas concentrations (dc/dt) was used to identify and remove spurious point measurements associated with analysis errors, leaking chambers (isolated decreases in concentration) and contamination or ebullition events (isolated increases in concentration) (0.3%, 0.7%, and 2.0% of CO₂ samples and 2.1%, 0.5%, and 1.1% of CH₄ samples, respectively). In all flux measurements, at least three or more gas samples remained so that dc/dt and its coefficient of determination (r^2) were determined using least squares linear regression. We did not use r^2 as an additional quality control criteria as many

of our CH₄ fluxes were near zero and tended to have low r² values due to only small variations in the point sample concentrations (see also Clark et al. 2020). 40% and 32% of the 227 CH₄ flux measurements and 97% and 92% of the 227 CO₂ flux measurements had r² over 0.80 and 0.90, respectively. Positive fluxes indicate emissions of gases to the atmosphere and negative fluxes indicate uptake by the surface.

2.2.4.1 Upscaling

Chamber fluxes of ER were upscaled from the plot scale (individual chamber) to the footprint scale using the footprint weighted average method and to the basin scale using the area weighted average method (Budishchev et al. 2014). The chamber ER and air temperature from the EC tripod (T_a) were used to determine R₁₀, the base respiration at 10 C°, and Q₁₀, the temperature sensitivity coefficient, using EQ 2.3 for five of the six surface classes (Fig 2.1) (Laforce, 2018) (Table 2.3).

$$ER = R_{10} Q_{10}^{\frac{(T_a - 10)}{10}} \quad \text{EQ2.3}$$

Half hourly footprint scale estimates (ER_{FS}) were calculated by multiplying ER derived from EQ 2.3 for each surface class by the footprint source area fraction and summing over classes. Basin scale estimates (ER_{BS}) were estimated the same way but using the mean source area fractions of the basin (Table 2.2). As there were no open water class ER estimates, ER from open water was assumed to be zero.

In contrast to ER, there are no standard empirical functions to estimate temporal variations in NME. Instead, we used ordinary least squares regression (OLS) to estimate NME. The most important environmental controls over F_{CH4} were VWC and T_s (discussed below). Continuous observations of these factors at the flux chambers were not available, instead chamber NME were grouped by vegetation class and fit to VWC and T_s measured in the soil pits

near the EC station. Half hourly footprint scale (NME_{FS}) and basin scale (NME_{BS}) estimates were then estimated using the OLS parameters for each surface class using the same procedures for ER_{FS} and ER_{BS} .

	Q_{10}	$R_{10} \mu\text{mol m}^{-2} \text{s}^{-1}$	R^2
Sedge	2.1	3.8	0.82
Upland	1.9	4.1	0.55
Grass	1.6	4.0	0.55
Shrub	1.8	2.7	0.46
Sparse	1.0	1.9	0.01
Night-time EC observations (n=100)	1.6	2.9	0.47

Table 2.3: The ER temperature sensitivity (Q_{10}) and base respiration (R_{10}) estimated by Laforce (2018) and estimated from nighttime EC footprint observations.

2.2.5 Factor Selection and Gap Filling

We used an exploratory approach to identify the smallest set of factors that best predicted half hourly EC-derived NEE and NME without overfitting the dataset using a series of neural networks (NN). We started with 10 factors: four meteorological variables [$PPFD$, T_a , vapor pressure deficit (VPD) computed using the T_a and Rh data, three-dimensional wind speed (U) measured using the CSAT3 sonic anemometer], two soil variables [(VWC) and T_s averaged between the two soil pits near the EC tripod], and four source area fractions [Shrub (F_{Shrub}), Grass (F_{Shrub}), Sedge (F_{Sedge}), and Upland, (F_{Upland})]. The four source area variables correspond to surface classes sampled by the chambers. We excluded Water (F_{Water}) and Sparse (F_{Sparse}) fractions because its average contribution to the EC observations was only 0.2% and 2.2%,

respectively, and there were no chamber measurements for the Water class while chamber measurements indicated ER was low and NME was not significantly different from zero for the Sparse class. A number of these prediction factors were highly correlated but it was necessary to include them so the model could account for source area heterogeneity.

The NNs were trained iteratively on bootstrapped datasets. First NN were trained on each factor individually and the one with the lowest MSE was selected. Next, NN were trained on that factor in combination with one of the remaining nine. The best performing additional factor was again selected and this process was repeated until MSE failed to improve. The most parsimonious model was identified using the one standard error (*SE*) rule. Dybowski and Roberts (2001) give the standard error of a bootstrap estimate of a given error metric (e.g., $\theta = MSE$) to be

$$SE_{boot}(\theta) = \sqrt{\frac{1}{B-1} \sum_{b=1}^B (\theta_b - \theta_{boot})^2} \quad \text{EQ 2.4}$$

where θ_{boot} is the mean of the bootstrapped samples. The smallest set of factors where θ_{boot} was within one SE_{boot} of the minimum θ_{boot} for both NEE and NME were selected for further analysis. The outputs from the selected models are referred to as NEE_{NN} and NME_{NN} , respectively. NN modelling was done using the Keras Python library (Chollet et al. 2015), see the Appendix A for a more detailed explanation of the NN analysis.

Multiple Imputation (MI) was then used to gap fill the NEE and NME with the NEE_{NN} and NME_{NN} , respectively (Vitale et al. 2018). Of the 1296 half hourly flux observations 28.9% of F_{CO_2} and 31.3% of F_{CH_4} were missing or filtered out. There were a few gaps in the source area fractions needed to gap-fill the flux time series because the footprint function is not valid when $u_* < 0.1 \text{ m s}^{-1}$. When source area fractions were missing, they were gap-filled by using the mean

source are fraction observed for winds within $\pm 5^\circ$ of the observed wind direction. The meteorological and soil data were continuous and did not need to be gap-filled.

2.2.5.1 Flux Partitioning

NEE is negative when there is net uptake of CO₂ by the ecosystem and positive when there is net emission. ER and GPP are always positive, ER represents the sum of heterotrophic and autotrophic respiration and GPP represents photosynthetic uptake of CO₂. Night-time NEE observations (e.g., PPFD $\leq 10 \mu\text{mol m}^{-2} \text{s}^{-1}$) are typically used to quantify ER because GPP ~ 0 (Aubinet et al. 2012). We fit the limited night-time EC observations available (n=95) to EQ 2.3 for comparison with the ER measured using the chambers. We used the fitted values to model daytime ER and approximate NEE by fitting the daytime data to a light response curve Aubinet et al. (2012).

$$NEE = \frac{1}{2c} (\alpha \text{PPFD} + \beta - \sqrt{(\alpha \text{PPFD} + \beta)^2 - 4\alpha\beta c \text{PPFD}}) + \text{ER} \quad \text{EQ 2.5}$$

where α is the initial slope of the light response curve, β is GPP at saturation, and c is a curvature parameter. These estimates are referred to as ER_{Q10} and NEE_{Q10}.

Some NN analyses of NEE have trained separate models for night-time and daytime conditions for partitioning purposes (Papale & Valentini, 2003). However, these methods are not practical during the Arctic summer as the sun did not set at Illisarvik until July 28th, over halfway through the study period. There were not enough night-time samples to train a separate NN. Instead, we estimated ER by calculating NEE_{NN} at PPFD = 0 $\mu\text{mol m}^{-2} \text{s}^{-1}$ for all observations, henceforth referred to as ER_{NN}. This is a projection outside of the observed parameter space resulting in greater uncertainty and a wider confidence interval around ER_{NN} than NEE_{NN}. Calculation of confidence intervals for NN outputs is discussed in Appendix A.

2.2.5.2 Factor Analysis

The trained NNs were used to investigate how individual factors influenced NEE and NME. The partial first derivative of the model response to one controlling factor was calculated while keeping all other inputs fixed. For example, the partial first derivative, $\frac{\partial \text{NEE}}{\partial \text{PPFD}}$, is an approximation of the NEE light response curve under a specific set of conditions. Similarly, NME_{NN} can be used to approximate NME response to controls like VWC or T_s . For both fluxes, the selected models contained at least one source area fraction variable, indicating the vegetation type(s) which had significant influence over NEE and NME. Additionally, we mapped NEE_{NN} and NME_{NN} to 100% coverage for individual surface classes to see how fluxes at Illisarvik may change as vegetation succession continues. For example, to project to 100% Sedge coverage, we set the other surface classes to 0% and left the other environmental factors unchanged. This allows for an estimation of how carbon fluxes may change if vegetation succession leads Illisarvik to look more like the DTLB studied in Alaska.

2.3 Results

During the 29-day study, half-hourly T_a and T_s ranged between 0.4 and 26.2°C and 4.4 and 11.0°C, respectively (Fig 2.2a). Day length and maximum solar altitude decreased from 24 hours to 19.25 hours and 41.6° to 35.4°, but daily PPFD was more influenced by variations in cloud cover. Precipitation (19 mm) fell on 14 of the 28 days with trace snowfall on three of those days, but VWC of the soils decreased throughout the period (Fig 2.2b). At the onset of the study period, VWC was high and soils were saturated with ponding in the sedge areas. By the end of the study most of this surface water had dried up. On July 11th average thaw depth (cm) was 37, 45, 51, 64, 81 at Upland, Sedge, Grass, Shrub, and Sparse classes, respectively. By

August 6th, average thaw depth had increased to 45, 62 and 66 cm at Upland, Sedge and Grass surface classes and over 100 cm at both the Shrub and Sparse classes.

A strong low-pressure system stalled off the coast between day of year (DOY) 199 and 204. This caused westerly winds to occur much more frequently than is typical for July and August. The 50%, 80% and 90% flux F_{Clim} contours are shown in Fig 2.1a. Mean source area fractions indicate the EC observations were skewed towards the Grass surface class and under-sampled the Shrub class, but the range of surface classes sampled was diverse enough to allow for testing of the impact of source area fraction on the fluxes (Table 2.2).

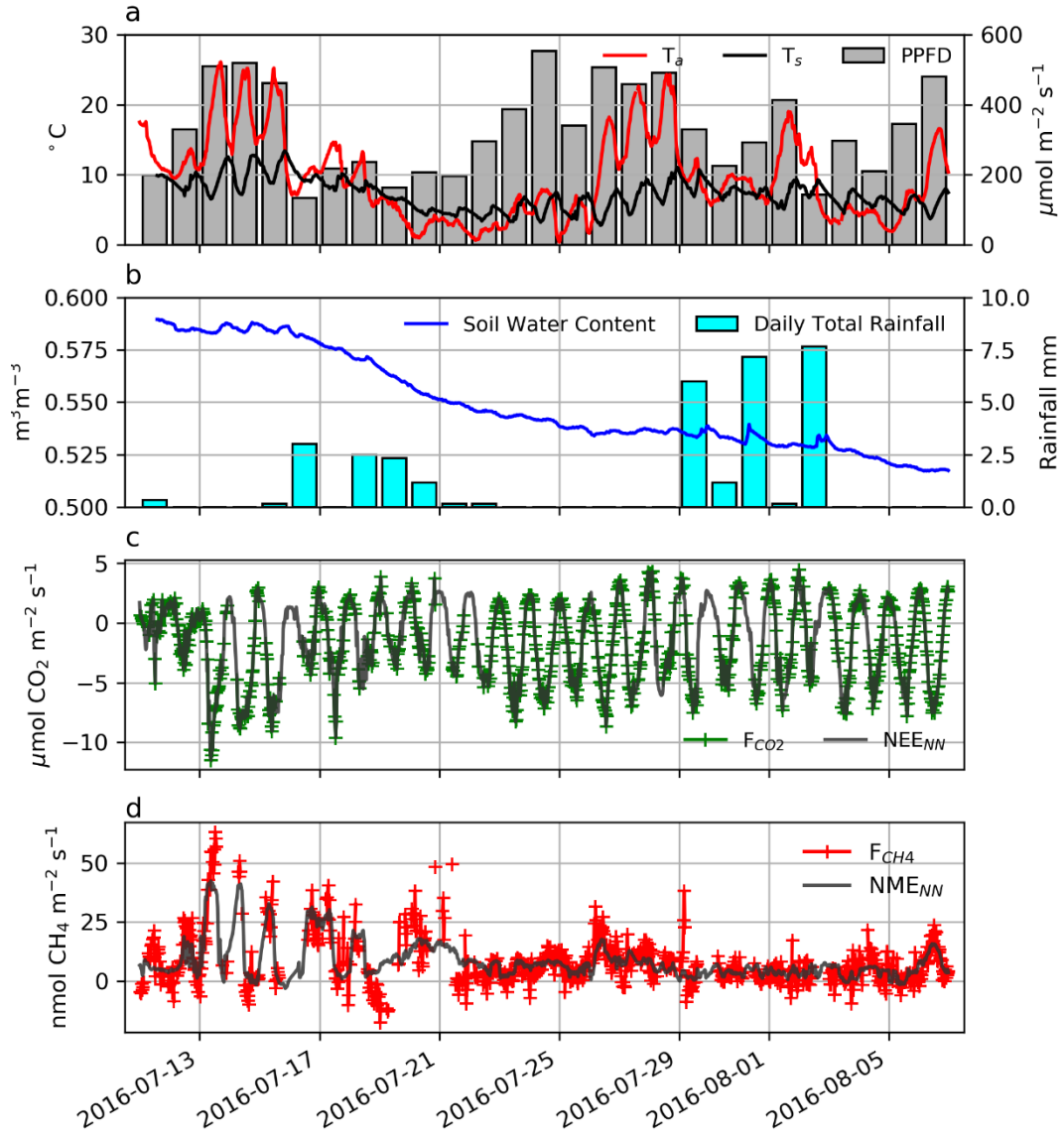


Figure 2.2 a) Half hourly air and soil temperatures, displayed along with photosynthetic photon flux density (PPFD). **b)** Hourly soil volumetric water content and daily total precipitation. **c)** Half hourly F_{CO_2} (green) and NEE_{NN} (grey), and **d)** half hourly F_{CH_4} (red) and NME_{NN} .

2.3.1 EC Observations

Half hourly observations of F_{CO_2} and F_{CH_4} along with the NEE_{NN} and NME_{NN} used to gap-fill the time series are shown in (Fig 2.2c & d). Gap-filled daily NEE ranged from -3.7 to -0.2 g C-CO₂ m⁻² d⁻¹ with a mean -1.5 [CI_{95%} ± 0.2] g C-CO₂ m⁻² d⁻¹. Day to day variability was

considerable but there was no notable trend in NEE over the peak growing season. The half hourly NEE during the study period reached a minimum of $-10.4 \mu\text{mol CO}_2 \text{ m}^{-2} \text{ h}^{-1}$ just before solar noon and peaked at $4.7 \mu\text{mol CO}_2 \text{ m}^{-2} \text{ h}^{-1}$ around midnight (Fig 2.2c). NEE_{NN} was used to gap-fill the flux data because it was in good agreement with F_{CO_2} observation ($r^2 = 0.91$). Daily ER_{NN} was estimated to be $2.2 [\text{CI}_{95\%} \pm 0.9] \text{ g C-CO}_2 \text{ m}^{-2} \text{ d}^{-1}$ with corresponding GPP of $3.7 \text{ g C-CO}_2 \text{ m}^{-2} \text{ d}^{-1}$. ER_{NN} was in poor agreement ($R^2 = 0.35$, $n= 95$) with night time F_{CO_2} observations. For comparison, EQ 2.3 provided a better fit ($R^2 = 0.47$) with night-time EC data, and ER_{Q10} was estimated to be $3.0 \text{ g C-CO}_2 \text{ m}^{-2} \text{ d}^{-1}$. However, NEE_{Q10} did not fit F_{CO_2} as well ($r^2 = 0.80$) as NEE_{NN} .

Gap-filled daily NME was modest and decreased over the study period. It ranged from 2.0 to $25.1 \text{ mg C-CH}_4 \text{ m}^{-2} \text{ d}^{-1}$ with a mean of $8.7 [\text{CI}_{95\%} \pm 0.4] \text{ mg C-CH}_4 \text{ m}^{-2} \text{ d}^{-1}$ (Fig 2.2d). NME_{NN} was used to gap-fill the flux data because it provided a reasonable fit ($r^2 = 0.62$) to F_{CH_4} observations. NME did not constitute a significant component of the carbon balance and thus the flux footprint area was a carbon sink during the peak growing season with negative GWP after accounting for the greater GWP of CH_4 .

2.3.2 Chamber Observations

ER was highest in the Sedge, Upland, and Grass classes where fluxes were very similar at $5.5 [\text{CI}_{95\%} \pm 1.2]$, $5.4 [\text{CI}_{95\%} \pm 1.2]$ and $4.9 [\text{CI}_{95\%} \pm 0.7] \text{ g C-CO}_2 \text{ m}^{-2} \text{ d}^{-1}$. Shrub ER was significantly less ($3.5 [\text{CI}_{95\%} \pm 0.6] \text{ g C-CO}_2 \text{ m}^{-2} \text{ d}^{-1}$) than the other vegetated classes and Sparse ER was the lowest among the classes ($2.0 [\text{CI}_{95\%} \pm 0.3] \text{ g C-CO}_2 \text{ m}^{-2} \text{ d}^{-1}$) (Fig 2.3a). The Q_{10} and R_{10} values also differed between vegetation classes: ER in the Sedge was the most sensitive to changes in air temperature and modelled values provided the best fit ($R^2 = 0.82$) to observations.

Upland and Grass had the highest base respiration and fit observations moderately well (Table 2.3).

NME was more variable between vegetation classes than ER (Fig 2.3b & c). Sedge was a very strong CH₄ source at 114.7 [CI_{95%} ± 15.3] mg C-CH₄ m⁻² d⁻¹. Shrub and Grass were very weak sources, 0.7 [CI_{95%} ± 0.3] and 0.4 [CI_{95%} ± 0.3] mg C-CH₄ m⁻² d⁻¹, respectively. Sparse was neutral. Upland was a net CH₄ sink -1.1 [CI_{95%} ± 0.4] mg C-CH₄ m⁻² d⁻¹. Sedge and Shrub were NME were positively correlated with T_s ($r=0.61$, $p < 0.01$; $r=0.35$, $p = 0.04$) respectively and VWC ($r=0.58$, $p < 0.01$; $r=0.5$, < 0.01) respectively. They also had a positive correlation with T_a, while Upland NME was negatively correlated with T_a. Grass and Sparse did not have any significant correlations.

Footprint-scaled chamber fluxes were 59% and 47% higher than ER_{NN} or gap-filled NME, respectively. Mean ER_{FS} was 3.5 g C-CO₂ m⁻² d⁻¹ [CI_{95%} ± 0.1], it fit ER_{Q10} very well ($R^2 = 0.95$) as would be expected and ER_{NN} moderately well ($R^2 = 0.46$). Mean NME_{FS} was 12.8[CI_{95%} ± 1.3] mg C-CH₄ m⁻² d⁻¹, it did not fit NME_{NN} well ($R^2 = 0.30$). At the basin scale, ER_{BS} (3.4 [CI_{95%} ± 0.1] g C-CO₂ m⁻² d⁻¹) was slightly lower than ER_{FS} because of the exclusion of upland areas. NME_{BS} was higher (15.2 [CI_{95%} ± 0.1] g C-CO₂ m⁻² d⁻¹) because of the greater sedge fraction in the basin than the footprint because the (Table 2.2).

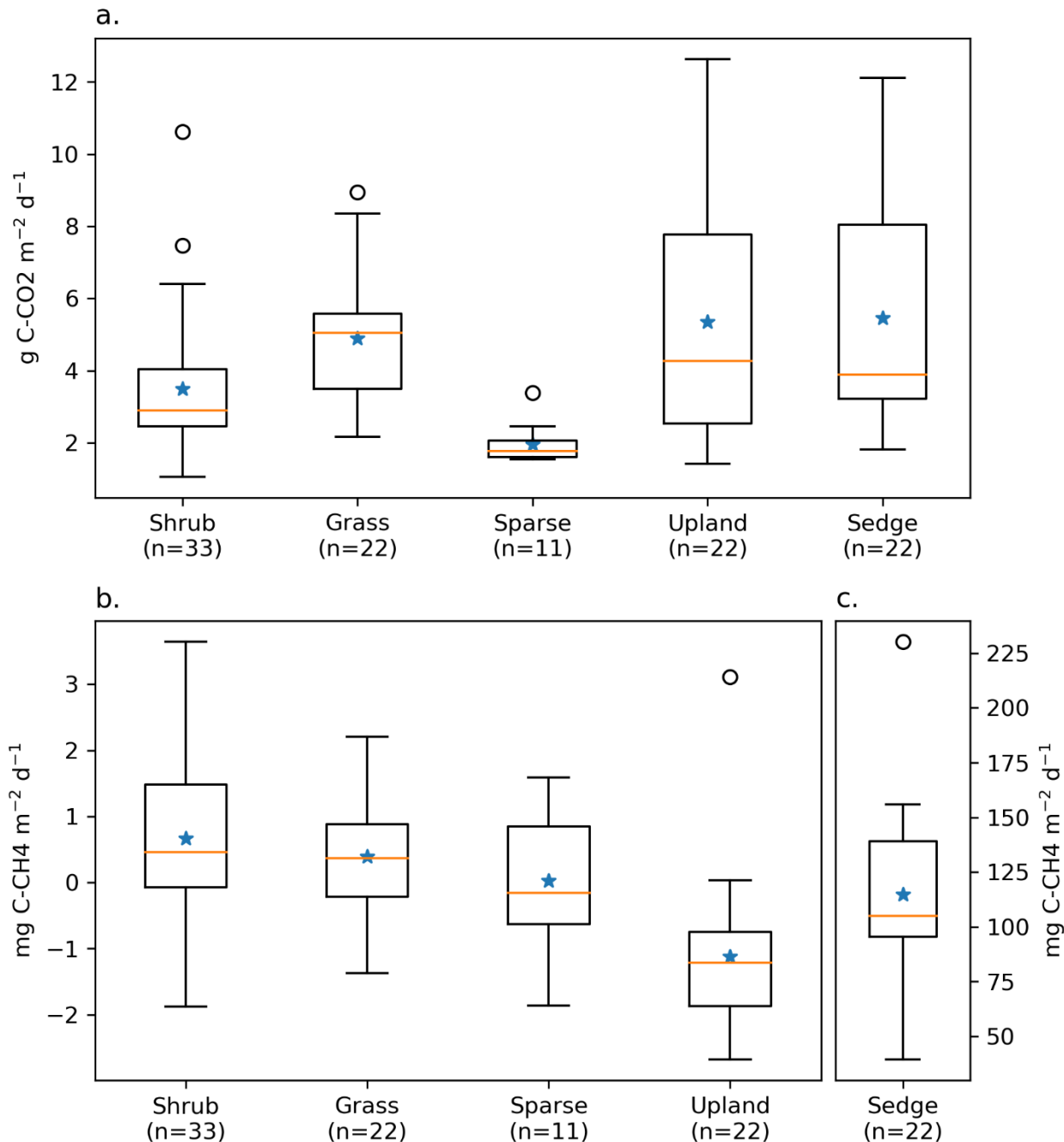


Figure 2.3: Boxplot of a) ER, b) NME and c) NME fluxes measured using closed chambers, grouped by vegetation class. The orange lines represent the median, blue stars represent means, the boxes indicate the interquartile range (Q3-Q1), the whiskers indicate Q1-(1.5*IQR) and Q3+(1.5*IQR), and the circles represent outliers extending beyond the whiskers. Note the scale for c) Sedge is different.

2.3.3 NEE Response to Environmental Factors and Vegetation Type

NEE_{NN} ($r^2 = 0.91$) was estimated using four factors: PPFD , VPD , VWC , and F_{Shrub} .

PPFD is the primary control over NEE: a NN trained on PPFD alone provided a reasonable fit ($r^2 = 0.83$). The three additional factors, VPD , VWC , and F_{Shrub} , helped NEE_{NN} fit a wider variety of conditions. Examining the partial first derivative of NEE_{NN} under different conditions provides interpretation of the modelled light response curves (Fig 2.4). The minimum values represent the peak light use efficiency and are analogous to α in eq. 5 (Fig 2.4b). With increasing PPFD , light use becomes less efficient and approaches zero as the light response nears light saturation (Fig 2.4b).

VPD was a secondary control over NEE. Increasing VPD increased peak light use efficiency and net CO_2 uptake until a threshold, above which it had a strong limiting effect (Fig 2.4a & b). For example, under dry atmospheric conditions (e.g. $\text{VPD} = 1.5 \text{ kPa}$), peak light use is less efficient ($-12 \text{ nmol CO}_2 \mu\text{mol}^{-1} \text{ photon}$) than under more humid conditions ($-18 \text{ nmol CO}_2 \mu\text{mol}^{-1} \text{ photon}$). The value of this VPD threshold was dependent upon soil moisture: from 1 kPa when VWC was highest to 0.25 Pa when VWC was low. Mapping NEE_{NN} and ER_{NN} at $F_{\text{Shrub}} = 100\%$, $F_{\text{Shrub}} = 0\%$, and $F_{\text{Shrub}} = 36\%$ (F_{Clim}), shows that VWC and F_{Shrub} were the primary controls over ER and thus influenced NEE (Fig 2.4c & d). We can see from the partial first derivatives of NEE_{NN} that increasing VWC increases ER from Shrub areas. In the absence of shrubs, increasing VWC inhibits ER although it is important to note that variations in VWC were subtle ranging from 51.7% to 59.0%. The partial first derivative of NEE_{NN} shows that VWC slightly limits NEE from non-Shrub areas and significantly reduces it in Shrub areas.

2.3.4 NME Response to Environmental Factors and Vegetation Type

NME_{NN} ($r^2 = 0.62$) was estimated using five factors: F_{Sedge} , F_{Shrub} , VWC , T_s , and U .

NME was more variable and less dependent on any one factor than NEE which is why the NME_{NN} needed an extra factor and had a lower r^2 score. Source area had a significant effect on NME , and it was encouraging that the model contained F_{Sedge} and F_{Shrub} since Sedge and Shrub were the strongest CH_4 source and largest footprint component, respectively. These two factors can combine to map NME under three general situations: we can extrapolate to $F_{\text{Sedge}} = 100\%$ and $F_{\text{Shrub}} = 0\%$ or $F_{\text{Sedge}} = 0\%$ and $F_{\text{Shrub}} = 100\%$, or represent actual F_{Clim} where $F_{\text{Sedge}} = 11\%$ and $F_{\text{Shrub}} = 37\%$ (Table 2.2). Some upland tundra was included in the F_{Clim} estimate, which reduced NME .

VWC was the primary climatic driver identified by NME_{NN} . Wetter soils had a consistent positive effect on NME which was strongest when F_{Sedge} was high (Fig 2.5a & b). Between driest and wettest conditions, estimated NME increased: by an order of magnitude at $F_{\text{Sedge}} = 100\%$, 4-fold at $F_{\text{Shrub}} = 100\%$, and from neutral to a source at F_{Clim} (Fig 2.5a). Higher T_s generally had a negative effect on NME (Fig 2.5c & d). The negative correlation between T_s and VWC ($r = 0.54, < 0.01$) may have contributed to this result. NME_{NN} performance improved less with the addition of U indicating the NME_{NN} was near saturation and its effects are less relevant. Higher U had a weak limiting effect on NME when VWC was high and increased NME when VWC was low (not shown).

2.4 Discussion

2.4.1 Carbon balance and Controlling Factors

Compared to other DTLB, Illisarvik has drier soils and greater shrub and grass cover (Table 2.4). Peak growing season CO_2 uptake at Illisarvik was greater than at most wet sedge-

dominated DTLB (Table 2.4; Zona et al. 2010, Sturtevant and Oechel, 2013; Lara et al. 2015).

These differences may be due to differences in the periods of observation and year to year variability but may also be due to the presence of more productive shrubs and slightly warmer climate at Illisarvik. Mean 1980-2010 T_a at Utqiagvik (formerly Barrow, AK) is -11.2 °C (US National Climate Data Centre, 2020). Tuktoyaktuk, the closest station to Illisarvik is 1.1° warmer. Shrub cover is expected to have a number of impacts on the microclimate and carbon cycle of Arctic tundra (eg. Myers-Smith et all, 2011). Typically, greater deciduous shrub cover is expected to increase GPP as a result of greater leaf area and photosynthetic potential compared to graminoid-dominated tundra (Sweet et al. 2015; Street et al. 2018). GPP was greater at Illisarvik compared to the young wet-sedge dominated DTLB in Alaska (Zona et al. 2010). It was more similar to Katyk which has significant dwarf shrub cover, predominately *Betula nana* and *Salix pulchra* (van der Molen et al. 2007).

Differences in ER among tundra environments can be related to substrate availability, soil moisture and temperature and thaw depth, among other factors (Sturtevant and Oechel, 2013). The ‘snow-shrub hypothesis’ (Sturm et al. 2001) describes the potential for greater snow trapping in shrub communities which insulates soils in winter, leads to increased decomposition and nutrient availability and promotes further shrub growth. At Illisarvik, snow blowing in off the Arctic Ocean results in large snow drifts within the basin where snow depth correlates with vegetation height (Wilson et al. 2019). Wilson et al. (2019) concluded that the soils within the Illisarvik basin were warmer than those of the surrounding dwarf-shrub tundra in part through these snow-shrub interactions. Although our chamber observations suggested Shrub ER is lower than ER from other vegetation classes, this may have been an artifact as the taller shrubs (>40 cm) could not fit inside the chambers. In another study, chamber ER increased with greater

shrub cover in upland tundra (Ge et al. 2017). ER at Illisarvik was greater than the ER observed at both the young wet-sedge DTLB in Barrow (Zona et al. 2010) and at the shrub/wet sedge DTLB at Katyk where thaw depth was much shallower (45 to >100 cm at Illisarvik vs. 25 to 40 cm at Katyk; van der Molen et al. 2007). The importance of F_{Shrub} in describing temporal variations in half hourly NEE within the flux footprint at Illisarvik is further evidence of the importance of shrub cover on tundra carbon cycle processes in this environment.

PPFD and *VPD* were the most important factors for predicting half hourly NEE. This was to be expected as they are typically the primary controls over GPP (Aubinet et al. 2012). The limiting effects of VPD are consistent another study using NN to analyse NEE at a deciduous forest site (Moffat et al. 2012) and has been found at other tundra sites (Euskirchen et al. 2012; López-Blanco et al. 2017). *VWC* was also important at Illisarvik. Zona et al. (2010) found *VWC* could explain 70% of the variability in daily peak season ER in young DTLB. Similarly, Kittler et al. (2016) found drier soils increased ER and decreased NEE after a wet tundra drainage experiment in Siberia, consistent with our results at Illisarvik when F_{Shrub} was low.

As expected, NME at Illisarvik was about half that observed at the Alaskan DTLB sites where soils were wetter with greater sedge cover (Table 2.4, Zona et al. 2009; Lara et al. 2015). NME at Katyk was even higher than the Barrow DTLB and had a significant impact on the greenhouse gas (GHG) balance for this site (van der Molen et al. 2007; Parmentier et al. 2011). In our NN modelling of NME at Illisarvik, F_{Sedge} was the most important factor for predicting half hourly F_{CH_4} . Sedges are aquatic plant species with arenchymatous tissues that act as conduits for CH_4 from below the water table to the atmosphere and limits CH_4 oxidation by methanotrophs in aerobic surface soils (Lai et al. 2009). The inclusion of F_{Shrub} further refined

the model, allowing it to better fit the site-specific distribution of vegetation types. Budishchev et al. (2014) found shrub and sedge fraction had a significant influence on F_{CH_4} at Katyk.

Vegetation type is the dominant control over NME across multiple tundra landscapes and our results further support that (Davidson et al. 2016).

VWC was the second most important factor, which was expected as CH₄ production occurs in anaerobic environments and has been linked to variability in CH₄ emission in many other studies (e.g. Zona et al. 2009; Nadeau et al. 2013; Olefeldt et al. 2013). Soil temperature (T_s) was the third most important factor. Higher T_s increase the oxidation potential of methanotrophs (Liu et al. 2016; King and Adamsen, 1992), so this result was expected for the drier portions of the basin and upland tundra. However, this was not expected for the sedge areas because most studies find NME in sedges is positively correlated to T_s (Olefeldt et al. 2013). The negative correlation between T_s and VWC may partly explain this.

2.4.2 Upscaling

ER_{FS} and NME_{FS} were about 59% and 47% greater than the gap filled EC estimates. Discrepancies between EC and chamber observations are common and have been attributed to differences in measurement techniques, the small sample size of chamber observations, and sampling bias since all chamber measurements were taken during the day with fair weather (Katayanagi et al. 2005; Chaichana et al. 2018). Meijide et al. (2011) found that chamber NEE could be up to twice as large as EC observations and Riederer et al. (2014) also found chamber NME estimates were about 30% higher than EC estimates. Others have been more successful, yielding upscaled chamber NME fluxes within 10% of EC observations (Zhang et al. 2012; Budishchev et al. 2014; Davidson et al. 2017). A potential reason for the disagreement with

ER_{FS} may be the lack of direct observations by the EC system under low-light conditions.

Another potential source of error for the upscaling is inaccuracies in the vegetation map.

2.4.3 Future Trajectories

Presently, peak growing season carbon uptake at Illisarvik is greater than similarly aged landscape features on the Barrow Peninsula, Alaska and more similar to levels observed at Katyk, Siberia. NME is well below levels observed at any other DTLB studied, making this site a stronger GHG sink than other DTLB. However, the basin at Illisarvik will continue to evolve and the trajectory it takes could significantly alter its carbon balance. Historically, DTLB on Richards Island and the Tuktoyaktuk Peninsula evolve into sedge wetlands, as do DTLB on the Barrow Peninsula (Ovendend, 1986; Lara et al. 2015). Active maintenance of the outlet channel at Illisarvik has artificially lowered soil moisture and flooding and potentially limited this transition thus far (C. Burn, personal communication 2016).

If Illisarvik follows the same trajectory as older DTLB in the area and becomes dominated by sedge wetlands, NME will increase significantly. Figure 2.5a shows that with extrapolations to full Sedge cover ($F_{Sedge} = 100\%$), NME would be similar to values on the Barrow Peninsula (Zona et al. 2009). If the basin instead transitions into a shrub dominated DTLB similar to those of Old Crow Flats, Yukon (Lantz et al. 2015), NME_{NN} would remain similar to current levels meaning the basin would remain a weak source of CH_4 . These are projections well beyond F_{Clim} fractions observed so confidence in the specific values predicted is low.

The effects of changing shrub/sedge cover on Illisarvik's growing season NEE are less straightforward than on NME. Partly because Shrub cover had less overall influence on NEE_{NN} . Figure 2.4c. shows the model suggests ER decreases and NEE increases with increasing shrub

coverage when soils are slightly drier, but has the opposite effect under wetter conditions. To our knowledge, only few winter season (e.g. Zona et al. 2016) and no year-round studies of DTLB NEE and NME have been published to help evaluate the factors influencing carbon losses through the non-growing season months. Further observation year-round is needed to better understand the implications of continued vegetation change on the carbon balance of DTLB such as Illisarvik.

2.5 Conclusions

This study investigated NEE, GPP, ER and NME in the Illisarvik experimental DTLB using EC and chamber data. To our knowledge this is the first such study conducted in a DTLB outside of the Barrow Peninsula or Siberia. Illisarvik is a carbon sink during the growing season with NME only having a small effect on the net carbon balance. Our flux observations were generally in agreement with other studies but show how shrub-dominated DTLB such as Illisarvik and Katyk in Siberia differ from sedge-dominated DTLB on the Barrow Peninsula. Illisarvik's growing season net carbon uptake was greater than young and ancient DTLB on the Barrow Peninsula and more similar to the shrub dominated ancient DTLB in Siberia. NME at Illisarvik was lower than all published DTLB studies likely due to better drainage and more diverse vegetation. A longer, more comprehensive study would be needed to resolve the annual carbon budget for Illisarvik.

Chamber measurements of ER and NME from different land cover classes within and outside the Illisarvik basin added context to the EC observations. Vegetation class (and associated difference in terrain and soil properties) had only a small but significant impact on NEE and ER but was one of the dominant controls over NME. Sedge areas were a strong source of CH₄, other vegetation types in the basin were weak sources, and upland areas were a net sink.

These results suggest that NME in particular will change as the Illisarvik DTLB vegetation communities continue to evolve.

Chapter 3: Controls on Carbon Dioxide and Methane fluxes from a Low-Center Polygonal Peatland in the Mackenzie River Delta

A version of Chapter 3 has been published. Skeeter, J., Christen, A., & Henry, G. H. R. (2022). Controls on carbon dioxide and methane fluxes from a low-center polygonal peatland in the Mackenzie River Delta, Northwest Territories. *Arctic Science*, 1–27. <https://doi.org/10.1139/as-2021-0034>

3.1 Introduction

The Canadian Arctic has experienced significant recent warming: mean annual temperatures increased 2.3 K from 1948 to 2016 (Zhan et al. 2019). Warming in the north is expected to accelerate with median estimates from CMIP5 suggesting an additional 2.1 K and 7.8 K by the 2080's under RCP2.6 and RCP8.5, respectively (Zhang et al. 2019). Warming has and will continue to have significant impacts across the Canadian Arctic, including: permafrost degradation and increased active layer thickness, decreased snow cover and longer snow free seasons, changes in surface energy balance, and tundra greening (Derksen et al. 2019; Frost et al. 2020).

Approximately 500 Pg of carbon (C) is contained in the top meter of permafrost soils globally, with some of the highest concentrations in wetland areas which are primarily located along river lowlands on river deltas (Hugelius et al, 2014). Climate change related disturbances put these shallow permafrost C stocks at risk for release into the atmosphere, as carbon dioxide (CO_2) and methane (CH_4) via aerobic and anaerobic respiration, respectively (Tarnocai et al. 2009; Hugelius et al. 2014; Schuur et al. 2015; Turetsky et al. 2020). Conversely, longer

growing seasons, more liquid water availability, and consequently enhanced plant growth could have the opposite effect increasing CO₂ uptake in some areas (Prowse et al, 2009).

The Mackenzie River Delta is the second largest Arctic delta after the Lena Delta in Siberia (Burn and Kokelj, 2009) and is in one of the fastest warming regions in the world (Zhang et al. 2000, IPCC, 2013). The Delta is a broad alluvial plain (13,000 km²) that grades from boreal forest in the south to low shrub tundra and sedge wetlands in the north (Burn and Kokelj, 2009). Major Arctic delta lowlands, such as the Mackenzie River Delta, are important in the regional C-balance as they contain high C-stocks in a relatively small area (Schuur et al. 2015). Further, frequent flooding and water-saturated peatlands provide an environment particularly conducive to anaerobic conditions and hence CH₄ emissions. Despite its size and potential importance as a hotspot for C emissions, to date there has been little work done to quantify the C balance of the Mackenzie Delta. A series of airborne CH₄ flux observations in July of 2012 and 2013 provided delta-scale estimates of peak growing season methane emissions, but considerable spatial and interannual variability was observed (Kohnert et al. 2014). Delta-wide emissions were estimated to be 38 Gg CH₄ annually, with pockets of geologic strong emissions (> 87 nmol m⁻² s⁻¹) observed over discontinuous permafrost in the north western delta accounting for 17% of annual emissions (Kohnert et al, 2017). Kohnert et al. (2018) estimated fluxes from the boreal southern half of the delta and the tundra northern half to be to be 23 nmol m⁻² s⁻¹ and 42 nmol m⁻² s⁻¹ respectively. However, their estimates for the northern delta could be up to 40% geologic in origin (Kohnert et al. 2017). In situ observations of fluxes in the Mackenzie Delta are needed to put these airborne estimates in context, especially given the considerable emissions reported by Kohnert et al. (2017) for the northern portions of the delta.

This contribution reports field-scale measurements of CO₂ and CH₄ fluxes from a representative peatland site in the Northern Mackenzie River Delta. Net ecosystem exchange (NEE) of CO₂ and net methane exchange (NME) of CH₄ were measured at Fish Island, a low-center polygonal peatland during the growing season and early senescent period using the eddy covariance (EC) approach (Aubinet et al. 2012) in 2017. Net ecosystem exchange (NEE) of CO₂ was calculated from fluxes and storage change and NEE was separated into ecosystem respiration (ER) and gross primary productivity (GPP), $NEE = ER - GPP$. Net methane exchange (NME) was calculated from fluxes and storage change. The primary goals of our study were to: 1) measure growing season NEE and NME at Fish Island; 2) Determine the main environmental drivers of CO₂ and CH₄ fluxes using Neural Network analysis; and 3) Investigate the role of microtopography and landscape heterogeneity in driving the observed fluxes.

3.2 Materials and Methods

3.2.1 Study Site

The study took place at Fish Island (69°22'20.20"N, 134°52'51.92"W, WGS 84), which is located on the Big Lake Delta Plain in the north-eastern part of the Mackenzie River Delta, Northwest Territories, Canada (Fig 3.1). Fish Island is in the sparsely populated Inuvialuit Settlement Region, and the nearest communities are Tuktoyaktuk and Inuvik. The Big Lake Delta Plain is crisscrossed by a network of low-center ice wedge polygons and is subject to infrequent episodic flooding; sedimentation rates are low compared with western portions of the delta (Morse et al. 2012; Morse & Burn, 2013). Fish Island (19 km²) is dominated by low-center polygons that are broadly representative of this portion of the delta. Permafrost under the Big Lake delta plain is continuous and thick (400 to 600 m), so we can expect CH₄ emissions observed in this area are strictly biogenic in origin (Kohnert et al. 2017). The Mackenzie Delta

sits atop one of the largest oil and gas deposits in the Arctic (Gautier et al. 2009). Continuous permafrost acts as a cap, but there are sporadic strong natural gas emissions in the western portions of the delta where permafrost is discontinuous (Walter et al. 2012; Kohnert et al. 2017).

Vegetation at Fish Island varies with microtopography. The flat low-polygon centers make up the most land area and are covered by a dense mat of *Sphagnum* spp. moss along with *Equisetum* spp., and *Carex* spp. A patchwork of ridges ~10-20 cm high bound the polygon centers and hosted a more diverse mix of vegetation including a canopy of dwarf *Salix* spp. Degraded ridges form troughs 5-10 cm deep that are frequently ponded and host *Carex* spp. and *Eriophorum angustifolium*. Fish Island is largely undisturbed with the exception of the defunct Taglu microwave tower, which has since been removed.



Figure 3.1. False color composite 100 m resolution LANDSAT8 image (bands 3, 4, and 5) of the Mackenzie Delta with imagery spanning the dates of the 2017 study period. Labeled on the map are the study site at Fish Island and the nearby communities of Tuktoyaktuk and Inuvik. The approximate bounds of the Big Lake Delta Plain are represented with the white hatch marks (Morse & Burn, 2013). Coordinate Reference System: NAD83 UTM zone 10N. LANDSAT8 data is provided by the United States Geological Survey and was downloaded using Google Earth Engine.

3.2.2 Data Collection

A tripod equipped with an EC system was placed 400 m south east of the river channel and 300 m north east of Taglu tower on Fish Island ($69^{\circ}22'20.20''\text{N}$, $134^{\circ}52'51.92''\text{W}$). EC measurements were collected from 0:00 day of year (DOY) 174 (June 23rd) to 12:30 DOY 256 (September 13th) 2017 and drone imagery was collected on DOY 174, 191, 233, and 256 using a Phantom 3 drone (DJI, Shenzhen, China). The drone images were used to map the study site and monitor vegetation change in the vicinity of the EC station though the study period (Fig 3.2). The imagery was processed using Open Drone Map (2021) to create georeferenced 10 cm resolution orthophotos for each date. The orthophotos were used to create a landscape classification by manually digitizing the boundaries between microtopographic features within a 150 m radius of the EC tower. The landscape classification was then converted to a 2 m resolution raster image centered on the tripod, henceforth referred to as the landscape classification map (LCM), to match the resolution of the flux footprint analysis (discussed in Section 3.2.2.1).

A sensitivity analysis was conducted to assess spatial variability within the LCM and estimate the distribution of LCM classes. A random sample of points ($n = 100$) were generated within the 150 m radius of the EC tower, and the proportion of points falling within each LCM class was calculated. This was repeated 2501 times (equivalent to the number of CO₂ flux samples) and used to calculate the mean landscape fraction (LF) of each class with a 95%

confidence interval. The LF for polygon centers, rims, and troughs, were 66.1 [CI_{95%} ± 0.3] %, 28.7 [CI_{95%} ± 0.2] %, 5.1 [CI_{95%} ± 0.3] % respectively.

Since 2008 there has been an automatic weather station (AWS) at the site operated by the NWT Water Resources Department. recording temperature, radiation, wind speed and direction, snow depth, and rainfall (NWT Water Resources, 2019). Mean annual air temperature (T_a) over the last decade (August 2008 – July 2019) was -8.5°C, whereas the 30-year (1980-2010) climate normal at Tuktoyaktuk (60 km east) was -10°C (Environment Canada. 2016). Over the ten years at Fish Island, July was the warmest month with a mean of 11.6°C and January was the coldest at -24.5°C. Mean annual precipitation was 117 mm yr⁻¹, with the majority falling as rain in the summer and autumn. Snow cover typically lasts from late September or October to late May.

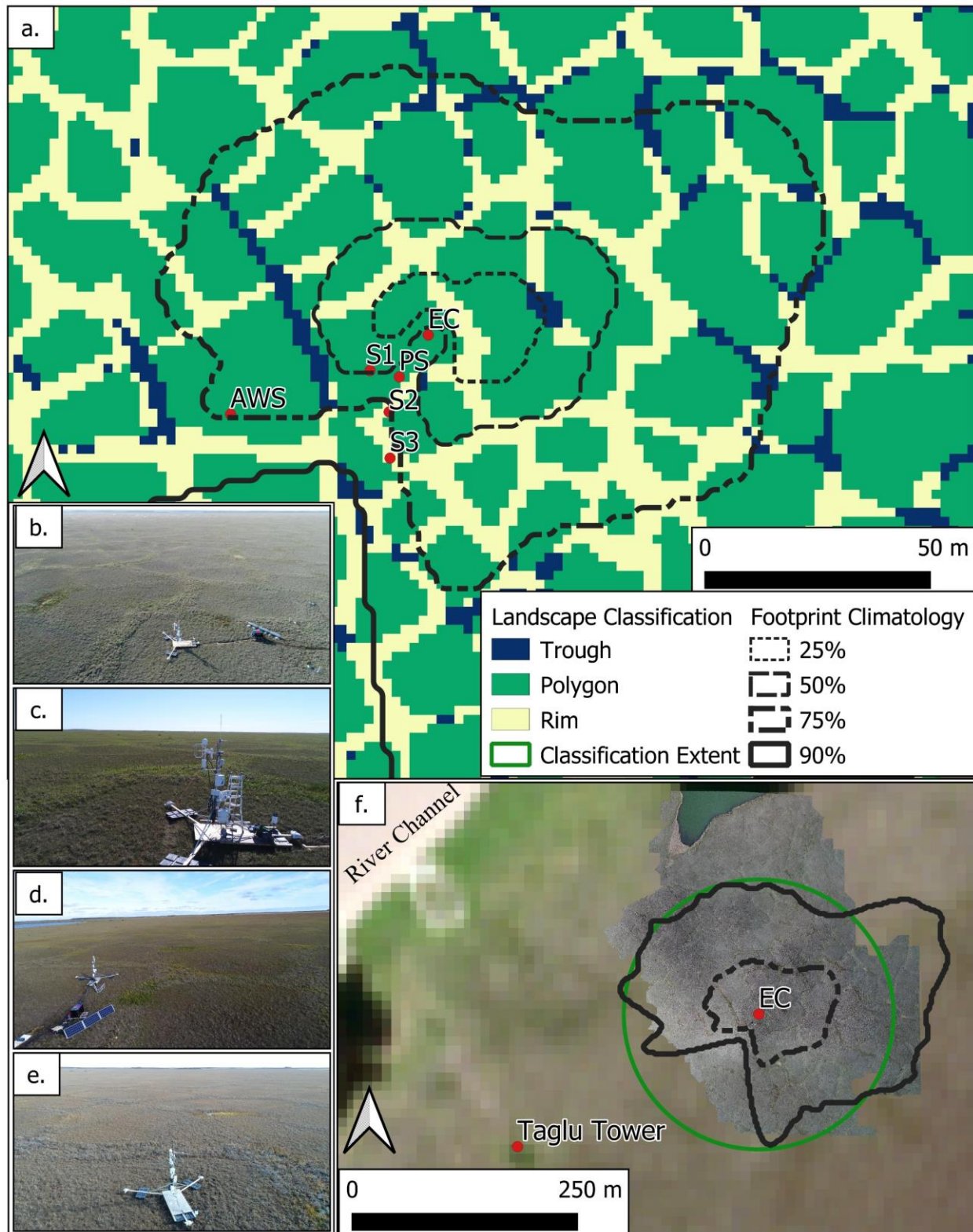


Figure 3.2. a) The cumulative flux footprint climatology (25%, 50%, 75% and 90%) is shown overlaid on the landscape classification map (LCM). Labels on the map correspond to: the EC system (EC), soil stations 1-3 (S1, S2, S3), the power supply (PS), and the NWT Water Resource Department's Automated Weather Station (AWS). b-e) Oblique drone photos showing the EC system and vegetation at different points during summer and fall 2017: looking south-east on DOY 174 (b.) and DOY 191 (c.) and looking northeast from behind the EC system on DOY 233 (d.) and DOY 256 (e.). f) Inset map showing the location of the EC station, 75% and 90% flux footprint contours and the area covered by the LCM, and a 10cm orthophoto created from drone imagery captured on June 23rd. This is overlain on a 10 m resolution composite Sentinel 2 image generated using Google Earth Engine with imagery spanning the summer 2020. Also shown are the location of the Taglu tower and the River Channel. Coordinate Reference System: NAD83 UTM zone 10N. Sentinel 2 data is provided by the Copernicus Sentinel Data and was downloaded using Google Earth Engine.

3.2.2.1 EC Fluxes

The EC system measured fluxes of CO₂ (F_{CO_2}) and CH₄ (F_{CH_4}) over the study period. It consisted of a closed-path infrared CO₂/H₂O gas analyzer (IRGA, model LI-7200, LI-COR Inc., Lincoln, NE, USA; LI-COR), an open-path CH₄ analyzer (model LI-7700, LI-COR) and a CSAT3 sonic anemometer (Campbell Scientific Inc, Logan, UT, USA; CSI) mounted on a tripod at a measurement height (zm) of 2.87 m (Fig. 3.1). The EC data and air pressure (Pa) were logged on a LI-7550 Analyzer Interface Unit (LI-COR). The CSAT3 was oriented to the northeast (35°) because northerly and easterly winds are most common for this time of year (NWT Water Resources, 2019). Due to an error setting up the LI-7550, fluxes were only logged at 1Hz until 12:00 DOY 193, the settings were corrected after this and the fluxes were logged at 10Hz for the remainder of the study period. In principal, the low sampling frequency does not cause a bias in the mean flux, but does increase the variance (Bosveld and Beljaars, 2001). This is supported by experimental observations (Rinne et al. 2008; Holl et al. 2019). To confirm this error had limited impact on our results we down sampled the July flux data for the period following the error correction (July 13th – 29th). We artificially generated a 1Hz dataset by selecting every tenth value from the raw data, and processed it using the same steps as detailed

below. Student's t-tests indicated no significant difference between the mean values of the 10 Hz data and the down sampled 1 Hz data for either CO₂ or CH₄ fluxes. Boxplots of the results 1 and 10 Hz fluxes are shown in Fig B1.

Half-hourly fluxes were calculated with EddyPro V.6.2.0 (LI-COR). The software performed statistical assessments (Vickers and Mart, 1997), low and high frequency spectral corrections (Moncrieff et al. 1997 and 2004), and a double rotation (Wilczak et al. 2001). For the open path LI-7700, the WPL density correction was applied (Webb et al. 1980) with spectroscopic correction following McDermitt et al. (2011). For the closed path LI-7200 density corrections were calculated following Ibrom et al (2007). Quality control flags (0-2) of were assigned following Mauder and Foken (2004) and fluxes with a flag of 2 were discarded (4.6% and 10.8% of F_{CO_2} and F_{CH_4} data, respectively).

Post processing treatments were conducted as follows: 1) Removing LI-7700 observations during precipitation events (0.2% of F_{CH_4} data). 2) Removing LI-7700 observations when signal strength (*RSSI*) from the LI-7700 was below 20% (13.3% of all data). Methane concentrations and F_{CH_4} were plotted against (received signal strength indicator, *RSSI*) to confirm this was an acceptable threshold (Fig B2). Low *RSSI* values can result from condensation or dust on the mirror of the LI-7700. We elected not to use a cleaning pump at this site because of the limited power supply. This resulted in more missing F_{CH_4} data but extended the lifespan of the power supply for measuring fluxes. 3) Removing observations with mean wind direction from $215^\circ \pm 30^\circ$ (8.3% and 7.1% of F_{CO_2} and F_{CH_4} data, respectively) to avoid uncertainties associated with the wake of the sonic anemometer. 4) Storage correcting by calculating net fluxes (NEE and NME) as the sum of the observed scalar flux (F_{CO_2} and F_{CH_4}) and the rate of change in their scalar concentrations at z_m following Aubinet et al. (2001). 5)

Removal of spurious half-hourly measurements (4.1% and 3.3% of NEE and NME data, respectively) using the median absolute deviation about the median method following Papale et al. (2006). 6) Filtering fluxes by friction velocities (u_*) below an 0.1 m s^{-1} (4.4% and 2.3% of NEE and NME data). We confirmed that this value was suitable by calculating an iteratively determined u_* threshold (0.094 m s^{-1}) following Papale et al. (2006). In total, quality control and post processing removed 22% and 55% of F_{CO_2} and F_{CH_4} observations respectively.

Additionally, there was a 14-day gap in flux observations from 00:30 DOY 240 to 16:30 DOY 254 due to insufficient power supply from the solar panels. The CSAT3 and climate station remained operational, but the Li-7200 and Li-7700 were shut down.

The flux footprint was calculated following Kljun et al. (2015). All variables needed for footprint calculations were collected onsite, except planetary boundary layer height. Inverse distance weighting was used to interpolate these values from 3-hour reanalysis data for the 25 nearest grid points spanning the domain $68^{\circ}30'N$ to $70^{\circ}N$ and $134^{\circ}W$ to $135^{\circ}40'W$. Half hourly values were then approximated from the 3-hour value using linear interpolation. The flux footprint was calculated at a spatial resolution of 2 m^2 over a $2000 \text{ m} \times 2000 \text{ m}$ grid centered on the tripod for all valid half hourly measurement periods: $u_* > 0.1 \text{ m s}^{-1}$ and mean wind direction $\neq 215^{\circ} \pm 30^{\circ}$. The half hourly footprints were intersected with the landscape classification to determine the relative flux contribution of low-center polygons (F_{Cnt}), rims (F_{Rim}), and troughs (F_{Tro}) to each measurement. The contribution from outside the landscape classification (F_{Out}) was calculated as $1 - (F_{Cnt} + F_{Rim} + F_{Tro})$. To allow for a direct comparison with the source area fractions, the LF values weighted by $(1-F_{Out})$, using the median value of F_{Out} to calculate the adjusted landscape fraction (ALF).

Neural Networks (NN) were used to: identify relevant environmental controls over NEE and NME, gap fill the time series, and partition NEE into its component fluxes ER and GPP. Various studies have applied NNs to flux data to identify and analyze flux drivers (Moffat et al. 2010; Briegel et al. 2020; Skeeter et al. 2020), investigate the influence of spatial heterogeneity (Morin et al. 2015; Skeeter et al. 2020), and to gap-fill time series of NEE and NME (Papale and Valentini, 2003, Dengel et al. 2013; Knox et al. 2015; Skeeter et al. 2020). The steps for identifying relevant controls, gap filling, and flux partitioning are discussed in section 3.2.5.

3.2.2.2 Weather and Soil Measurements

Climate data at the EC site were logged on a CR1000 datalogger every 1 second and averages/totals stored at 5-minute intervals. A NRLite net radiometer (Kipp & Zonen, Delft, Netherlands) measured net all-wave radiation (R_n) and a SQ-110 quantum sensor (Apogee Instruments, Logan, UT, USA) measured photosynthetic photon flux density ($PPFD$) at 3 m a.g.l, and a HMP35 (CSI) measured T_a and humidity (RH) in a shielded, naturally ventilated screen all at 2 m a.g.l. on the same tripod as the EC system. A tipping bucket rain gauge (R.M Young Company, Travers City, MI, USA) was mounted 2 m south of the tripod at a height of 0.4 m.

Soil temperature, moisture, and water table depth data were recorded at 30-minute intervals on three separate, automatic soil sites, each operated by a CR10x datalogger (CSI) at three locations near the tripod (Fig 3.2a): one in polygon a center (S1), one on a polygon rim (S2), and one on a border between the rim and the center (S3). At each of the soil sites, soil temperatures (T_s) were recorded with custom made type-T thermocouples at depths of 2.5, 5, and 15 cm, volumetric water content (θ_w) was measured with CS616 water content reflectometers (CSI) at 0.1 m depth, and water table depth (W_{td}) was sampled with PLS probes (CSI). The

climate and soil stations S1 and S2 operated uninterrupted from June 23rd (day 175) until September 13th 2017 (DOY 257). On July 17th an animal dug up and destroyed the thermocouples and CS616 at S3. The PLS probes were installed at the base of the active layer and adjusted to account for increasing thaw depth on July 10th & August 1st. Thaw depth (*TD*) was measured during each site visit by inserting a graduated steel probe into the ground to point of refusal. Thaw depths were measured ten times for both polygon rims and centers and the median value calculated for each set of observations. Canopy heights were also measured for polygon rims and centers on each site visit using the median value of 10 replications.

The sun remains above the horizon much of the summer at 69°N. The date of the first sunset and timing subsequent sunrises and sunsets is important for understanding NEE and partitioning GPP and ER. We obtained the timing of sunrises and sunsets from a sunrise/sunset calculator (National Research Council Canada, 2012). We used this information to one-hot encode a Daytime variable. Every half-hourly measurement period occurring before the first sunset or between sunrise and sunset was assigned a value of one. Measurements between sunset and sunrise were assigned a value of zero. If a sunrise or sunset occurred during a measurement period, the encoding was set to 1, as the purpose of this coding is to identify periods with no GPP.

3.2.2.3 Chamber Measurements

In addition to EC measurements, ER was independently measured using the closed chamber method on two site visits (DOY 191, and DOY 233). Closed chamber measurements were sampled using a LI-700 (LI-COR) mounted in a custom made portable automated chamber as described by Christen et al. (2017). ER was measured at polygon centers (ERCnt) and rims (ERRim) using eight and four replications, respectively. Opaque PVC collars were inserted 10

cm into the ground on DOY 173. Before each measurement, chamber heights were measured with four repetitions per collar. Then the transparent PVC sensor head was placed over the collar and covered with an opaque canvas bag to block out all sunlight. The sampling period lasted two minutes and fluxes were then calculated following Christen et al. (2017). Due to limited time and resources, we were only able to collect a small number of samples and we were unable to collect chamber observations of GPP. The small sample size limits the conclusions we can draw from the chamber data, but these data are still valuable because they provide context to our EC observations and allows for comparison with other sites.

3.2.3 Feature Identification & Gap-Filling

3.2.3.1 Neural Networks

Neural networks (NN) are flexible machine learning methods that make no prior assumptions about functional relationships within a dataset and are ideally suited to perform non-linear, multivariate regression (Hornik et al. 1991; Melesse and Hanley, 2005; Desai et al. 2008). The goal of an NN is to approximate a target function as:

$$f(X, w) = t(X) - \varepsilon(X) \quad \text{EQ 3.1}$$

where $t(X)$ is the target (e.g. NEE's response to environmental drivers), $\varepsilon(X)$ the noise, and $X = [x_0, x_1, \dots, x_M]$ is the set of input variables; M denotes the number of inputs variables and $x_0 = 1$ is a bias term (Khosravi et al. 2011). In the context of EC measurements, this means that if all relevant climate and ecosystem information are available to a network, the remaining variability can be attributed to noise in the measurement (Moffat et al. 2010).

Here we used feed-forward dense NN with a single hidden layer:

$$f(X, w) = \sum_{h=1}^H \beta_h g(\sum_{m=0}^M \gamma_{hm} x_m) \quad \text{EQ 3.2}$$

Where $g(\cdot)$ is a non-linear transfer function, here we used the rectified linear activation unit (ReLU) (Anders and Korn, 1999). H denotes the number of hidden nodes in the network. The weights $w = [\beta_1 \dots \beta_H, \gamma_{10} \dots \gamma_{HM}]$ are randomly initialized and after each model iteration are updated by backpropagating the error through the network, β are the weights of the output layer and γ are the weights of the hidden layer. Weights are adjusted in the direction that decrease the error and training continues. We used early stopping to terminate training when the mean squared error (MSE) of a test data set failed to improve for 10 consecutive iterations. The test set consisted of 10% of the training data, and was not used if fitting $f(X, w)$. Early stopping prevents $f(X, w)$ from overfitting the training data (Weigend and Lebaron, 1994; Sarle, 1995; Tetko et al. 1995; Sarle, 2014). When using early stopping, the choice of H is somewhat arbitrary, but H must be large enough to ensure the model has sufficient flexibility (Sarle 2014). We set H to 1/30th the number of training samples.

To account for the random initialization of w and further minimize overfitting, stratified bootstrapping (with replacement) was used to generate a set of 30 bootstrapped training data sets (B). Separate $f(X, w)_i$ were trained on each bootstrapped training set and for each model and validation metrics: root mean squared error (RMSE) and the coefficient of determination (r^2) were calculated using the out of bag (OOB) bootstrapped samples. Thus, the final response model response was calculated as:

$$F(X) = \frac{1}{B} \sum_{b=1}^B f_b(X, W) \quad \text{EQ 3.3}$$

where $F(X)$ is the response of NEE or NME to a set of inputs (environmental drivers). The variance of the model outputs is:

$$\sigma^2(X) = \frac{1}{B-1} \sum_{b=1}^B (f_b(X, W) - F(X))^2 \quad \text{EQ 3.4}$$

A confidence interval (CI) for $F(X)$ can be calculated as $F(X) \pm t_{(1-\alpha, df)}\sigma(X)$, where $t_{(1-\alpha, df)}$ is the students t -score, $1-\alpha$ is the desired confidence level, and df are the degrees of freedom that are set to the number of bootstrapped samples B .

3.2.3.2 The Weights Method

Our NN analysis used the Weights method (Gevrey et al. 2003) to quantify the relative influence of various inputs on NEE and NME and to prune the NN to reduce the number of input variables. This method has been used to study the influence of inputs for ecological modelling (Lee et al. 2003; Olden, et al. 2004; Fischer 2015; Liyanaarachchi et al. 2020), but to our knowledge, it has yet to be applied to EC flux data. For both NEE or NME, $F(X)$ were initially trained on 21 initial inputs X including: radiation (R_n , PPFD, Daytime), atmospheric conditions (T_a , vapor pressure deficit [VPD], Pa), wind (U , u_*), flux contribution (F_{Cn}, F_{Rim}, F_{Tro}), and subsurface (T_s [all depths, polygon center & rim], VWC [polygon center & rim], W_{TD}, TD) variables. These X were chosen because they potentially influence NEE or NME.

After training, we calculated the partial derivatives (d_{ji}) of each input factor x_m in X for every sample ($j=1, \dots, N$), where N is the total number of flux observations:

$$d_{jm} = S_j \sum_{h=1}^H \beta_h \gamma_{mh} \max \begin{cases} 0, & I_{hj} \leq 0 \\ 1, & I_{hj} > 0 \end{cases} \quad \text{EQ 3.5}$$

where S_j is the derivative of the output with respect to the input, β_h and γ_{mh} are the weights of the output and hidden neurons and I_{hj} is the response of the h^{th} hidden neuron for the input $x_{j,m}$. The max function is the first derivative of the ReLu activation function. d_{ji} were averaged over the bootstrapped datasets and plotted to visualize the influence of factors. Because the inputs and the target must be standardized (mean=0, standard deviation =1) before training an NN, d_{ji} are not in the units of NEE or NME rather they can be interpreted in terms of relative

magnitude (i.e. compared between inputs). When $d_{ji} < 0$ the respective input has a negative influence on the target and when $d_{ji} > 0$ it has a positive influence.

Next, the sum the of partial derivatives (SD_m) and sum of the squared partial derivates were calculated (SSD_m) for each input m:

$$SD_m = \sum_{j=1}^J d_{ji} \quad \text{EQ 3.6}$$

$$SSD_m = \sum_{j=1}^J (d_{ji})^2 \quad \text{EQ 3.7}$$

The sign of the SD_m indicates whether the variable has a net positive or negative influence on the output (over the input domain). The SSD_m describes the relative magnitude of the variables influence (if d_{ji} changes sign, SD_m is reduced but SSD_m is not). The SSD_m values for each input were then normalized by the sum of all SSD values to quantify the relative influence (RI) of each input factor. The 21-input model served as a benchmark to gauge the performance of a "pruned" model using only the inputs X with over 2.5% influence. Amir et al. (2020) suggests removing inputs that have less than a 5% influence on the model, we used twice as many initial inputs as they did, so we chose 2.5%. The SSD_m of the pruned models were calculated and used to gauge the relative influence of the flux drivers. Additionally, the partial derivatives for some the most important drivers were plotted to visualize their relative influence.

The B=30 pruned models for both NEE and NME were then run on the time series of drivers over the full study period. The 30 bootstrapped model outputs were averaged and used to estimate mean NEE and NME by gap-filling the NEE and NME time series. Most drivers just had nearly complete records (>99%), brief gaps in the drivers were gap filled with linear interpolation (up to 60 minutes). Wind speed and u_* had slightly more missing records (99% and 98% complete respectively) and were also gap filled with linear interpolation. The footprint

drivers had more missing values (95% complete), F_{Cnt} , F_{Rim} , F_{Tro} were gap filled using their respective mean values, binned by wind direction in 10° intervals. Confidence intervals for NEE and NME were calculated using the total variance of multiple imputations, which is the sum of variance between and within imputations.

3.2.3.3 Partitioning NEE

Typically, NEE is gap-filled using flux-partitioning algorithms that model ER using T_s or T_a and GPP using *PPFD* (e.g., Aubinet et al. 2012; Lee et al. 2017) where $\text{NEE} = \text{ER} - \text{GPP}$. However, these methods require nighttime observations to estimate ER and, thus, do not perform well for Arctic summertime measurements due to the limited number of samples available during low light conditions (Kutzbach et al. 2007; Runkle et al. 2013). We tested a Q10 T_a response curve (eq. 9.4 in Aubinet 2012) and a logistic T_s response curve (eq. 1 in Lee et al. 2017) using each of the six T_s measurements to gauge their effectiveness when trained on the limited number ($n = 186$) of ER samples.

A NN trained on CO₂ fluxes will just estimate NEE rather than the component fluxes ER and GPP. To compensate for this, we estimated daytime ER with the pruned NN by using an artificial “dark” input set (Skeeter et al. 2020). The inputs *Daytime* and *PPFD* were both set to zero and any $R_n > 0$ were also set to zero. This approximation projects ER well beyond conditions under which it was actually observed, so caution needs to be taken when interpreting the output. However, the NN performed better than the traditional methods when estimating nighttime ER (see Ecosystem respiration section). Therefore, we feel this is the best option for estimating ER and is useful for comparing to the ER chamber observations. The ER estimate and confidence interval were obtained by “gap-filling” the sparse record of nighttime NEE ($n = 186$) observations using the same procedure as for NEE and NME.

3.3 Results

The spring flood peaked on June 1st in 2017 at the nearby (4 km) Big Lake gauge station (Environment Canada, 2020). It is unlikely the site was inundated during the flood but satellite imagery indicated Fish Island was snow free by May 31st. Vegetation had started to turn green at the onset of the study period, but was still mostly brown (Fig 3.2b). A rapid green-up occurred over the first couple weeks of the study period. Vegetation height increased from 8 to 14 cm in the polygon centers and 13 to 23 cm on polygon rims between June 23rd and August 21st after which it did not change appreciably. Thaw depths increased steadily from 20 cm (DOY 174) to 50 cm (DOY 256) for polygon centers and was consistently 2 cm deeper for polygon rims.

Compared to the same dates (June 23rd to September 13th) from the AWS record on Fish Island (2009-2018) the 2017 study period was the third warmest and second wettest on record. Over the 82-day study, T_a ranged between -0.1 and 24.8 °C and mean T_a was 10.6 °C (Fig 3.3a). Soil temperatures peaked in August before decreasing along with a decline in daily R_n . Polygon rim T_s were warmer than centers at all depths, and the difference was most pronounced at 5 cm depth with a mean difference of 2.3 °C. $PPFD$ was highly variable day to day depending on cloud conditions and decreased through the study period (Fig 3.3b). The first sunset was on DOY 206 (July 25th), after which the day length began to rapidly decrease. Precipitation during the study period (100 mm) fell on 33 days contributing to the near-record wet conditions in 2017. The water table depth in polygon centers averaged 13 cm below the surface, ranging from 19 cm in July to 5 cm in September (Fig 3.3c). The base of the active layer under polygon rims was above the water table until July 21st, after which a perched water table formed.

The flux footprint climatology is shown in Figure 3.2a. Analysis of half hourly footprints indicates that the source area of NEE and NME observations were predominately sourced from within the LCM, median F_{Out} was 10.9% and 11% for NEE and NME respectively. Relative to the ALF, F_{Cntr} tended to be slightly overrepresented while F_{Rim} and F_{Tro} were slightly underrepresented, but they were all within the interquartile range (Table 3.1). A chi square test ($\chi^2 = 3.58$, $p = 0.61$) indicated the median values of F_{Cntr} , F_{Rim} , and F_{Tro} were not significantly different than the expected ALF values. Wind speeds were highly variable and there were multiple strong storm events with gusts up to 30 m s^{-1} (see Fig 3.3d). The 2017 study period had the second highest average wind speed on the AWS record.

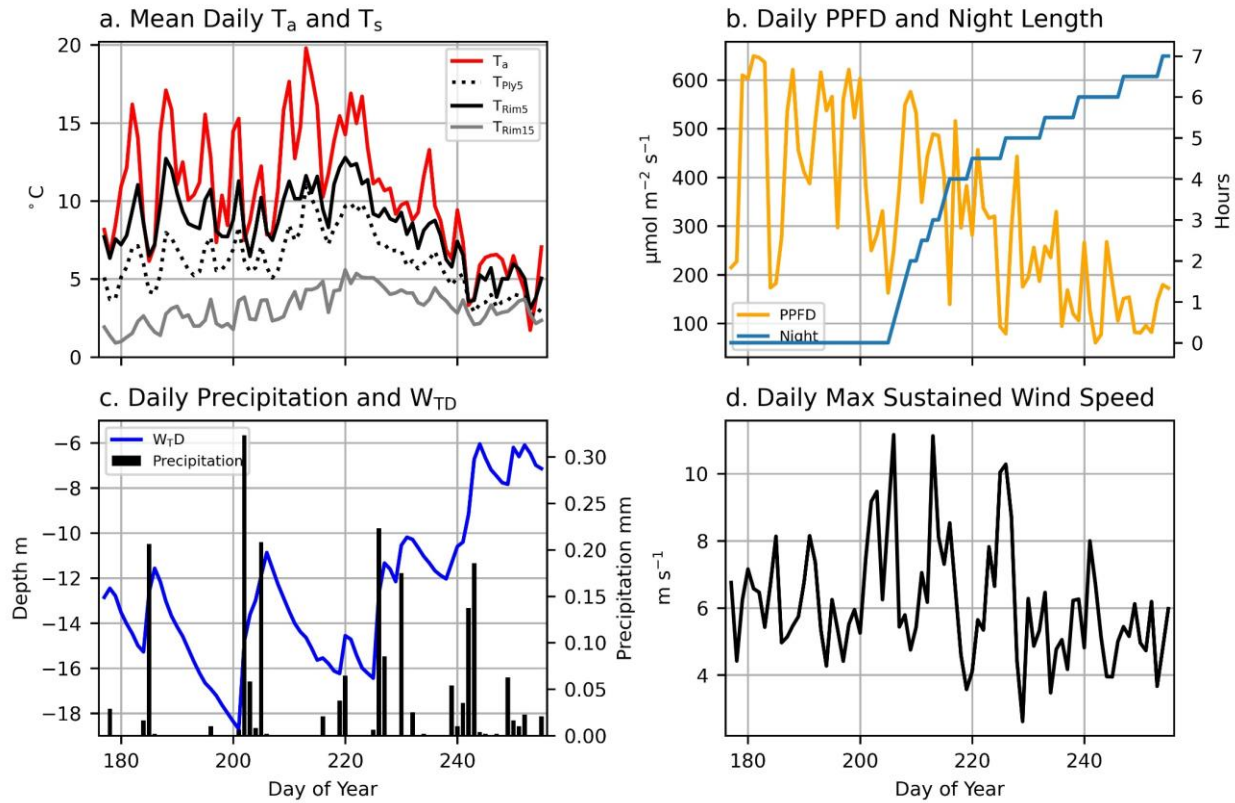


Figure 3.3. Climate and water level measurements during the 2017 study period: a) Daily mean T_a in red and daily mean T_s at 5 cm for polygon centers (dotted line) rims at 5cm (solid black line), and rims at 15cm (solid grey line) b) Mean daily PPFD and length of each night after the first sunset. c) Total daily precipitation (black bars) and mean daily W_{TD} (blue line). d) Daily maximum sustained half hourly wind speed at 2.89 m (black).

Table 3.1 Descriptive statistics of the source area for half hourly NME Observations. Despite NEE having over 1,000 more half hourly observations, the quantiles for NEE were nearly identical ($\pm 1\%$). Column headers for the landscape class flux contributions show their fractional cover in landscape classification map. The adjusted landscape fraction (ALF) values shown at the bottom are the landscape fraction (LF) estimates weighted by $(1 - F_{Out})$, using the 50th percentile value of F_{Out} .

	F_{Cnt}	F_{Rim}	F_{Tro}	F_{Out}
Minimum	33.0%	5.1%	0.0%	7.3%
25 th Percentile	58.7%	20.6%	1.8%	10.5%
50 th Percentile	62.8%	22.4%	3.4%	11.0%
75 th Percentile	63.7%	28.3%	4.8%	11.4%
Maximum	77.5%	56.4%	9.4%	18.1%
ALF	58.8%	25.6%	4.6%	N/A

3.3.1 Seasonal and Daily Trends

Figure 3.4 shows the course of observed NEE and NME and daily gap-filled NEE and NME over the study period. During the entire study period, Fish Island was a net sink for CO₂ with mean NEE of -0.60 [$CI_{95\%} \pm 0.04$] $\mu\text{mol m}^{-2} \text{s}^{-1}$. Day to day NEE varied depending on cloud conditions. CO₂ uptake increased during the early season until peaking in early-mid July

(DOY 190) as vegetation matured (Fig 3.2c). Net CO₂ uptake remained high through July then as day length and sun angle decreased through August. The site became a net CO₂ source by the end of the study period as plant life senesced (Fig 3.2d & e).

The site was a net CH₄ source during the study period with mean NME of 27.7 [CI_{95%} ± 0.35] nmol m⁻² s⁻¹. Day to day NME was less variable than NEE, but there were significant spikes associated with high wind events (discussed below). Methane emissions increased slightly through the beginning of the study period, peaking on DOY 202 then abruptly decreasing. Through the rest of the period, NME was consistently lower and continued to decrease through September. Light precipitation, condensation, and fog were common in the latter half of the study period, resulting in a large number of missing observations from this period due to low RSSI values.

Figure 3.5a & b shows the daily cycle of CO₂ and CH₄ exchange for the period when both CO₂ uptake and CH₄ emission were greatest. During this period, NEE was negative for most of the day, about 18 hours on average. Average maximum CO₂ uptake peaked at 9:00 LST (-3.16 μmol m⁻² s⁻¹) and plateaued over an extended period in the middle of the day. Maximum net CO₂ emissions occurred around 0:00 LST, but these observations do not represent ER because the sun was still above the horizon. Methane fluxes had a distinct daily cycle as well, and were negatively correlated with NEE (Pearson's r = -0.63). Average maximum daily NME (49.2 nmol m⁻² s⁻¹) was double the average minimum (24.3 nmol m⁻² s⁻¹) and similar to NEE, there was a mid-day plateau. Figure 3.5c & d shows the daily cycle in late August, just before the power system failed, when there were five to six hours of night-time per day. Night-time NEE (0.95 μmol m⁻² s⁻¹) during this period do represent ER. Peak CO₂ uptake occurred at noon

and there was no mid-day plateau. The diurnal cycle in NME was still present as well, but the magnitude of emissions decreased substantially.

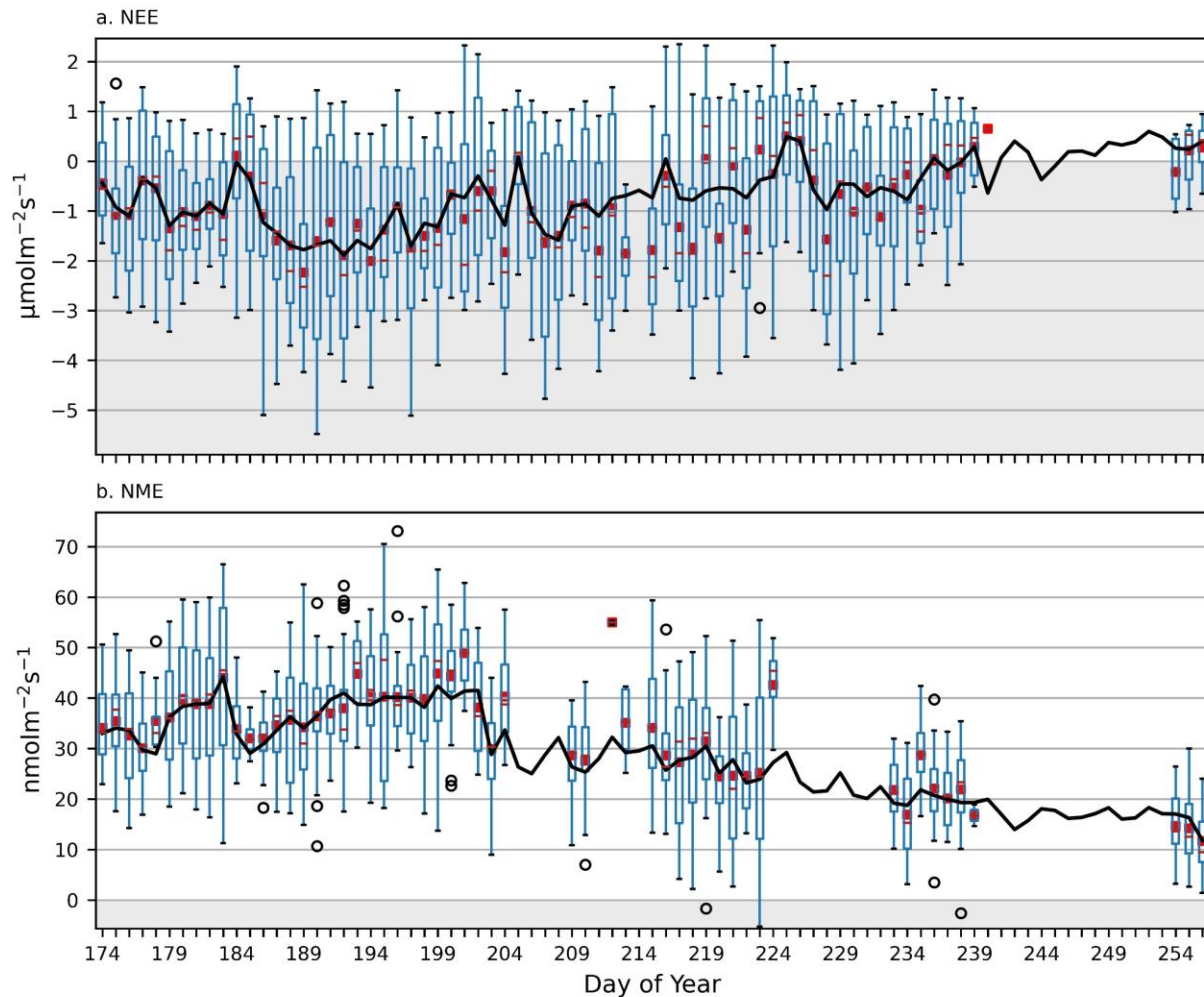


Figure 3.4. Daily measured NEE and NME (boxplot) and mean gap filled (black line) NEE and NME over the study period. For the boxplots, the red line indicates the median, the red square is the mean, the box represents the inner quartile range (Q1-Q3), the whiskers are 1.5 times the inner quartile range ending at the farthest data point within that interval, and circles represent outliers. Grey shading represents a net sink and no shading represents a net source.

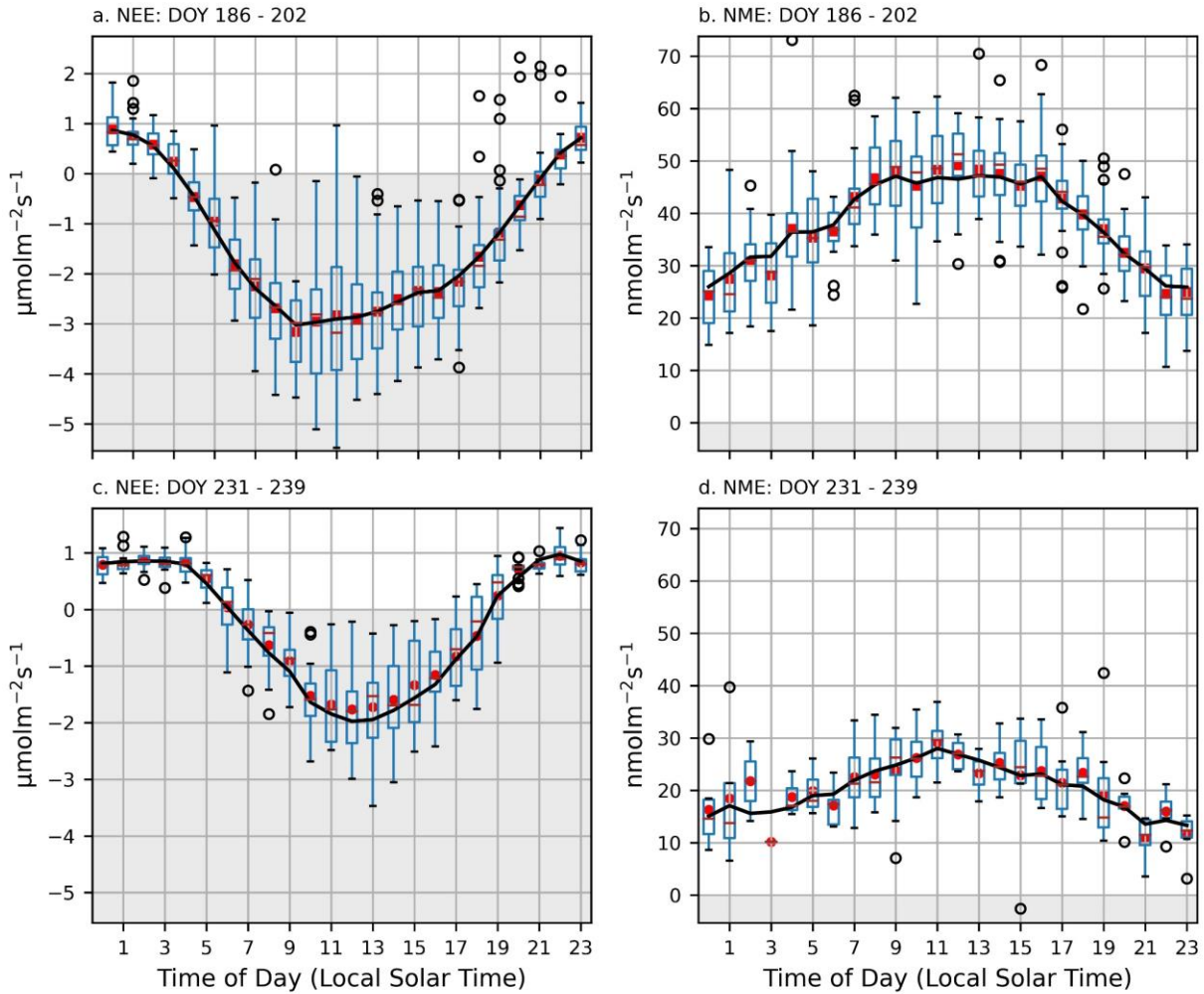


Figure 3.5. Diurnal (hourly) course of measured NEE and NME (boxplot) and mean gap filled (black line) NEE and NME early in the study period (a & b) and late in the study period (c & d). For the boxplots, the red line indicates the median, the red square is the mean, the box represents the inner quartile range (Q1-Q3), the whiskers are 1.5 times the inner quartile range ending at the farthest data point within that interval, and circles represent outliers. Grey shading represents a net sink and no shading represents a net source.

3.3.2 Net Ecosystem Exchange

3.3.2.1 Flux Drivers

The model trained on NEE performed very well on the OOB validation data ($r^2 = 0.93$, RMSE = $0.39 \mu\text{mol m}^{-2} \text{s}^{-1}$) and performance only dropped slightly compared to the benchmark ($r^2 = 0.95$). Pruning selected 8 inputs for NEE, which are listed in Table 3.2. Photosynthetic photon flux density (PPFD) is the dominant driver of GPP, and is the primary control over NEE

(64% RI). The partial first derivatives of *PPFD* (Fig 3.6a) show a strong negative influence that begins to decrease in magnitude at $100 \mu\text{mol m}^{-2} \text{s}^{-1}$. The function reaches a minimum around $750 \mu\text{mol m}^{-2} \text{s}^{-1}$ (dependent upon the other drivers), above which it has a weak positive influence. The *PPFD* response is modulated by the other drivers, primarily *VPD* (8% RI). It had a strong negative effect over NEE at low *VPD*, that reached an “optimal” value around 340 Pa (Fig 3.6b). At higher *VPD*, it was a strong limiting factor over GPP. The response curve of NEE to *PPFD* shows that all else being equal, high *VPD* (1000 Pa) can limit CO₂ uptake by more than $0.5 \mu\text{mol m}^{-2} \text{s}^{-1}$ relative to the optimal value (Fig 3.7a).

Thaw depth (7% RI), gave the model a seasonal signal which influenced both GPP and ER. Low thaw depths (early season) had a negative influence, NEE trended more negative as vegetation matured (Fig 3.6c). The model response shows a minimum around 0.35 m, below this point, all being else being equal NEE trends positive. Figure 3.7b. shows the model response to *TD* for “typical” daytime and nighttime conditions. During daytime, maximum CO₂ uptake can be seen around the timing of the minima identified in Fig 3.6c. With radiative inputs fixed to “dark” values, ER decreases steadily from a maximum during the early season, then leveled out around 0.4 m (corresponds to DOY 226) at about $1.0 \mu\text{mol m}^{-2} \text{s}^{-1}$. We had limited nighttime NEE observations, and none before DOY 206, so the confidence interval around the modeled ER was broader.

The model identified soil temperature at 5 cm (T_{Cn5} RI 7%) as the main driver of ER. Above 3 °C, increasing T_{Cn5} consistently increased ER (Fig 3.6d). This was modulated by T_{Rim5} (5% RI) and T_{Rim15} (3% RI) that had moderately negative influences at lower temperatures (Fig 3.6e & f). At higher temperatures the negative T_{Rim5} influence was negligible and T_{Rim15} became a positive driver. Polygon center and rim temperatures at 5 cm were highly correlated ($r = 0.81$)

and moderately to weakly correlated with T_{Rim15} (T_{Cnt5} r = 0.58, T_{Rim5} = 0.19). Rims were consistently warmer than centers, but the magnitude of the temperature gradient ($T_{A5} = T_{Rim5} - T_{Cnt5}$) decreased through the study (Fig 3.3a). Daily maximum T_{A5} was in the late afternoon and minimum was in the late night/early morning. The response of NEE to typical late afternoon and late night T_{A5} is shown in Figure 3.7c. There was a strong response to T_{Cnt} at higher temperatures, but the response was muted or even reversed at lower values. Temperatures at 15 cm also had a diurnal signal, but they were much more muted. In the model, T_{Rim15} had more impact on the seasonality of NEE, with higher temperatures at depth indicating increased respiration throughout the soil profile.

Table 3.2. The relative influence (RI) of the inputs of the pruned NN over NEE, along with their correlation (r) to half hourly NEE.

Rank	Symbol	Factor	RI	Sign	r
1	<i>PPFD</i>	Photon Flux Density	64%	-	-0.79
2	<i>VPD</i>	Vapour Pressure Deficit	8%	-	-0.44
3	<i>T_{Cnt5}</i>	Soil Temperature 5cm, Polygon Centers	7%	+	0.12
4	<i>TD</i>	Thaw Depth	7%	-	0.20
5	<i>Daytime</i>	Day / Night	6%	-	-0.36
6	<i>T_{Rim5}</i>	Soil Temperature 5cm, Polygon Rims	5%	-	-0.35
7	<i>T_{Rim15}</i>	Soil Temperature 15cm, Polygon Rims	3%	+	0.49
8	<i>U</i>	Wind Speed	1%	-	-0.09

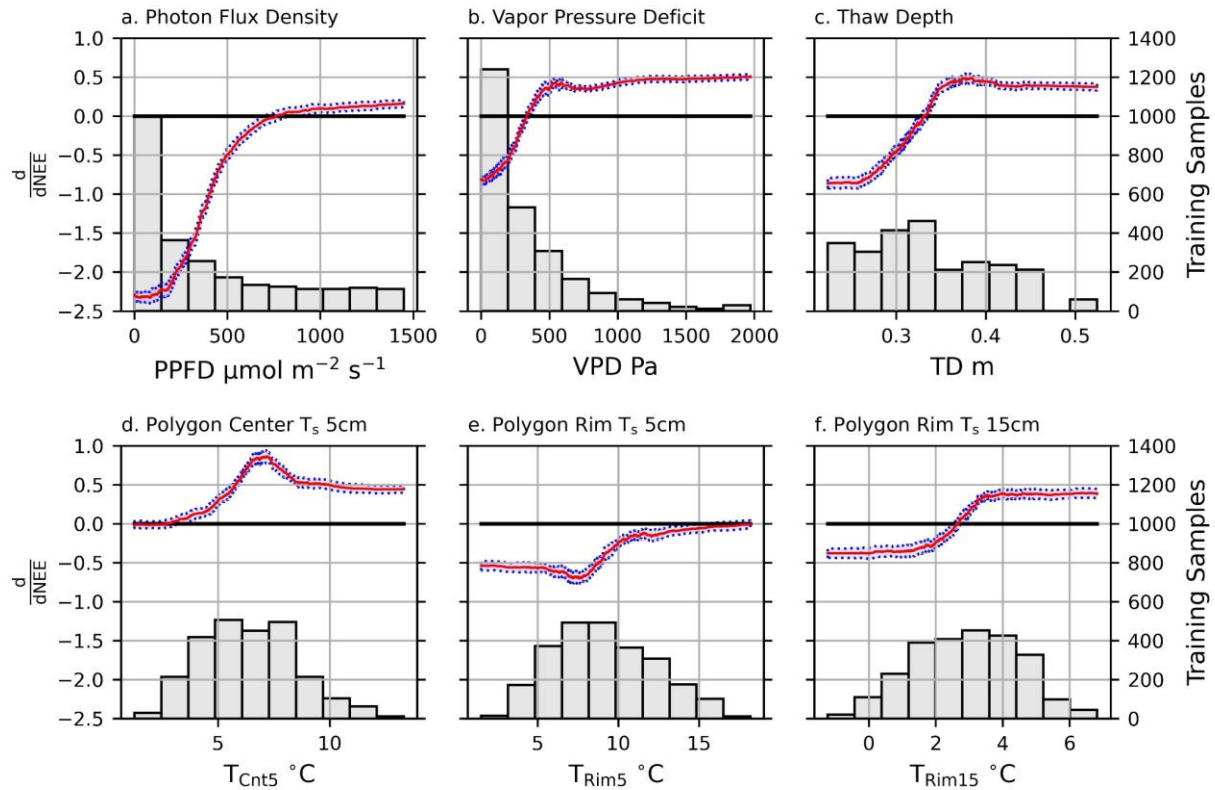


Figure 3.6. The mean sum of squared derivatives (SSD) for six of the input factors for the NEE model are shown in red, with a 95% confidence interval shown in blue. Y-axis labels on the left correspond to the SSD values. Also shown (grey bars) are histograms of the distribution of the input variables in the training set. The Y-axis labels on the right correspond to the number of training samples (half-hourly observations).

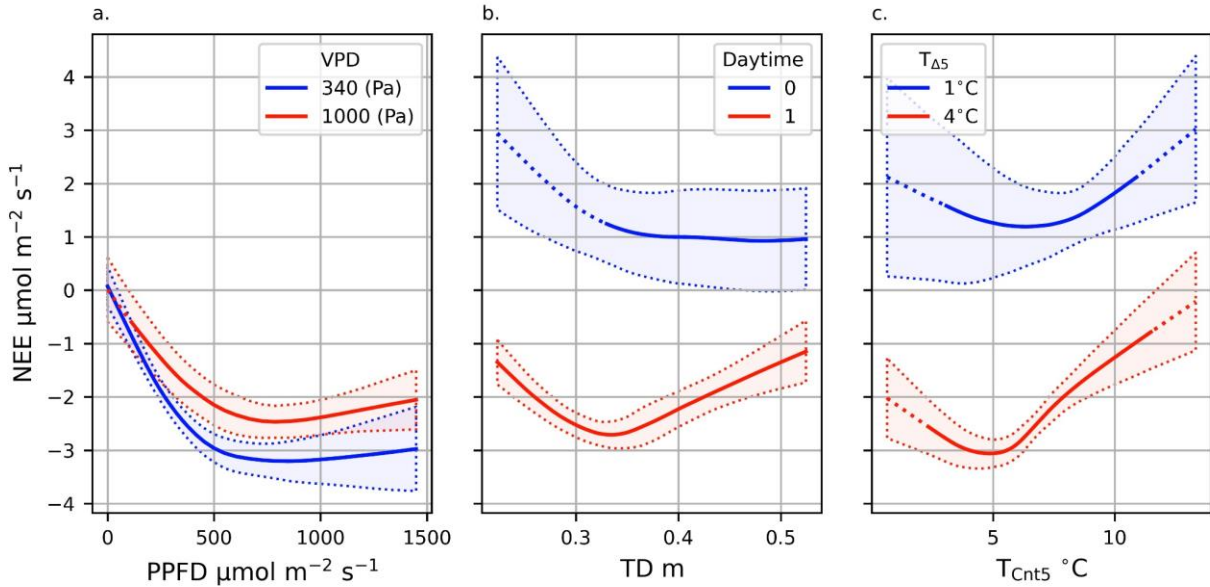


Figure 3.7. Modeled estimated NEE under different conditions, unless otherwise specified, all inputs were fixed to their median value. a) Daytime NEE response to photon flux density at optimal and high vapor pressure deficits. b) NEE response to thaw depth for daytime and nighttime. c) NEE response to polygon center temperatures at 5cm daytime and nighttime conditions, with a center-rim temperature gradients of 4°C and 1°C respectively. For each plot, the solid lines represent the mean modeled NME response, the dotted line is the mean response estimated outside conditions that were actually observed, and the shaded area bounded by the dots is the 95% confidence interval around the estimate.

3.3.2.2 Ecosystem Respiration

Mean estimated ER was $1.54 [\text{CI}_{95\%} \pm 0.87]$ $\mu\text{mol m}^{-2} \text{s}^{-1}$, which suggests a mean GPP around $2.14 \mu\text{mol m}^{-2} \text{s}^{-1}$. This is an extrapolation well beyond conditions the model was trained on (see Fig 3.8b), so there is more uncertainty around this prediction. The nighttime ER validation statistics for the model ($r^2 = 0.58$, RMSE = $0.23 \mu\text{mol m}^{-2} \text{s}^{-1}$) show this method outperformed the Q_{10} response curve ($r^2 = 0.32$, RMSE = $0.28 \mu\text{mol m}^{-2} \text{s}^{-1}$) and the best logistic soil temperature curve fit ($T_{Rim2.5}$: $r^2 = 0.45$, RMSE = $0.26 \mu\text{mol m}^{-2} \text{s}^{-1}$). The NN does a better job of approximating ER, especially at higher and lower NEE (Fig 8a). The chamber data gave us increased confidence in our NN derived ER estimate (Fig 8b). Due to the limited sample size, here we report the median and inner quartile range (IQR). Median ER_{Rim} over the two collection days was $2.77 [\text{IQR } 2.33 - 4.05] \mu\text{mol m}^{-2} \text{s}^{-1}$ was more than double ER_{Cntr} $1.09 [\text{IQR } 0.90 - 1.39] \mu\text{mol m}^{-2} \text{s}^{-1}$. Median values between sites also decreased from $1.57 \mu\text{mol m}^{-2} \text{s}^{-1}$ n DOY 191 to $1.08 \mu\text{mol m}^{-2} \text{s}^{-1}$ n DOY 233. Our NN derived ER estimate is between median ER_{Cntr} and ER_{Rim} and also showed a decreasing seasonal pattern.

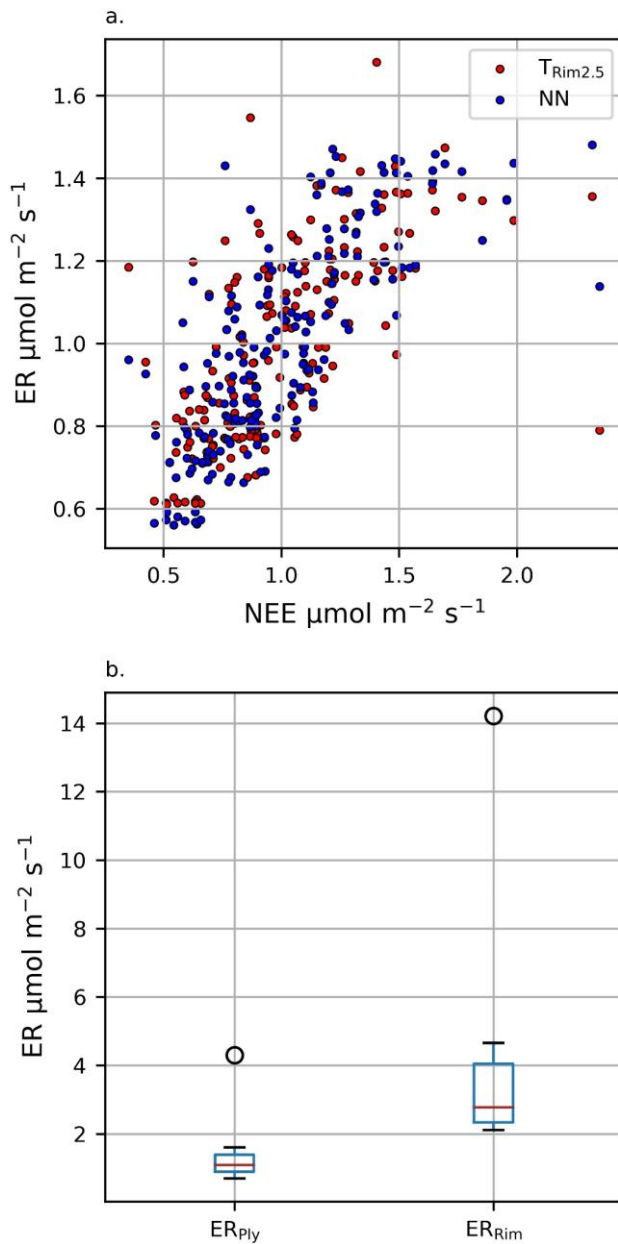


Figure 3.8. a) Nighttime NEE measurements plotted against modeled ER derived by the NN (blue) and logistic temperature response curve fit to $T_{\text{Rim}2.5}$ (red). b) Boxplots of the distribution of flux chamber observations of ER for polygon centers (ER_{Cnt} , $n = 16$) and rims (ER_{Rim} , $n = 8$) aggregated over the two measurement days. Also shown, are the nighttime ER observations from the EC system ($n = 186$). For the boxplots, the red line indicates the median, the box represents the inner quartile range (Q1-Q3), the whiskers are 1.5 times the inner quartile range ending at the farthest data point within that interval, and circles represent outliers. Note the y-axis for a & b are not on the same scale.

3.3.3 Net Methane Exchange

The model trained on NME performed reasonably well on the OOB validation data ($r^2 = 0.73$, RMSE = $6.53 \text{ nmol m}^{-2} \text{ s}^{-1}$) and performance dropped only slightly compared with the benchmark ($r^2 = 0.74$). Pruning selected 8 inputs for NME, which are shown with their RI in Table 3.3. The model could not resolve NME as accurately as it could NEE, which is partly due to the smaller number of training samples for NME (1441) vs. NEE (2501). This meant the model had fewer nodes (reduced flexibility) in addition to having less exposure to training data. Additionally, CH₄ fluxes do not have one dominant driver like CO₂ fluxes so the response function is more difficult for the model to resolve.

Net radiation (RI = 34%) had the highest influence, the model derivatives of (Fig 3.9a) show a positive influence that begins to decrease in magnitude around $150 \text{ W m}^{-2} \text{ s}^{-1}$ and reached a maximum around $320 \text{ W m}^{-2} \text{ s}^{-1}$. Thaw depth was the primary seasonal control (RI = 12%), which had a consistently negative influence (Fig 3.9b). The increase in magnitude of negative effect around 0.3 m coincided with the decrease in NME after DOY 202 (Fig 3.4b). The influence of R_n in the early and late season is plotted in Figure 3.10a. Leaving all other drivers fixed, a TD increase from 0.3 to 0.45 m decreases NME from 10 to $17 \text{ nmol m}^{-2} \text{ s}^{-1}$ at low ($0 \text{ W m}^{-2} \text{ s}^{-1}$) and high ($350 \text{ W m}^{-2} \text{ s}^{-1}$) R_n respectively. The shape of the curves is similar, but later in the season NME does not increase as rapidly with R_n. This would explain the lack of a mid-day plateau seen in the late season (Fig 3.5d).

Polygon center temperatures at 15 cm (RI = 6%) had a daily and seasonal signal. The seasonal trend closely mirrored T_{Rim15} (Fig 3.3c.), peaking in mid-august then decreasing. The daily maxima and minima occurred around 1:00 LST and 14:00 LST respectively; the mean daily range was greater in the early season (3°C) than late season (2°C). This pattern

corresponds well with the cycles shown in NME (Fig 3.5 b & d). The derivative of T_{Cn15} shows a net negative influence on NME, emissions increase until 2.5 °C above which they decrease (Fig 3.9c). The parabolic response with to T_{Rim15} is shown at two water table depths (Fig 3.10b). Water table depth (RI = 4%) had a modest negative influence over NME. NME decreased as the W_{TD} got closer to the surface, which was unexpected.

The model identified two highly correlated sets of inputs U and u_* ($r^2 = 0.92$) and F_{Rim} and F_{Ply} ($r^2 = 0.94$) as well. The wind and footprint variables had combined RIs of 37% and 6%, respectively. The model derivatives of U (negative) and u_* (positive) had inverse effects, indicating that the ratio between the two was important (Fig 3.9 d & e). Friction velocity increases proportionally with wind speed, but the ratio is not fixed. It was on average 8.1% of U with a standard deviation of 1.1%. All else equal, at $U = 5 \text{ ms}^{-1}$, a difference of $\pm 1 \text{ std.}$ can result in a $10 \text{ nmol m}^{-2} \text{ s}^{-1}$ difference in NME (Fig 3.10 c).

With source area fractions, F_{Rim} increased roughly proportionally with decreasing F_{Ply} with deviations caused by F_{Tro} to a much lesser extent F_{Out} . The effect of changing land cover in the source was generally small, but not insignificant. Figure B1 shows projections of NME across the range of F_{Rim} and F_{Cn1} with deviations in F_{Rim} to reflect the range of F_{Tro} . Estimating NME over the study period with F_{Rim} and F_{Cn1} fixed to ALF, the model predicts a slightly lower NME $26.6 [\text{CI}_{95\%} \pm 4.3] \text{ nmol m}^{-2} \text{ s}^{-1}$.

Table 3.3. Environmental controls over NME identified by model pruning, along with their relative influence to the model and their Pearson's correlation coefficient to half hourly NME.

Rank	Symbol	Factor	RI	Sign	r
1	R_n	Net Radiation	34%	+	0.66
2	u_*	Friction Velocity	20%	+	0.23

3	U	Wind Speed	17%	-	0.34
4	TD	Thaw Depth	12%	-	-0.46
5	T_{Cnt15}	Soil Temperature 15cm, Polygon Center	6%	-	-0.58
6	W_{TD}	Water Table Depth	5%	-	-0.45
7	F_{Rim}	Rim Fraction	4%	-	-0.19
8	F_{Ply}	Center Fraction	2%	-	0.19

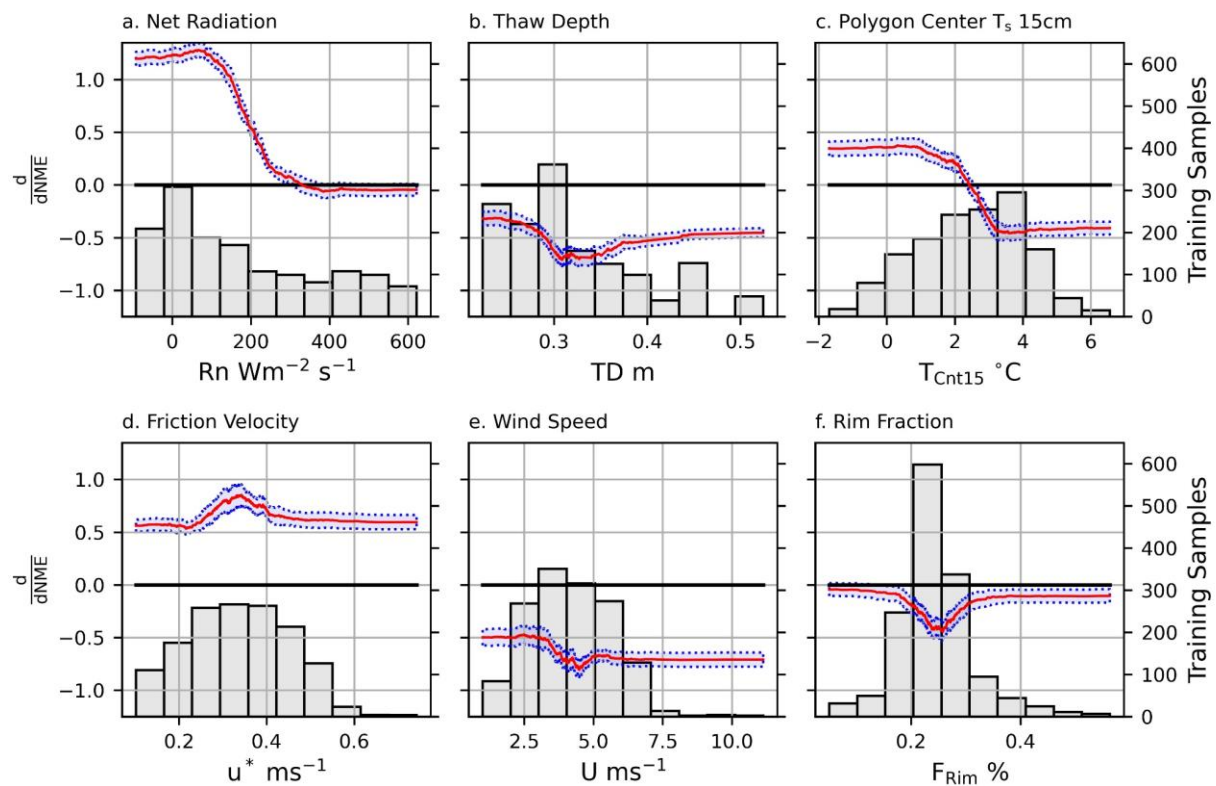


Figure 3.9. The mean sum of squared derivative (SSD) for six of the input factors for the NME model are shown in red, with a 95% confidence interval shown in blue. Y-axis labels on the left correspond to the SSD values. Also shown (grey bars) are histograms of the distribution of the input variables in the training set. The Y-axis labels on the right correspond to the input counts for each bin.

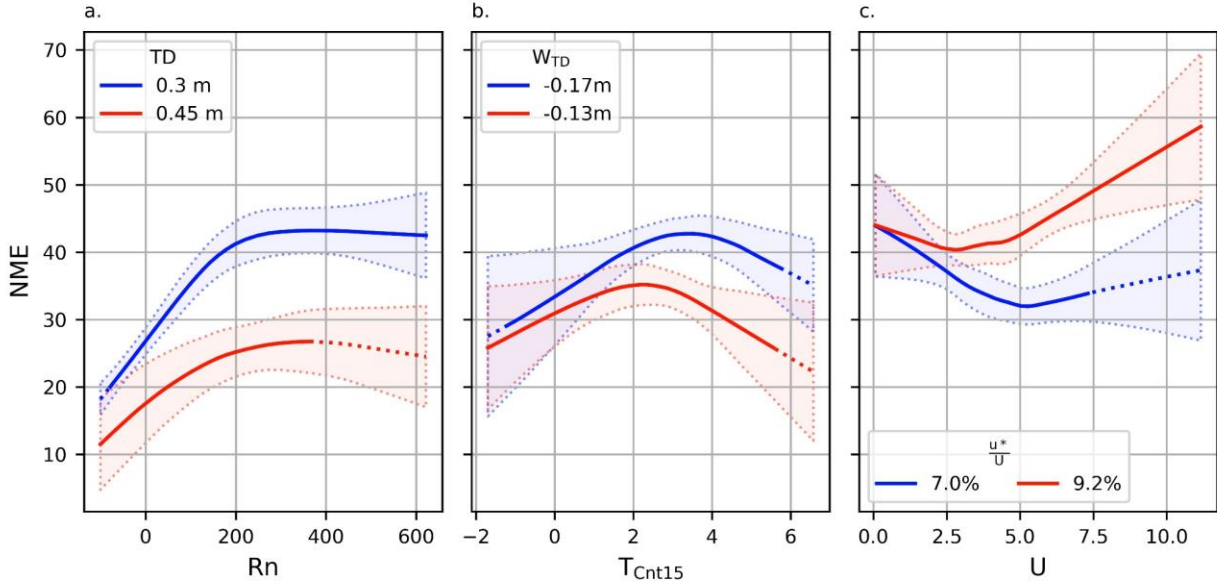


Figure 3.10. Modeled estimated NME under different conditions. Unless otherwise specified, thaw depth was set to 0.3 m and all other inputs were fixed to their median value. a) NME response to net radiation for thaw depth (TD) representative of early season (0.3 m) and late season (0.45 m) conditions. b) NME response to polygon center temperatures (TCnt15) at two water table depth (WTD). c) NME wind speeds (U) with friction velocity (u_*) set to 7% and 9.2% of U. For each plot, the solid lines represent the mean modeled NME response, the dotted line is the mean response estimated outside conditions that were actually observed, and the shaded area bounded by the dots is the 95% confidence interval around the estimate.

3.4 Discussion

3.4.1 Flux Drivers

Neural networks are ideally suited for modeling the numerous nonlinear relationships that influence carbon fluxes. However, a NN will fit any pattern in a data set, real or artificial, so care must be taken to ensure the results are plausible and repeatable. If a NN is treated as a black box (e.g. Jarvis and Stauch, 2003), we have no way of knowing what it is actually doing. Plotting the model output response to specific drivers is beneficial (Moffat et al. 2010; Skeeter et al. 2020), but when working in multidimensional feature space there is no way to assess all possible combinations of drivers. To our knowledge, this is the first study to apply the weights method (Gevrey et al. 2003) to a NN analysis of EC data. This method allowed us to assess each

variable's relative influence and visualize the relationship by plotting their partial first derivatives, which was especially useful for highly correlated inputs like wind speed and friction velocity.

3.4.1.1 Spatial Variability

In low-center polygonal landscapes, polygon centers are depressed relative to rims. Relief was about 10-20 cm at Fish Island, whereas a site on Samoylov Island in Siberia's Lena Delta had up to 50 cm (Sachs et al. 2010). Anaerobic respiration is favored in the depressed areas, promoting CH₄ production, and inhibiting ER and CH₄ consumption (Lai 2009). Our chamber ER data show higher ER from rims than centers at Fish Island. Similar patterns have been found in chamber ER studies of low-center polygon sites near Barrow (Utqiagvik), AK (Olivas et al. 2011) and Samoylov Island, Siberia (Eckhardt et al. 2019). At Samoylov Island, NME differed by an order of magnitude between centers and rims as well (Sachs et al. 2010). However, rim GPP was higher and lower than center GPP at the Alaskan and Siberian sites, respectively (Olivas et al. 2011; Eckhardt et al. 2019). The rims at Fish Island had more shrub cover than either of the other sites, so we cannot assume the GPP response here would be similar to either the Alaskan or Siberian sites.

At the plot scale, there was significant spatial heterogeneity at Fish Island. The NN analysis indicated polygon rim and center fraction were both relevant for NME, with a combined influence of 6%. Polygon rims had lower NME than centers and both had lower NME than troughs. The source area fractions are not drivers of landscape scale CH₄ per se. Rather they highlight substantial spatial heterogeneity in CH₄ fluxes at Fish Island and indicate location bias had a minor impact on observed NME (Schmid and Lloyd, 1999). Following a three-tier site-footprint representative index based on the dominant landcover fraction and chi-square analysis,

our site's footprint would be classified as Medium (Chu et al. 2001). Projecting to the ALF shown in Table 3.1 estimates that landscape scale NME is about $1 \text{ nmol m}^{-2} \text{ s}^{-1}$ lower. This projection can also be used to infer that if permafrost degradation leads to the development of more troughs at Fish Island in the future, landscape scale NME will go up.

For NEE the temperature gradient between rims and centers was relevant, which indicates that microtopography has an effect on landscape scale CO₂ fluxes at Fish Island. Footprint source area inputs were not identified as important drivers (RI > 2.5%) of NEE by the benchmark model, so they were pruned. In the benchmark NEE model, polygon rim (RI = 1.9%) and center (RI = 1.7%) ranked 12th and 14th among the initial 21 inputs, indicating they had little influence on footprint scale NEE compared with the selected drivers. At very low values (e.g. $F_{Rim} < 10\%$), the benchmark model predicts more negative NEE, which supports the chamber observations of reduced ER in polygon centers, but conditions like that accounted for less than 4% of our flux observations. For further comparison, trough fraction ranked 21st (RI = 0.5%) and 9th (RI = 2.4%) in the benchmark NEE and NME models respectively. The low importance assigned to the source area fractions suggests the placement of the tripod relative to microtopographic features did not have an appreciable impact on the NEE observed.

The resolution of the landscape classification and footprint function (Kljun et al. 2015) may have been limiting factors. However, the average polygon was only 270 m^2 ($\sim 16.5 \text{ m}$ across), whereas the 50% and 90% contours for the typical flux footprint were 2300 m^2 and 6500 m^2 , respectively. Given the relatively small size of the polygons and the regularity with which they repeat across space, the spatial heterogeneity at Fish Island mostly averages out at the footprint scale.

3.4.1.2 Net Ecosystem Exchange: Flux Partitioning

The NN analysis identified *PPFD* as the primary control over GPP, and highlighted VPD as the main limiting factor of GPP, which was expected (Aubinet et al. 2012). This relationship has been identified by NN analysis in other studies (Mofat et al. 2010; Skeeter et al. 2020) and has been noted at other wet tundra sites across the Arctic (Kwon et al. 2006; Fox et al. 2008). The model selected polygon center temperatures at 5cm as the dominant driver, which makes sense given that polygon centers cover the majority of the land area (66%) at the site. It also indicated that the center-rim temperature gradient played an important role in modulating ER. Other studies have found surface temperature rather than soil temperatures to be the primary control over ER in tundra environments (Kutzbach et al. 2007; Runkle et al. 2013). We lacked an observation of surface temperature and would consider adding it in a future study. However, temperatures throughout the upper layers of peat were been shown to be strong predictors of ER at a polygonal peatland site in Salluit, QC (Gangon et al. 2017). Further, given the flexibility of NN to account for interactions between variables we are confident this provides a better estimate than soil surface temperature alone could.

When modeling NEE, the network does not inherently differentiate between ER and GPP. Rather it conflates the signals of the two responses into one output. Some studies have trained the NN separately on night-time and daytime conditions to resolve ER (Papale and Valentini, 2003). This approach was not well suited for our site. Instead, we used the *Daytime* variable to give the model the ability to differentiate between night and day without splitting our training data. Skeeter et al. (2020) approximated ER using a NN by setting radiative inputs to “nighttime” values, but they did not use a *Daytime* variable, and their NN underperformed relative to a Q_{10} curve. We found adding *Daytime* drastically increased the model’s ability to

resolve ER which we support with comparisons to the Q_{10} and logistic temperature response curves. It also allowed us to estimate ER over the full study period, despite the limited number of nighttime observations, using an artificial “dark” dataset.

Our NN derived ER ($1.54 \mu\text{mol m}^{-2} \text{s}^{-1}$) was between the ER_{Cntr} and ER_{Rim} , which gives us confidence in our estimate. Using the half-hourly footprint source area fractions, we can spatially weight our chamber observations. Assuming polygon center/rim distribution outside the LCM mirrors the distribution within it, and ER from troughs is between ER_{Cntr} and ER_{Rim} we get an estimate of 1.62 [IQR 1.34 to 2.22] $\mu\text{mol m}^{-2} \text{s}^{-1}$. This is a rough, back of the envelope comparison, but it does further support using this method to estimate ER.

Mean gap-filled NEE, estimated ER and GPP at Fish Island all exceeded ranges observed at a low-center polygon sites in Alaska (Olivas et al. 2011) and Siberia (Eckhardt et al. 2019) using flux chambers. We attribute the differences in GPP to: 1) The lower latitude of Fish Island (69°) compared with the Alaskan (71°) and Siberian (72°) sites. 2) More productive vegetation at Fish Island, e.g. *Salix* spp. were absent at the Alaskan and Siberian sites. Differences in ER are attributable to colder soil temperatures and shallower thaw depths (25 cm) and (35 cm) at the Alaskan and Siberian sites respectively (Olivas et al. 2011; Eckhardt et al. 2019).

3.4.1.3 Net Methane Exchange

There was a significant diurnal cycle in NME throughout the season, and this was identified by the NN selecting R_n as the dominant driver. Many studies in Arctic, sub-Arctic, and peatland sites have not found a distinct diurnal cycles in CH_4 fluxes (Rinne et al. 2007; Sachs et al. 2008; Nadeau et al. 2013; Lee et al. 2017; Rößger et al. 2019b). However, mid-day maxima in NME have been observed at sub-Arctic fens in the Hudson Bay lowlands (Chanton et al. 1992) and Siberia (Veretennikova and Dyukarev 2017). In the Siberian fen, mid-day NME

was three times the nighttime values (Veretennikova and Dyukarev 2017), which is even greater than observed at Fish Island. They proposed diurnal temperature variations explain the cycle. We postulate the same is occurring at Fish Island, given the model selected polygon center temperatures at 15 cm (T_{Cnt15}) as an auxiliary driver and the diurnal cycle in T_{Cnt15} . However, we cannot overlook the potential role of plant mediated transport as another driving factor (Wang and Han 2005). Given the strong positive correlation between NEE and NME, we think this hypothesis merits further investigation as well.

Water table depth (W_{TD}) is known to be a primary determinant of CH₄ production and consumption in peatlands (Kutzbach et al. 2004; Lai, 2009). However, Arctic sites with little variation in W_{TD} have found its influence to be negligible (Sachs et al. 2008; Rößger et al. 2019b). At Fish Island, decreasing water table depth had a weak negative influence, which was unexpected. We propose three explanations for this: 1) The range of water table depth was fairly small over the study period. This reasoning was given to explain a similar pattern at a bog in the James Bay lowlands (Nadeau et al. 2013). 2) Data during/after precipitation events when the water table rose rapidly were generally filtered out due to low signal strength (RSSI). Using the unfiltered data, we see strong peaks associated with rising water table, but these signals are unreliable so more studies would be needed to verify this. Gagnon et al. (2017) found precipitation events created conditions that suppressed ER in a polygonal peatland. It is probable that the same thing occurs at Fish Island and leads to elevated NME. 3) Significant loss of data in the second half of the study period means we lack NME observations for many specific combinations of thaw depths and water table levels, limiting the model's ability to resolve the relationship between these drivers. To adequately resolve the influence of water table depth and its interaction with thaw depth, a multi-year data set would be needed.

Perhaps the most interesting finding of our NN analysis is the complex relationship of NME with wind speed (U) and friction velocity (u_*). Spikes in NME associated with high friction velocity have been observed at a low-center polygon site in Siberia (Sachs et al. 2008) and a peatland in the James Bay lowlands (Nadeau et al. 2013). One explanation is that gas transfer between open water and the atmosphere increases proportionally to the third power of the windspeed (Sachs et al. 2010; Wanninkhof and McGillis, 1999). This likely had some effect because of the ponded troughs within the footprint. However, most of the land area was consistently above the water table. Instead, we frame the hypothesis that high winds and turbulence may enhance pressure pumping (Laemmel et al. 2017; Mohr et al. 2016) that ventilates the aerobic peat layer in the polygon center. We hypothesize that pressure pumping reduces the time CH_4 is subject to methanotrophy within the aerobic layer of peat and therefore enhances net CH_4 emissions transporting it more quickly from the anaerobic layer to the atmosphere. Given that high wind events ventilate CH_4 that would otherwise be consumed, a change in storm frequency paired with an increase in the duration of the snow free season could lead to an increase in emissions from sites like Fish Island, a hypothesis that requires further exploration.

3.4.2 Carbon Balance

The low-center polygonal terrain at Fish Island was a net CO_2 sink ($-0.6 \mu\text{mol m}^{-2} \text{s}^{-1}$) and a net CH_4 source ($27.7 \text{ nmol m}^{-2} \text{s}^{-1}$) during the 2017 study. Overall, NME had a relatively minor impact on net carbon uptake (-49.5 g C m^{-2}) over the 82-day study period (Figure 3.11). Our estimate of NME matches well with median daytime NME measured by aircraft (17 to 35 $\text{nmol m}^{-2} \text{s}^{-1}$) in vicinity of Fish Island (Kohnert et al. 2017).

A short EC study at Illisarvik, a young drained thermokarst lake basin 17 km to the northeast, is the only observation of NEE available in the scientific literature for comparison in the region (Skeeter et al. 2020). Peak growing season NEE and NME respectively were 1.5 and 0.3 times the magnitude observed at Fish Island. Vegetation at Illisarvik is diverse and basin scale fluxes are not representative of the Fish Island. Compared with chamber fluxes at Illisarvik, ER_{Rim} was most similar to dense *Salix* spp. plots at Ilisarvik ($3.4 \pm 0.6 \text{ } \mu\text{mol m}^{-2} \text{ s}^{-1}$) whereas ER_{Cnt} was below even bare soil plots ($1.9 \pm 0.3 \text{ } \mu\text{mol m}^{-2} \text{ s}^{-1}$). NME was low across vegetation types at Illisarvik, except for sedge plots ($110 \pm 14.7 \text{ nmol m}^{-2} \text{ s}^{-1}$) that were well above even maximum half-hourly NME ($73 \text{ nmol m}^{-2} \text{ s}^{-1}$) measured at Fish Island (Skeeter et al. 2020). The only other study in the region is from manual chamber measurements on high-center polygons near Tuktoyaktuk (Martin et al. 2017). Polygon and wet-trough ER ($1.2 \pm 0.7 \text{ } \mu\text{mol m}^{-2} \text{ s}^{-1}$) were comparable to ER_{Cnt}; polygon center NME was negligible but wet-trough NME ($150 \pm 236 \text{ nmol m}^{-2} \text{ s}^{-1}$) was very high (Martin et al. 2017). No areal fraction for this site was given, so there is no landscape scale estimate to compare between these two types of polygonal terrain.

Lacking more studies of carbon fluxes in the Mackenzie Delta, we can compare current results with Samoylov Island ($72^\circ 22' \text{ N}, 126^\circ 30' \text{ E}$) in Siberia's Lena River Delta which has been intensively studied with both EC and chamber methods (Sachs et al. 2008 & 2010; Eckhardt et al. 2019; Holl et al. 2019; Rößger et al. 2019a and b). Mean air temperature (-12.8°C) and annual precipitation (321 mm) at Samoylov are colder and wetter than Fish Island (Rößger et al. 2019b). Samoylov Island has two morphological units, a river terrace with low-center polygonal tundra and a floodplain (Kutzbach et al. 2007). The distribution of polygon rims (60% - 65%) and centers (35% - 40%) and microtopographic relief (up to 50 cm) on the terrace is quite different than at Fish Island, but the vegetation communities present (sedges,

mosses, dwarf shrubs), and mean thaw depths (0.49 m) were comparable. Two vegetation communities were at the floodplain site: dense *Salix* spp. up to 1 m tall and *Carex* spp. with dwarf *Salix* spp. Relative to Fish Island, TD (0.7 - 0.9 m) and W_{TD} (0.4-0.5 m) were deeper. Neither unit is directly analogous to Fish Island, but they can help contextualize our results.

At the floodplain site, averaged over 2014 and 2015, peak growing season and late season NEE respectively were more negative ($-1.77 \mu\text{mol m}^{-2} \text{s}^{-1}$) and positive ($0.77 \mu\text{mol m}^{-2} \text{s}^{-1}$) respectively than at Fish Island (Rößger et al. 2019a). They attribute the unexpectedly high productivity of this site to regular nutrient input from the spring flood (van Huissteden et al. 2005; Rößger et al. 2019a). At the adjacent river terrace, a 14-year record shows this site is consistently a growing season CO₂ sink, over comparable periods (see Fig 9 Holl et al. 2019), net CO₂ uptake at Fish Island between DOY 200 and 234 in 2017 ($-23.1 \text{ g C-CO}_2 \text{ m}^{-2}$) was greater than all but one year at the terrace site at Samoylov Island. Interannual variability was significant and, in some years, cold season emissions offset growing season uptake (Holl et al. 2019). NME at the floodplain ($15 \text{ nmol m}^{-2} \text{s}^{-1}$) and terrace ($13 \text{ nmol m}^{-2} \text{s}^{-1}$) were well below levels observed at Fish Island (Sachs et al. 2008; Rößger et al. 2019b). These lower methane emissions can partly be explained by the better drainage of the floodplain and difference in microtopography rim/center distribution at the terrace site. Additionally, Fish Island's growing season is warmer; mean July air temperatures of 11.6°C compared to 9.5°C at Samoylov, which may also contribute to higher NME as well (Holl et al. 2019; NWT Water Resources 2019).

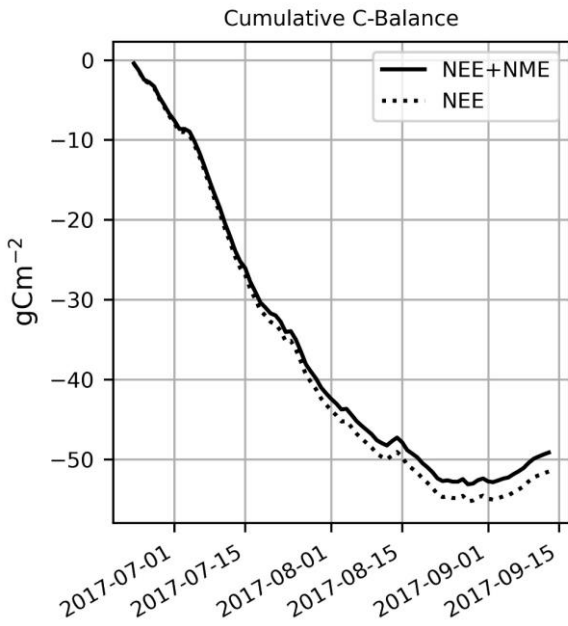


Figure 3.11. The cumulative daily Carbon balance in g C m^{-2} with and without accounting for NME.

3.5 Conclusions

This is the first study to directly and continuously measure growing season NEE and NME within the Mackenzie River Delta by means of eddy covariance. The site, a low-center polygonal peatland at Fish Island was a C sink during the study period with NME having only a minor impact on net C uptake. NME was within the range observed by aircraft in the Northern Mackenzie Delta. Fish Island was a stronger CH₄ source than similar landscapes in the Lena River Delta (Siberia) whereas CO₂ exchange was comparable. We used a NN approach to identify major drivers of NEE and NME at different temporal scales. Variations in light level and temperature were the main controls over diurnal net carbon dioxide uptake, whereas thaw depth and phenology were the main seasonal controls. Methane emissions measured at Fish Island were higher than comparable studies on river delta sites in the Arctic and were influenced by the interaction of numerous of factors including thaw and water table depth, soil temperatures and net radiation. The high NME and significant interannual variability in flood and climate

conditions at this site highlight the need for longer term studies in this region. Additionally, the enhanced NME during high wind events calls for further studies to allow for a process-based understanding of the mechanisms. More research is needed to carefully test the pressure pumping hypothesis and its implications on global-level Arctic CH₄ emissions.

Chapter 4: Modeling Interannual Variability of Carbon Fluxes at a Low-Center Polygon Ecosystem in the Mackenzie River Delta

Chapter 4 has been written with the intent of submitting to *Arctic Science* as a follow up paper for the publication stemming from Chapter 3. At the time of thesis submission, this chapter should be under review.

4.1 Introduction

Climate change is warming the Canadian Arctic at about three times the global rate due to Arctic amplification (Flato et al. 2019). Amplification of warming in polar regions is caused by a number of feedback mechanisms, most notably positive local lapse-rate feedback, with ice-albedo, Planck, and cloud cover feedbacks playing subsidiary roles (Stuecker et al. 2018; Flato et al. 2019). Warming has already caused and will continue to cause significant impacts across the Canadian Arctic, including: permafrost degradation (e.g., increased active layer thickness and thermokarst), longer growing seasons, tundra greening, and shifting wetland distribution (Derkzen et al. 2019; Frost et al. 2020; Myers-Smith et al. 2020; Turetsky et al. 2020; Kreplin et al. 2021). These impacts can alter the C-balance of Arctic landscapes and lead to positive and negative feedbacks that can further exacerbate or help remediate warming, respectively.

Of particular concern are ice-rich permafrost lowlands because they contain high C-stocks and are hotspots for CH₄ emissions (Olefeldt et al. 2013; Schuur et al. 2015; Kohnert et al. 2018). Lowland tundra ecosystems are characterized by substantial spatial heterogeneity that is not well resolved by the models used to project the ecological response to climate change (Lara et al. 2020). The Canadian Arctic is underrepresented by existing Eddy Covariance (EC) sites used to measure ecosystem C fluxes, so we lack a baseline understanding of C exchange in

tundra lowlands (Delwiche et al. 2021; Pallandt et al. 2021). This makes it difficult to anticipate how C fluxes will change across this region with climate warming.

The Mackenzie Delta is a broad alluvial plain ($13,000 \text{ km}^2$) that grades from boreal forest in the south to shrub tundra and sedge wetlands in the north (Burn, 2017). Most of the delta is inaccessible except by boat or aircraft, consequently there has been little work done to quantify the C-balance of the Mackenzie Delta. A delta-wide aircraft study showed the region is a strong source of methane (CH_4) emissions, both geologic and biogenic in origin (Kohnert et al., 2017; Kohnert et al., 2018). They did not measure carbon dioxide (CO_2) exchange across the delta, and the current C-balance of the Mackenzie Delta remains poorly understood.

There has been only one study of in-situ ecosystem-scale C fluxes in the Mackenzie Delta. Skeeter et al. (2022) measured fluxes of CO_2 (F_{CO_2}) and CH_4 (F_{CH_4}) at a low-center polygon (LCP) ecosystem on Fish Island in the northeastern Mackenzie Delta during the 2017 growing season (June 23rd – September 13th). They conducted a neural network (NN) analysis which identified key drivers of half-hourly F_{CO_2} and F_{CH_4} and showed the LCP ecosystem at Fish Island was a net CO_2 sink and CH_4 source respectively during the 2017 field season. Weather records of a co-located automatic weather station show that, there is significant interannual variability in growing season temperatures and precipitation at Fish Island. This suggests that the C balance of one growing season is not representative of net C exchange over multi-year timescales. Strong interannual variability in net C uptake during the growing season has also been reported for LCP ecosystems on Alaska's North Slope (Dengel et al. 2021) and Siberia's Lena Delta (Holl et al. 2019).

The aim of the current study was to build on the analysis of Skeeter et al. (2022) by investigating the interannual variability of flux drivers at the LCP ecosystem on Fish Island.

Using an 11-year record of hourly data from an automated weather station (AWS) on Fish Island combined with reanalysis and satellite data, we present an investigation of the interannual variability of flux drivers at Fish Island. The primary goals of this study were to: 1) quantify inter annual variability in drivers of Net Ecosystem Exchange (NEE) and Net Methane Exchange (NME) at the LCP ecosystem on Fish Island; and 2) investigate the potential range of fluxes during the snow-free season by modelling the response of NEE and NME to key flux drivers.

4.2 Data and Methods

4.2.1 Study Site

Fish Island is in the northeastern Mackenzie River Delta, Northwest Territories, Canada (Fig 4.1). The island is part of the Big Lake Delta Plain (BLDP), an alluvial platform the northeastern Mackenzie Delta that is subject to episodic flooding during the spring freshet and experiences low sedimentation rates ($\sim 1 \text{ mm yr}^{-1}$) (Morse & Burn, 2013). Snowmelt on the BLDP occurs between mid-May and early June, coinciding with the spring freshet. The growing season starts in June and lasts until senescence begins in August (Skeeter et al. 2022). Winter begins by late-September or October when freezing conditions return and the snowpack begins to accumulate.

Ice wedges and polygonal microtopography are widespread across the BLDP (Morse et al. 2012). An LCP ecosystem covers the north and central portions of Fish Island (Figure 4.2). The LCP ecosystem consists of peat rich polygon centers (10 - 20 m across) separated by low (10 – 20 cm) elevated ridges (2 – 4 m wide). Vegetation present in the LCP ecosystem is mainly peat moss (*Sphagnum* spp.), sedge (*Carex* spp.), horsetail (*Equisetum* spp.), and cotton sedge

(*Eriophorum angustifolium*), along with dwarf willows (*Salix* spp.) on the elevated ridges between polygons.

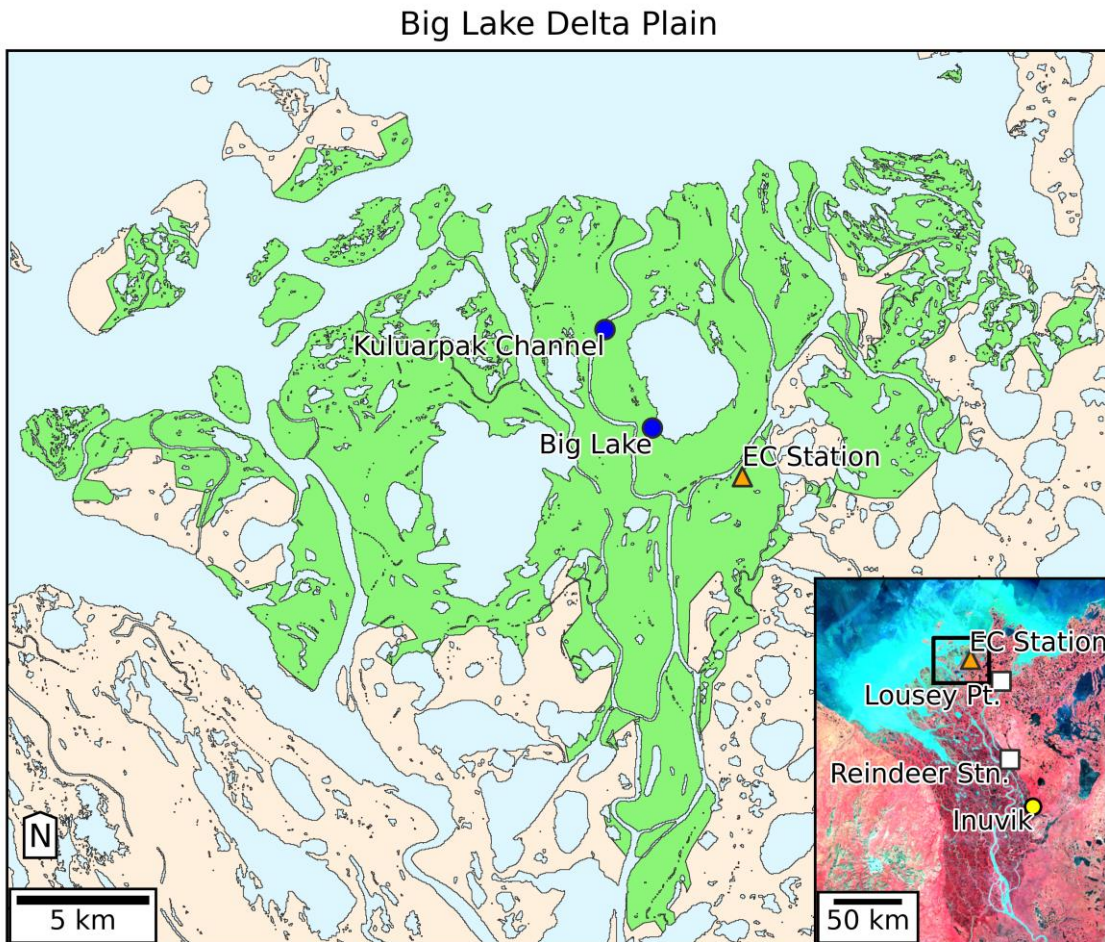


Figure 4.1. The Big Lake Delta Plain (BLDP) in green following the boundaries defined by Morse & Burn (2013). Land areas that are not part of the BLDP are shown in tan. Also shown is the EC Station at Fish Island as an orange triangle and the two Environment Canada gauge stations as blue circles. The inset map shows a false color composite MODIS image of the Mackenzie River Delta and surrounding uplands. The delta is visible in darker red while the surrounding uplands are in lighter red. The white squares show the location of the two Circumpolar Active Layer Monitoring (CALM) sites and the yellow circle shows the location of the community of Inuvik.

4.2.1.1 Flux Observations

An Eddy Covariance (EC) station ($69^{\circ}22'20.2''\text{N}$, $134^{\circ}52'51.9''\text{W}$) was placed in the LCP ecosystem on Fish Island (Figure 4.2). It measured fluxes of CO_2 (F_{CO_2}) and CH_4 (F_{CH_4}) from 00:00 (Mountain Daylight Time) June 23rd to 12:30 September 13th 2017 (Skeeter et al. 2022). This time period is henceforth referred to as the 2017 field season. The EC system consisted of a closed-path infrared $\text{CO}_2/\text{H}_2\text{O}$ gas analyzer (IRGA, model LI-7200, LI-COR Inc., Lincoln, NE, USA; LI-COR), an open-path CH_4 analyzer (model LI-7700, LI-COR) and a CSAT3 sonic anemometer (Campbell Scientific Inc, Logan, UT, USA; CSI) mounted on a tripod at a measurement height (z_m) of 2.87 m. Flux data were logged on a LI-7550 Analyzer Interface Unit (LI-COR). During this period, the CSAT3 was operational, but the Li-7200 and Li-7700 were shut down. Half hourly fluxes, along with vapor pressure deficit (VPD), mean wind speed (U), and friction velocity (u_*) were calculated in Eddy Pro according to the settings described in Skeeter et al. (2022). The Kljun et al. (2015) footprint model was used to estimate the source area of the half-hourly fluxes. Flux footprints were overlaid on a high-resolution (2 m) landscape classification created using drone imagery to estimate the source area fractions of polygon rims (F_{Rim}) and polygon centers (F_{Cntr}) for each observation.

Climate data were logged on a CR1000 datalogger (CSI) every 1 second and averages/totals were stored at 5-minute intervals. Net all-wave radiation (R_n ; NRRLite net radiometer, Kipp & Zonen, Delft, The Netherlands) and photosynthetic photon flux density were measured at 3 m (PPFD; SQ-110 quantum sensor, Apogee Instruments, Logan, UT, USA), and air temperature (T_a) and humidity were measured (HMP35, CSI) at 2 m a.g.l. These instruments were installed on the same tripod as the EC system. A tipping bucket rain gauge (R.M Young Company, Travers City, MI, USA) was mounted 2 m south of the tripod at 0.4 m a.g.l.

Soil temperature, soil moisture, and water table depth data were recorded at 30-minute intervals on CR10x dataloggers (CSI) at automatic soil stations near the tripod: one in a polygon center and one on a polygon rim. Soil temperatures were recorded at depths of 5 and 15 cm depth in both the polygon center and rim (T_{Cnt5} , T_{Cnt15} , T_{Rim5} , and T_{Rim15}) with custom made type-T thermocouples. Water table depth (W_{td}) was sampled with a PLS probe (CSI) in the polygon center. The climate and soil data were collected continuously over the 2017 field season and there were no missing data in the climate record. Thaw depth (TD) was measured in polygon centers (10 replications) during five site visits by inserting a graduated steel probe into the ground to point of refusal. Linear interpolation was used to estimate TD between observations. In addition to the variables discussed above, one-hot-coded variable (*daytime*) dictating if the sun was above/below the horizon; mean sun angle $>-0.5^{\circ}$ during an observation period, was calculated following equations presented in Meeus, (1991).

Skeeter et al. (2022) used neural network (NN) models to identify and map the functional relationships governing C fluxes at Fish Island. They identified eight key drivers of half-hourly F_{CO_2} and estimated the relative influence (RI) of each driver over F_{CO_2} (Table 4.1). They used these relationships to gap fill F_{CO_2} in order to estimate NEE over the 2017 field season. Here, NEE = ER – GPP, where GPP (Gross Primary Productivity) is the total photosynthetic uptake of CO₂ by plants and ER is Ecosystem Respiration. GPP and ER are always positive; negative NEE indicates net CO₂ uptake by the ecosystem and positive NEE indicates net CO₂ emission. Photon flux density (RI = 64%) was the primary driver of NEE as it controls GPP, which was also modulated by VPD. Soil temperature mainly controlled ER and TD mapped seasonality in the model.

Skeeter et al. (2022) also identified eight drivers of F_{CH4} (Table 4.2). These relationships were used to gap fill F_{CH4} in order to estimate NME over the 2017 field season. Here, NME is the difference between methanogenesis (production of CH₄) and methanotrophy (consumption of CH₄) by microbes in the soil. Negative NME indicates net CH₄ uptake by the ecosystem and positive NME indicates net CH₄ emission. The relationships governing F_{CH4} were complex; TD mapped seasonality in the model, U and u_* influenced the rate of CH₄ transport, and the remaining parameters influenced both CH₄ methanogenesis and methanotrophy.

In this study, we are working with hourly resolution AWS and reanalysis data. To match the resolution of those data, hourly averages of the drivers listed in Tables 4.1 and 4.2 (excluding T_D , F_{Ccnt} and F_{Rim}) along with hourly averages of T_a and dewpoint (T_{dew}) and total hourly rainfall ($Rain$) were calculated. These hourly averages are henceforth referred to as the field season observations (FSO). Additionally, the FSO dataset included hourly averages of F_{CO2} and F_{CH4} , but hours with missing flux observations were excluded. Hourly flux averages were used to help validate upscaled flux estimates (discussed in section 4.2.4.1).

Table 4.1. Key drivers of CO₂ fluxes identified by Skeeter et al. (2022) ranked by their relative influence (RI) in the NN model ensemble, determined using the weights method (Gevrey et al. 2003). Corresponds to Table 3.2 in Chapter 3

Factor	Symbol	RI
Photon Flux Density	$PPFD$	64%
Vapour Pressure Deficit	VPD	8%
Soil Temperature 5cm, Polygon Centers	T_{Cnt5}	7%
Thaw Depth	TD	7%
Day / Night	$Daytime$	6%
Soil Temperature 5cm, Polygon Rims	T_{Rim5}	5%

Soil Temperature 15cm, Polygon Rims	T_{Rim15}	3%
Wind Speed	U	1%

Table 4.2. Key drivers of CH₄ fluxes identified by Skeeter et al. (2022) ranked by their relative influence (RI) in the NN model ensemble, determined using the weights method (Gevrey et al. 2003). Corresponds to Table 3.3 in Chapter 3

Factor	Symbol	RI
Net Radiation	R_n	34%
Friction Velocity	u_*	20%
Wind Speed	U	17%
Thaw Depth	TD	12%
Soil Temperature 15cm, Polygon Center	T_{Cnt15}	6%
Water Table Depth	W_{TD}	5%
Rim Fraction	F_{Rim}	4%
Center Fraction	F_{Ply}	2%

4.2.1.2 Landscape Classification Map

A Normalized Difference Vegetation Index (NDVI) based landscape classification map was created for Fish Island to assess the representativeness of the data from the 2017 field season. Maximum annual NDVI values were calculated from LANDSAT8 Level 1 TOA data (bands 4 & 5) to create an annual greenest pixel (GP) composite image. The 15 m resolution GP composite was created using Google Earth Engine (Gorelick et al. 2017). The LANDSAT8 data are available from 2014 onwards so the GP composite had eight bands (2014 – 2021). For each year, every LANDSAT8 image covering any portion of the BLDP between DOY 196 and DOY

227 was obtained and filtered for cloud cover (<20%). The maximum NDVI value for each pixel was then calculated for each year and added to the composite image.

A landscape classification map of Fish Island was created using a random forest (RF) regression model (Figure 4.2a). A set of training areas were created to represent three classes: 1) Low-Center Polygons, 2) shrub tundra and 3) open water. For class 1, the 90% contour of the flux footprint served as the training area (6.5 ha). For class 2 and 3, training areas were manually outlined over representative locations on Fish Island, referencing a 1 m resolution ESRI Worldview satellite base map in ArcGIS pro (6.9 and 6.8 ha, respectively). The shrub tundra class is characterized by greener vegetation that is clearly distinguished on satellite imagery. For the open water class, a set of training polygons were drawn covering the rivers and lakes in the area visible on satellite imagery. The RF model was trained on 67% of the pixels in each training area, the remaining 33% were used to generate a confusion matrix and calculate a prediction accuracy (fraction of pixels correctly classified) to evaluate the landscape classification performance.

The prediction accuracy of the RF classification was 96%. The classification map shows that Fish Island is approximately 53% LCP (10.1 km^2), 42% shrub tundra (8.1 km^2) and 5% open water (0.9 km^2). To provide further validation, a K means cluster analysis was run with 6 classes (not shown). The K means analysis split the water and shrub tundra areas into multiple classes while identifying one contiguous area (10.4 km^2) that was closely aligned with the LCP class delineated by the RF classification. Given this, we feel the fluxes observed at the EC station can generally be considered representative of the broader LCP ecosystem at Fish Island.

Fish Island Landscape Classification

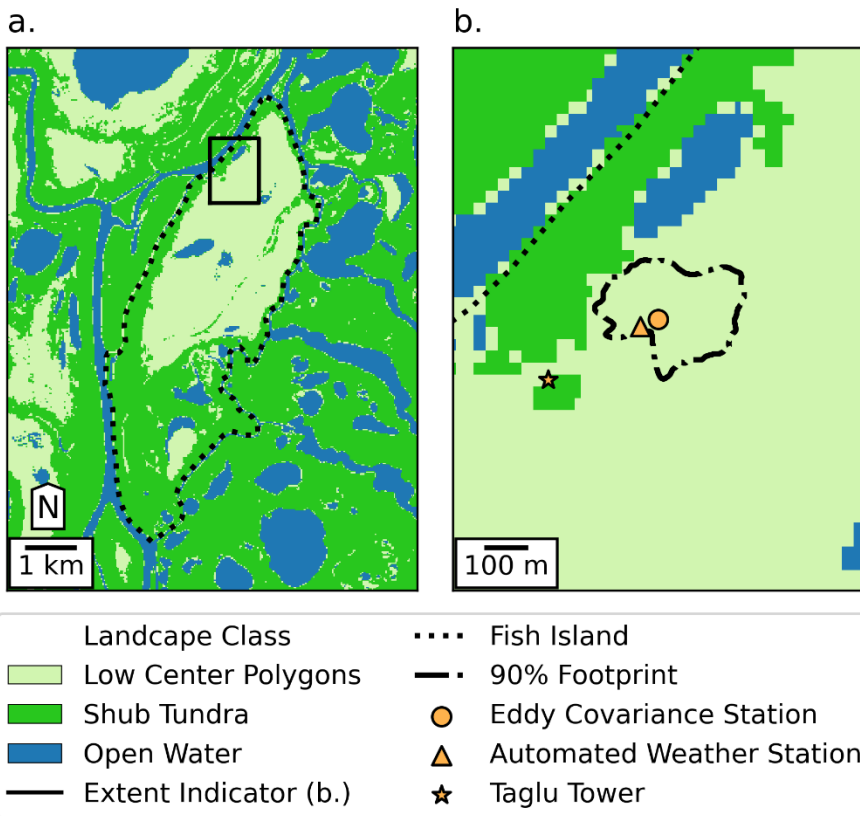


Figure 4.2. a. The landscape classification map for Fish Island showing the distribution of Low-Center Polygons, shrub tundra and open water areas. b. The boundaries of Fish Island and the 90% contour of the cumulative flux footprint from Skeeter et al. (2022) are shown along with the location of the eddy covariance station and the automated weather station.

4.2.2 Data Sources

In this study, we created a Flux Driver Time Series (FDTs), consisting of estimated mean hourly values of the variables listed in Tables 4.1 and 4.2. The FDTs spans 2009 to 2019 and was used to investigate interannual variability of flux drivers in the LCP ecosystem at Fish Island. The data were also used as inputs for the NN models from Skeeter et al. (2022) to estimate temporally upscaled NEE and NME over each snow-free season from 2009 to 2019. The FDTs was based on in-situ observations from an Automated Weather Station (AWS). The AWS only recorded a limited set of variables so ERA5-Land reanalysis data were used to help

estimate some variables (see Section 4.2.3). The ERA-5 reanalysis data, along with MODIS data and some auxiliary datasets were also used to investigate the seasonality of flooding and snow cover over a longer time period, from 2000 and 2020, to provide additional context to the FDTS and upscaled estimates.

4.2.2.1 Automated Weather Station

In August 2008 an AWS was installed at Fish Island ($69^{\circ} 22' 19.67''$ N, $134^{\circ} 52' 55.93''$ W), operated by the NWT Water Resources Department. The AWS recorded hourly data on a CR1000 data logger equipped with a CFM100-XT data module (Campbell Scientific Inc, Logan, UT, USA; CSI). The AWS measured wind speed (U) and direction (Dir) at 2.9 m with a 05103AP-10-L Wind Monitor (RM Young, Traverse City, MI, USA), air temperature (T_a) at 2 m with a 44212 Temperature Thermilinear Probe (CSI), incoming and outgoing longwave (LW) and shortwave (SW) radiation at 1.55 m with a CNR2 4-component net radiometer (Kipp & Zonen, Delft, NL). On August 21st, 2009 an unheated TE525M Tipping Bucket (Texas Electronics, Dallas, TX, USA) was installed to measure rainfall ($Rain$). No sub-surface data are available for the AWS. Data were obtained through personal communications with the NWT Department of Environment and Natural Resources.

The EC station was located 47.2 m northeast of the AWS in 2017. Observations from the two stations were in strong agreement over this period (Table 4.3). Coverage for most AWS variables were good over the full period of record (August 28th 2008 – August 11th 2020). Rainfall is missing until August 21st 2009 and during periods of snowfall. Between October and April, 2% of U observations are missing. All other data are nearly complete over the full period of record. There were two data gaps for site maintenance: a 23-hour gap July 26-27th, 2016 and a two-hour gap July 23rd, 2014. Data gaps of two-hour or less were filled with linear

interpolation. Longer gaps were filled using the average of corresponding hourly values for the day before and after the gap.

Table 4.3. The slope (m), intercept (b), coefficient of determination (r^2), and root mean squared error (RMSE) for the regression line: $Y=m X + b$, where Y are field season observations (FSO) from the EC station and X are the hourly AWS observations during the 2017 field season. These regression parameters were used to scale AWS observations for inclusion in the FDTs (see section 4.2.3.1).

FSO Variable	AWS Variable	Slope	Intercept	r^2	RMSE
T_a	T_a	0.99	0.02	0.99	0.54 K
R_n	R_n	0.98	14.84	0.98	$25.7 \text{ W m}^{-2} \text{ s}^{-1}$
$PPFD^*$	SW	2.39	0	0.99	$38.8 \mu\text{mol m}^{-2} \text{ s}^{-1}$
u_*^*	U	0.94	0.22	0.94	0.42 m s^{-1}

* For PPFD, b was fixed to zero, since the AWS data included net SW, not incoming SW. **For U, the regression line was calculated using only precipitation free hours.

4.2.2.2 ERA5 Reanalysis

One-hour resolution ERA5-Land reanalysis data produced by the European Center for Medium-Range Weather Forecasting (ECMWF) were used to complement the AWS data (Muñoz 2019). The ERA5 data were obtained at 11 km grid resolution from Google Earth Engine. Fish Island was covered by parts of three grid cells, so the spatially weighted mean of each hourly value was calculated over Fish Island. The data included estimates of T_a and dewpoint (T_{dew}) at 2 m, fractional snow cover (SC%), and estimates of T_s and volumetric water content (θ_w) at three depth levels: 1 (0-7 cm), 2 (7-28 cm), and 3 (28-100 cm). The ERA5 data covered January 1st 2000 to December 31st 2020.

The reanalysis estimates of T_a during the 2017 field season were in strong agreement with FSO T_a ($r^2 = 0.90$; RMSE 1.52 K) and with AWS T_a over the full period of record ($r^2 = 0.96$;

RMSE 2.95 K). Given the strong fit with AWS T_a , a simple linear regression model ($r^2 = 0.97$, RMSE = 2.73 K) was used to scale the ERA5 T_a to AWS T_a so it could yield a better approximation of long-term air temperatures at Fish Island for the dates outside the AWS period of record. The ERA5 estimate of T_{dew} was in moderate agreement with FSO T_{dew} ($r^2 = 0.71$; RMSE 1.66 K) and the reanalysis appears underestimates the maritime influences at Fish Island (Fig 4.3a). For example, when winds were off the ocean from the northwest (315° to 360°) T_{dew} estimates were much less accurate ($r^2 = 0.33$; RMSE 2.16 K) compared to when winds were from the southeast (135° to 180°) with no maritime influence ($r^2 = 0.86$; RMSE 1.19 K).

The ERA5 sub-surface data (T_s and θ_w) are integrated over depth levels and are not directly comparable to observations from the soil stations in 2017. The ERA5 T_s estimates at levels one and two were moderately correlated with FSO T_{Rim5} and T_{Cnt5} respectively but ERA5 tended to over/under estimate the daily maximum/minimums. Polygon rims are elevated and drier than polygon centers, which explains why T_{Rim5} had a better association with ERA5 T_s . The relationships with hourly FSO temperatures at 15 cm were weak for ERA5 T_s estimates at all levels, but did improve when averaged daily (not shown). ERA5 estimated θ_w values at both levels were well correlated with W_{TD} .

Table 4.4. A correlation matrix (Pearson r) showing the association between FSO drivers (rows) and ERA5 reanalysis estimates (columns).

		Field Season Observations				
		T_{Rim5}	T_{Cnt5}	T_{Rim5}	T_{Rim15}	W_{TD}
ERA5 Estimates	T_s (Level 1)	0.86	0.65	-0.15	-0.11	-0.66
	T_s (Level 2)	0.75	0.82	0.29	0.30	-0.85
	T_s (Level 3)	0.36	0.56	0.56	0.60	-0.53

	θ_w (Level 1)	-0.48	-0.47	0.08	0.08	0.90
	θ_w (Level 2)	-0.51	-0.52	-0.01	0.00	0.92

4.2.2.3 Additional Data

Daily 500 m resolution Nadir Bidirectional Reflectance Distribution Function Adjusted Reflectance (NBAR) MODIS data were obtained using Google Earth Engine. The NBAR data product is a daily composite of surface reflectance covering every pixel of the global land surface; it is derived from an algorithm which models of the surface reflectivity using multi-date, multi-angular, cloud-free, atmospherically corrected, surface reflectance observations (Wanner et al. 1997; Lucht et al. 2000; Schaaf 2021). Daily NBAR data are modelled using observations from MODIS instruments on the Terra and Aqua satellites over a 16-day period, with the image date centered on the 9th day, weighted data as a function of quality, coverage, and distance (temporal) from the day of interest (Schaaf et al. 2002; Schaaf 2021). The NBAR data aims to minimize missing data due to cloud cover while providing representative estimates of reflectivity (Schaaf, 2021).

The NBAR data were spatially averaged across the LCP ecosystem at Fish Island (defined by the landscape classification map in Fig 4.2) and used to calculate daily NDVI (Bands 1 & 2), Normalized Difference Water Index (NDWI) (Bands 2 & 4), and Normalized Difference Snow Index (NDSI) (Bands 4 & 6) for the periods between April 1st and October 31st, each year from 2000 to 2020. The NBAR data had good coverage, but there are missing data in September (4%) and October (25%) due to cloudy conditions and low light levels. These data gaps were filled with linear interpolation. The MODIS derived NDSI values (excluding gaps) were well correlated with ERA5 SC% ($r^2 = 0.83$).

A second MODIS data product, 500 m resolution, cumulative 8-day Gross Primary Productivity (GPP) estimates were also obtained using Google Earth Engine (Running et al. 2015). The GPP estimates are based on a radiation used efficiency model: $GPP = \varepsilon * APAR$, where APAR is absorbed photosynthetically active radiation (APAR) and $\varepsilon = \varepsilon_{max} * T_{min,scalar} * VPD_{scalar}$ (Running and Zhao. 2019). Here, ε_{max} is a maximum radiation use efficiency conversion parameter and $T_{min,scalar}$ and VPD_{scalar} are T_a and VPD scaling functions; where values of T_a and VPD are derived from GEOS-5 reanalysis estimates (Rienecker et al. 2008; Running and Zhao. 2019). The ε_{max} parameter and two scaling functions are biome specific, drawn from a lookup table based on a 16-class global landscape classification scheme, which does not distinguish between Arctic wetlands and temperate or tropical wetlands (Friedl and Sulla-Menashe 2019; Running and Zhao. 2019).

Running and Zhao (2019) estimate APAR from remotely sensed observations of the fraction of photosynthetically active radiation (FPAR) absorbed, where: $FPAR = APAR/IPAR \approx NDVI$. Here, IPAR is incident photosynthetically active radiation and which is derived from GEOS-5 reanalysis estimates and FPAR is derived from MODIS instruments on the Terra and Aqua satellites (Rienecker et al. 2008; Myneni et al. 2015; Running et al. 2015; Running and Zhao. 2019). While GPP is estimated daily, only 8-day summations are publicly available. The GPP estimates were downloaded for the same time period as the NBAR data and were also spatially averaged across the LCP ecosystem at Fish Island.

Two other datasets were incorporated for additional context. Hydrometric data were available from 2008 to 2017 for Kuluarpak Channel (9 years) and Big Lake (7 years) gauge stations 8 km and 4 km northwest of Fish Island, respectively (Environment and Climate Change Canada, 2022). These data were used to help determine when the spring freshet occurred.

Finally, we obtained maximum annual TD data from Lousey Point and Reindeer Depot, two Circumpolar Active Layer Monitoring network sites (CALM, 2022). Lousey Point is an upland site on Richard's Island, 22 km east of Fish Island and Reindeer Depot is a forested site in the delta 86 km south of Fish Island. The TD data included values from 2000 to 2017. Both CALM stations had thicker active layers than Fish Island, but the data were useful to provide an independent assessment of our estimate of TD in the FDTs. The location of the gauge stations and CALM sites relative to the EC station are shown in Figure 4.1.

4.2.3 Creating the Flux Driver Time Series

There were 14 variables included in the FDTs, eight drivers of NEE and six drivers of NME, with two (TD and U) driving both NEE and NME. The *Daytime* parameter was calculated as described in section 4.2.1, but averaged hourly to match the resolution of the FDTs. All other drivers required different approaches for estimation. For the purpose of creating the FDTs, these drivers are grouped into four categories: five atmospheric drivers ($PPFD$, R_n , VPD , U , and u_*), five soil drivers (T_{Cn5} , T_{Rim5} , T_{Cn15} , T_{Rim15} , and W_{TD}), one seasonal driver (T_D), and two source area drivers (F_{Rim} and F_{Rim}).

4.2.3.1 Atmospheric Drivers

Two atmospheric drivers (U and R_N) were directly measured by the AWS. These values were scaled using the regression parameters listed in Table 4.3. While AWS U and R_N were highly correlated with FSO U and R_N , the NN models were finely tuned to the observations from the EC station and a consistent bias in AWS inputs will induce significant error in the estimates. This is especially important for R_N as it is the primary driver of NME. After scaling the AWS data to the FSO data, we can assume the residuals are randomly distributed and will not induce

significant bias in the upscaled flux estimates. Since *PPFD* is almost linearly related to *SW*, it was also estimated using the regression parameters in Table 4.3.

Friction velocity (u_*) is strongly dependent upon U , but varies depending on turbulence conditions and changing surface roughness. Skeeter et al (2022) found that a complex relationship existed between U and u_* where higher u_* at a given U increased CH₄ fluxes. They hypothesized this relationship was indicative of pressure pumping, which operates over short timescales (Mohr et al., 2016; Laemmel et al., 2017; Skeeter et al. 2022). Investigating the influence of pressure pumping is beyond the scope of this analysis. However, given the high weights on both U and u_* in the NN model (Table 4.2), a reasonable approximation of u_* is essential for estimating NME. Based on the 2017 field data, the ratio of u_* to U decreased with increasing wind speed so a linear model would overestimate u_* at high U and result in overestimated NME. Further, during daytime u_* was generally higher at any given wind speed than at night and residuals of a linear fit between u_* and U showed weak correlations with sensible heat fluxes. To account for these issues, an exponential regression function was used to estimate u_* :

$$u_* = a U^b + c R_N \quad \text{EQ4.1}$$

This equation was fit to half hourly observations from the 2017 field season (not the hourly FSO), using only precipitation-free observation periods. K-fold (K=30) cross validation was used to help prevent overfitting. Using EQ4.1 provided a reasonable approximation ($r^2 = 0.92$, RMSE = 0.039 m s⁻¹); the coefficients were $a = 0.082$ m s⁻¹, $b = 0.96$ m s⁻¹, and $c = 6 \times 10^{-5}$ m³J⁻¹. The exponent b helped prevent overestimation of u_* during high wind events and small value of c slightly increased/decreased u_* depending on radiation levels. Hourly u_* values were

then we calculated for the FDTs using these coefficients and the scaled estimates of U and R_N discussed above.

Estimating the last atmospheric driver (*VPD*) required ERA5 data because the AWS did not observe humidity. First, ERA5 T_{dew} was scaled to FSO T_{dew} with Ordinary Least Squares (OLS) regression. Seven factors were incorporated in the model, including ERA5 T_{dew} and T_a , along with AWS T_a , SW , LW , and the v component (north/south) and u component (north/south) wind vectors. K-fold (K=30) cross validation was used to help prevent overfitting, and all inputs were z-score normalized before training so the OLS coefficients could be ranked on the same scale. Any scaled estimates of T_{dew} where $T_{dew} > \text{AWS } T_a$, were fixed to AWS T_a ; this amounted to 17% of all hourly estimates from June – September, ranging from 4.6% in July to 28.9% in September. The model provided a reasonable estimation of T_{dew} ($r^2 = 0.88$, RMSE = 1.03 K); the z-normalized OLS coefficients and scaled T_{dew} estimates are shown in Figure 4.3b. and 4.3c. respectively. Finally, the Clausius-Clapeyron equation was used to calculate *VPD* from FSO scaled T_{dew} and AWS T_a . The AWS T_a did not require scaling, because it had a very strong fit ($r^2 = 0.99$) and minimal bias compared to FSO T_a . The final *VPD* estimate ($r^2 = 0.89$, RMSE = 116 hPa) generally provided a good approximation compared to FSO VPD (Fig 4.3 d).

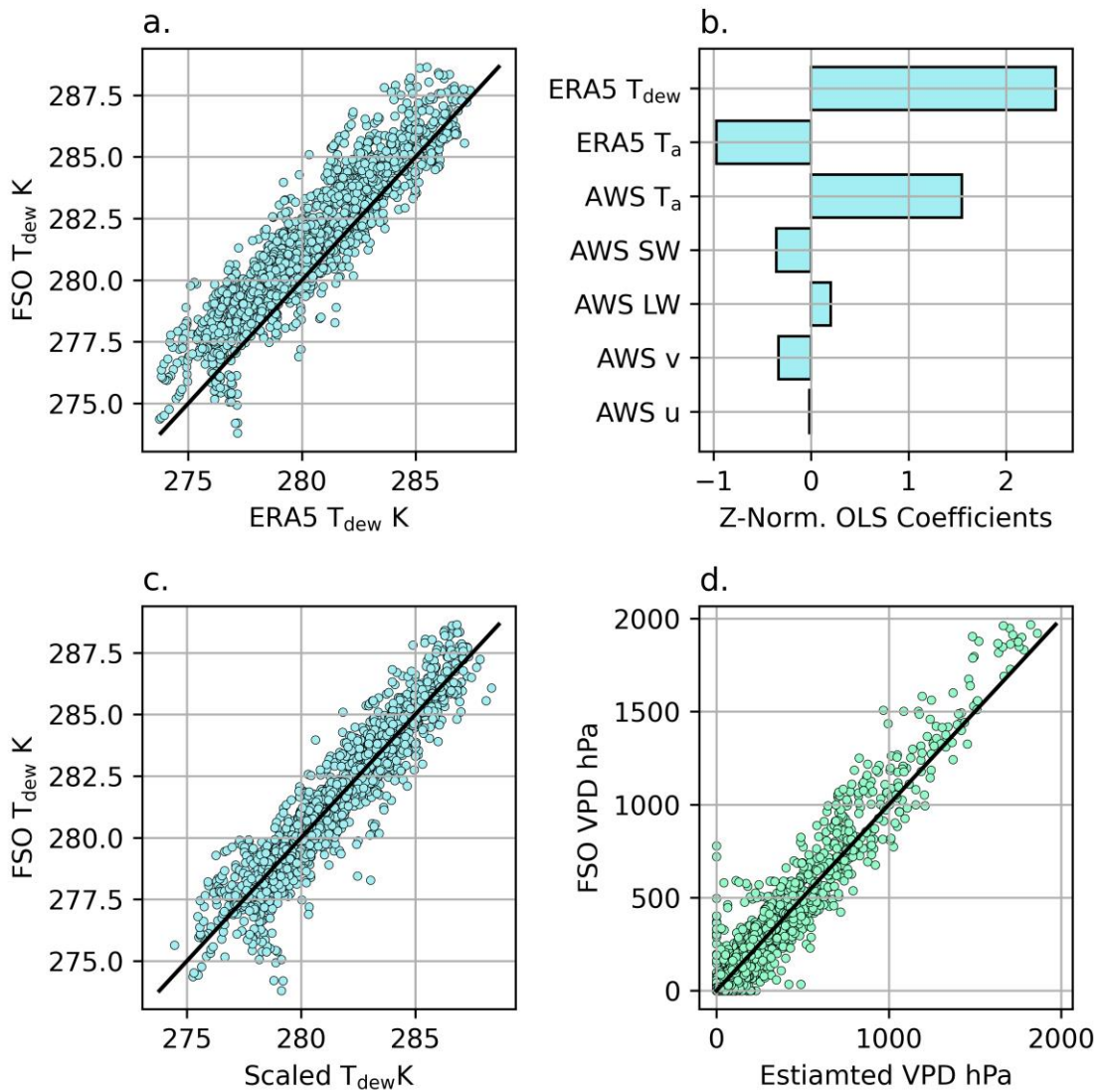


Figure 4.3 A comparison of observed T_{dew} from the 2017 field season (FSO) and ERA5 estimated T_{dew} is shown in (a.) The relative weights of the OLS model used to scale ERA5 T_{dew} to FSO T_{dew} are shown in (b.) and the resulting scaled estimates of T_{dew} are shown compared to FSO T_{dew} in (c.). The final estimate of VPD is shown compared to FSO VPD in (d.). In a., c., and d. the black lines represent at 1:1 relationship.

4.2.3.2 Soil Drivers

Estimating the soil drivers required careful consideration because of the lack of in-situ sub-surface observations at the AWS. Ordinary Least Squares (OLS) regression models were trained on a large ($n=11$) set of inputs and used to select the optimal parameters for estimating

W_{TD} and the four T_s drivers (T_{Cnt5} , T_{Rim5} , T_{Cnt15} , and T_{Rim15}). K-fold (K = 30) cross validation was utilized to prevent overfitting and make this approach more rigorous. The 11 inputs included: the five ERA5 sub-surface variables: T_s at levels 1, 2, and 3 and θ_w at levels 1 and 2; AWS observations of T_a , SW , and LW ; and time three-time lagged AWS T_a variables. For the time lagged T_a rolling averages were calculated over 6-hour, 12-hour, and 40-day intervals (~1/2 the duration of the 2017 field season). All 11 inputs were z-score normalized so the OLS coefficients could be ranked on the same scale (Table 4.5). The final values for each soil driver in the FDTs were taken as the average output of the k-fold OLS models.

Table 4.5. The relative weight of each of the 11 inputs for the k-fold OLS models used to estimate each soil driver. Inputs from ERA5 data are shown in blue, inputs from the AWS hourly data in orange, and time averaged AWS inputs are shown in yellow. Validation statistics: coefficient of determination (r^2) and root mean square error (RMSE) values are shown in grey.

	T_{Cnt5}	T_{Rim5}	T_{Cnt15}	T_{Rim15}	W_{TD}
r^2	0.91	0.89	0.92	0.9	0.95
RMSE	0.72 K	1.12 K	0.92 K	0.90 K	0.01 m
T_s (level 1)	4%	11%	5%	3%	1%
T_s (level 2)	12%	7%	19%	18%	10%
T_s (level 3)	5%	0%	2%	2%	12%
θ_w (level 1)	1%	4%	4%	2%	20%
θ_w (level 2)	2%	0%	5%	7%	25%
SW	5%	7%	14%	8%	2%
LW	1%	6%	0%	5%	4%
T_a	20%	22%	18%	21%	1%
Mean T_a 6 hr	36%	36%	23%	21%	2%

Mean T_a 12 hr	5%	8%	1%	3%	3%
Mean T_a 40 d	9%	0%	8%	10%	19%

4.2.3.3 Seasonal Driver

Thaw depth (TD) mapped seasonality of both NEE and NME at Fish Island. This parameter was only observed on five site visits (10 repetitions per visit) during the 2017 field season. Because of the limited number of samples, TD was difficult to model. Over the 2017 field season, TD increased almost linearly by day of the year (DOY) (Fig 4.4). However, a linear fit overestimates TD outside those dates and could not be applied to other years. Our aim was to generate a physically meaningful estimate of TD informed by seasonality of the spring freshet, snowmelt, and freeze up.

First, we looked at the seasonality of flooding at Fish Island by plotting the hydrometric data Kuluarpak Channel and Big Lake (not shown). Water levels decreased rapidly with ice break up after the flood crested at Kuluarpak Channel and more gradually at Big Lake. The crest of the flood was manually identified for both gauge stations and the hydrometric data were compared with the NDWI data. Gauge heights at Kuluarpak Channel during May and June were correlated with NDWI values (Pearson $r = 0.88$, $p < 0.001$), but there was no significant association for Big Lake. When $NDWI > 0$, it indicates possible flooding (McFeeters, 1996). Days with $NDWI > 0.0$ and $NDWI > 0.15$, were flagged for possible and probable flooding, respectively. The last DOY each spring with $NDWI > 0$ was generally well associated with the crest of the flood at Kuluarpak Channel (Spearman $\rho = 0.87$, $p < 0.01$) and Big Lake (Spearman $\rho = 0.73$, $p = 0.06$).

Next, the seasonality of snow cover was investigated. MODIS data were used to identify the timing of snow melt ($\text{NDSI} < 0$) at Fish Island from 2000 to 2020. The NDWI and NDSI were highly correlated (Pearson $r = 0.97$, $p < 0.01$) and first DOY where $\text{NDSI} < 0$ and $\text{NDWI} < 0$ were also well correlated (Spearman $\rho = 0.95$, $p < 0.01$). The NDSI was not sensitive enough to identify when snowmelt starts nor is it sufficient for identifying when snowfall starts to accumulate every year because of frequent cloudy conditions and missing data in September and October. Plotting ERA5 SC% against NDSI (not shown) suggested ERA5 tended to estimate earlier snowmelt dates than were actually observed, but it more closely matches the NDSI data in September and October when data were available. The median ERA5 estimated SC% on the first day when $\text{NDSI} < 0$ was 0.04% and the median SC% on the first day in September or October with $\text{NDSI} > 0$ was 18.75%. These values were used as the basis for a daily snow cover classification (Table 4.6).

The CALM data for Lousey Point and Reindeer Depot showed moderate correlations with the number of snow free days and mean annual T_a . This supported using a metric based on T_a and snow conditions to estimate TD at Fish Island. Given the limited number of in-situ observations from 2017, a simple metric was needed to allow TD vary by year without overfitting a complex pattern. To achieve this, each DOY was assigned a thaw parameter t following a simple weighting scheme based on T_a and the snow cover classification (Table 4.6). Then, the 50 TD observations (5 days x 10 samples) from the 2017 field season were fit to an exponential regression model:

$$TD_{DOY} = a(\sum_{i=0}^{DOY} t_i)^b \quad \text{EQ.4.2}$$

which provided a strong fit with observed TD ($r^2 = 0.95$, RMSE = 0.02 m; $a = 0.03$ days, $b=0.67$). K-fold cross validation was used to prevent overfitting, but due to the limited sample

size only K=5 folds were used. Hourly TD for the FDTs were then linearly interpolated from daily values.

With the exponential function, TD increases rapidly with snowmelt and maximum TD is lower compared to a linear fit (Fig 4.4). Since EQ4.2 is monotonically increasing, TD remains fixed at its maximum value until the end of the year. In reality, the active layer refreezes from the top and bottom and a portion of the active layer remains thawed well into early winter (Natali et al. 2019). However, there is no reasonable way to incorporate these dynamics here and estimating C fluxes during early winter is beyond the scope of this analysis.

To see if these TD estimates were reasonable, maximum annual TD estimates for Fish Island were compare to the CALM data. For the 2009 to 2017 period, maximum TD at Lousey Point (Spearman $\rho = 0.90$ $p < 0.01$) and Reindeer Depot (Spearman $\rho = 0.82$ $p = 0.01$) were generally in good agreement with estimated maximum TD for the LCP ecosystem. Extending T_a estimates back to 2000 using ERA5 data (see section 4.2.2.2), estimated TD at Fish Island maintained statistically significant correlations with both Lousey Point (Spearman $\rho = 0.87$ $p < 0.01$) and Reindeer Depot (Spearman $\rho = 0.69$ $p < 0.01$).

To check for the plausibility of early season projections, estimates where $TD > 0$ in May and June were compared to mean daily soil driver estimates (W_{TD} , T_{Cn15} , and T_{Cn15}). Simple linear regression equations with TD as the Y and the soil drivers as the X variables respectively were calculated to identify the X intercept. The fit for W_{TD} ($r^2 = 0.83$) suggested the intercept of 0.087 m [$CI_{95\%} \pm 0.004$], i.e., the water table was typically estimated above the ground surface in polygon centers until TD drops below ~ 0.09 m. There was only one day (May 26th, 2010) where estimated W_{TD} was below the base of the active layer ($W_{TD} = -0.019$; $TD = 0.013$), for this day W_{TD} was fixed to TD . It was encouraging that this is the only implausible estimate of W_{TD} over

the full 2009 to 2019 period. The fit with T_{Cnt5} ($r^2 = 0.73$) suggested a disconnect at shallow thaw depths: when $T_{Cnt5} = 0$ °C, $TD = 0.142$ m [CI_{95%} ± 0.003]. The fit with T_{Cnt15} ($r^2 = 0.72$) shows the disparity was not persistent; when $T_{Cnt15} = 0$, $TD = 0.186$ m [CI_{95%} ± 0.002]. Given the simplicity of the thaw parameter and EQ4.2, these relationships are encouraging.

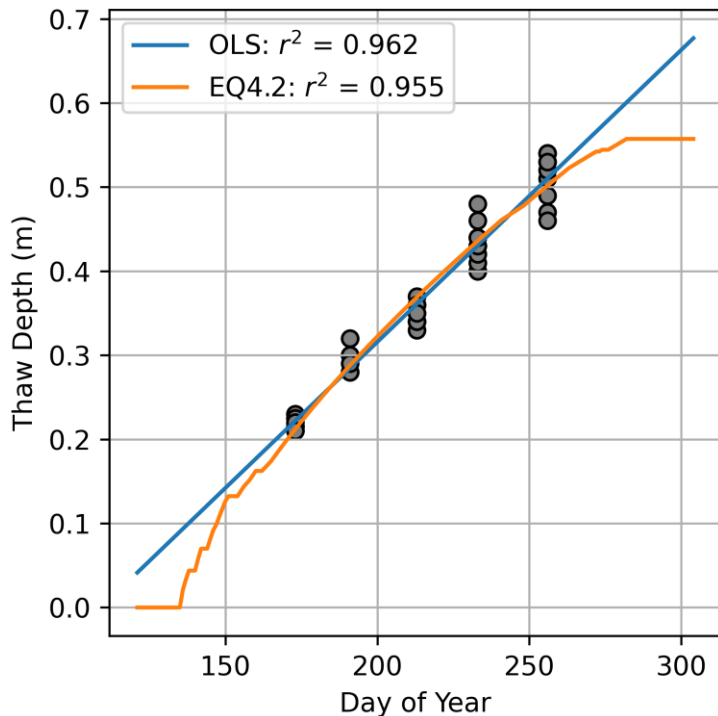


Figure 4.4. Estimation of daily thaw depth (TD) in 2017 using OLS regression as a function of the day of year (DOY), compared to estimating using EQ4.2. Grey circles represent the TD observations from the 2017 field season.

Table 4.6. The three criteria used to calculate the daily thaw parameter (t) and their respective multipliers, where the daily value is the product of the two snow-cover multipliers (s_1 and s_2) and a temperature multiplier (m_1): $t = s_1 s_2 m_1$.

Criteria		Multiplier
Mean Daily ERA5 Snow Cover %		s_1
SC% ≥ 95%	Snowpack	0
SC% ≥ 18.75; SC% < 95.0	Significant snow cover	0.25
SC% ≥ 0.04; SC% < 18.75	Patchy snow	0.375
SC% < 0.04	Snow-free	0.5

Daily MOIDS NDSI Value		s_2
$NDSI \geq 0$	Snow	1
$NDSI < 0$	Snow-free	2
Mean Daily AWS Air Temperature		m_1
$T_a < 0.5 \text{ } ^\circ\text{C}$	Not Thaw day	0
$T_a \geq 0.5 \text{ } ^\circ\text{C}$	Thaw day	1

4.2.3.4 Source Area Drivers

The two source area parameters (F_{Cnt} and F_{Rim}) were set to their relative areal fractions ($F_{Cnt} = 58.8\%$ and $F_{Rim} = 25.6\%$) determined from a high resolution (2m) landscape classification map created by Skeeter et al. (2022). This is slightly different than the median source area distribution ($F_{Cnt} = 62.8\%$ and $F_{Rim} = 23.4\%$) from the footprint climatology at the EC station in 2017 (Skeeter et al. 2017). The intention was to produce upscaled NME estimates that were more broadly representative of the LCP rather than fit to the specific geometry of the footprint climatology of the EC station.

4.2.4 Temporal Upscaling

The NN models consisted of ensembles of 30 different models (one ensemble for NEE and another for NME) trained on bootstrapped samples of the half hourly flux data from the 2017 field season. Here, we estimated hourly NEE and NME as the ensemble means for the respective fluxes. Confidence intervals were calculated using the ensemble variance (Skeeter et al. 2022). Once hourly NEE and NME were calculated, the hourly C balance was calculated as: $C = NEE + NME$, where NEE and NME are in g CO₂-C and g CH₄-C, respectively.

4.2.4.1 Seasonal Comparison

The functional relationships mapped by the NN models are based on observations during portions of the growing season and senescent period from only one year. The NN are capable of

projecting beyond conditions they were trained on, but care must be taken to ensure that conditions in the LCP ecosystem are not fundamentally different from what was observed during the 2017 field season (ie. significant snow cover or flooding). Estimates of NEE and NME in this study are restricted to the snow-free seasons from 2009 to 2019. The snow-free season started at the end of the spring flood/snowmelt period, on the first day each year with both NDWI < 0 & NDSI < 0. The snow-free season ended with the arrival of winter snowfall, which was defined as the first day in September with SC% > 18.75% or NDSI > 0. This definition approximately delineates the portion of the year without significant flooding or snow cover, while ignoring light snow accumulations during the growing season which subsequently melted. This allows us to extend beyond the dates measured by Skeeter et al (2022) while excluding time periods for which the functional relationships identified by the NN models of are clearly invalid.

Each snow-free season included a different number of observations/dates from each year, so it makes inter-annual comparison with some parameters (eg. PPFD) less meaningful. Therefore, a 96-day growing season was defined spanning [DOY 161 to 256; June 9th/10th – September 12th/13th] of each snow-free season from 2009 to 2019. This allowed for standardized comparisons between years. These dates are fully within the snow-free season each year and should be fully inclusive of the growing season and much of the senescent period. They include the complete 2017 field season and projections two weeks earlier than the first date measured in 2017. They also match the 8-day resolution of the MODIS GPP estimates, so they could be incorporated in the analysis. Dates falling outside the growing season are collectively referred as the shoulder seasons. The shoulder seasons are of different lengths each year and confidence in these projections was reduced, but fluxes were calculated over these periods to get a sense of how much growing season CO₂ uptake could be offset during these periods.

4.2.4.2 Flux Validation

Half-hourly NEE and NME estimated by Skeeter et al (2022) were used as benchmarks to evaluate the FDTs estimates. These model estimates were averaged hourly to match the resolution of the FDTs, and are denoted as NEE_B and NME_B , respectively. Validation statistics (r^2 and RMSE) were calculated to compare our estimates of NEE and NME to FSO F_{CO_2} and F_{CH_4} respectively. The same statistics were also calculated comparing NEE_B and NME_B to FSO F_{CO_2} and F_{CH_4} , respectively. Any decrease in model performance relative to the benchmarks are attributable inaccuracies in the FDTs. For NME, since source area ($F_{C_{nt}}$ and $F_{R_{im}}$) influenced the flux observations, we took a subset of the FDTs for 2017 and substituted hourly averages of $F_{C_{nt}}$ and $F_{R_{im}}$ calculated by Skeeter et al. (2022) for the $F_{C_{nt}}$ and $F_{R_{im}}$ values that were fixed in the FDTs and re-estimated NME for this subset of the FDTs. This allowed for a more direct comparison with the F_{CH_4} observations.

4.2.4.3 Flux Partitioning and Independent Assessment

The 8-day MODIS derived GPP estimates were used to provide an independent assessment of our CO₂ flux estimates beyond the 2017 field season. The MODIS derived GPP estimates cannot be considered representative of GPP at Fish Island because the biome specific parametrization scheme does not differentiate between Arctic wetlands and temperate/tropical wetlands (Friedl and Sulla-Menashe 2019; Running and Zhao. 2019). However, they can serve as a general comparison for our upscaled flux estimates and assist in gauging model performance between years. For this comparison, first we needed to estimate GPP; the NN model used to estimate NEE does not explicitly partition NEE into GPP and ER. Skeeter et al. (2022) showed the NN model can be used to estimate daytime ER by projecting NEE to “nighttime” conditions ($PPFD = 0$ and $Daytime = 0$). However, this approach did not perform well early in the 2017

season because nighttime observations were not available to constrain the model until DOY 205; projections of daytime ER at low TD yielded unrealistic values that did not agree with chamber ER observations (Skeeter et al. 2022).

We used this approach to estimate hourly daytime ER and then calculated hourly GPP for all daytime observations as $GPP = ER - NEE$. Hourly confidence intervals for GPP were calculated as the sum of the respective confidence intervals for the NEE and ER estimates. Hourly daytime GPP estimates were then summed by 8-day interval to match the resolution of the MODIS data. Validation statistics (r^2 and RMSE) were calculated to see how our 8-day GPP estimates compared to the MODIS derived GPP estimates. The comparison was limited to 8-day intervals with mean $TD > 0.3$ m to avoid unrealistic early-season ER projections.

4.3 Results

4.3.1 Climatology

4.3.1.1 Snow-free Seasons

The duration of each snow-free season estimated using MODIS and ERA5 data from 2000 to 2020 are shown in Figure 4.5. Theil-Sen slope suggests there may have been a slight increasing trend in the duration of the snow-free season (median slope = 0.83 days year⁻¹, CI_{95%} [0.0, 1.8]). The duration of the snow-free season had a moderate correlation with mean annual T_a ($r^2 = 0.44$) and mean T_a from 2000 to 2020 (ERA5 T_a scaled to the AWS T_a see section 4.2.2.2). The 2009 to 2019 period had slightly longer snow-free seasons (median 117 days) than the other 10 years (2000 - 2008 & 2020; median 112 days) and mean T_a from 2009 and 2019 (-8.2 °C) was warmer than the years outside this period (-9.9 °C).

The timing of the spring flood/snowmelt varied by 19 days over the 21-year MODIS record (range DOY 146 – DOY 165). The Theil-Sen slope suggests there were decreasing trends

in both the timing of snowmelt (first DOY with NDSI < 0; median slope = -0.4 days year⁻¹, CI_{95%} [-0.9, 0.0]) and the end of the spring freshet (first DOY with NDWI<0; median slope = -0.8 days year⁻¹, CI_{95%} [-1.3, -0.1]). The timing of winter snowfall was more variable (35 days) but the dates were not confirmed by satellite observations every year because they were inferred from ERA5 data for 10 out of the 11 years. We elected to use NDSI when available for a more conservative approach. The September/October MODIS data was insufficient for trend analysis, but the ERA5 data (first DOY with SC%>18.75) suggested a trend towards later dates for significant snowfall (median slope = 1.4 days year⁻¹, CI_{95%} [0.4, 2.8]).

It appears unlikely the LCP ecosystem experienced significant inundation most years. However, the NDWI data shows evidence of a probable spring flooding (NDWI > 0.15) in 2004 (1 day), 2009 (5 days) and 2020 (7 days). This would suggest a return interval for flooding was ~ 7 years, but more years of data and in-situ observations would be needed to validate this assertion. The DOY of the end of snowmelt (NDSI<0) and end of the flood (NDWI<0) were not significantly different (Mann-Whitney U, p=0.11), likely because the two metrics are highly correlated (Pearson r = 0.98, p < 0.01). However, snowmelt did lag behind by up to 15 days (2015), suggesting snowmelt was not controlled by flooding in every year.

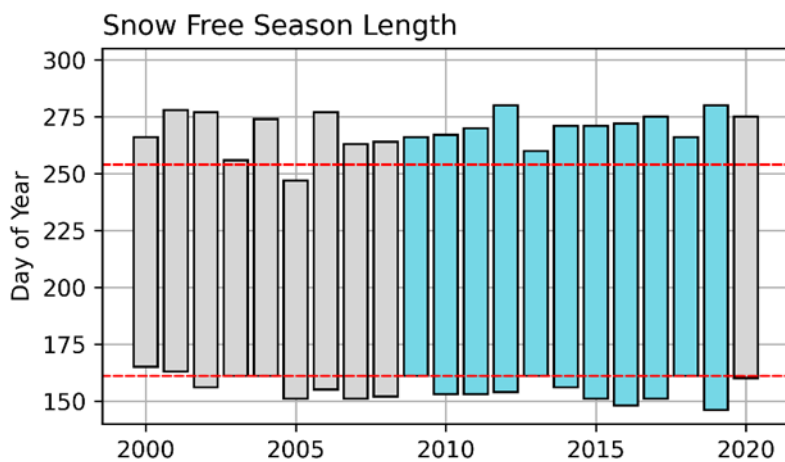


Figure 4.5. The duration of the snow-free period from 2000 to 2020. The snow-free seasons from 2009 to 2019, coinciding with the FDTs are highlighted in light blue. The horizontal red dashed lines demarcate the mid-season period DOY 161 to 256.

4.3.1.2 Flux Drivers

Radiative input (*PPFD*) varied drastically from day to day over the snow-free season, peaking around the summer solstice then decreasing gradually to low levels by the autumnal equinox (Fig 4.6a.). Over the 2009 to 2019 study period, radiative fluxes (R_N) were relatively consistent between most growing seasons, but 2015 was notably cloudier than other years (Fig 4.7a.). Daily T_a were typically above 0 °C between mid-May (DOY 136) and late-September (DOY 270) (Fig 4.6b). Mean growing season T_a was usually between 7 °C and 10.5 °C (Fig 4.7b). The year 2012 was a significant outlier with mean T_a of 12.5 °C, which is reflected in anomalously high VPD as well (Fig 4.7c). Soil temperatures at 5 cm were highly correlated with T_a ($r^2 = 0.8$) and they rose above 0 °C about 20 days after T_a during spring thaw but there was no substantial lag during freeze-up. At 15 cm depth, soil temperatures were less variable compared to 5 cm depth but followed a similar pattern. Thaw lagged behind T_a by about 35 days but freeze up was closely linked (Fig 4.6c). Mean growing season T_{Cntr15} were generally < 2.5 °C, with the exception of 2012 (Fig 4.7d).

Total growing season rainfall (2010 – 2019, *2009 is missing) was highly variable, from 47 mm in 2011 to 130 mm in 2015 (Fig 4.7e). Spring and early summer are dry at Fish Island while late summer receives considerably more precipitation. Average rainfall in June and August were 12 mm and 46 mm, respectively. Estimated W_{TD} reflected this pattern; the water table was near or above the surface during snowmelt, dropped rapidly as the active layer thawed, then slowly increased later in the season (Fig 4.6d). The year 2018 was an outlier with mean growing season $W_{TD} = -0.09$ m (Fig 4.7f). It was the coldest growing season ($T_a = 7.2$ °C),

second wettest (115 mm) and also had the shallowest maximum TD due to a cold spring and a late snowmelt (Fig 4.7g).

Mean hourly U over all growing seasons was 3.6 m s^{-1} (hourly $\sigma = 1.7$) and did not differ drastically between growing seasons. However, the number of days with high wind events (at least one hour with $U > +2 \sigma$) did (Fig 4.7h), ranging from 10 in 2009 to 23 in 2019. Maximum NDVI each growing season was between 0.63 in 2009 and 0.51 in 2019 (Fig 4.7i). There was a downward trend in NDVI over the study period (Theil-Sen slope $CI_{95\%} [-0.015, -0.003]$). Maximum NDVI values were negatively correlated with growing season rainfall (Spearman $\rho = -0.6$, $p < 0.01$) and W_{TD} (Spearman $\rho = -0.53$, $p < 0.01$) while it was positively correlated with mean growing season VPD (Spearman $\rho = 0.59$, $p < 0.01$).

Daily Conditions at Fish Island, May - October (2009-2019)

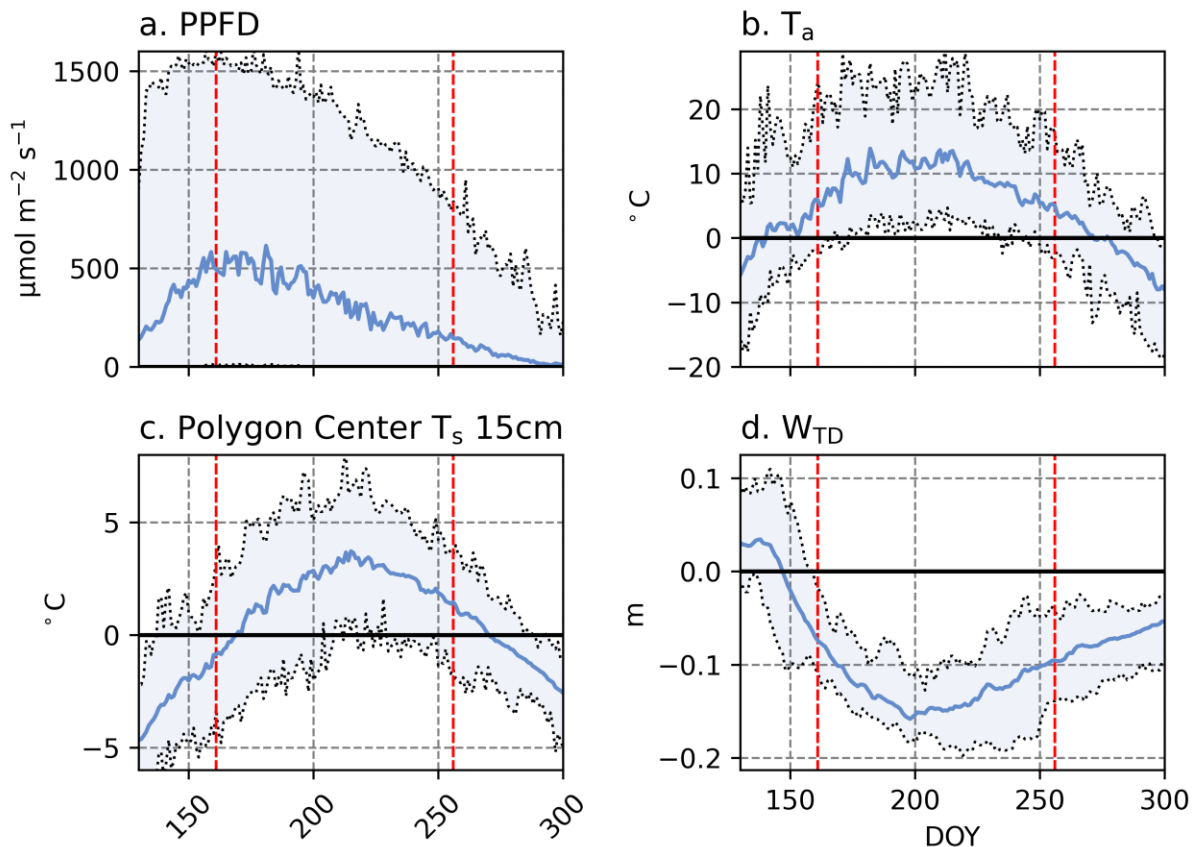


Figure 4.6. Observed daily Photosynthetic Photon Flux Density (a.), Air Temperature (b.), estimated soil temperatures in polygon centers at 15 cm (c.), and estimated water table depth in polygon centers (d.). The solid blue lines show the mean daily values averaged across the 11 study years (2009 to 2019) and the shaded areas bounded by the dashed black lines represent the daily ranges (max/min hourly values). The vertical red dashed lines demarcate the growing season period (DOY 161 – 256).

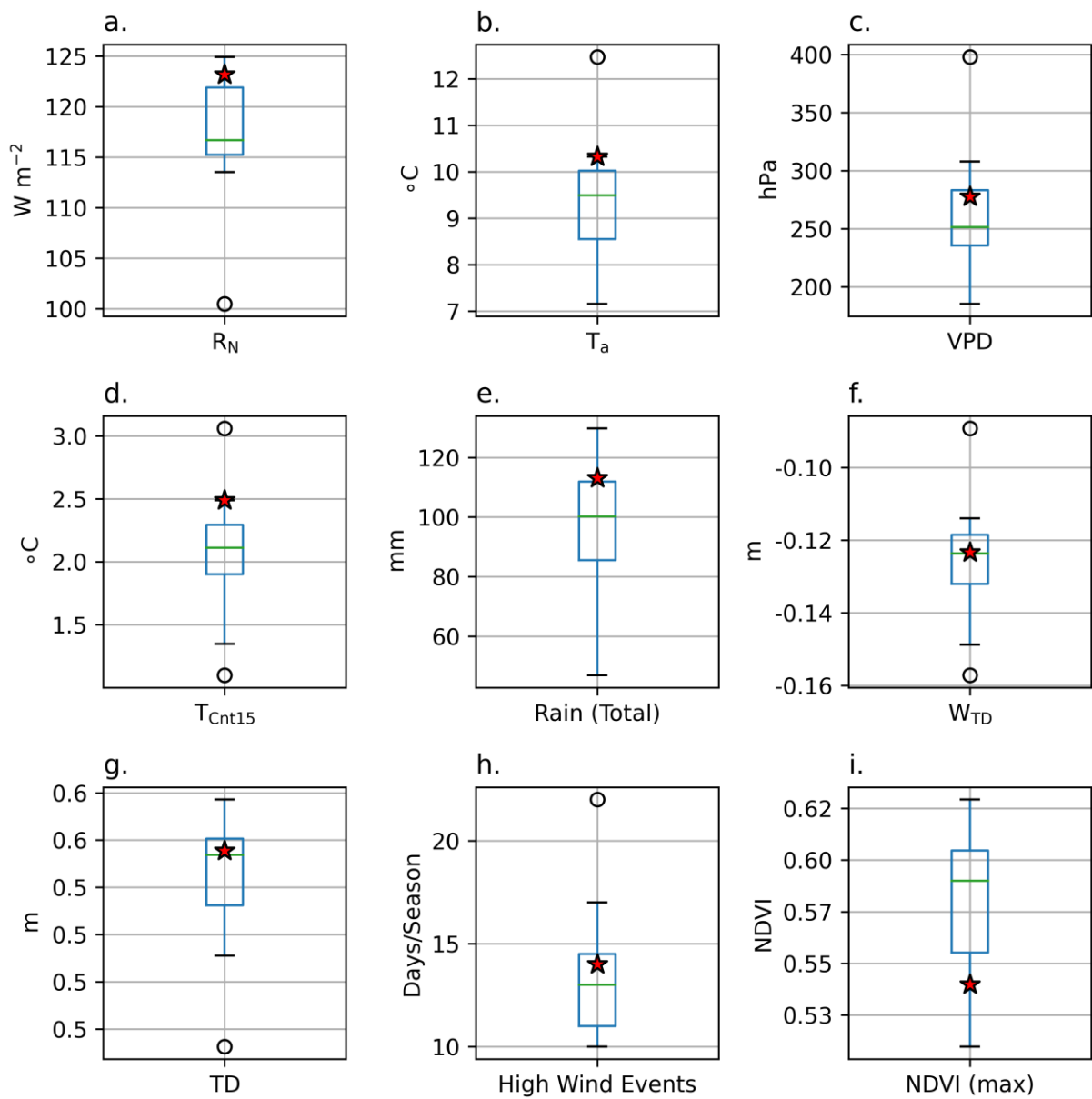


Figure 4.7. Boxplots of mean growing season net radiation (a.), air temperatures (b.), vapor pressure deficit (c.), and polygon center temperatures at 15 cm (d.). Total growing season precipitation (2009 is missing) is shown in (e.) and mean growing season W_{TD} is in (f.). Estimated maximum snow-free season TD is shown in (g.). The frequency of high wind events (Number of days per season with at least one hourly $U > 2\sigma$) per growing season is shown in (h.). Finally, maximum growing season NDVI is in (i.). The green lines represent the median, the boxes indicate the interquartile range ($Q_3 - Q_1$), the whiskers indicate $Q_1 - (1.5 \times \text{IQR})$ and $Q_3 + (1.5 \times \text{IQR})$, and the circles represent outliers extending beyond the whiskers. The star represents the mean value for the 2017, when eddy covariance measurements were operated.

4.3.2 Flux Estimates

4.3.2.1 Carbon Balance

Mean snow-free season C flux was estimated to be $-34.9 \text{ mg C m}^{-2} \text{ d}^{-1}$ [$\text{CI}_{95\%} \pm 48.9$]. This equates to a mean cumulative flux of $\text{CI}_{95\%} [-98, 17] \text{ g C m}^{-2}$ per snow-free season. During the growing season, the LCP ecosystem was estimated to be a consistent CO_2 sink, but the shoulder CO_2 season emission may have offset growing season CO_2 uptake in some years (Fig 4.8). The LCP ecosystem was estimated to be a consistent CH_4 source over the full snow-free season, but NME was a fairly small component of the LCP ecosystem's net-C balance. Methane emissions were estimated to offset 4.9% of growing season C uptake, and accounted for about 3.1% of net shoulder season C emissions respectively (Fig 4.8). It is unclear from this analysis whether the LCP ecosystem at Fish Island is a net C sink or source over the snow-free season.

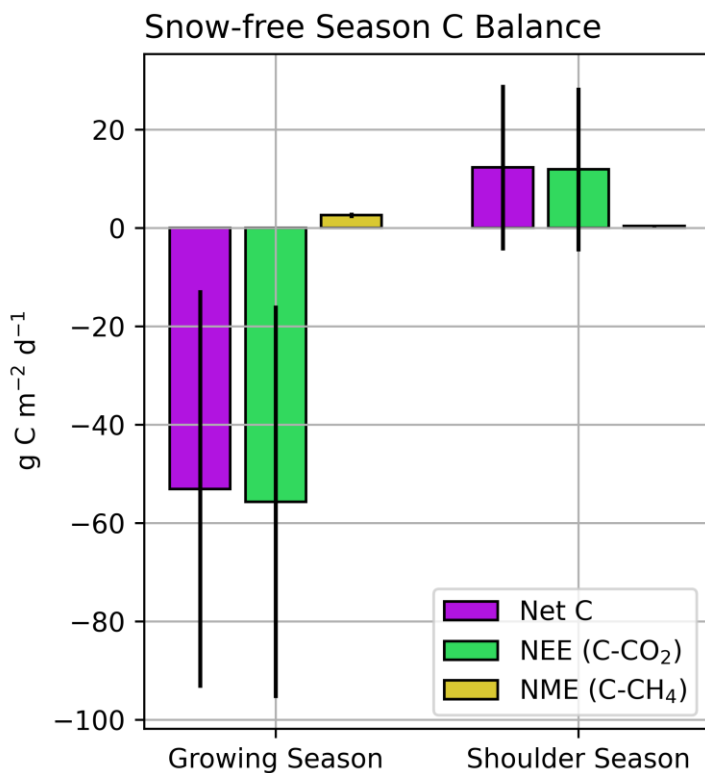


Figure 4.8. Modeled cumulative C fluxes (purple), separated into the growing season (DOY 161 - 256), and shoulder season (DOY < 161 + DOY > 256), averaged over the 2009 to 2019 period. The component fluxes Net Ecosystem Exchange (green) and Net Methane Exchange (gold) are also shown. The growing season is always defined as 96 days, but the shoulder seasons are of variable length, ranging from 4 to 39 days each year.

4.3.2.2 Flux Evaluation

Validation statistics comparing hourly estimates of NEE and NME derived from the FDTs to FSO F_{CO_2} and F_{CH_4} are shown in Table 4.7. Their respective benchmarks (NEE_B and NME_B), which were presented by Skeeter et al (2022) are also shown. Estimated NEE provided a strong fit ($r^2 = 0.92$) with F_{CO_2} while NME provided a reasonable fit as well fit ($r^2 = 0.74$) with F_{CH_4} . For NEE, the validations metrics show a slight increase in RMSE ($0.1 \mu\text{mol m}^{-2} \text{s}^{-1}$) relative to the benchmark NEE_B (Skeeter et al. 2022). However, mean NEE over the 2017 study season was still well within the margin of error (CI_{95%}) relative to NEE_B. The drop in performance was slightly more substantial for NME relative to the benchmark, RMSE increased by $1.1 \text{ nmol m}^{-2} \text{s}^{-1}$, but mean NME over the 2017 study season was still well within the margin of error for NME_B as well.

The NN and MODIS derived GPP estimates for the LCP ecosystem at Fish Island were generally in agreement (Fig 4.9). The RMSE was $0.57 \text{ g CO}_2\text{-C m}^{-2} \text{ d}^{-1}$ and the r^2 value was 0.68. Mean GPP estimated by the NN model (DOY 209 onwards) was $1.46 \text{ g CO}_2\text{-C m}^{-2}$ [CI_{95%} ± 0.95], while the MODIS derived GPP estimate for the same period was $1.37 \text{ g CO}_2\text{-C m}^{-2}$ [CI_{95%} ± 0.20]. On a yearly basis, the NN and MODIS estimated GPP compared reasonably well ($r^2 > 0.45$) most years, with the exceptions of notable outliers ($r^2 < 0$) in of 2009 and 2018. In 2009, there was a significant flood event while 2018 was the coldest year during the study period and had anomalously low TD estimates. In these two years our GPP estimates were significantly higher than the MODIS GPP estimates.

Table 4.7. Validation statistics (r^2 and RMSE) and along with mean NEE and NME over the 2017 study season (DOY 174 – DOY 256) estimated using the Flux Drive Time Series (FDTD). Validation statistics are provided the hourly benchmarks NEE_B and NME_B as well. *Hourly NME were calculated using observed source area fractions substituted for the fixed source area values. (Validation for the original half hourly estimates are shown in parenthesis Skeeter et al. 2022 for reference).

Estimate	r^2	RMSE	2017 Study Season Mean
FDTD Estimated NEE	0.92	$0.40 \mu\text{mol m}^{-2} \text{s}^{-1}$	$-0.61 \mu\text{mol m}^{-2} \text{s}^{-1}$ [CI _{95%} ± 0.28]
Skeeter et al. (2022)	0.96	$0.29 \mu\text{mol m}^{-2} \text{s}^{-1}$	$-0.59 \mu\text{mol m}^{-2} \text{s}^{-1}$ [CI _{95%} ± 0.29]
NEE_B	(0.95)	($0.33 \mu\text{mol m}^{-2} \text{s}^{-1}$)	
FDTD Estimated NME *	0.74	$5.6 \text{ nmol m}^{-2} \text{s}^{-1}$	$27.1 \text{ nmol m}^{-2} \text{s}^{-1}$ [CI _{95%} ± 3.9]
Skeeter et al. (2022)	0.83	$4.5 \text{ nmol m}^{-2} \text{s}^{-1}$	$27.5 \text{ nmol m}^{-2} \text{s}^{-1}$ [CI _{95%} ± 4.2]
NME_B	(0.75)	($5.6 \text{ nmol m}^{-2} \text{s}^{-1}$)	

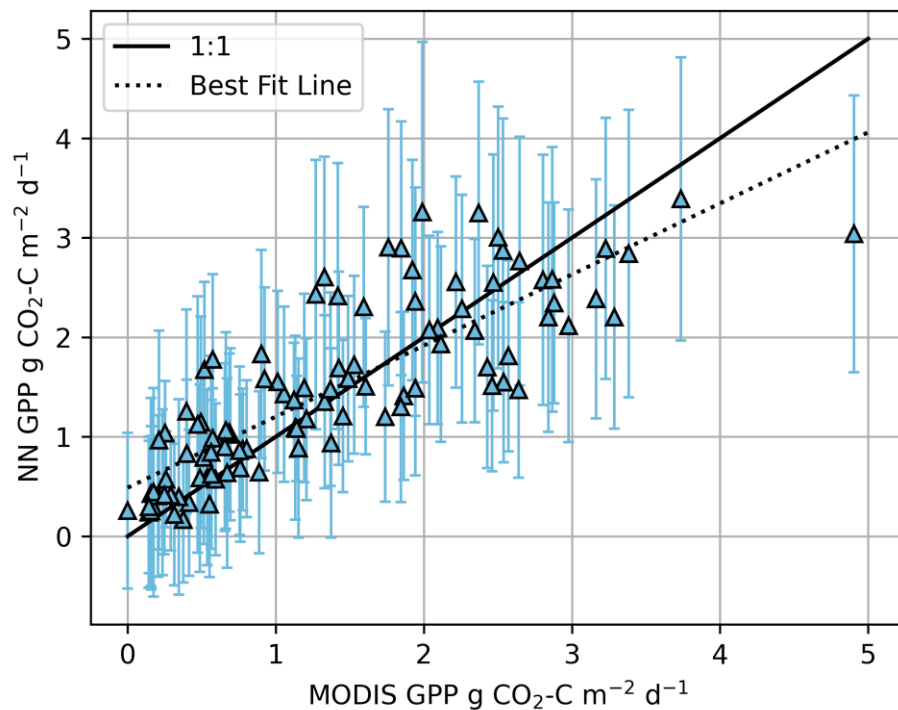


Figure 4.9. Comparison of our mean GPP estimates and MODIS derived GPP estimates. The black line represents a 1:1 relationship and the dashed line is the line of best. The error bars show the with 95% confidence intervals for NN estimated GPP.

4.3.3 Seasonal and Inter-Seasonal Variability

The LCP ecosystem quickly transitions from a net CO₂ source to a net sink in mid-June (Fig 4.10a). Daily NEE is consistently negative from around the summer solstice until mid-August. The transition back to a net CO₂ source is more gradual, and typically occurred by early-September. Modeled confidence intervals are widest in the early and late season, the magnitude of ER during these periods may be overestimated because we are projecting *TD* beyond the range the NN were trained on (see section 4.4.1). Table 4.8 shows correlations with key flux drivers during the growing season at various timescales. Hourly NEE was dictated by variability in *PPFD*, as it was the primary driver of *F_{CO₂}* (RI = 64%). At longer timescales the influence of *VPD* became more pronounced while day-to-day variability masked any significant relationships with *PPFD*. The seasonal course of NME showed a sharp increase early in the growing season which peaks in mid-July followed by a significant decrease (Fig 4.10b). The ecosystem remained a net CH₄ source over the full snow-free season. Emissions by the end of the growing season were half those during the peak, but modeled confidence intervals were much wider late in the season. Net Radiation and *TD* were the dominant controls over NME across timescales (Table 4.8).

Variability in NEE between growing seasons was considerable, ranging from -0.75 g CO₂-C m⁻² d⁻¹ [CI_{95%} ± 0.45] in 2009 to -0.25 g CO₂-C m⁻² d⁻¹ [CI_{95%} ± 0.55] in 2018 (Fig 4.10c). The year 2018 was a significant outlier, attributable to a late snowmelt, cold temperatures, and high *W_{TD}*. The warmest year (2012) also had reduced CO₂ uptake (-0.45 g CO₂-C m⁻² d⁻¹ [CI_{95%} ± 0.44]), attributable to the higher *VPD* and greater *TD*. Although *VPD* had a net negative effect on NEE, at levels above ~300 hPa it had a strong limiting effect and mean *VPD* in 2012 was 414 hPa. While all but one growing season were estimated to be net CO₂ sinks, extending to the full

snow-free season shows mean NEE was still negative each year but only three years (2009, 2010, and 2013) had $\text{CI}_{95\%}$ which did not span zero.

Variability in NME was less drastic between growing seasons. The LCP ecosystem was estimated to be a consistent growing season CH_4 source, ranging from $29.4 \text{ mg CH}_4\text{-C m}^{-2} \text{ d}^{-1}$ [$\text{CI}_{95\%} \pm 6.3$] in 2012 to $23.7 \text{ mg CH}_4\text{-C m}^{-2} \text{ d}^{-1}$ [$\text{CI}_{95\%} \pm 6.3$] in 2015 (Fig 4.10d). The cloudy conditions in 2015 kept R_N low, and since it was the primary driver of NME ($\text{RI} = 34\%$), CH_4 fluxes were suppressed. The year 2012 was anomalously warm, which resulted the lowest average W_{TD} and paired with high R_N , this led to elevated NME. Here W_{TD} was a weak ($\text{RI} = 5\%$) negative driver of F_{CH_4} , i.e., all else equal a deeper water table will result in higher NME (Skeeter et al. 2022).

At the full snow-free season scale ($n=11$), mean NEE was negatively correlated maximum NDVI and positively correlated with mean July T_a , the length of the snow-free season, and the timing of the first snowfall (Table 4.9). Warmer summer temperatures and longer snow-free seasons were both associated with reduced CO_2 uptake. Mean NME was positively associated with the timing of the spring flood and snowmelt. Only maximum NDVI and July T_a had significant correlations with cumulative C uptake exchange. The correlation analysis was conducted using leave-one-out cross validation to for a more robust assessment of the associations give the limited sample size.

Table 4.8. Pearson r correlation coefficient for NEE and NME with key flux drivers, averaged over the specified time intervals. Only correlations significant to $p < 0.05$ with $r^2 > 0.3$ are shown.

NEE	Hourly (n=25,344)	1-Day (n=3,748)	8-Day (n=132)	16-Day (n=66)	24-Day (n=44)	32-Day (n=33)
PPFD	-0.55	--	--	--	--	-0.56

<i>VPD</i>	--	--	-0.58	-0.64	-0.65	-0.71
NME		1-Day	8-Day	16-Day	24-Day	32-Day
<i>R_N</i>	+0.78	+0.72	+0.79	+0.81	+0.84	+0.89
<i>TD</i>	-0.64	-0.66	-0.70	-0.73	-0.78	-0.83

Table 4.9. Correlation statistics (Spearman ρ) for mean snow-free season NEE and NME and cumulative C exchange compared to select snow-free season variables. Only correlations with $p>0.1$ are shown, correlations significant to $p < 0.05$ are shown in bold. To control for potential outliers, leave-one-out cross validation was used. The ρ and p values presented are the median values of the n=11 permutations.

	Mean NEE	Mean NME	Cumulative C Exchange
Snowmelt (NDSI <0)	--	+0.62	--
Flood (NDWI <0)	--	+0.79	--
Maximum NDVI	-0.71	--	-0.73
Snowfall (NDSI>0 / SC% > 18.75)	+0.57	--	--
Snow-free season length	+0.64	--	
Mean July T_a	+0.68	--	+0.64

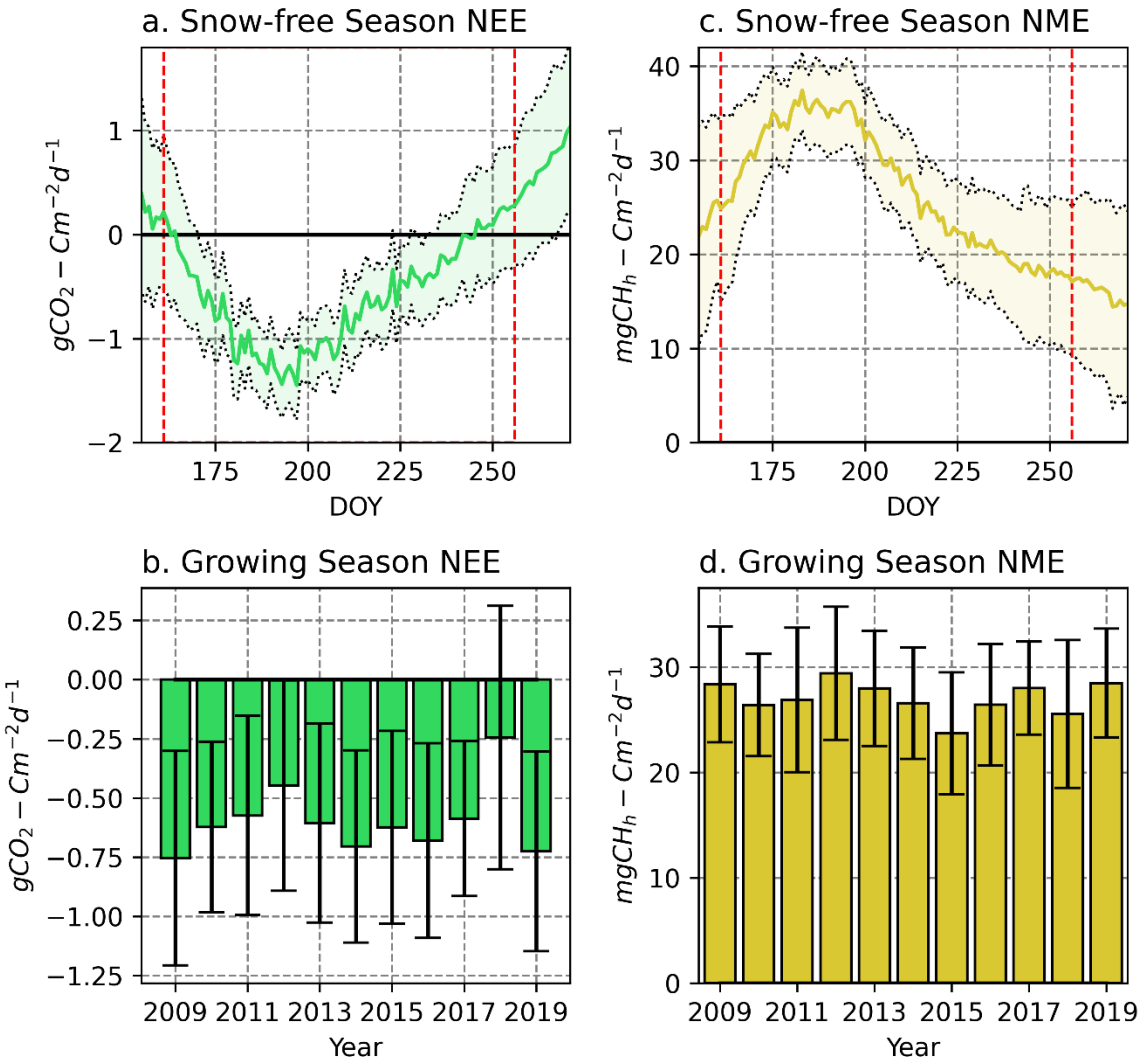


Figure 4.10 a. Mean daily NEE across all snow-free seasons. Shaded areas represent the 95% confidence interval. b. Mean NEE over each growing season. Error bars represent the 95% confidence interval. b. Shows the same as a. but for NME. d. Shows the same as b. but for NME. As in Figure 4.6, the vertical red dashed lines demarcate the growing season. The x-axis in (a. & b.) spans the median start and end dates of the snow-free season DOY 155 and 271 respectively. Averages/confidence in intervals outside of the growing season include some days which were not part of the snow-free season and are shown for reference.

4.4 Discussion

The dataset from an AWS at Fish Island along with ERA5 reanalysis data were used to create a time series of flux drivers in order to upscale F_{CO_2} and F_{CH_4} from observations during a single field season (2017) to eleven snow-free seasons from 2009 to 2019. MODIS and ERA5

data were used to define the snow-free seasons and contextualize the duration of the 2009 to 2019 within a longer period of record. The modelling results we present here are meant to explore the potential range of carbon fluxes at this Low-Center Polygon (LCP) ecosystem in the Mackenzie River Delta. The climatology shows that there is considerable interannual and inter-seasonal variability in flux drivers at Fish Island. We are generally confident of our estimates during the growing-seasons but outliers (e.g., 2009 and 2018) and shoulder season projections should be taken with caution.

4.4.1 Uncertainty

The validation metrics suggest the growing season NEE estimates are generally accurate for conditions similar to the 2017 training data. Further, the mean GPP estimates (NN vs. MODIS) had overlapping CI_{95%} and only differed by 0.09 g CO₂-C m⁻² d⁻¹ and 8-day GPP estimates were generally in good agreement ($r^2 = 0.68$). The MODIS comparison cannot directly validate our NN estimates because the MODIS GPP data product is also an estimate, but the general agreement is encouraging.

The validation metrics give us less confidence in the NME estimates. Two factors influencing NME (U and u_*) are hypothesized to drive NME via pressure pumping hence ventilating the peat during gusty conditions (Mohr et al., 2016; Laemmle et al., 2017; Skeeter et al. 2022). Hourly averaging would likely suppress that effect. Further, the function used to estimate u_* (EQ1) was too simplistic to capture these dynamics. Comparing the MODIS GPP data, with our estimates showed a moderate correlation across most years but it indicated the 2018 estimate may be skewed by overestimated ER early in the growing season.

The NN estimates have narrower confidence intervals for conditions similar to observations they were trained on. Intervals widen considerably for projections beyond the

domain of the training data. This is reflected in the width of the confidence intervals for the 2017 growing season for NEE ($\text{CI}_{95\%} \pm 0.33 \text{ g CO}_2\text{-C m}^{-2} \text{ d}^{-1}$) and NME ($\pm 4.4 \text{ mg CH}_4\text{-C m}^{-2} \text{ d}^{-1}$) compared to the 2018 growing season for NEE ($\pm 0.56 \text{ g CO}_2\text{-C m}^{-2} \text{ d}^{-1}$) and NME ($\pm 7.0 \text{ mg CH}_4\text{-C m}^{-2} \text{ d}^{-1}$). The largest source of uncertainty is the estimate of thaw depth. This driver essentially maps seasonality of both NEE and NME. The thaw depth estimates are based on a limited number of samples from a single year (2017) fit to a simple model. Given that maximum annual thaw depth is well correlated with the CALM sites at Lousey Point, the estimates are likely reasonable enough to guide seasonality in the model, but there are no data to validate the outlier in 2018.

The NN derivatives show NEE has a parabolic relationship with TD (Skeeter et al. 2022). Increasing TD enhances NEE until the middle portion of the season and then begins to limit it. The relative influence (RI) of TD was only 7%, so the effects of poorly resolved TD were probably small-to-moderate over most of the range. The lack of significant correlations with TD at daily or multi-day timescales supports this assertion. However, at very shallow TD (e.g., 0.06 m in 2018), it may result in significant an overestimation of ER. Excluding $TD < 0.15$ in 2018 (~the first week of the growing season), the range was reduced but the $\text{CI}_{95\%}$ still spanned zero ($\text{CI}_{95\%} [-0.97, 0.14] \text{ g CO}_2\text{-C m}^{-2} \text{ d}^{-1}$ compared to the full 2018 growing season $\text{CI}_{95\%} [-0.78, 0.42] \text{ g CO}_2\text{-C m}^{-2} \text{ d}^{-1}$). For NME, TD has a RI of 15% and NN derivatives show a monotonically decreasing relationship with NME (Skeeter et al. 2022). Over or underestimating TD could cause the model to substantially over/underestimating late season NME. Modeled CH_4 fluxes were correlated with TD across all timescales so it is clear the estimate is heavily dependent upon the TD estimate.

4.4.2 Spatial Representativeness

The landscape classification suggests the LCP ecosystem (tundra with similar maximum annual NDVI to the 90% flux footprint) covers $\sim 10 \text{ km}^2$ of the 19 km^2 Fish Island. It is likely mean snow-free season NEE across this 10 km^2 area falls somewhere in the $\text{CI}_{95\%}$ range [-0.88, 0.09] g CO₂-C m⁻² d⁻¹ estimated by the model. Low-center polygons like those at Fish Island are pervasive across the Big Lake Delta Plain, so the LCP on adjacent islands may have similar NEE as well (Burn and Kokelj, 2009; Morse et al. 2012; Morse and Burn, 2013). However, we argue the flux data makes it not possible to upscale in both space and time from a single season's observations of carbon fluxes from one location within the LCP ecosystem.

Spatial heterogeneity significantly influenced F_{CH_4} at the footprint scale during the field measurements in 2017. Given the location bias of the 2017 EC observations there is added uncertainty and these estimates may not be spatially representative (Schmid and Lloyd 1999; Skeeter et al. 2022). Here, source area fractions (F_{Cnt} and F_{Rim}) were fixed to their average distributions within 300 m of the EC station, as determined by a high-resolution drone imagery classification map (Skeeter et al. 2022). The intention was to account for the location bias to some degree, but the landcover classification is still only valid for the immediate vicinity of the EC station. It is encouraging however, that our $\text{CI}_{95\%}$ for NME for July in 2012 and 2013, (31.3, 39.9] nmol m⁻² s⁻¹), overlaps with aircraft measurements of CH₄ fluxes made in the vicinity of Fish Island (17 to 35 nmol m⁻² s⁻¹) during July 2012 and 2013 (Kohnert et al. 2018).

With warming and permafrost degradation, it is likely some of the ice wedges in the LCP ecosystem will degrade, leading to more ponding and lower vegetation cover (Morse and Burn 2013). This could potentially increase NME, but direct observations would be needed for verification of this hypothesis. Shrubs currently cover $\sim 8 \text{ km}^2$ of Fish Island, and warming may

lead to some shrub encroachment into the LCP (Myers-Smith et al. 2020; Chen et al. 2021). However low-center polygons are at lower risk to shrub encroachment than high center polygons (Fraser et al. 2014; Moffat et al. 2016). The shrubby portions of Fish Island are likely to be a stronger CO₂ sink and weaker CH₄ source than the LCP ecosystem. Observations from a shrub tundra site in a drained thermokarst lake at Illisarvik 10 km NE of Fish Island, during the 2016 growing season had NEE and NME that were respectively 1.6 and 0.3 times the magnitude of estimates for the LCP ecosystem on Fish Island over the same time period (Skeeter et al. 2020).

4.4.3 Carbon Balance

We have confidence that the LCP ecosystem at Fish Island was a net C sink averaged over the 2009-2019 growing seasons with a CI_{95%} of NEE [-96, -14] g C m⁻² per growing season, but interannual climate variability was significant. Both the coldest (2018) and warmest (2012) growing seasons had CI_{95%} which spanned zero. Further, we estimated that shoulder season C emissions may offset a significant fraction of growing season CO₂ uptake. Net C fluxes for the early (snowmelt to DOY 161) and late (DOY 256 to snowfall) shoulder seasons were estimated to be CI_{95%} [-0.5, 1.2] g C m⁻² d⁻¹ and CI_{95%} [-0.1, 1.4] g C m⁻² d⁻¹, respectively.

Our findings are broadly in alignment with two longer term flux studies from LCP ecosystems in Alaska (Dengel et al. 2021) and Siberia (Holl et al. 2019) and shorter-term analysis for two other Siberian sites (van der Molen et al. 2007; Sachs et al. 2008). Dengel et al. (2021) present a seven-year record of (2013 to 2019) of June to September NEE and mean F_{CH_4} (not gap-filled) for a LCP site near Utqiagvik, AK (Table 4.10). Confidence intervals for June – September NEE (only snow-free days) at Fish Island overlap with their estimates each year, but suggest net CO₂ uptake in the LCP ecosystem at Fish Island was probably less than their site (median difference ~ 0.33 μmol m⁻² s⁻¹). The site at Utqiagvik was considerably colder, so ER at

Fish Island is likely higher and would explain much of this difference. Model derivatives presented in Skeeter et al. (2022) show ER has a monotonically increasing relationship with T_{Cn5} , which would support this hypothesis. Their estimate of F_{CH4} is not gap-filled so it cannot be directly compared, but our results suggest the LCP ecosystem at Fish Island is a stronger CH₄ source than the one at Utqiagvik. Over-winter measurements of CH₄ fluxes from the site at Utqiagvik between 2013 to 2015 suggest the September – May period accounted for ~43% of the annual CH₄ budget (Zona et al. 2016). For the same to be true of the LCP ecosystem at Fish Island, mean over-winter NME would need to be ~ 5.0 mg CH₄-C m⁻² d⁻¹ [CI_{95%} ± 1.0].

Holl et al. (2019) present cumulative CO₂-C uptake over the peak growing seasons (DOY 200 – DOY 235) from 2002 to 2017 for an LCP ecosystem at Samoylov Island, in Siberia's Lena River Delta. They do not present error bounds for their estimates of CO₂ uptake each year, but yearly values ranged from -25 to -9 g CO₂-C m⁻² with a median of -15 g CO₂-C m⁻². Over the same timeframe, our estimate for cumulative CO₂ uptake was -25.2 [CI_{95%} ± 12.9] which suggests the LCP ecosystem at Fish Island is a stronger CO₂ sink during the peak growing season. Their analysis also shows shoulder season fluxes were enough to offset growing season uptake, making the site a net C source in some years (Holl et al. 2019). Sachs et al. (2008) analyzed CH₄ fluxes at Samoylov Island for the 2006 snow-free season (June 9th – September 19th) and found CH₄ fluxes ~ 18.7 mg CH₄ m⁻² d⁻¹ (no error bounds provided), which is well below the snow-free season CI_{95%} at Fish Island [25.3, 46.2] mg CH₄ m⁻² d⁻¹. At Samoylov Island, air and soil temperatures over the 2006 season, along with maximum thaw depth in 2006 were within ranges observed/estimated for the LCP ecosystem at Fish Island between 2009 and 2019. Samoylov received more precipitation (158 mm) than any season at Fish Island and the water table was closer to the surface than at Fish Island, which may explain some of the

difference. However, the two LCP ecosystems had different ratios of polygon rims to centers which likely explains much of the disparity. At Fish Island, polygon center and rims covered ~ 66 % and 29 % of the land surface respectively (the other 5% was ponded troughs) while the land surface at Samoylov was ~ 40% polygon centers and 60% polygon rims (Sachs et al. 2008; Skeeter et al. 2022). They did observe the same seasonal pattern of high early season CH₄ emissions followed a decreasing pattern through over the growing season (Sachs et al. 2008).

The NEE model projects significant emissions early in the 2018 growing season (1.4 g CO₂-C [CI_{95%} ± 1.1]). This is likely an over-estimate, but the projection cannot be ruled out entirely. Large pulses of CO₂ (1.2 ±0.2 g CO₂-C m⁻²) have been observed during spring thaw at a polygonal tundra site in Alaska (Raz-Yaseef et al. 2017). Earlier snowmelt has been associated with longer growing seasons and enhanced NEE over the growing season in some low Arctic tundra sites (Lafleur and Humphreys 2008; Luus et al. 2013). While others have found early season heatwaves led to significant CO₂ emissions at Samoylov Island in the Lena Delta (Runkle et al. 2013; Holl et al. 2019). The MOIDS data suggests a long-term trend towards earlier spring floods and snowmelts, but there was no trend over the 2009-2019 period and our analysis did not find a significant association between NEE and the timing of snowmelt.

Observations from Alaska suggest delayed freeze up in autumn can completely offset growing season CO₂ uptake (Zona et al. 2016; Commane et al. 2017). This is supported by model projections for the circumpolar region (Natali et al. 2019). Recent work analyzing EC observations from a variety of tundra ecosystems across the circumpolar region also found earlier snowmelts were associated with reduced late season CO₂ uptake (Zona et al. 2022). Our analysis generally supports these findings as longer snow-free seasons were positively correlated with NEE, but we cannot say to what degree growing season CO₂ uptake at Fish Island is offset.

Modeling for the Alaskan north slope suggest warmer growing seasons will increase CO₂ uptake enough to offset losses from warming during the cold season (Tao et al. 2021). However, we found NEE had a positive association with July temperatures, which would suggest this assertion does not apply to the LCP ecosystem at Fish Island. Hashemi et al. (2021) also found ER from polygonal tundra near Utqiagvik, AK was more sensitive to increasing air temperatures than drained thermokarst lakes or moist upland tundra. This further supports our argument finding that warmer temperatures at Fish Island will reduce net CO₂ uptake.

Table 4.10. Comparison of mean June – September NEE and F_{CH4} presented in Dengel et al. (2021) to modeled NEE and NME at Fish Island over the same time periods. From 2013 to 2015, and 2018, the snow-free season dates (denoted by the *) did not perfectly align with the averaging interval. Estimates for just the snow-free seasons are shown in black. Projections over the full time period are shown in blue only for comparison but should be taken with caution as model projections during flooding or snow cover are tenuous. Mean June – September air temperatures are also shown for both sites.

	Utqiagvik, AK Dengel et al. (2021)			Fish Island, NWT This Study		
	Year	NEE ± 1 SE $\mu\text{mol m}^{-2} \text{s}^{-1}$	$F_{CH4} \pm 1 \text{ SE}$ $\text{nmol m}^{-2} \text{s}^{-1}$	T _a	NEE ± CI _{95%} $\mu\text{mol m}^{-2} \text{s}^{-1}$	NME ± CI _{95%} $\text{nmol m}^{-2} \text{s}^{-1}$
2013 * 6/10 – 9/30	-0.89 ± 0.02	19.61 ± 0.42	2.6	-0.33 ± 0.51 -0.54 ± 0.42	26.65 ± 5.32	8.0
2014 * 6/5 – 9/30	-0.45 ± 0.02	13.92 ± 0.26	1.75	-0.42 ± 0.47 -0.48 ± 0.45	24.39 ± 5.68	7.5
2015 * 6/1 – 9/28	-0.84 ± 0.02	25.06 ± 0.45	3.2	-0.38 ± 0.46 -0.42 ± 0.45	22.13 ± 6.07	7.6
2016	-0.74 ± 0.02	18.27 ± 0.35	3.5	-0.41 ± 0.47	23.78 ± 6.70	8.1
2017	-0.73 ± 0.02	20.05 ± 0.33	3.5	-0.36 ± 0.39	24.95 ± 5.13	8.8

2018 *6/10 – 9/25	-0.52 ± 0.02	14.61 ± 0.36	2.2	0.05 ± 0.66 -0.17 ± 0.58	24.18 ± 7.15	5.5
2019	-0.74 ± 0.02	23.42 ± 0.45	5.0	-0.44 ± 0.47	25.34 ± 5.76	7.5

4.5 Conclusions and Future Research

In the absence of long-term observations of carbon exchange in the Mackenzie River Delta region, our study investigated the influence of climate variability by extrapolating observations from a single study season to an eleven-year timeseries. We are confident this LCP ecosystem is a net C sink during the growing season from 2009 to 2019. However, we cannot claim the site was a C sink when estimates are extended to include shoulder seasons. Given the relationships between reduced net C uptake and warmer temperatures, further observations are needed to better understand and project how climate change will affect the carbon balance of this region. The association between reduced net C uptake and longer snow-free seasons shows it is imperative any future study include these time periods. Continuous annual measurements are not necessarily practical in a remote Arctic location like Fish Island, but any future study should at least make efforts to include the weeks before snow melt through to the end of early winter freeze up.

As our 2017 field study (Skeeter et al. 2022) provides the only existing direct dataset on measured NEE anywhere in the region future observations should target a more diverse set of landscapes. If Fish Island were revisited, a nested study with multiple towers at different heights could be used to better assess the role of microtopographic features. By including different

proportions of polygon rims, centers, and degraded troughs, space-for-time substitution could be used to and anticipate how future changes to thaw depth and hydrology in the LCP ecosystem may influence the carbon balance.

Chapter 5: Conclusion

5.1 Summary of Results

This thesis was the first study to monitor carbon fluxes using eddy covariance methods in the Mackenzie River Delta. Growing season fluxes of CO₂ and CH₄ were observed at Illisarvik, a drained thermokarst lake basin, in 2016 and at Fish Island, a low center polygonal peatland, in 2017. This research used neural networks to identify primary controls over carbon exchange at these two sites, and used neural networks to conduct a temporal upscaling experiment for fluxes at Fish Island. The key findings of this research are:

- 1) Both Illisarvik and Fish Island were growing season CO₂ sinks. Illisarvik was a weak CH₄ source, but with patches of very high fluxes in wet areas dominated by sedges. Fish Island was a moderately strong CH₄ source.
- 2) Temporal upscaling indicated significant interannual variability in growing season NEE and NME at Fish Island. Climate warming could reduce the CO₂ sink strength of Fish Island. Compared to two similar low center polygon ecosystems with long-term eddy covariance records:
 - a. Fish Island is likely a weaker growing season CO₂ sink and stronger growing season CH₄ source than a low center polygon ecosystem near Utqiagvik, Alaska.
 - b. Fish Island may be both a stronger growing season CO₂ sink CH₄ source than a low center polygon ecosystem at Samoylov Island, in the Lena River Delta.
- 3) Spatial heterogeneity was a significant factor influencing carbon fluxes at Fish Island and Illisarvik.
 - a. Both NEE and NME at Illisarvik varied significantly between different vegetation types

- b. At Fish Island, polygonal microtopography had a significant influence over NME but had no influence over NEE.
- c. Neural network analysis and footprint modelling can be combined with to help account for, and model the influence of, spatial heterogeneity on eddy covariance flux observations.

5.2 Methodological Contributions

Neural Networks are powerful tools for learning about non-linear systems. Thus far, they have been underutilized in ecosystem research, and specifically to study eddy covariance datasets, because they are frequently treated as “black boxes”. However, with careful inspection, they can provide very useful insights into key processes. Using the weights method, we can visualize the relative contributions of input parameters across their training domains. This allows us to ensure that the features the models learn are indeed plausible, and not just artifacts of the training data. Further, we can map flux responses across the training domain and make projections based on unseen conditions. This is a key advantage over random forest models, one of the other popular methods for working the eddy covariance data. Model projections must be treated with caution and inspected for physical plausibility, but they are incredibly useful for situations where in-situ observations are not available.

Model training, pruning, and feature selection are very much iterative processes which requires careful consideration. With large multivariate datasets, different combinations of inputs can yield similar results. This will occur when dealing with cross-correlated inputs (e.g. Shrub & Sedge fraction in Chapter 2). Sedge fraction drives NME, but shrub fraction has an inverse correlation with sedge fraction. The model does not differentiate between causation and correlation. Further, NN are randomly initialized and there is no guarantee that the set of

weights minimizing validation error identified by one model is the true minima. The key to compensating for these issues is repetition; using bootstrapping, training multiple randomly initialized models, and averaging outputs across them. Any one model will be biased towards the training data it is fed, but a collection of 30 randomly initialized models trained on 30 different bootstrapped iterations of the data will average out the error and produce a more stable result. Further, bootstrapping allows us to calculate confidence intervals using the variance of ensemble estimates/projections, which is an essential for sound analysis.

5.3 Implications & Future Research

Illisarvik appears to be a robust CO₂ sink and weak CH₄ source. This helps confirm the postulations that thermokarst lake drainage and the subsequent vegetation succession could act as a small buffer to climate change in the future (van Huissteden et al. 2011; Turetsky et al. 2020). At a global scale, however, the net mediating effect of thermokarst lake drainage is likely inconsequential. Turetsky et al. (2020) estimate drainage will only offset ~ 20% of the emissions caused by thermokarst activity in the first place. Given this, thermokarst lake drainage does not appear to be a mechanism capable of having any tangible negative climate feedback effect.

The low center polygon tundra at Fish Island was a robust growing season C sink. Modelling suggests that this pattern persisted across the most recent decade. However, interannual variability was significant and the model projections in Chapter 4 suggest that C sink strength varied by a factor of two or three over the time period studied. Warmer July temperatures were correlated with decreased CO₂ uptake, which suggests the polygonal ecosystem at Fish Island may not experience the boost in CO₂ uptake that is anticipated to be associated with warmer growing seasons in some other tundra ecosystems (Tao et al. 2021).

5.3.1 Cold Season Fluxes

While we only measured fluxes during the growing season, it is clear from a number of studies that cold season fluxes remain a significant source of uncertainty (Natali et al. 2019).

Winter methane fluxes accounted for about 40% of the annual CH₄ budget at a low center polygon site in Alaska. Pulses of CO₂ and CH₄ during the spring melt may also be significant (Raz-Yaseef et al. 2017). Early season heatwaves before vegetation begins to grow can lead to significant emissions (Holl et al. 2019).

Chapter 4 suggests shoulder season fluxes may have offset a substantial portion of growing season CO₂ uptake in the low center polygon ecosystem at Fish Island. Some years could have been net C sources annually, which is generally in alignment with observations from Alaska (Commane et al. 2017). However, to understand the magnitude of the potential offset, we need observations from outside the growing season. Late season eddy covariance measurements at remote arctic sites are challenging; low light levels mean solar panels are not a viable power source while infrared gas analyzers like the LI-7700 used to measure CH₄ fluxes require heating, leading to higher power demands. If Fish Island, or a similar site, were the focus of a longer-term campaign, perhaps a small wind turbine could be incorporated to extend battery life.

5.3.2 Methane Fluxes

Our measurements of CH₄ fluxes were the first such conducted in these landscapes of the Mackenzie River Delta. They are generally in agreement with aircraft observations by Kohnert et al. (2018). Our observations show complex transport mechanisms influence NME at this site, which require further investigation. The complex relationship between NME and turbulence conditions (interactions between U and u_*) highlighted by the NN analysis in Chapter 3 are

likely indicative of pressure pumping. This mechanism ventilates peat and can lead to more CH₄ bypassing methanotrophy in the soil profile above the saturated zone. With a longer snow free season and / or stormier conditions, this could lead to a net increase in CH₄ emissions due to a net decrease in methanotrophy. It is difficult to say much about the magnitude of this impact without a longer-term time series of observations because of the limited number of storm events per season. Additionally, we were unable to adequately tease out the relationship between thaw depth and water table depth. These drivers vary on long timescales, relative to a single growing season. Multiple combinations of thaw and water table depths are needed to better map the relationships, which requires a multi season dataset.

5.3.3 Landscape Change and Remote Sensing

There is a wealth of data available on platforms like Google Earth Engine that can be leveraged to compliment in-situ observations and in some cases, they can minimize the need for field observations. The global GPP product clearly does not work very well for Fish Island, but given a longer-term dataset, relationships with NDVI, snow-cover, flooding, and a local parameterization scheme could likely be developed with machine learning to allow for real-time (estimated) monitoring. This could likely be accomplished with a few years of data or perhaps spatially/temporally disjointed data sets from comparable sites.

5.3.4 Neural Network Architecture

One of the directions I am most excited to explore in the future is how different neural network architectures can be leveraged to better resolve the functional relations in flux datasets. The models I present here are “simple” dense neural networks. They consist of one layer of hidden nodes, and have been shown to be capable of mapping any continuous function to an arbitrary degree of accuracy (Hornik et al. 1991). However, that is no guarantee the function

mapped is physically meaningful. By using multiple-layers with relevant inputs and specific types of activation functions, networks can be constructed in such a manner that they map ER and GPP separately (Tramontana et al. 2020).

Another method, long-short term memory (LSTM) networks offer promising opportunities as well. To my knowledge, they have not been applied to eddy covariance data. These networks are designed specifically to handle time series. By incorporating memory nodes into their architecture, they can map time-lags; information from any number of previous time steps can be allowed to influence the present estimate. This could prove incredibly useful for CH₄ fluxes, where the mechanisms governing production, transport, and consumption spatially and temporally disjointed. For example, a pressure pumping event could rapidly ventilate a layer of peat and cause pulse of CH₄ emissions. Following the spike, CH₄ fluxes may be depressed for some time period due to decreased CH₄ concentration in the peat matrix. A LSTM could learn this pattern. The single season of flux data from Fish Island was insufficient for an LSTM. For proper cross validation, they require many thousands of datapoints because they must be trained on continuous blocks of time which makes bootstrapping more difficult. I would suggest time-blocks an order of magnitude longer than the time scale of the hypothesized lag could be sufficient. A few years of data could be broken into large chunks and leave-n-out cross validation to be used to train an ensemble of LSTM models.

5.4 Reflections

Unfortunately, I feel that my thesis research was a misuse of resources. I did not intend it to be, nor did anyone else involved, but when I reflect and ask questions like: “Could more benefit have come from investing these resources more directly in Inuvialuit communities?” and “Does the value of the information we collected offset the tons of CO₂ emissions we generated?”

I cannot say I feel the ends justified the means. The work presented in Chapter 3 was initially intended to be part of a broader set of research, including longer-term monitoring and subsequent research by future graduate students. Had that come to fruition, perhaps I would feel differently. Chapter 4 is my best attempt to provide some long-term context to the findings presented in Chapter 3, but projecting estimates over 11 snow-free seasons based on 82-days of observations from one field season is clearly tenuous.

I do not say this to discredit my research, there is clear value in it. Rather I say this to emphasize what I have learned from this process and how I hope to apply these lessons as I move forward in my career. If our priority is just extracting information, the research only serves to perpetuate colonialism (Liboiron 2021). Long-term datasets are essential for understanding ecosystem scale responses to climate change and this type of research must continue. While exploratory research is important, any future work in a remote location such as Fish Island should have a concrete plan for long-term implementation. In the future, more effort should be put into training Indigenous scientists and technicians and involving local stakeholders in the research process. By fostering community engagement, long-term research campaigns can be more robust and efficient over longer timescales.

Bibliography

Amiri, B., Dizène, R., & Dahmani, K. (2020). Most relevant input parameters selection for 10-min global solar irradiation estimation on arbitrary inclined plane using neural networks.

International Journal of Sustainable Energy, 39(8), 779–803.

<https://doi.org/10.1080/14786451.2020.1758104>

Anders, U., & Korn, O. (1999). Model selection in neural networks. *Neural Networks*, 12(2), 309–323. [https://doi.org/10.1016/S0893-6080\(98\)00117-8](https://doi.org/10.1016/S0893-6080(98)00117-8)

Aubinet, M., Vesala, T., & Papale, D. (Eds.). (2012). *Eddy Covariance: A Practical Guide to Measurement and Data Analysis* (2012 edition). Springer.

Baldocchi, D. D. (2003). Assessing the eddy covariance technique for evaluating carbon dioxide exchange rates of ecosystems: Past, present and future. *Global Change Biology*, 9(4), 479–492.

<https://doi.org/10.1046/j.1365-2486.2003.00629.x>

Baldocchi, D., Falge, E., Gu, L., Olson, R., Hollinger, D., Running, S., Anthoni, P., Bernhofer, C., Davis, K., Evans, R., Fuentes, J., Goldstein, A., Katul, G., Law, B., Lee, X., Malhi, Y., Meyers, T., Munger, W., Oechel, W., ... Wofsy, S. (2001). FLUXNET: A New Tool to Study the Temporal and Spatial Variability of Ecosystem-Scale Carbon Dioxide, Water Vapor, and Energy Flux Densities. *Bulletin of the American Meteorological Society*, 82(11), 2415–2434.

[https://doi.org/10.1175/1520-0477\(2001\)082<2415:FANTTS>2.3.CO;2](https://doi.org/10.1175/1520-0477(2001)082<2415:FANTTS>2.3.CO;2)

Bao, T., Xu, X., Jia, G., Billesbach, D. P., & Sullivan, R. C. (2021). Much stronger tundra methane emissions during autumn freeze than spring thaw. *Global Change Biology*, 27(2), 376–387.

<https://doi.org/10.1111/gcb.15421>

Billings, W., & Peterson, K. (1980). Vegetational Change and Ice-Wedge Polygons Through the Thaw-Lake Cycle. *Arctic and Alpine Research*, 12(4), 413–432. <https://doi.org/10.2307/1550492>

- Bliss, L. C., Courtin, G. M., Pattie, D. L., Riewe, R. R., Whitfield, D. W. A., & Widden, P. (1973). Arctic tundra ecosystems. *Annual Review of Ecology and Systematics*, 4(1), 359–399.
- Blume-Werry, G., Milbau, A., Teuber, L. M., Johansson, M., & Dorrepaal, E. (2019). Dwelling in the deep – strongly increased root growth and rooting depth enhance plant interactions with thawing permafrost soil. *New Phytologist*, 223(3), 1328–1339. <https://doi.org/10.1111/nph.15903>
- Breiman, L. (2001). Random forests. *Machine Learning*, 45(1), 5–32.
- Briegel, F., Lee, S. C., Black, T. A., Jassal, R. S., & Christen, A. (2020). Factors controlling long-term carbon dioxide exchange between a Douglas-fir stand and the atmosphere identified using an artificial neural network approach. *Ecological Modelling*, 435, 109266. <https://doi.org/10.1016/j.ecolmodel.2020.109266>
- Burba, G. (2013). *Eddy Covariance Method for Scientific, Industrial, Agricultural and Regulatory Applications: A Field Book on Measuring Ecosystem Gas Exchange and Areal Emission Rates*. LI-COR Biosciences.
- Burn, C. R. (2002). Tundra lakes and permafrost, Richards Island, western Arctic coast, Canada. *Canadian Journal of Earth Sciences*, 39(8), 1281–1298. <https://doi.org/10.1139/e02-035>
- Burn, C. R. (2017). Mackenzie Delta: Canada's Principal Arctic Delta. In O. Slaymaker (Ed.), *Landscapes and Landforms of Western Canada* (pp. 321–334). Springer International Publishing. https://doi.org/10.1007/978-3-319-44595-3_23
- Burn, C. R., & Kokelj, S. V. (2009). The environment and permafrost of the Mackenzie Delta area. *Permafrost and Periglacial Processes*, 20(2), 83–105. <https://doi.org/10.1002/ppp.655>
- Burn, C. R., Lewkowicz, A. G., & Wilson, M. A. (2021). Long-term field measurements of climate-induced thaw subsidence above ice wedges on hillslopes, western Arctic Canada. *Permafrost and Periglacial Processes*, 32(2), 261–276. <https://doi.org/10.1002/ppp.2113>

- CALM. (n.d.). *Circumpolar Active Layer Monitoring Network)—International Permafrost Association*. Retrieved March 12, 2022, from <https://ipa.arcticportal.org/products/gtn-p/calm>
- Canada, E. and C. C. (2011, October 31). *Canadian Climate Normals—Climate—Environment and Climate Change Canada*. https://climate.weather.gc.ca/climate_normals/index_e.html
- Cannone, N., Ponti, S., Christiansen, H. H., Christensen, T. R., Pirk, N., & Guglielmin, M. (2019). Effects of active layer seasonal dynamics and plant phenology on CO₂ land-atmosphere fluxes at polygonal tundra in the High Arctic, Svalbard. *CATENA*, 174, 142–153.
<https://doi.org/10.1016/j.catena.2018.11.013>
- Carlson, J. B. (1975). Lodestone Compass: Chinese or Olmec Primacy?: Multidisciplinary analysis of an Olmec hematite artifact from San Lorenzo, Veracruz, Mexico. *Science*, 189(4205), 753–760.
<https://doi.org/10.1126/science.189.4205.753>
- CAVM Team. (2003). *Circumpolar Circumpolar Arctic Vegetation Map. (1:7,500,000 scale) Vegetation Map* [Map]. U.S. Fish and Wildlife Service, Anchorage, Alaska.
<https://www.geobotany.uaf.edu/cavm/>
- Chaichana, N., Bellingrath-Kimura, S. D., Komiya, S., Fujii, Y., Noborio, K., Dietrich, O., & Pakoktom, T. (2018). Comparison of Closed Chamber and Eddy Covariance Methods to Improve the Understanding of Methane Fluxes from Rice Paddy Fields in Japan. *Atmosphere*, 9(9), 356. <https://doi.org/10.3390/atmos9090356>
- Chanton, J. P., Whiting, G. J., Showers, W. J., & Crill, P. M. (1992). Methane flux from *Peltandra virginica*: Stable isotope tracing and chamber effects. *Global Biogeochemical Cycles*, 6(1), 15–31. <https://doi.org/10.1029/91GB02969>

Chen, A., Lantz, T. C., Hermosilla, T., & Wulder, M. A. (2021). Biophysical controls of increased tundra productivity in the western Canadian Arctic. *Remote Sensing of Environment*, 258, 112358. <https://doi.org/10.1016/j.rse.2021.112358>

Chen, Y., Lara, M. J., Jones, B. M., Frost, G. V., & Hu, F. S. (2021). Thermokarst acceleration in Arctic tundra driven by climate change and fire disturbance. *One Earth*, 4(12), 1718–1729. <https://doi.org/10.1016/j.oneear.2021.11.011>

Chollet, F. & others. (2015). *Keras*. <https://keras.io>

Christen, A., Jassal, R. S., Black, T. A., Grant, N. J., Hawthorne, I., Johnson, M. S., Lee, S.-C., & Merkens, M. (2017). Summertime greenhouse gas fluxes from an urban bog undergoing restoration through rewetting. *Mires & Peat*, 17.

Commane, R., Lindaas, J., Benmergui, J., Luus, K. A., Chang, R. Y.-W., Daube, B. C., Euskirchen, E. S., Henderson, J. M., Karion, A., Miller, J. B., Miller, S. M., Parazoo, N. C., Randerson, J. T., Sweeney, C., Tans, P., Thoning, K., Veraverbeke, S., Miller, C. E., & Wofsy, S. C. (2017). Carbon dioxide sources from Alaska driven by increasing early winter respiration from Arctic tundra. *Proceedings of the National Academy of Sciences*, 114(21), 5361–5366.

<https://doi.org/10.1073/pnas.1618567114>

Cunada, C. L., Lesack, L. F. W., & Tank, S. E. (2018). Seasonal Dynamics of Dissolved Methane in Lakes of the Mackenzie Delta and the Role of Carbon Substrate Quality. *Journal of Geophysical Research: Biogeosciences*, 123(2), 591–609. <https://doi.org/10.1002/2017JG004047>

Cunada, C. L., Lesack, L. F. W., & Tank, S. E. (2021). Methane emission dynamics among CO₂-absorbing and thermokarst lakes of a great Arctic delta. *Biogeochemistry*, 156(3), 375–399. <https://doi.org/10.1007/s10533-021-00853-0>

Delwiche, K. B., Knox, S. H., Malhotra, A., Fluet-Chouinard, E., McNicol, G., Feron, S., Ouyang, Z., Papale, D., Trotta, C., Canfora, E., Cheah, Y.-W., Christianson, D., Alberto, M. C. R., Alekseychik, P., Aurela, M., Baldocchi, D., Bansal, S., Billesbach, D. P., Bohrer, G., ... Jackson, R. B. (2021). FLUXNET-CH4: A global, multi-ecosystem dataset and analysis of methane seasonality from freshwater wetlands. *Earth System Science Data*, 13(7), 3607–3689.

<https://doi.org/10.5194/essd-13-3607-2021>

Dengel, S., Billesbach, D., & Torn, M. S. (2021). Influence of Tundra Polygon Type and Climate Variability on CO₂ and CH₄ Fluxes Near Utqiagvik, Alaska. *Journal of Geophysical Research: Biogeosciences*, 126(12), e2021JG006262. <https://doi.org/10.1029/2021JG006262>

Dengel, S., Zona, D., Sachs, T., Aurela, M., Jammet, M., Parmentier, F. J. W., Oechel, W., & Vesala, T. (2013). Testing the applicability of neural networks as a gap-filling method using CH₄ flux data from high latitude wetlands. *Biogeosciences*, 10(12), 8185–8200.

<https://doi.org/10.5194/bg-10-8185-2013>

Derkson, C., Burgess, D., Duguay, C., Howell, S., Mudryk, L., Smith, S., Thackeray, C., & Kirchmeier-Young, M. (2019). Changes in snow, ice, and permafrost across Canada. *Canada's Changing Climate Report. Edited by E. Bush and DS Lemmen. Government of Canada, Ottawa, Ont., Canada*, 194–260.

Desai, A. R., Richardson, A. D., Moffat, A. M., Kattge, J., Hollinger, D. Y., Barr, A., Falge, E., Noormets, A., Papale, D., Reichstein, M., & Stauch, V. J. (2008). Cross-site evaluation of eddy covariance GPP and RE decomposition techniques. *Agricultural and Forest Meteorology*, 148(6), 821–838. <https://doi.org/10.1016/j.agrformet.2007.11.012>

Dilke, O. A. W. (1961). Maps in the Treatises of Roman Land Surveyors. *The Geographical Journal*, 127(4), 417–426. <https://doi.org/10.2307/1792795>

Dou, X., & Yang, Y. (2018). Estimating forest carbon fluxes using four different data-driven techniques based on long-term eddy covariance measurements: Model comparison and evaluation. *Science of The Total Environment*, 627, 78–94.

<https://doi.org/10.1016/j.scitotenv.2018.01.202>

Eckhardt, T., Knoblauch, C., Kutzbach, L., Holl, D., Simpson, G., Abakumov, E., & Pfeiffer, E.-M. (2019). Partitioning net ecosystem exchange of CO₂ on the pedon scale in the Lena River Delta, Siberia. *Biogeosciences*, 16(7), 1543–1562. <https://doi.org/10.5194/bg-16-1543-2019>

Ensom, T. P., Burn, C. R., & Kokelj, S. V. (2012). Lake- and channel-bottom temperatures in the Mackenzie Delta, Northwest Territories¹This article is one of a series of papers published in this CJES Special Issue on the theme of Fundamental and applied research on permafrost in Canada.²Polar Continental Shelf Project Contribution 03511. *Canadian Journal of Earth Sciences*, 49(8), 963–978. <https://doi.org/10.1139/e2012-001>

Environemnt Canada. (2016). *Tuktoyaktuk Climate Normals 1980-2010*. Environment Canada, Ottawa, ON.

Environemnt Canada. (2020). *Daily Water Level Graph for BIG LAKE AT TAGLU ISLAND (10LC020) [NT]*—Water Level and Flow—Environment Canada.
https://wateroffice.ec.gc.ca/report/historical_e.html?stn=10LC020&dataType=Daily¶meterType=Level&year=2017&mode=Graph

Eshel, G., Dayalu, A., Wofsy, S. C., Munger, J. W., & Tziperman, E. (2019). Listening to the Forest: An Artificial Neural Network-Based Model of Carbon Uptake at Harvard Forest. *Journal of Geophysical Research: Biogeosciences*, 124(3), 461–478. <https://doi.org/10.1029/2018JG004791>

- Estiarte, M., & Peñuelas, J. (2015). Alteration of the phenology of leaf senescence and fall in winter deciduous species by climate change: Effects on nutrient proficiency. *Global Change Biology*, 21(3), 1005–1017. <https://doi.org/10.1111/gcb.12804>
- Euskirchen, E. S., Bret-Harte, M. S., Scott, G. J., Edgar, C., & Shaver, G. R. (2012). Seasonal patterns of carbon dioxide and water fluxes in three representative tundra ecosystems in northern Alaska. *Ecosphere*, 3(1), art4. <https://doi.org/10.1890/ES11-00202.1>
- Fine, I. V., Cherniawsky, J. Y., Rabinovich, A. B., & Stephenson, F. (2008). Numerical Modeling and Observations of Tsunami Waves in Alberni Inlet and Barkley Sound, British Columbia. *Pure and Applied Geophysics*, 165(11–12), 2019–2044. <https://doi.org/10.1007/s00024-008-0414-9>
- Fischer, A. (2015). How to determine the unique contributions of input-variables to the nonlinear regression function of a multilayer perceptron. *Ecological Modelling*, 309, 60–63.
- Flato, G., Gillett, N., Arora, V., Cannon, A., & Anstey, J. (2019). *Modelling Future Climate Change; Chapter 3 in Canada's Changing Climate Report*. 74–111.
- Foken, T., Göockede, M., Mauder, M., Mahrt, L., Amiro, B., & Munger, W. (2004). Post-Field Data Quality Control. In X. Lee, W. Massman, & B. Law (Eds.), *Handbook of Micrometeorology* (pp. 181–208). Springer Netherlands. https://doi.org/10.1007/1-4020-2265-4_9
- Forbes, B. C., Ebersole, J. J., & Strandberg, B. (2001). Anthropogenic Disturbance and Patch Dynamics in Circumpolar Arctic Ecosystems. *Conservation Biology*, 15(4), 954–969. <https://doi.org/10.1046/j.1523-1739.2001.015004954.x>
- Ford, K. R., Harrington, C. A., & St. Clair, J. B. (2017). Photoperiod cues and patterns of genetic variation limit phenological responses to climate change in warm parts of species' range: Modeling diameter-growth cessation in coast Douglas-fir. *Global Change Biology*, 23(8), 3348–3362. <https://doi.org/10.1111/gcb.13690>

- Fox, A. M., Huntley, B., Lloyd, C. R., Williams, M., & Baxter, R. (2008). Net ecosystem exchange over heterogeneous Arctic tundra: Scaling between chamber and eddy covariance measurements. *Global Biogeochemical Cycles*, 22(2). <https://doi.org/10.1029/2007GB003027>
- Fraser, R. H., Lantz, T. C., Olthof, I., Kokelj, S. V., & Sims, R. A. (2014). Warming-Induced Shrub Expansion and Lichen Decline in the Western Canadian Arctic. *Ecosystems*, 17(7), 1151–1168. <https://doi.org/10.1007/s10021-014-9783-3>
- French, H. (2017). Thermokarst Processes and Landforms. In *The Periglacial Environment 4e* (pp. 169–192). John Wiley & Sons, Ltd. <https://doi.org/10.1002/9781119132820.ch8>
- French, H. M. (2017a). Aggradational Permafrost Landforms. In *The Periglacial Environment 4e* (pp. 139–167). John Wiley & Sons, Ltd. <https://doi.org/10.1002/9781119132820.ch7>
- French, H. M. (2017b). Ground Freezing, Permafrost and the Active Layer. In *The Periglacial Environment 4e* (pp. 63–85). John Wiley & Sons, Ltd. <https://doi.org/10.1002/9781119132820.ch4>
- Frolking, S., Roulet, N., & Fuglestvedt, J. (2006). How northern peatlands influence the Earth's radiative budget: Sustained methane emission versus sustained carbon sequestration. *Journal of Geophysical Research: Biogeosciences*, 111(G1). <https://doi.org/10.1029/2005JG000091>
- Frost, G. V., Bhatt, U. S., Epstein, H. E., Myers-Smith, I., Phoenix, G. K., Berner, L. T., Bjerke, J. W., Forbes, B. C., Goetz, S. J., Kerby, J. T., Macander, M. J., Park, T., Raynolds, M. K., Tømmervik, H., & Walker, D. A. (2020). *Arctic Report Card 2020: Tundra Greenness*. <https://doi.org/10.25923/46RM-0W23>
- Furgal, C., & Prowse, T. D. (2008). Northern Canada. In *From Impacts to Adaptation: Canada in a Changing Climate 2007* (pp. 57–118). Government of Canada, Ottawa, ON.

Gagnon, S., Allard, M., & Nicosia, A. (2017). Diurnal and seasonal variations of tundra CO₂ emissions in a polygonal peatland near Salluit, Nunavik, Canada. *Arctic Science*, 4.

<https://doi.org/10.1139/AS-2016-0045>

Gareis, J. A. L., & Lesack, L. F. W. (2020). Ice-out and freshet fluxes of CO₂ and CH₄ across the air–water interface of the channel network of a great Arctic delta, the Mackenzie. *Polar Research*.

<https://doi.org/10.33265/polar.v39.3528>

Geeves, K. (2019). *Carbon quality and quantity in lake sediments and their relationship with pore-water and lake-water methane among lakes of the Mackenzie River Delta, Western Canadian Arctic* [Thesis, Environment: Department of Geography]. <https://summit.sfu.ca/item/19286>

Gevrey, M., Dimopoulos, I., & Lek, S. (2003). Review and comparison of methods to study the contribution of variables in artificial neural network models. *Ecological Modelling*, 160(3), 249–264. [https://doi.org/10.1016/S0304-3800\(02\)00257-0](https://doi.org/10.1016/S0304-3800(02)00257-0)

Gorelick, N., Hancher, M., Dixon, M., Ilyushchenko, S., Thau, D., & Moore, R. (2017). Google Earth Engine: Planetary-scale geospatial analysis for everyone. *Remote Sensing of Environment*, 202, 18–27. <https://doi.org/10.1016/j.rse.2017.06.031>

Hashemi, J., Zona, D., Arndt, K. A., Kalhori, A., & Oechel, W. C. (2021). Seasonality buffers carbon budget variability across heterogeneous landscapes in Alaskan Arctic Tundra. *Environmental Research Letters*. <https://doi.org/10.1088/1748-9326/abe2d1>

Healy, R. W., Striegl, R. G., Russell, T. F., Hutchinson, G. L., & Livingston, G. P. (1996). Numerical evaluation of static-chamber measurements of soil—atmosphere gas exchange: Identification of physical processes. *Soil Science Society of America Journal*, 60(3), 740–747.

Hengl, T., Nussbaum, M., Wright, M., Heuvelink, G., & Graeler, B. (2018). Random forest as a generic framework for predictive modeling of spatial and spatio-temporal variables. *PeerJ*, 6, e5518. <https://doi.org/10.7717/peerj.5518>

Heskes, T. (1997). Practical Confidence and Prediction Intervals. *Advances in Neural Information Processing Systems*, 176–182.

Holl, D., Wille, C., Sachs, T., Schreiber, P., Runkle, B. R. K., Beckebanze, L., Langer, M., Boike, J., Pfeiffer, E.-M., Fedorova, I., Bolshianov, D. Y., Grigoriev, M. N., & Kutzbach, L. (2019). A long-term (2002 to 2017) record of closed-path and open-path eddy covariance CO₂ net ecosystem exchange fluxes from the Siberian Arctic. *Earth System Science Data*, 11(1), 221–240. <https://doi.org/10.5194/essd-11-221-2019>

Hornik, K. (1991). Approximation capabilities of multilayer feedforward networks. *Neural Networks*, 4(2), 251–257.

Hugelius, G., Strauss, J., Zubrzycki, S., Harden, J. W., Schuur, E. A. G., Ping, C.-L., Schirrmeister, L., Grosse, G., Michaelson, G. J., Koven, C. D., O'Donnell, J. A., Elberling, B., Mishra, U., Camill, P., Yu, Z., Palmtag, J., & Kuhry, P. (2014). Estimated stocks of circumpolar permafrost carbon with quantified uncertainty ranges and identified data gaps. *Biogeosciences*, 11(23), 6573–6593. <https://doi.org/10.5194/bg-11-6573-2014>

Ibrom, A., Dellwik, E., Flyvbjerg, H., Jensen, N. O., & Pilegaard, K. (2007). Strong low-pass filtering effects on water vapour flux measurements with closed-path eddy correlation systems. *Agricultural and Forest Meteorology*, 147(3–4), 140–156.

<https://doi.org/10.1016/j.agrformet.2007.07.007>

IPCC. (2013). *Climate Change 2013: The Physical Science Basis. Contribution of Working Group I to the Fifth Assessment Report of the Intergovernmental Panel on Climate Change*. Cambridge University Press. <https://doi.org/10.1017/CBO9781107415324>

IPCC. (2021). *Climate Change 2021: The Physical Science Basis. Contribution of Working Group I to the Sixth Assessment Report of the Intergovernmental Panel on Climate Change*. Cambridge University Press.

Irvin, J., Zhou, S., McNicol, G., Lu, F., Liu, V., Fluet-Chouinard, E., Ouyang, Z., Knox, S. H., Lucas-Moffat, A., Trotta, C., Papale, D., Vitale, D., Mammarella, I., Alekseychik, P., Aurela, M., Avati, A., Baldocchi, D., Bansal, S., Bohrer, G., ... Jackson, R. B. (2021). Gap-filling eddy covariance methane fluxes: Comparison of machine learning model predictions and uncertainties at FLUXNET-CH4 wetlands. *Agricultural and Forest Meteorology*, 308–309, 108528.

<https://doi.org/10.1016/j.agrformet.2021.108528>

Iversen, C. M., Sloan, V. L., Sullivan, P. F., Euskirchen, E. S., McGuire, A. D., Norby, R. J., Walker, A. P., Warren, J. M., & Wullschleger, S. D. (2015). The unseen iceberg: Plant roots in arctic tundra. *New Phytologist*, 205(1), 34–58. <https://doi.org/10.1111/nph.13003>

Joabsson, A., Christensen, T. R., & Wallén, B. (1999). Vascular plant controls on methane emissions from northern peatforming wetlands. *Trends in Ecology & Evolution*, 14(10), 385–388.

[https://doi.org/10.1016/S0169-5347\(99\)01649-3](https://doi.org/10.1016/S0169-5347(99)01649-3)

Katayanagi, N. (2005). Spatial variability of greenhouse gas fluxes from soils of various land uses on a livestock farm in southern Hokkaido, Japan. *Phyton (Austria) Special Issue: "APGC 2004"*, 45, 309–318.

Keenan, T. F., & Richardson, A. D. (2015). The timing of autumn senescence is affected by the timing of spring phenology: Implications for predictive models. *Global Change Biology*, 21(7), 2634–2641. <https://doi.org/10.1111/gcb.12890>

Khosravi, A., Nahavandi, S., Creighton, D., & Atiya, A. F. (2011). Comprehensive Review of Neural Network-Based Prediction Intervals and New Advances. *IEEE Transactions on Neural Networks*, 22(9), 1341–1356. <https://doi.org/10.1109/TNN.2011.2162110>

Kim, Y., Johnson, M. S., Knox, S. H., Black, T. A., Dalmagro, H. J., Kang, M., Kim, J., & Baldocchi, D. (2020). Gap-filling approaches for eddy covariance methane fluxes: A comparison of three machine learning algorithms and a traditional method with principal component analysis. *Global Change Biology*, 26(3), 1499–1518. <https://doi.org/10.1111/gcb.14845>

Kim, Y., Lee, B.-Y., Suzuki, R., & Kushida, K. (2016). Spatial characteristics of ecosystem respiration in three tundra ecosystems of Alaska. *Polar Science*, 10(3), 356–363. <https://doi.org/10.1016/j.polar.2015.12.001>

King, G. M., & Adamsen, A. P. S. (1992). Effects of Temperature on Methane Consumption in a Forest Soil and in Pure Cultures of the Methanotroph *Methylomonas rubra*. *Appl. Environ. Microbiol.*, 58(9), 2758–2763.

Kittler, F., Burjack, I., Corradi, C. A. R., Heimann, M., Kolle, O., Merbold, L., Zimov, N., Zimov, S., & Gockede, M. (2016). Impacts of a decadal drainage disturbance on surface-atmosphere fluxes of carbon dioxide in a permafrost ecosystem. *Biogeosciences*, 13(18), 5315–5332. <https://doi.org/10.5194/bg-13-5315-2016>

Kljun, N., Calanca, P., Rotach, M. W., & Schmid, H. P. (2015). A simple two-dimensional parameterisation for Flux Footprint Prediction (FFP). *Geoscientific Model Development*, 8(11), 3695–3713.

Knoblauch, C., Spott, O., Evgrafova, S., Kutzbach, L., & Pfeiffer, E.-M. (2015). Regulation of methane production, oxidation, and emission by vascular plants and bryophytes in ponds of the northeast Siberian polygonal tundra. *Journal of Geophysical Research: Biogeosciences*, 120(12), 2525–2541. <https://doi.org/10.1002/2015JG003053>

Knox, S. H., Jackson, R. B., Poulter, B., McNicol, G., Fluet-Chouinard, E., Zhang, Z., Hugelius, G., Bousquet, P., Canadell, J. G., Saunois, M., Papale, D., Chu, H., Keenan, T. F., Baldocchi, D., Torn, M. S., Mammarella, I., Trotta, C., Aurela, M., Bohrer, G., ... Zona, D. (2019). FLUXNET-CH₄ Synthesis Activity: Objectives, Observations, and Future Directions. *Bulletin of the American Meteorological Society*, 100(12), 2607–2632. <https://doi.org/10.1175/BAMS-D-18-0268.1>

Knox, S. H., Matthes, J. H., Sturtevant, C., Oikawa, P. Y., Verfaillie, J., & Baldocchi, D. (2016). Biophysical controls on interannual variability in ecosystem-scale CO₂ and CH₄ exchange in a California rice paddy. *Journal of Geophysical Research: Biogeosciences*, 121(3), 978–1001. <https://doi.org/10.1002/2015JG003247>

Kohnert, K., Juhls, B., Muster, S., Antonova, S., Serafimovich, A., Metzger, S., Hartmann, J., & Sachs, T. (2018). Toward understanding the contribution of waterbodies to the methane emissions of a permafrost landscape on a regional scale—A case study from the Mackenzie Delta, Canada. *Global Change Biology*, 24(9), 3976–3989. <https://doi.org/10.1111/gcb.14289>

Kohnert, K., Serafimovich, A., Hartmann, J., & Sachs, T. (2014). Airborne measurements of methane fluxes in Alaskan and Canadian tundra with the research aircraft Polar 5. *Berichte Zur Polar- Und Meeresforschung= Reports on Polar and Marine Research*, 673. https://doi.org/10.2312/BzPM_0673_2014

Kohnert, K., Serafimovich, A., Metzger, S., Hartmann, J., & Sachs, T. (2017). Strong geologic methane emissions from discontinuous terrestrial permafrost in the Mackenzie Delta, Canada.

Scientific Reports, 7(1), 1–6. <https://doi.org/10.1038/s41598-017-05783-2>

Kokelj, S. V., Lantz, T. C., Solomon, S., Pisaric, M. F., Keith, D., Morse, P., Thienpont, J. R., Smol, J. P., & Esagok, D. (2012). Using multiple sources of knowledge to investigate northern environmental change: Regional ecological impacts of a storm surge in the outer Mackenzie Delta, NWT. *Arctic*, 257–272.

Kreplin, H. N., Santos Ferreira, C. S., Destouni, G., Keesstra, S. D., Salvati, L., & Kalantari, Z. (2021). Arctic wetland system dynamics under climate warming. *WIREs Water*, 8(4), e1526. <https://doi.org/10.1002/wat2.1526>

Kutzbach, L., Wagner, D., & Pfeiffer, E.-M. (2004). Effect of microrelief and vegetation on methane emission from wet polygonal tundra, Lena Delta, Northern Siberia. *Biogeochemistry*, 69(3), 341–362. <https://doi.org/10.1023/B:BIOG.0000031053.81520.db>

Kwon, H.-J., Oechel, W. C., Zulueta, R. C., & Hastings, S. J. (2006). Effects of climate variability on carbon sequestration among adjacent wet sedge tundra and moist tussock tundra ecosystems. *Journal of Geophysical Research: Biogeosciences*, 111(G3).

<https://doi.org/10.1029/2005JG000036>

Laemmel, T., Mohr, M., Schack-Kirchner, H., Schindler, D., & Maier, M. (2017). Direct Observation of Wind-Induced Pressure-Pumping on Gas Transport in Soil. *Soil Science Society of America Journal*, 81(4), 770–774. <https://doi.org/10.2136/sssaj2017.01.0034n>

Lafleur, P., Humphreys, E., St.Louis, V., Myklebust, M., Papakyriakou, T., Poissant, L., Barker, J., Pilote, M., & Swystun, K. (2012). Variation in Peak Growing Season Net Ecosystem Production

Across the Canadian Arctic. *Environmental Science & Technology*, 46, 7971–7977.

<https://doi.org/10.1021/es300500m>

Lafleur, P. M., & Humphreys, E. R. (2008). Spring warming and carbon dioxide exchange over low Arctic tundra in central Canada. *Global Change Biology*, 14(4), 740–756.

<https://doi.org/10.1111/j.1365-2486.2007.01529.x>

Lai, D. Y. F. (2009). Methane Dynamics in Northern Peatlands: A Review. *Pedosphere*, 19(4), 409–421.

Lantz, T. C., & Kokelj, S. V. (2008). Increasing rates of retrogressive thaw slump activity in the Mackenzie Delta region, N.W.T., Canada. *Geophysical Research Letters*, 35(6).

<https://doi.org/10.1029/2007GL032433>

Lantz, T. C., & Turner, K. W. (2015). Changes in lake area in response to thermokarst processes and climate in Old Crow Flats, Yukon. *Journal of Geophysical Research-Biogeosciences*, 120(3), 513–524. <https://doi.org/10.1002/2014JG002744>

Lantz, T., Kokelj, S., & Fraser, R. (2015). Ecological recovery in an Arctic delta following widespread saline incursion. *Ecological Applications*, 25, 140915094202006.

<https://doi.org/10.1890/14-0239.1>

Lara, M. J., McGuire, A. D., Euskirchen, E. S., Genet, H., Yi, S., Rutter, R., Iversen, C., Sloan, V., & Wullschleger, S. D. (2020). Local-scale Arctic tundra heterogeneity affects regional-scale carbon dynamics. *Nature Communications*, 11(1), 4925. <https://doi.org/10.1038/s41467-020-18768-z>

Lara, M. J., McGuire, A. D., Euskirchen, E. S., Tweedie, C. E., Hinkel, K. M., Skurikhin, A. N., Romanovsky, V. E., Grosse, G., Bolton, W. R., & Genet, H. (2015). Polygonal tundra geomorphological change in response to warming alters future CO₂ and CH₄ flux on the Barrow Peninsula. *Global Change Biology*, 21(4), 1634–1651. <https://doi.org/10.1111/gcb.12757>

Lee, H., Schuur, E., Inglett, K., Lavoie, M., & Chanton, J. (2012). *The rate of permafrost carbon release under aerobic and anaerobic conditions and its potential effects on climate.*

<https://doi.org/10.1111/J.1365-2486.2011.02519.X>

Lee, J. H. W., Huang, Y., Dickman, M., & Jayawardena, A. W. (2003). Neural network modelling of coastal algal blooms. *Ecological Modelling*, 159(2), 179–201. [https://doi.org/10.1016/S0304-3800\(02\)00281-8](https://doi.org/10.1016/S0304-3800(02)00281-8)

Lee, S.-C., Christen, A., Black, A. T., Johnson, M. S., Jassal, R. S., Ketler, R., Nesic, Z., & Merkens, M. (2017). Annual greenhouse gas budget for a bog ecosystem undergoing restoration by rewetting. *Biogeosciences*, 14(11), 2799–2814.

Lee, S.-C., Christen, A., Black, T. A., Jassal, R. S., Briegel, F., & Nesic, Z. (2021). Combining flux variance similarity partitioning with artificial neural networks to gap-fill measurements of net ecosystem production of a Pacific Northwest Douglas-fir stand. *Agricultural and Forest Meteorology*, 303, 108382. <https://doi.org/10.1016/j.agrformet.2021.108382>

Liboiron, M. (2021). Decolonizing geoscience requires more than equity and inclusion. *Nature Geoscience*, 14(12), 876–877. <https://doi.org/10.1038/s41561-021-00861-7>

Liu, Y., Liu, X., Cheng, K., Li, L., Zhang, X., Zheng, J., Zheng, J., & Pan, G. (2016). Responses of Methanogenic and Methanotrophic Communities to Elevated Atmospheric CO₂ and Temperature in a Paddy Field. *Frontiers in Microbiology*, 7. <https://doi.org/10.3389/fmicb.2016.01895>

Livensperger, C., Steltzer, H., Darrouzet-Nardi, A., Sullivan, P. F., Wallenstein, M., & Weintraub, M. N. (2019). Experimentally warmer and drier conditions in an Arctic plant community reveal microclimatic controls on senescence. *Ecosphere*, 10(4), e02677. <https://doi.org/10.1002/ecs2.2677>

- Liyanaarachchi, V. C., Nishshanka, G. K. S. H., Nimarshana, P. H. V., Ariyadasa, T. U., & Attalage, R. A. (2020). Development of an artificial neural network model to simulate the growth of microalga Chlorella vulgaris incorporating the effect of micronutrients. *Journal of Biotechnology*.
- Lucht, W., Schaaf, C. B., & Strahler, A. H. (2000). An algorithm for the retrieval of albedo from space using semiempirical BRDF models. *IEEE Transactions on Geoscience and Remote Sensing*, 38(2), 977–998. <https://doi.org/10.1109/36.841980>
- Lüers, J., Westermann, S., Piel, K., & Boike, J. (2014). Annual CO₂ budget and seasonal CO₂ exchange signals at a high Arctic permafrost site on Spitsbergen, Svalbard archipelago. *Biogeosciences*, 11(22), 6307–6322. <https://doi.org/10.5194/bg-11-6307-2014>
- Lund, M., Lafleur, P. M., Roulet, N. T., Lindroth, A., Christensen, T. R., Aurela, M., Chojnicki, B. H., Flanagan, L. B., Humphreys, E. R., Laurila, T., Oechel, W. C., Olejnik, J., Rinne, J., Schubert, P., & Nilsson, M. B. (2010). Variability in exchange of CO₂ across 12 northern peatland and tundra sites. *Global Change Biology*, 16(9), 2436–2448. <https://doi.org/10.1111/j.1365-2486.2009.02104.x>
- Mackay, J., R. (1981). *An experiment in lake drainage, Richards Island, Northwest Territories: A progress report*. 63–68.
- Mackay, J. R. (1999). Periglacial features developed on the exposed lake bottoms of seven lakes that drained rapidly after 1950, Tuktoyaktuk Peninsula area, western Arctic coast, Canada. *Permafrost and Periglacial Processes*, 10(1), 39–63. [https://doi.org/10.1002/\(SICI\)1099-1530\(199901/03\)10:1<39::AID-PPP305>3.3.CO;2-I](https://doi.org/10.1002/(SICI)1099-1530(199901/03)10:1<39::AID-PPP305>3.3.CO;2-I)
- Mackay, J. R. (2000). Thermally induced movements in ice-wedge polygons, western Arctic coast: A long-term study. *Géographie Physique et Quaternaire*, 54(1), 41–68.

Mackay, J. R., & Burn, C. R. (2002). The first 20 years (1978-1979 to 1998-1999) of active-layer development, Illisarvik experimental drained lake site, western Arctic coast, Canada. *Canadian Journal of Earth Sciences*, 39(11), 1657–1674. <https://doi.org/10.1139/E02-068>

Männistö, E., Korrensalo, A., Alekseychik, P., Mammarella, I., Peltola, O., Vesala, T., & Tuittila, E.-S. (2019). Multi-year methane ebullition measurements from water and bare peat surfaces of a patterned boreal bog. *Biogeosciences*, 16(11), 2409–2421. <https://doi.org/10.5194/bg-16-2409-2019>

Marsh, P., Russell, M., Pohl, S., Haywood, H., & Onclin, C. (2009). Changes in thaw lake drainage in the Western Canadian Arctic from 1950 to 2000. *Hydrological Processes*, 23(1), 145–158. <https://doi.org/10.1002/hyp.7179>

Martin, A. F., Lantz, T. C., & Humphreys, E. R. (2017). Ice wedge degradation and CO₂ and CH₄ emissions in the Tuktoyaktuk Coastlands, Northwest Territories. *Arctic Science*, 4(1), 130–145.

Mauder, M., & Foken, T. (2004). *Documentation and Instruction Manual of the Eddy Covariance Software Package TK2*. <https://doi.org/10.5194/bg-5-451-2008>

McDermitt, D., Burba, G., Xu, L., Anderson, T., Komissarov, A., Riensche, B., Schedlbauer, J., Starr, G., Zona, D., Oechel, W., Oberbauer, S., & Hastings, S. (2011). A new low-power, open-path instrument for measuring methane flux by eddy covariance. *Applied Physics B*, 102(2), 391–405. <https://doi.org/10.1007/s00340-010-4307-0>

McFeeters, S. K. (1996). The use of the Normalized Difference Water Index (NDWI) in the delineation of open water features. *International Journal of Remote Sensing*, 17(7), 1425–1432.

McGuire, A. D., Lawrence, D. M., Koven, C., Clein, J. S., Burke, E., Chen, G., Jafarov, E., MacDougall, A. H., Marchenko, S., Nicolsky, D., Peng, S., Rinke, A., Ciais, P., Gouttevin, I., Hayes, D. J., Ji, D., Krinner, G., Moore, J. C., Romanovsky, V., ... Zhuang, Q. (2018).

- Dependence of the evolution of carbon dynamics in the northern permafrost region on the trajectory of climate change. *Proceedings of the National Academy of Sciences*, 115(15), 3882–3887. <https://doi.org/10.1073/pnas.1719903115>
- Meeus, J. (1991). Astronomical algorithms. *Richmond*.
- Meijide, A., Manca, G., Goded, I., Magliulo, V., Tommasi, P. di, Seufert, G., & Cescatti, A. (2011). Seasonal trends and environmental controls of methane emissions in a rice paddy field in Northern Italy. *Biogeosciences*, 8(12), 3809–3821. <https://doi.org/10.5194/bg-8-3809-2011>
- Mekonnen, Z. A., Riley, W. J., Berner, L. T., Bouskill, N. J., Torn, M. S., Iwahana, G., Breen, A. L., Myers-Smith, I. H., Criado, M. G., Liu, Y., Euskirchen, E. S., Goetz, S. J., Mack, M. C., & Grant, R. F. (2021). Arctic tundra shrubification: A review of mechanisms and impacts on ecosystem carbon balance. *Environmental Research Letters*, 16(5), 053001.
<https://doi.org/10.1088/1748-9326/abf28b>
- Melesse, A. M., & Hanley, R. S. (2005). Artificial neural network application for multi-ecosystem carbon flux simulation. *Ecological Modelling*, 189(3), 305–314.
<https://doi.org/10.1016/j.ecolmodel.2005.03.014>
- Merbold, L., Kutsch, W. L., Corradi, C., Kolle, O., Rebmann, C., Stoy, P. C., Zimov, S. A., & Schulze, E.-D. (2009). Artificial drainage and associated carbon fluxes (CO₂/CH₄) in a tundra ecosystem. *Global Change Biology*, 15(11), 2599–2614. <https://doi.org/10.1111/j.1365-2486.2009.01962.x>
- Mo, Y., Qi, X., Li, A., Zhang, X., & Jia, Z. (2020). Active Methanotrophs in Suboxic Alpine Swamp Soils of the Qinghai–Tibetan Plateau. *Frontiers in Microbiology*, 11, 580866.
<https://doi.org/10.3389/fmicb.2020.580866>

Moffat, A. M., Beckstein, C., Churkina, G., Mund, M., & Heimann, M. (2010). Characterization of ecosystem responses to climatic controls using artificial neural networks. *Global Change Biology*, 16(10), 2737–2749. <https://doi.org/10.1111/j.1365-2486.2010.02171.x>

Moffat, A. M., Papale, D., Reichstein, M., Hollinger, D. Y., Richardson, A. D., Barr, A. G., Beckstein, C., Braswell, B. H., Churkina, G., Desai, A. R., Falge, E., Gove, J. H., Heimann, M., Hui, D., Jarvis, A. J., Kattge, J., Noormets, A., & Stauch, V. J. (2007). Comprehensive comparison of gap-filling techniques for eddy covariance net carbon fluxes. *Agricultural and Forest Meteorology*, 147(3–4), 209–232. <https://doi.org/10.1016/j.agrformet.2007.08.011>

Moffat, N., Lantz, T., Fraser, R., & Olthof, I. (2016). Recent Vegetation Change (1980–2013) in the Tundra Ecosystems of the Tuktoyaktuk Coastlands, NWT, Canada. *Arctic, Antarctic, and Alpine Research*, 48, 581–597. <https://doi.org/10.1657/AAAR0015-063>

Mohr, M., Laemmel, T., Maier, M., & Schindler, D. (2016). Analysis of Air Pressure Fluctuations and Topsoil Gas Concentrations within a Scots Pine Forest. *Atmosphere*, 7(10), 125. <https://doi.org/10.3390/atmos7100125>

Moncrieff, J. B., Massheder, J. M., de Bruin, H., Elbers, J., Friberg, T., Heusinkveld, B., Kabat, P., Scott, S., Soegaard, H., & Verhoef, A. (1997). A system to measure surface fluxes of momentum, sensible heat, water vapour and carbon dioxide. *Journal of Hydrology*, 188, 589–611. [https://doi.org/10.1016/S0022-1694\(96\)03194-0](https://doi.org/10.1016/S0022-1694(96)03194-0)

Moncrieff, J., Clement, R., Finnigan, J., & Meyers, T. (2004). Averaging, Detrending, and Filtering of Eddy Covariance Time Series. In X. Lee, W. Massman, & B. Law (Eds.), *Handbook of Micrometeorology* (pp. 7–31). Springer Netherlands. https://doi.org/10.1007/1-4020-2265-4_2

- Morse, P. D., & Burn, C. R. (2013). Field observations of syngenetic ice wedge polygons, outer Mackenzie Delta, western Arctic coast, Canada. *Journal of Geophysical Research-Earth Surface*, 118(3), 1320–1332. <https://doi.org/10.1002/jgrf.20086>
- Morse, P. D., Burn, C. R., & Kokelj, S. V. (2012). Influence of snow on near-surface ground temperatures in upland and alluvial environments of the outer Mackenzie Delta, Northwest Territories. *Canadian Journal of Earth Sciences*, 49(8), 895–913. <https://doi.org/10.1139/e2012-012>
- Muñoz, S., J. (2019). ERA5-Land hourly data from 1981 to present [Data set]. Copernicus Climate Change Service (C3S) Climate Data Store (CDS). <https://doi.org/10.24381/CDS.E2161BAC>
- Myers-Smith, I. H., Forbes, B. C., Wilmking, M., Hallinger, M., Lantz, T., Blok, D., Tape, K. D., Macias-Fauria, M., Sass-Klaassen, U., Lévesque, E., Boudreau, S., Ropars, P., Hermanutz, L., Trant, A., Collier, L. S., Weijers, S., Rozema, J., Rayback, S. A., Schmidt, N. M., ... Hik, D. S. (2011). Shrub expansion in tundra ecosystems: Dynamics, impacts and research priorities. *Environmental Research Letters*, 6(4), 045509. <https://doi.org/10.1088/1748-9326/6/4/045509>
- Myers-Smith, I. H., Grabowski, M. M., Thomas, H. J. D., Angers-Blondin, S., Daskalova, G. N., Bjorkman, A. D., Cunliffe, A. M., Assmann, J. J., Boyle, J. S., McLeod, E., McLeod, S., Joe, R., Lennie, P., Arey, D., Gordon, R. R., & Eckert, C. D. (2019). Eighteen years of ecological monitoring reveals multiple lines of evidence for tundra vegetation change. *Ecological Monographs*, 89(2), e01351. <https://doi.org/10.1002/ecm.1351>
- Myers-Smith, I. H., Kerby, J. T., Phoenix, G. K., Bjerke, J. W., Epstein, H. E., Assmann, J. J., John, C., Andreu-Hayles, L., Angers-Blondin, S., Beck, P. S. A., Berner, L. T., Bhatt, U. S., Bjorkman, A. D., Blok, D., Bryn, A., Christiansen, C. T., Cornelissen, J. H. C., Cunliffe, A. M., Elmendorf,

- S. C., ... Wipf, S. (2020). Complexity revealed in the greening of the Arctic. *Nature Climate Change*, 10(2), 106–117. <https://doi.org/10.1038/s41558-019-0688-1>
- Myneni, R., Knyazikhin, Y., & Park, T. (2015). *MOD15A2H MODIS/Terra Leaf Area Index/FPAR 8-Day L4 Global 500m SIN Grid V006* [Data set]. NASA EOSDIS Land Processes DAAC. <https://doi.org/10.5067/MODIS/MOD15A2H.006>
- Nadeau, D. F., Rousseau, A. N., Coursolle, C., Margolis, H. A., & Parlange, M. B. (2013). Summer methane fluxes from a boreal bog in northern Quebec, Canada, using eddy covariance measurements. *Atmospheric Environment*, 81, 464–474. <https://doi.org/10.1016/j.atmosenv.2013.09.044>
- Natali, S. M., Holdren, J. P., Rogers, B. M., Trehearne, R., Duffy, P. B., Pomerance, R., & MacDonald, E. (2021). Permafrost carbon feedbacks threaten global climate goals. *Proceedings of the National Academy of Sciences*, 118(21). <https://doi.org/10.1073/pnas.2100163118>
- Natali, S. M., Watts, J. D., Rogers, B. M., Potter, S., Ludwig, S. M., Selbmann, A.-K., Sullivan, P. F., Abbott, B. W., Arndt, K. A., Birch, L., Björkman, M. P., Bloom, A. A., Celis, G., Christensen, T. R., Christiansen, C. T., Commane, R., Cooper, E. J., Crill, P., Czimczik, C., ... Zona, D. (2019). Large loss of CO₂ in winter observed across the northern permafrost region. *Nature Climate Change*, 9(11), 852–857. <https://doi.org/10.1038/s41558-019-0592-8>
- National Research Council Canada. (2012, August 7). *Sunrise/sunset calculator*. <https://nrc.canada.ca/en/research-development/products-services/software-applications/sun-calculator/>
- Nay, S. M., Mattson, K. G., & Bormann, B. T. (1994). Biases of Chamber Methods for Measuring Soil CO₂ Efflux Demonstrated with a Laboratory Apparatus. *Ecology*, 75(8), 2460–2463. <https://doi.org/10.2307/1940900>

NOAA. (n.d.). *Solar Calculation Details*. Retrieved March 7, 2022, from

<https://gml.noaa.gov/grad/solcalc/calcdetails.html>

Norman, J. M., Kucharik, C. J., Gower, S. T., Baldocchi, D. D., Crill, P. M., Rayment, M., Savage, K., & Striegl, R. G. (1997). A comparison of six methods for measuring soil-surface carbon dioxide fluxes. *Journal of Geophysical Research: Atmospheres*, 102(D24), 28771–28777.

<https://doi.org/10.1029/97JD01440>

NWT Water Resources. (2019). *Tagul Automated Weather Station Data (August 2008—July—2019)*.

NWT Water Resources Department. Yellowknife, NWT.

Olden, J. D., Joy, M. K., & Death, R. G. (2004). An accurate comparison of methods for quantifying variable importance in artificial neural networks using simulated data. *Ecological Modelling*, 178(3), 389–397. <https://doi.org/10.1016/j.ecolmodel.2004.03.013>

Olefeldt, D., Turetsky, M. R., Crill, P. M., & McGuire, A. D. (2013). Environmental and physical controls on northern terrestrial methane emissions across permafrost zones. *Global Change Biology*, 19(2), 589–603. <https://doi.org/10.1111/gcb.12071>

Olivas, P. C., Oberbauer, S. F., Tweedie, C., Oechel, W. C., Lin, D., & Kuchy, A. (2011). Effects of Fine-Scale Topography on CO₂ Flux Components of Alaskan Coastal Plain Tundra: Response to Contrasting Growing Seasons. *Arctic, Antarctic, and Alpine Research*, 43(2), 256–266.

<https://doi.org/10.1657/1938-4246-43.2.256>

Olthof, I., Fraser, R. H., & Schmitt, C. (2015). Landsat-based mapping of thermokarst lake dynamics on the Tuktoyaktuk Coastal Plain, Northwest Territories, Canada since 1985. *Remote Sensing of Environment*, 168, 194–204. <https://doi.org/10.1016/j.rse.2015.07.001>

O'Neill, H. B., & Burn, C. R. (2012). Physical and temporal factors controlling the development of near-surface ground ice at Illisarvik, western Arctic coast, Canada. *Canadian Journal of Earth Sciences*, 49(9), 1096–1110.

Ovenden, L. (1986). Vegetation Colonizing the Bed of a Recently Drained Thermokarst Lake (illisarvik), Northwest-Territories. *Canadian Journal of Botany-Revue Canadienne De Botanique*, 64(11), 2688–2692.

Pallandt, M., Kumar, J., Mauritz, M., Schuur, E., Virkkala, A.-M., Celis, G., Hoffman, F., & Göckede, M. (2021). Representativeness assessment of the pan-Arctic eddy-covariance site network, and optimized future enhancements. *Biogeosciences Discussions*, 1–42.

<https://doi.org/10.5194/bg-2021-133>

Papale, D., Reichstein, M., Aubinet, M., Canfora, E., Bernhofer, C., Kutsch, W., Longdoz, B., Rambal, S., Valentini, R., Vesala, T., & others. (2006). Towards a standardized processing of Net Ecosystem Exchange measured with eddy covariance technique: Algorithms and uncertainty estimation. *Biogeosciences*, 3(4), 571–583.

Papale, D., & Valentini, R. (2003). A new assessment of European forests carbon exchanges by eddy fluxes and artificial neural network spatialization. *Global Change Biology*, 9(4), 525–535.

<https://doi.org/10.1046/j.1365-2486.2003.00609.x>

Paul-Limoges, E., Christen, A., Coops, N., Black, T., & Trofymow, J. (2013). Estimation of aerodynamic roughness of a harvested Douglas-fir forest using airborne LiDAR. *Remote Sensing of Environment*, 136, 225–233. <https://doi.org/10.1016/j.rse.2013.05.007>

Prowse, T. D., Furgal, C., Melling, H., & Smith, S. L. (2009). Implications of Climate Change for Northern Canada: The Physical Environment. *AMBIO: A Journal of the Human Environment*, 38(5), 266–271. <https://doi.org/10.1579/0044-7447-38.5.266>

Ramirez, J. A., Baird, A. J., Coulthard, T. J., & Waddington, J. M. (2015). Ebullition of methane from peatlands: Does peat act as a signal shredder? *Geophysical Research Letters*, 42(9), 3371–3379.

<https://doi.org/10.1002/2015GL063469>

Raz-Yaseef, N., Torn, M. S., Wu, Y., Billesbach, D. P., Liljedahl, A. K., Kneafsey, T. J., Romanovsky, V. E., Cook, D. R., & Wullschleger, S. D. (2017). Large CO₂ and CH₄ emissions from polygonal tundra during spring thaw in northern Alaska. *Geophysical Research Letters*, 44(1), 504–513. <https://doi.org/10.1002/2016GL071220>

Riederer, M., Serafimovich, A., & Foken, T. (2014). Net ecosystem CO₂ exchange measurements by the closed chamber method and the eddy covariance technique and their dependence on atmospheric conditions. *Atmospheric Measurement Techniques*, 7(4), 1057–1064.

<https://doi.org/10.5194/amt-7-1057-2014>

Rienecker, M. N., Suarez, M. J., Todling, R., Bacmeister, J., Takacs, L., Liu, H. C., Gu, W., Sienkiewicz, M., Koster, R. D., Gelaro, R., Stajner, I., & Nielsen, J. E. (2008). The GEOS-5 Data Assimilation System—Documentation of Versions 5.0.1, 5.1.0, and 5.2.0. In M. J. Suarez (Ed.), *Technical Report Series on Global Modeling and Data Assimilation* (Vol. 27). National Aeronautics and Space Administration, Washington, DC.

Rinne, J., Ruitta, T., Pihlatie, M., Aurela, M., Haapanala, S., Tuovinen, J.-P., Tuittila, E.-S., & Vesala, T. (2007). Annual cycle of methane emission from a boreal fen measured by the eddy covariance technique. *Tellus Series B-Chemical and Physical Meteorology*, 59(3), 449–457.

<https://doi.org/10.1111/j.1600-0889.2007.00261.x>

Rößger, N., Wille, C., Holl, D., Göckede, M., & Kutzbach, L. (2019). Scaling and balancing carbon dioxide fluxes in a heterogeneous tundra ecosystem of the Lena River Delta. *Biogeosciences*, 16(13), 2591–2615. <https://doi.org/10.5194/bg-16-2591-2019>

- Rößger, N., Wille, C., Veh, G., Boike, J., & Kutzbach, L. (2019). Scaling and balancing methane fluxes in a heterogeneous tundra ecosystem of the Lena River Delta. *Agricultural and Forest Meteorology*, 266–267, 243–255. <https://doi.org/10.1016/j.agrformet.2018.06.026>
- Runkle, B. R. K., Sachs, T., Wille, C., Pfeiffer, E.-M., & Kutzbach, L. (2013). Bulk partitioning the growing season net ecosystem exchange of CO₂ in Siberian tundra reveals the seasonality of its carbon sequestration strength. *Biogeosciences*, 10(3), 1337–1349. <https://doi.org/10.5194/bg-10-1337-2013>
- Running, S., Mu, Q., M., & Zhao, M. (2015). *MOD17A2H MODIS/Terra Gross Primary Productivity 8-Day L4 Global 500m SIN Grid V006 [Data set]* NASA EOSDIS Land Processes DAAC. <https://doi.org/10.5067/MODIS/MOD17A2H.006>
- Running, S. W., & Zhao, M. (2019). *Daily GPP and Annual NPP (MOD17A2H/A3H) and Year-end Gap- Filled (MOD17A2HGF/A3HGF) Products NASA Earth Observing System MODIS Land Algorithm (For Collection 6)*. 35.
- Sachs, T., Giebels, M., Boike, J., & Kutzbach, L. (2010). Environmental controls on CH₄ emission from polygonal tundra on the microsite scale in the Lena river delta, Siberia. *Global Change Biology*, 16(11), 3096–3110. <https://doi.org/10.1111/j.1365-2486.2010.02232.x>
- Sachs, T., Wille, C., Boike, J., & Kutzbach, L. (2008). Environmental controls on ecosystem-scale CH₄ emission from polygonal tundra in the Lena River Delta, Siberia. *Journal of Geophysical Research-Biogeosciences*, 113, G00A03. <https://doi.org/10.1029/2007JG000505>
- Sarle, W. S. (1995). Stopped Training and Other Remedies for Overfitting. *Proceedings of the 27th Symposium on the Interface of Computing Science and Statistics*, 352–360.

Sarle, W. S. (2014). *Comp.ai.neural-nets FAQ, Part 3 of 7: GeneralizationSection—How many hidden units should I use?* Comp.Ai.Neural-Nets FAQ. <http://www.faqs.org/faqs/ai-faq/neural-nets/part3/section-10.html>

Schaaf, C. (2021). *MODIS User Guide V006 and V006.1*.

https://www.umb.edu/spectralmass/terra_aqua_modis/v006/introduction

Schaaf, C., Gao, F., Strahler, A., Lucht, W., Li, X., Tsang, T., Strugnell, N., Zhang, X., Jin, Y., Muller, J., Lewis, P., Barnsley, M., Hobson, P., Disney, M., Roberts, G., Dunderdale, M., Doll, C., d'Entremont, R., Hu, B., ... Roy, D. (2002). First operational BRDF, albedo nadir reflectance products from MODIS. *Remote Sensing of Environment*, 83(1–2), 135–148. [https://doi.org/10.1016/S0034-4257\(02\)00091-3](https://doi.org/10.1016/S0034-4257(02)00091-3)

Schaefer, K., & Jafarov, E. (2016). A parameterization of respiration in frozen soils based on substrate availability. *Biogeosciences*, 13(7), 1991–2001. <https://doi.org/10.5194/bg-13-1991-2016>

Schäfer, K. V. R., Duman, T., Tomasicchio, K., Tripathee, R., & Sturtevant, C. (2019). Carbon dioxide fluxes of temperate urban wetlands with different restoration history. *Agricultural and Forest Meteorology*, 275, 223–232. <https://doi.org/10.1016/j.agrformet.2019.05.026>

Schmid, H. P. (2002). Footprint modeling for vegetation atmosphere exchange studies: A review and perspective. *Agricultural and Forest Meteorology*, 113(1–4), 159–183. [https://doi.org/10.1016/S0168-1923\(02\)00107-7](https://doi.org/10.1016/S0168-1923(02)00107-7)

Schmid, H. P., & Lloyd, C. R. (1999). Spatial representativeness and the location bias of flux footprints over inhomogeneous areas. *Agricultural and Forest Meteorology*, 93, 195–209. [https://doi.org/10.1016/S0168-1923\(98\)00119-1](https://doi.org/10.1016/S0168-1923(98)00119-1)

- Schuur, E. A., Bockheim, J., Canadell, J. G., Euskirchen, E., Field, C. B., Goryachkin, S. V., Hagemann, S., Kuhry, P., Lafleur, P. M., & Lee, H. (2008). Vulnerability of permafrost carbon to climate change: Implications for the global carbon cycle. *AIBS Bulletin*, 58(8), 701–714.
- Schuur, E. a. G., McGuire, A. D., Schädel, C., Grosse, G., Harden, J. W., Hayes, D. J., Hugelius, G., Koven, C. D., Kuhry, P., Lawrence, D. M., Natali, S. M., Olefeldt, D., Romanovsky, V. E., Schaefer, K., Turetsky, M. R., Treat, C. C., & Vonk, J. E. (2015). Climate change and the permafrost carbon feedback. *Nature*, 520(7546), 171–179. <https://doi.org/10.1038/nature14338>
- Seider, J. H., Lantz, T. C., Hermosilla, T., Wulder, M. A., & Wang, J. A. (2022). Biophysical Determinants of Shifting Tundra Vegetation Productivity in the Beaufort Delta Region of Canada. *Ecosystems*. <https://doi.org/10.1007/s10021-021-00725-6>
- Sellers, P. J. (1987). Canopy reflectance, photosynthesis, and transpiration, II. The role of biophysics in the linearity of their interdependence. *Remote Sensing of Environment*, 21(2), 143–183. [https://doi.org/10.1016/0034-4257\(87\)90051-4](https://doi.org/10.1016/0034-4257(87)90051-4)
- Serikova, S., Pokrovsky, O. S., Laudon, H., Krickov, I. V., Lim, A. G., Manasypov, R. M., & Karlsson, J. (2019). High carbon emissions from thermokarst lakes of Western Siberia. *Nature Communications*, 10(1), 1552. <https://doi.org/10.1038/s41467-019-09592-1>
- Serrano-silva, N., Sarria-guzmán, Y., Dendooven, L., & Luna-guido, M. (2014). Methanogenesis and Methanotrophy in Soil: A Review. *Pedosphere*, 24(3), 291–307. [https://doi.org/10.1016/S1002-0160\(14\)60016-3](https://doi.org/10.1016/S1002-0160(14)60016-3)
- Skeeter, J. (2019). *June-Skeeter/Illisarvik_CFluxes*. https://github.com/June-Spaceboots/Illisarvik_CFluxes (Original work published 2019)

Skeeter, J., Christen, A., & Henry, G. H. R. (2022). Controls on carbon dioxide and methane fluxes from a low-center polygonal peatland in the Mackenzie River Delta, Northwest Territories.

Arctic Science, 1–27. <https://doi.org/10.1139/as-2021-0034>

Skeeter, J., Christen, A., Laforce, A.-A., Humphreys, E., & Henry, G. H. R. (2020). Vegetation Influence and Environmental Controls on Greenhouse Gas Fluxes from a Drained Thermokarst Lake in the Western Canadian Arctic. *Biogeosciences Discussions*, 1–25.

<https://doi.org/10.5194/bg-2019-477>

Smith, M. (1993). *Neural Networks for Statistical Modeling*. John Wiley & Sons, Inc.

Steedman, A., Lantz, T., & Kokelj, S. (2017). Spatio-Temporal Variation in High-Centre Polygons and Ice-Wedge Melt Ponds, Tuktoyaktuk Coastlands, Northwest Territories. *Permafrost and Periglacial Processes*, 28, n/a-n/a. <https://doi.org/10.1002/ppp.1880>

Streletschi, D., Anisimov, O., & Vasiliev, A. (2015). Chapter 10—Permafrost Degradation. In J. F. Shroder, W. Haeberli, & C. Whiteman (Eds.), *Snow and Ice-Related Hazards, Risks, and Disasters* (pp. 303–344). Academic Press. <https://doi.org/10.1016/B978-0-12-394849-6.00010-X>

Stuecker, M. F., Bitz, C. M., Armour, K. C., Proistosescu, C., Kang, S. M., Xie, S.-P., Kim, D., McGregor, S., Zhang, W., Zhao, S., Cai, W., Dong, Y., & Jin, F.-F. (2018). Polar amplification dominated by local forcing and feedbacks. *Nature Climate Change*, 8(12), 1076–1081.

<https://doi.org/10.1038/s41558-018-0339-y>

Stull, R. B. (Ed.). (1988). *An Introduction to Boundary Layer Meteorology*. Springer Netherlands.

<http://link.springer.com/10.1007/978-94-009-3027-8>

Sturtevant, C. S., Oechel, W. C., Zona, D., Kim, Y., & Emerson, C. E. (2012). Soil moisture control over autumn season methane flux, Arctic Coastal Plain of Alaska. *Biogeosciences*, 9(4), 1423–1440. <https://doi.org/10.5194/bg-9-1423-2012>

Sulla-Menashe, D., Gray, J. M., Abercrombie, S. P., & Friedl, M. A. (2019). Hierarchical mapping of annual global land cover 2001 to present: The MODIS Collection 6 Land Cover product. *Remote Sensing of Environment*, 222, 183–194. <https://doi.org/10.1016/j.rse.2018.12.013>

Sweet, S. K., Griffin, K. L., Steltzer, H., Gough, L., & Boelman, N. T. (2015). Greater deciduous shrub abundance extends tundra peak season and increases modeled net CO₂ uptake. *Global Change Biology*, 21(6), 2394–2409. <https://doi.org/10.1111/gcb.12852>

Tank, S., Lesack, L., & Hesslein, R. (2009). Northern Delta Lakes as Summertime CO₂ Absorbers Within the Arctic Landscape. *Ecosystems*, 12, 144–157. <https://doi.org/10.1007/s10021-008-9213-5>

Tao, J., Zhu, Q., Riley, W. J., & Neumann, R. B. (2021). Warm-season net CO₂ uptake outweighs cold-season emissions over Alaskan North Slope tundra under current and RCP8.5 climate. *Environmental Research Letters*, 16(5), 055012. <https://doi.org/10.1088/1748-9326/abf6f5>

Tarnocai, C., Canadell, J. G., Schuur, E. A. G., Kuhry, P., Mazhitova, G., & Zimov, S. (2009). Soil organic carbon pools in the northern circumpolar permafrost region. *Global Biogeochemical Cycles*, 23(2), n/a-n/a. <https://doi.org/10.1029/2008GB003327>

Tetko, I. V., Livingstone, D. J., & Luik, A. I. (1995). Neural network studies. 1. Comparison of overfitting and overtraining. *Journal of Chemical Information and Modeling*, 35(5), 826–833. <https://doi.org/10.1021/ci00027a006>

Tieszen, L. L. (2018). Photosynthesis and Respiration in Arctic Tundra Grasses: Field Light Intensity and Temperature Responses. *Arctic and Alpine Research*, 5(3), 239–251. <https://doi.org/10.1080/00040851.1973.12003703>

Tramontana, G., Migliavacca, M., Jung, M., Reichstein, M., Keenan, T. F., Camps-Valls, G., Ogee, J., Verrelst, J., & Papale, D. (2020). Partitioning net carbon dioxide fluxes into photosynthesis and

respiration using neural networks. *Global Change Biology*, 26(9), 5235–5253.

<https://doi.org/10.1111/gcb.15203>

Turetsky, M. R., Abbott, B. W., Jones, M. C., Anthony, K. W., Olefeldt, D., Schuur, E. A. G., Grosse, G., Kuhry, P., Hugelius, G., Koven, C., Lawrence, D. M., Gibson, C., Sannel, A. B. K., & McGuire, A. D. (2020). Carbon release through abrupt permafrost thaw. *Nature Geoscience*, 13(2), 138–143. <https://doi.org/10.1038/s41561-019-0526-0>

van der Molen, M. K., Huissteden, J. van, Parmentier, F. J. W., Petrescu, A. M. R., Dolman, A. J., Maximov, T. C., Kononov, A. V., Karsanaev, S. V., & Suzdalov, D. A. (2007). The growing season greenhouse gas balance of a continental tundra site in the Indigirka lowlands, NE Siberia. *Biogeosciences*, 4(6), 985–1003. <https://doi.org/10.5194/bg-4-985-2007>

van Huissteden, J., Berrittella, C., Parmentier, F. J. W., Mi, Y., Maximov, T. C., & Dolman, A. J. (2011). Methane emissions from permafrost thaw lakes limited by lake drainage. *Nature Climate Change*, 1(2), 119–123. <https://doi.org/10.1038/nclimate1101>

van Huissteden, J., Maximov, T. C., & Dolman, A. J. (2005). High methane flux from an arctic floodplain (Indigirka lowlands, eastern Siberia). *Journal of Geophysical Research: Biogeosciences*, 110(G2). <https://doi.org/10.1029/2005JG000010>

Vesala, T., Kljun, N., Rannik, Ü., Rinne, J., Sogachev, A., Markkanen, T., Sabelfeld, K., Foken, Th., & Leclerc, M. Y. (2008). Flux and concentration footprint modelling: State of the art. *Environmental Pollution*, 152(3), 653–666. <https://doi.org/10.1016/j.envpol.2007.06.070>

Vickers, D., & Mahrt, L. (1997). Quality Control and Flux Sampling Problems for Tower and Aircraft Data. *Journal of Atmospheric and Oceanic Technology*, 14(3), 512–526. <https://doi.org/10.1175/1520-0426>

- Virkkala, A.-M., Virtanen, T., Lehtonen, A., Rinne, J., & Luoto, M. (2018). The current state of CO₂ flux chamber studies in the Arctic tundra: A review. *Progress in Physical Geography: Earth and Environment*, 42(2), 162–184. <https://doi.org/10.1177/0309133317745784>
- Vitale, D., Bilancia, M., & Papale, D. (2018). A Multiple Imputation Strategy for Eddy Covariance Data. *Journal of Environmental Informatics*, 34(2), 68-87–87.
- Walker, D. A., Raynolds, M. K., Daniëls, F. J. A., Einarsson, E., Elvebakk, A., Gould, W. A., Katenin, A. E., Kholod, S. S., Markon, C. J., Melnikov, E. S., Moskalenko, N. G., Talbot, S. S., Yurtsev, B. A. (†), & Team, T. other members of the C. (2005). The Circumpolar Arctic vegetation map. *Journal of Vegetation Science*, 16(3), 267–282. <https://doi.org/10.1111/j.1654-1103.2005.tb02365.x>
- Walter, K. M., Smith, L. C., & Chapin, F. S. (2007). Methane Bubbling from Northern Lakes: Present and Future Contributions to the Global Methane Budget. *Philosophical Transactions: Mathematical, Physical and Engineering Sciences*, 365(1856), 1657–1676.
- Wang, Z.-P., & Han, X.-G. (2005). Diurnal variation in methane emissions in relation to plants and environmental variables in the Inner Mongolia marshes. *Atmospheric Environment*, 39(34), 6295–6305. <https://doi.org/10.1016/j.atmosenv.2005.07.010>
- Wanner, W., Strahler, A. H., Hu, B., Lewis, P., Muller, J.-P., Li, X., Schaaf, C. L. B., & Barnsley, M. J. (1997). Global retrieval of bidirectional reflectance and albedo over land from EOS MODIS and MISR data: Theory and algorithm. *Journal of Geophysical Research: Atmospheres*, 102(D14), 17143–17161. <https://doi.org/10.1029/96JD03295>
- Warren, F. J., & Egginton, P. (2008). Background Information: Concepts, Overviews and Approaches. *Impacts to Adaptation: Canada in a Changing Climate 2007*, 27–56.

- Webb, E., Pearman, G., & Leuning, R. (1980). Correction of Flux Measurements for Density Effects Due to Heat and Water-Vapor Transfer. *Quarterly Journal of the Royal Meteorological Society*, 106(447), 85–100. <https://doi.org/10.1002/qj.49710644707>
- Weeks, G. (2016). *Climate Change and the Fate of Dissolved Organic Carbon in the Mackenzie Delta, NWT*. <https://yorkspace.library.yorku.ca/xmlui/handle/10315/32800>
- Weigend, A. S., & Lebaron, B. (1994). *Evaluating Neural Network Predictors by Bootstrapping* (1994,35; SFB 373 Discussion Papers). Humboldt University of Berlin, Interdisciplinary Research Project 373: Quantification and Simulation of Economic Processes. <https://ideas.repec.org/p/zbw/sfb373/199435.html>
- Whalen, S. C., & Reeburgh, W. S. (1990). Consumption of atmospheric methane by tundra soils. *Nature*, 346(6280), 160–162. <https://doi.org/10.1038/346160a0>
- Wickland, K. P., Jorgenson, M. T., Koch, J. C., Kanevskiy, M., & Striegl, R. G. (2020). Carbon Dioxide and Methane Flux in a Dynamic Arctic Tundra Landscape: Decadal-Scale Impacts of Ice Wedge Degradation and Stabilization. *Geophysical Research Letters*, 47(22), e2020GL089894. <https://doi.org/10.1029/2020GL089894>
- Wilczak, J. M., Oncley, S. P., & Stage, S. A. (2001). Sonic Anemometer Tilt Correction Algorithms. *Boundary-Layer Meteorology*, 99(1), 127–150. <https://doi.org/10.1023/A:1018966204465>
- Wille, C., Kutzbach, L., Sachs, T., Wagner, D., & Pfeiffer, E.-M. (2008). Methane emission from Siberian arctic polygonal tundra: Eddy covariance measurements and modeling. *Global Change Biology*, 14(6), 1395–1408. <https://doi.org/10.1111/j.1365-2486.2008.01586.x>
- Wilson, M. A., Burn C. R., & Humphreys E. R. (2019). Vegetation Development and Variation in Near-Surface Ground Temperatures at Illisarvik, Western Arctic Coast. *Cold Regions Engineering 2019*, 687–695. <https://doi.org/10.1061/9780784482599.079>

Zhang, X. B., Vincent, L. A., Hogg, W. D., & Niitsoo, A. (2000). Temperature and precipitation trends in Canada during the 20th century. *Atmosphere-Ocean*, 38(3), 395–429.

<https://doi.org/10.1080/07055900.2000.9649654>

Zhang, X., Flato, G., Kirchmeier-Young, M., Vincent, L., Wan, H., Wang, X., Rong, R., Fyfe, J., Li, G., & Kharin, V. V. (2019). Changes in temperature and precipitation across Canada. *Canada's Changing Climate Report*, 112–193.

Zhu, X., Zhuang, Q., Gao, X., Sokolov, A., & Schlosser, C. A. (2013). Pan-Arctic land-atmospheric fluxes of methane and carbon dioxide in response to climate change over the 21st century.

Environmental Research Letters, 8(4), 045003. <https://doi.org/10.1088/1748-9326/8/4/045003>

Zona, D., Gioli, B., Commane, R., Lindaas, J., Wofsy, S. C., Miller, C. E., Dinardo, S. J., Dengel, S., Sweeney, C., Karion, A., Chang, R. Y.-W., Henderson, J. M., Murphy, P. C., Goodrich, J. P., Moreaux, V., Liljedahl, A., Watts, J. D., Kimball, J. S., Lipson, D. A., & Oechel, W. C. (2016). Cold season emissions dominate the Arctic tundra methane budget. *Proceedings of the National Academy of Sciences of the United States of America*, 113(1), 40–45.

<https://doi.org/10.1073/pnas.1516017113>

Zona, D., Lafleur, P. M., Hufkens, K., Bailey, B., Gioli, B., Burba, G., Goodrich, J. P., Liljedahl, A. K., Euskirchen, E. S., Watts, J. D., Farina, M., Kimball, J. S., Heimann, M., Göckede, M., Pallandt, M., Christensen, T. R., Mastepanov, M., López-Blanco, E., Jackowicz-Korczynski, M., ... Oechel, W. C. (2022). Earlier snowmelt may lead to late season declines in plant productivity and carbon sequestration in Arctic tundra ecosystems. *Scientific Reports*, 12(1), 3986.

<https://doi.org/10.1038/s41598-022-07561-1>

Zona, D., Lipson, D. A., Paw U, K. T., Oberbauer, S. F., Olivas, P., Gioli, B., & Oechel, W. C.

(2012). Increased CO₂ loss from vegetated drained lake tundra ecosystems due to flooding.

Global Biogeochemical Cycles, 26, GB2004. <https://doi.org/10.1029/2011GB004037>

Zona, D., Lipson, D. A., Zulueta, R. C., Oberbauer, S. F., & Oechel, W. C. (2011). Microtopographic controls on ecosystem functioning in the Arctic Coastal Plain. *Journal of Geophysical Research: Biogeosciences*, 116(G4). <https://doi.org/10.1029/2009JG001241>

Zona, D., Oechel, W. C., Kochendorfer, J., Paw U, K. T., Salyuk, A. N., Olivas, P. C., Oberbauer, S. F., & Lipson, D. A. (2009). Methane fluxes during the initiation of a large-scale water table manipulation experiment in the Alaskan Arctic tundra. *Global Biogeochemical Cycles*, 23, GB2013. <https://doi.org/10.1029/2009GB003487>

Zona, D., Oechel, W. C., Peterson, K. M., Clements, R. J., Paw U, K. T., & Ustin, S. L. (2010). Characterization of the carbon fluxes of a vegetated drained lake basin chronosequence on the Alaskan Arctic Coastal Plain. *Global Change Biology*, 16(6), 1870–1882.

<https://doi.org/10.1111/j.1365-2486.2009.02107.x>

Zulueta, R. C., Oechel, W. C., Loescher, H. W., Lawrence, W. T., & Paw U, K. T. (2011). Aircraft-derived regional scale CO₂ fluxes from vegetated drained thaw-lake basins and interstitial tundra on the Arctic Coastal Plain of Alaska. *Global Change Biology*, 17(9), 2781–2802.

<https://doi.org/10.1111/j.1365-2486.2011.02433.x>

Appendices

Appendix A

Typically, NEE is gap-filled using flux-partitioning algorithms that model ER and GPP separately using T_S and $PPFD$, respectively (e.g. Lee et al. 2017; Aubinet, 2012). However, this method requires night-time observations and thus does not perform well for Arctic summertime measurements due to the limited number of samples available during low light conditions. There are no widely agreed upon functional relationships for gap-filling NME since CH_4 production and consumption vary considerably both between different landcover types and environmental conditions. Some methods that have been used include: general linear models (GLM) (Zona et al. 2009), mean diurnal variation (Nadeau et al. 2014), and classification and regression trees (CART) (Nadeau et al. 2013; Sachs et al. 2008). We attempted to use a GLM and CART but they were not flexible enough to account for source area variability.

Neural networks (NN) are flexible machine learning methods that are ideally suited to perform non-linear, multivariate regression. They make no a priori assumptions about the functional relationships between the factors and responses. (Melesse and Hanley, 2005; Desai et al. 2008). NN are universal approximators; given enough hidden nodes a NN is capable of mapping any continuous function to an arbitrary degree of accuracy (Hornik et al. 1991). If all relevant climate and ecosystem information are available to a network, the remaining variability can be attributed to noise in the measurement (Moffat et al. 2010).

NN have been shown to be among the best performing methods for gap-filling NEE data for temperate forest and wetland sites (Papale et al. 2003; Moffat et al. 2007; Knox et al. 2016). They have also been used to gap-fill NME time series in sub-arctic wetlands, tundra sites, and wet sedge tundra (Dengel et al. 2013). NN have been used to identify and model factors

influencing NEE and to partition NEE into ER and GPP (Moffat et al. 2010). NNs have even been used to upscale fluxes from the ecosystem level to the continental scale (Dou and Yang, 2018; Papale et al, 2003).

A NN approximates a true regression function $F(X)$:

$$F(X) = t(X) - \varepsilon(X) \quad \text{EQ A1}$$

where $t(X)$ is the target function and $\varepsilon(X)$ the noise (Khosravi and Nahavandi, 2011). $X = [x_0, x_1, \dots, x_M]$ where $x_0 = 1$ is a bias term and $[x_1, \dots, x_M]$ are the independent variables. M denotes the number of independent variables. The network approximates $F(X)$ as $f(X, w)$ by mapping the relationship between X and the target. Here we used feed-forward dense NN with a single hidden layer:

$$f(X, w) = \sum_{h=1}^H \beta_h g(\sum_{m=0}^M \gamma_{hm} x_m) \quad \text{EQ A2}$$

$g(\cdot)$ is a non-linear transfer function, here we used the rectified linear activation unit (ReLU) (Anders and Korn, 1999). H denotes the number of hidden nodes in the network and must be assigned before training. Too many hidden nodes and the NN will overfit the training data, too few and it will underfit. Early stopping will prevent NN from overfitting training sets (Weigend, 1993; Sarle, 1995; Tetko et al. 1995). Therefore, it is more important to ensure a NN has enough hidden nodes to adequately map the target function (Smith, 1994). We set H to a function M , the number of training samples (N), and the number of targets (1):

$$H = \frac{N}{a*(M+1)} \quad \text{EQ A3}$$

This rule of thumb ensures a NN has sufficient flexibility to approximate the target response.

The weights $w = [\beta_1 \dots \beta_N, \gamma_{10} \dots \gamma_{NM}]$ are randomly initialized and after each model iteration

is updated by backpropagating the error through the network. N denotes the number of observations or targets. The error metric most commonly used is the mean squared error, MSE:

$$MSE = \sum_{i=1}^N (f(X_i) - t_i)^2 \quad \text{EQ A4}$$

The weights are adjusted in the direction that will decrease the error and training continues until a stopping criterion is reached. We chose to set aside 20% of the training data as a test set to be used for early stopping, and terminated training when the MSE of the test set failed to improve for 10 consecutive iterations.

Bootstrapping is used to account for model variability and estimate confidence and prediction intervals by training NN on B different realizations of the dataset, where B is the number of bootstrapped samples, we used $B = 30$ (Heskes, 1997; Khosravi & Nahavandi, 2010). An individual NN generates point outputs approximating a target function with no information on the confidence in those estimates (Khosravi & Nahavandi, 2010). However, there are usually multiple $f(X, w)$ that approximate $F(X)$ because of the random weight initializations (Weigend & LeBaron, 1994). As such, there are two sources of error we are concerned with, the accuracy of our estimation of $F(X)$ and the accuracy of our estimates with respect to the target. A confidence interval describes the first (e.g. $F(X) - f(X, w)$) while a prediction interval describes the latter (eg. $t(X) - f(X, w)$) (Heskes, 1997). By definition, a prediction interval contains the confidence interval because:

$$t(X) - f(X, w) = [F(X) - f(X, w)] + \varepsilon(X) \quad \text{EQ A5}$$

For $b = 1 \dots B$, a random sample with replacement of size p is drawn from the original dataset. Setting p equal to the size of the original dataset yields a set of B training sets each containing approximately 67% of the original dataset. The 33% leftover from each bootstrap sampled can

be used for model validation (Heskes, 1997). The average of our ensemble of networks can then serve as our approximation of $F(X)$:

$$F(X) = \frac{1}{B} \sum_{b=1}^B f_b(X, W) \quad \text{EQ A6}$$

The variance of the model outputs is:

$$\sigma^2(X) = \frac{1}{B-1} \sum_{b=1}^B (f_b(X, W) - F(X))^2 \quad \text{EQ A7}$$

A confidence interval (CI) for $F(X)$ can be calculated as $F(X) \pm t_{(1-\alpha, df)} \sigma(X)$, where t is the students t-score, $1-\alpha$ is the desired confidence level, and df are the degrees of freedom which are set to the number of bootstrapped samples B . NN performance can be seen to improve with the inclusion of more factors, until the model saturates and becomes over-parametrized (Fig A1).

Random forests (RF) are said to be among the best performing gap filling methods for NME (Kim et al. 2020). And it has been claimed that aggregating many regression trees in a RF prevents overfitting (Breiman, 2001;). We did not find this to be the case. Following the methods outlined in Kim et al. (2020): a RF with 400 trees and no restrictions on tree size fit F_{CH4} nearly perfectly ($R^2 = 0.98$). Without considerable limitations on tree size, the RF will just learn the dataset rather than the relationships present. It is our view that this tree is extremely overfit, as highlighted by the example in Figure A2. Further, RF models do not allow for straightforward visualization of functional relationships in a dataset. Plotting F_{CH4} against VWC, which is the dominant environmental control identified does not reveal a meaningful relationship like Figure 2.5 a & c. Individual decision trees can be examined within the RF, but those are difficult to interpret beyond the first few splits, and each tree will be different. Lastly, RF are incapable of projecting beyond the parameter space observed which limited their applicability for this study (Fig A2). This presents an issue because may gaps in EC data arise from data filtering

(e.g. clear calm nights, precipitation events) and are by definition outside the parameter space observed.

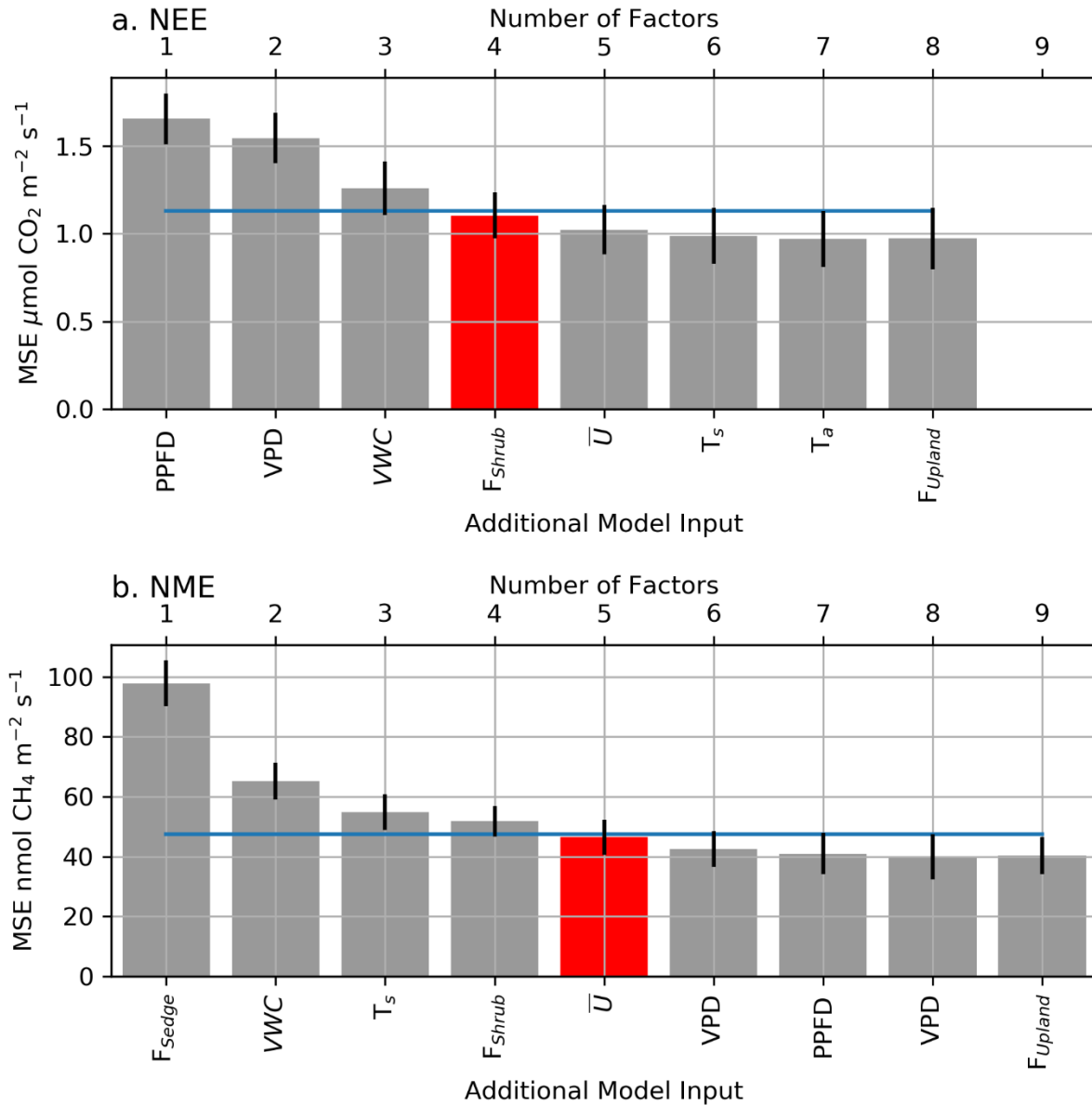


Figure A.5.1: The averaged mean squared error (MSE) of the bootstrapped Neural Network model validation datasets, with error bars showing one standard error (SE). The x axis shows models of increasing size from left to right (1-9 factors), and the label indicates the factor added to the model at each step. The blue line indicates the 1-SE rule threshold and the red bar indicates the model selected by the 1-SE rule.

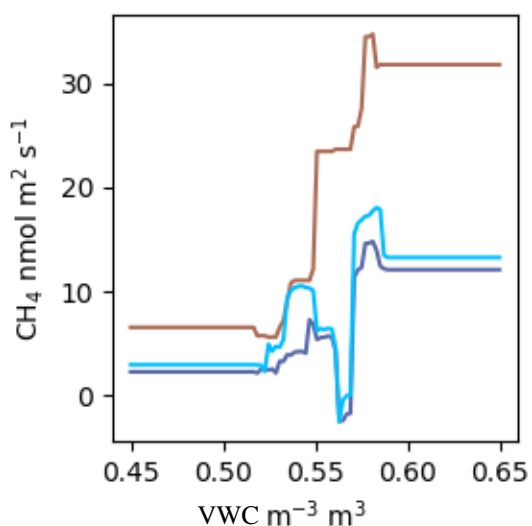


Figure A.5.2: F_{CH_4} estimated by a RF using the same factors as the NN model. The colours correspond to the scenarios in Fig 5a. VWC was estimated over the range 0.45 to 0.65.

Appendix B

This section contains supplemental figures supporting Chapter 3.

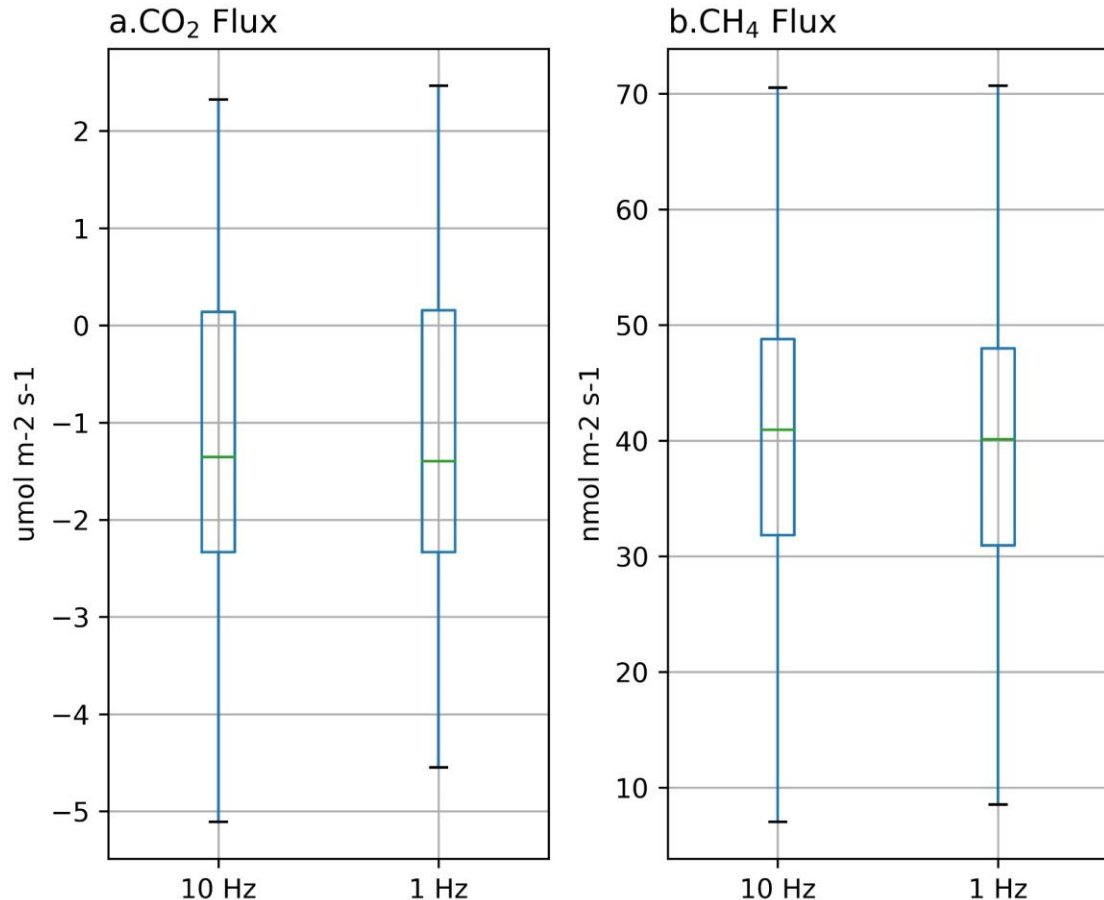


Figure B.1. Boxplots of the 10 Hz flux data and down sampled 1hz flux data (every tenth value) for the period of July 13th – 29th (a. CO₂ and b. CH₄). The mean of the 10 and 1hz CO₂ fluxes for this period were -1.195 and 1.196, respectively with standard deviations of 1.485 and 1.481, respectively. The mean of the 10 and 1hz CH₄ fluxes for this period were -39.59 and 39.40, respectively with standard deviations of 11.17 and 11.77, respectively.

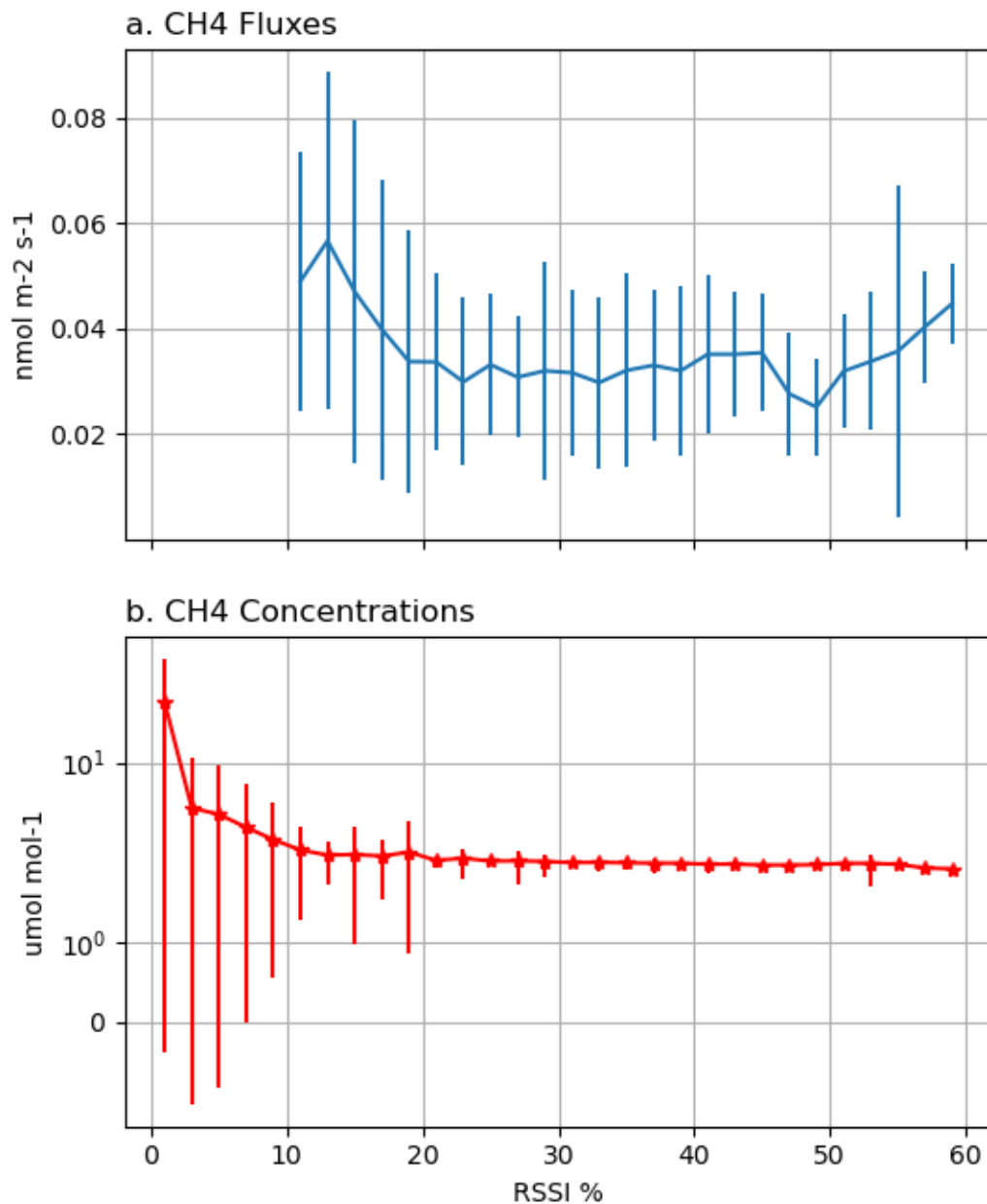


Figure B.2. CH₄ fluxes before post processing (a.) and CH₄ concentrations (b.) plotted against RSSI %. Note the y-axis of b. is plotted on a symmetric log scale. RSSI is the signal strength index for the LI-7700 CH₄ analyzer.

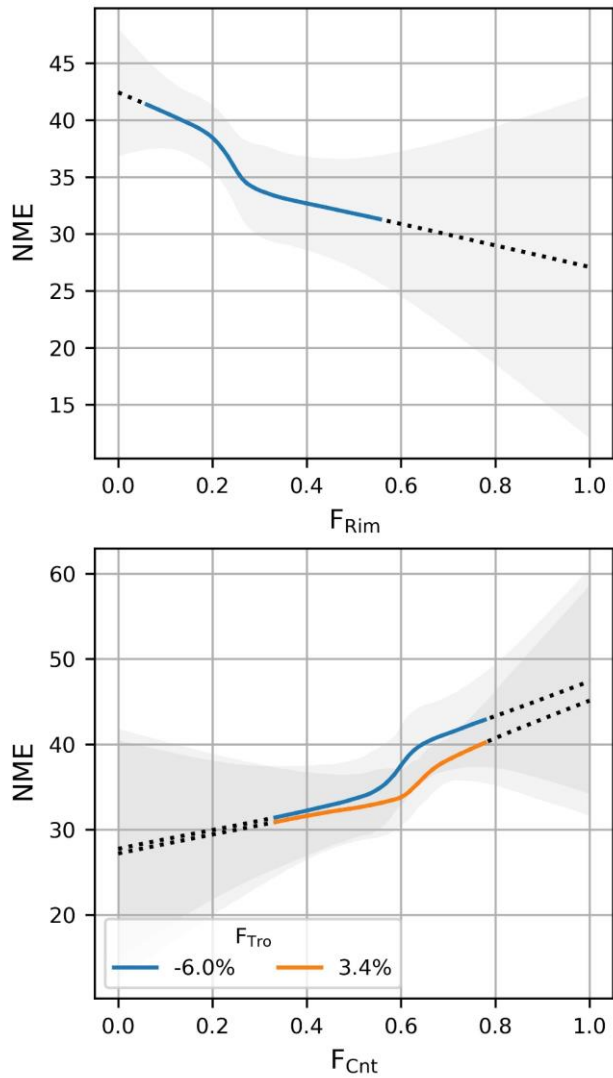


Figure B.3. Modeled estimates of NME under average conditions from 0-100% F_{Rim} (a.) and F_{Cnt} (b.) For a. linear regression was used to calculate F_{Cnt} from F_{Rim} (slope = -0.809, intercept = 0.810, r^2 = 0.936). For b. linear regression was used to calculate F_{Rim} from F_{Cnt} (slope = -1.157, intercept = 0.952, r^2 = 0.936) but F_{Rim} was offset by +3.4% and -6.0% to reflect the range of observed trough fraction (F_{Tro}). Troughs are minor fraction of the total landscape, but they may be disproportionate CH₄ sources because they were frequently below the water table in 2017. All other drivers were fixed at their median values.